STARS

2009

Phase-field Simulation Of Microstructural Development Induced By Interdiffusion Fluxes Under Multiple Gradients

Rashmi Mohanty
University of Central Florida

PHASE-FIELD SIMULATION OF MICROSTRUCTURAL DEVELOPMENT INDUCED BY INTERDIFFUSION FLUXES UNDER MULTIPLE GRADIENTS

by

RASHMI RANJAN MOHANTY
M.E, Indian Institute of Science, Bangalore, India
B.E, National Institute of Technology, Rourkela, India

A dissertation submitted in partial fulfillment of the requirements
for the degree of Doctor of Philosophy
in the Department of Mechanical, Materials and Aerospace Engineering
in the College of Engineering and Computer Science
at the University of Central Florida
Orlando, Florida

Spring Term
2009

Major Professor: Yongho Sohn

ABSTRACT

The diffuse-interface phase-field model is a powerful method to simulate and predict mesoscale microstructure evolution in materials using fundamental properties of thermodynamics and kinetics. The objective of this dissertation is to develop phase-field model for simulation and prediction of interdiffusion behavior and evolution of microstructure in multi-phase binary and ternary systems under composition and/or temperature gradients. Simulations were carried out with emphasis on multicomponent diffusional interactions in single-phase system, and microstructure evolution in multiphase systems using thermodynamics and kinetics of real systems such as Ni-Al and Ni-Cr-Al. In addition, selected experimental studies were carried out to examine interdiffusion and microstructure evolution in Ni-Cr-Al and Fe-Ni-Al alloys at 1000°C. Based on Onsager's formalism, a phase-field model was developed *for the first time* to simulate the diffusion process under an applied temperature gradient (i.e., thermotransport) in single- and two-phase binary alloys.

Development of concentration profiles with uphill diffusion and the occurrence of zero-flux planes were studied in single-phase diffusion couples using a regular solution model for a hypothetical ternary system. Zero-flux plane for a component was observed to develop for diffusion couples at the composition that corresponds to the activity of that component in one of the terminal alloys. Morphological evolution of interphase boundary in solid-to-solid two-phase diffusion couples (*fcc-γ* vs. *B2*-β) was examined in Ni-Cr-Al system with actual thermodynamic data and concentration dependent chemical mobility. With the instability introduced as a small initial compositional fluctuation at the interphase boundary, the evolution of the interface morphology was found to vary largely as a function of terminal alloys and related composition-

dependent chemical mobility. In a binary Ni-Al system, multiphase diffusion couples of fcc-γ vs. $L1_2$-γ', γ vs. $\gamma+\gamma'$ and $\gamma+\gamma'$ vs. $\gamma+\gamma'$ were simulated with alloys of varying compositions and volume fractions of second phase (i.e., γ'). Chemical mobility as a function of composition was employed in the study with constant gradient energy coefficient, and their effects on the final interdiffusion microstructure was examined. Interdiffusion microstructure was characterized by the type of boundaries formed, i.e. Type 0, Type I, and Type II boundaries, following various experimental observations in literature and thermodynamic considerations. Volume fraction profiles of alloy phases present in the diffusion couples were measured to quantitatively analyze the formation or dissolution of phases across the boundaries. Kinetics of dissolution of γ' phase was found to be a function of interdiffusion coefficients that can vary with composition and temperature.

The evolution of interdiffusion microstructures in ternary Ni-Cr-Al solid-to-solid diffusion couples containing fcc-γ and $\gamma+\beta$ (fcc+B2) alloys was studied using a 2D phase-field model. Alloys of varying compositions and volume fractions of the second phase (β) were used to simulate the dissolution kinetics of the β phase. Semi-implicit Fourier-spectral method was used to solve the governing equations with chemical mobility as a function of compositions. The simulation results showed that the rate of dissolution of the β phase (i.e., recession of $\beta+\gamma$ two-phase region) was dependent on the composition of the single-phase γ alloy and the volume fraction of the β phase in the two-phase alloy of the couple. Higher Cr and Al content in the γ alloy and higher volume fraction of β in the $\gamma+\beta$ alloy lower the rate of dissolution. Simulated results were found to be in good agreement with the experimental observations in ternary Ni-Cr-Al solid-to-solid diffusion couples containing γ and $\gamma+\beta$ alloys.

For the first time, a phase-field model was developed to simulate the diffusion process under an applied temperature gradient (i.e., thermotransport) in multiphase binary alloys. Starting from the phenomenological description of Onsager's formalism, the field kinetic equations are derived and applied to single-phase and two-phase binary system. Simulation results show that a concentration gradient develops due to preferential movement of atoms towards the cold and hot end of an initially homogeneous single-phase binary alloy subjected to a temperature gradient. The temperature gradient causes the redistribution of both constituents and phases in the two-phase binary alloy. The direction of movement of elements depends on their atomic mobility and heat of transport values.

This work is dedicated to my parents.

ACKNOWLEDGMENTS

I would like to express my sincere gratitude to Dr. Yong-Ho Sohn, my adviser, who has provided me continuous support, guidance and encouragement. Without his help, this dissertation would not have been possible. My sincere appreciation goes to all the committee members. I would also like to thank all the faculty and staffs of the department of Mechanical, Materials and Aerospace Engineering (MMAE), Advanced Materials Processing and Analysis Center (AMPAC), and Materials Characterization Facility (MCF) for their cooperation throughout my Ph.D. Special thanks to all my colleagues in the Laboratory of Materials and Coatings for Extreme Environment (MCEE) for their support and help. Finally, my special thanks go to my family and friends for their support and understanding.

TABLE OF CONTENTS

LIST OF FIGURES

LIST OF TABLES

CHAPTER 1
INTRODUCTION

1.1. General Background

The phenomenon of atomic migration or diffusion has been the subject of investigation for more than 150 years. Though diffusion is important in non-crystalline materials, the majority of diffusion studies are concerned with crystalline solids. The reason behind this can be attributed to the fact that diffusion plays an important and often a decisive role in many phase transformations and microstructure evolution processes, which generally control the properties and subsequently the performance of a crystalline solid. Experimental studies of diffusion generally pertain to the determination of diffusion coefficients that usually provide an understanding of the diffusional interactions among the components and the overall diffusion behavior of the material. The experimental procedure and the diffusion formalism used for these studies are fairly straightforward for a binary system. However, most of the commercial material systems usually contain more than two components where multicomponent diffusion is the norm. Due to manifold increase in interactions among the components the diffusion formalism as well as the experimental investigations become increasingly difficult and cumbersome as the number of components increases in a system.

A basis for the study of interdiffusion behavior in multicomponent systems is Onsager's formalism [1,2] that provides an extension of Fick's law to enable the inclusion of more than two components in its description. This involves the determination of $(n - 1)^2$ interdiffusion coefficients in an n-component system. For example, description of diffusion in a ternary system requires the determination of four interdiffusion coefficients. These coefficients can be

determined experimentally by means of two independent isothermal diffusion couples, which have one common composition in their diffusion zone, or in other words their composition paths cross each other [3,4]. When the interdiffusion coefficients are assumed constant, an analytical solution to the diffusion equation by means of an error function can easily describe the isothermal composition profiles of a diffusion couple. But in practice, the interdiffusion coefficients are generally composition dependent and an analytical error function solution may not be adequate to describe the composition profiles. Hence, numerical methods are often sought for this purpose. Furthermore, because of the difficulty associated, the experimental determination of diffusion coefficients in a multicomponent system may not be always viable.

Diffusion requires driving forces for the atomic migration. A single driving force or a combination of several driving forces may be present, which can influence the diffusion process. The driving force arises due to several factors including a chemical potential gradient, applied electrostatic field, and an applied temperature gradient. To attain thermodynamic equilibrium it is not only necessary that temperature and pressure be the same throughout, but also the chemical potentials of elements are the same everywhere in the system. Under such cases Fick's law may not be adequate to describe the interdiffusion process and a more phenomenological approach is necessary, where the diffusion flux needs to be represented as a function of all the driving forces acting on the system [5]. In this approach the non-equilibrium diffusion fluxes are represented by the gradients in chemical potentials instead of the gradients in compositions as used in the Fick's law. This theory of non-equilibrium thermodynamics known as thermodynamics of irreversible processes is based on certain fundamental postulates derived from Onsager's phenomenological theorem. The approach expresses atomic fluxes of components as linear combinations of all the

relevant forces where more fundamental parameters such as atomic mobilities can be used instead of diffusivities.

It is well known that being a thermally activated process, interdiffusion can significantly alter the microstructure of a material under high temperature, which can affect its performance. Such effects of interdiffusion are often encountered in various practical applications. One application where the effect of interdiffusion becomes evident is at the interface of two materials joined together to serve as a substrate-coating assembly for high temperature operations, as in gas turbine blades. In these systems the microstructure of the coating typically contains a high temperature resistant second phase dispersed in a matrix, which acts as a protective barrier for high temperature oxidation and corrosion, e.g. bond coats in thermal barrier coatings. As a specific example, Nickel based overlay coatings are extensively used in high temperature applications of aero and marine gas turbine engines. These coatings are generally used as external protective oxidation resistant coatings (ORCs) or as bond coats between the superalloy substrate and the ceramic layer in thermal barrier coatings (TBC). The primary role of ORCs and bond coats is to provide adequate Al for selective oxidation to form an external protective Al_2O_3 layer or a thermally grown oxide (TGO) layer of Al_2O_3, respectively [6]. The performance and lifetime of these coatings depend on the stability of the Al-rich high temperature phase, e.g. B2-β (NiAl) or L1$_2$-γ' (Ni$_3$Al). It has been observed that the continuous oxidation and coating-substrate interdiffusion simultaneously depletes the Al content in the coatings causing dissolution of β or γ' phase that consequently results in the failure of coatings [7-9]. Interdiffusion can also cause Kirkendal porosity at the interface leading to the failure of the coating. Diffusion of additive elements in superalloy substrate for high temperature strengthening can adversely affect the thermo-mechanical properties at the interface, including

3

phase constituents and adherence qualities of the oxide scale. Extensive experimental studies have been carried out to study the interdiffusion behavior and lifetime of γ (Ni) + γ' (L1$_2$) coatings on γ (Ni) substrates in Ni-Al alloys [9-14]. Similarly, dissolution of β (B2) phase in γ vs. $\gamma+\beta$ diffusion couples in the Ni-Cr-Al system has been investigated [15,16]. All these studies utilized diffusion couple experiments containing single-phase vs. single-phase, single-phase vs. two-phase and two-phase vs. two-phase couples under isothermal conditions.

One of the most important focuses in recent years in many industrial applications has been to minimize the material volume used while increasing the efficiency and functionality. This has initiated a trend of continuously decreasing length scales of materials in various applications and increasing operating temperatures. With the mounting fuel constraints and the goal for higher integration and further miniaturization, the above trend is going to continue in the future. This could result in a tremendous increase in the temperature gradient under which materials operate in various applications. Some of the important areas of concern are the gas turbine blades, nuclear fuel materials and electronic circuits in microelectronic industries.

As described earlier, diffusion can occur under the influence of various driving forces; one of them is an applied temperature gradient. Temperature-gradient induced mass transport is generally known as thermotransport or thermomigration. This can be defined as the development of a concentration gradient in an otherwise homogeneous material due to temperature gradient. Thermotransport can cause constituent and phase redistribution in a material, and therefore has the potential to induce unwanted phase transformations and/or changes in mechanical and physical properties of the materials.

The main objective of this research is to use computational methods to simulate and predict the interdiffusion behavior and microstructure evolution in materials in the presence of chemical and temperature gradients. Due to advances in numerical methods and computational power, many computational techniques are now frequently employed to model diffusional phase transformations and microstructure evolutions in multicomponent alloys. With the knowledge of materials properties and parameters, and with the help of the aforementioned phenomenological description these computational modeling techniques can also predict interdiffusion behavior in multicomponent material systems. The phase-field model over the past two decades has developed into a powerful tool for modeling meso-scale microstructure evolution in materials. Originally developed for modeling solidification [17-21], the phase-field model owing to its ability to treat multi-phase systems with complicated interface conditions, soon found its applicability in simulating a wide range of processes such as spinodal decomposition [22-29], order-disorder transformations [30-33], cubic to tetragonal transformation [34-39] grain growth and coarsening [40-47], martensitic transformation [48,49], etc. Based on a diffuse interface theory [50], phase-field model can describe the microstructure within the limit of the corresponding sharp interface description. In this model the microstructure is described by a set of field variables, which vary smoothly over the interfaces. Unlike sharp interface models, phase-field model does not require explicit tracking of the interface and accommodates Gibbs-Thompson effect in its description [51]. Moreover, the available thermodynamic and kinetic databases can be directly linked to the phase-field model [52-54] to perform simulations on real alloy systems.

There are a limited number of works reported that simulate and predict the interdiffusion microstructure between the coating and substrate interface by computer modeling [55-56].

5

Though phase-field model has been used in the past to predict microstructure evolution in various material systems, only recently Wu et al. [53,57] used the phase-field model to predict interdiffusion microstructure in multiphase diffusion couples. In this work the phase-field model is used to simulate the interdiffusion behavior in multicomponent diffusion couples under isothermal conditions.

Most of the phase-field simulation studies reported in literature are concerned with the presence of chemical potential gradient under isothermal conditions. There are many studies on continuous transformations and heat treatment processes [58-59] and only a few have been attempted to simulate diffusion behavior under an applied electric field, i.e. electromigration [60-61]. But to the authors knowledge there have been no predictive modeling works reported to account for the thermotransport phenomenon under an applied temperature gradient. In the second part of this work, a phase-field model has been developed for the first time to simulate thermotransport.

1.2 Outline of the Dissertation

The objective of this dissertation is to develop phase-field model for simulation and prediction of interdiffusion behavior and evolution of microstructure in multi-phase binary and ternary systems under composition and/or temperature gradients. Simulations were carried out with emphasis on multicomponent diffusional interactions in single-phase system, and microstructure evolution using thermodynamics and kinetics of real systems such as Ni-Al and Ni-Cr-Al. Selected experimental interdiffusion studies were carried out in Ni-Cr-Al and Fe-Ni-Al alloys to examine the phenomena of demixing of two-phase diffusion couples. For the first

time, a phase-field model was developed to simulate thermotransport in multiphase binary alloys. The dissertation document has been organized into nine chapters.

Chapter 1 contains a brief introduction to the interdiffusion process with some examples related to high temperature applications including thermotransport. The chapter also describes the objective of the present research and the applicability of the phase-field model to simulate solid-state phase transformations and microstructure evolutions under different driving forces.

In Chapter 2, a classical phenomenological description of diffusion based on Fick's law and irreversible thermodynamics is presented. Chapter 3 presents a concise description of the procedure for phase-field model in terms of free energy description and evolution equations along with various numerical techniques. Given this background, phase-field simulation carried out for single-phase and two-phase diffusion couples in one and two dimensions is reported in Chapter 4. Development and analysis of composition profiles in single-phase diffusion couples is described with respect to the thermodynamic description of the system. Also, the development of planar and non-planar interfaces in two-phase solid-to-solid diffusion couples is examined based on initial interface perturbation and composition-dependent chemical mobility.

In Chapter 5, a 2D phase-field model is used to predict the interdiffusion microstructures in γ vs. γ', γ vs. $\gamma+\gamma'$ and $\gamma+\gamma'$ vs. $\gamma+\gamma'$ solid-to-solid diffusion couples in Ni-Al system. Movement of boundaries and dissolution or formation of phases across the boundary is analyzed. Chapter 6 reports the simulation of interdiffusion microstructure of γ vs. $\gamma+\beta$ and $\gamma+\beta$ vs. $\gamma+\beta$ diffusion couples in Ni-Cr-Al system. The dissolution of β phase as a function of composition was studied and compared with experimental results in the literature.

Results from experimental investigations of diffusion couples in Ni-Cr-Al and Fe-Ni-Al alloys are reported and examined with corresponding phase-field simulations in Chapter 7.

In Chapter 8 presented a development of a phase-field model to investigate the diffusion process under an applied thermal gradient or the thermomigration for the first time. Starting from the phenomenological description of Onsager, the field kinetic equations are derived and applied to single-phase and two-phase systems. Constituents and phase redistribution under the gradient of concentration and temperature are presented and discussed with respect to thermo-kinetic coefficients.

Chapter 9 summarizes the contribution of this study and discusses the future directions.

1.3 References

[1]   L. Onsager, Phys. Rev., 1931, 37, 405-26; 1932, 38, pp.2265-79.

[2]   L. Onsager, Ann. NY Acad. Sci., 1965, 46, pp. 241-65.

[3]   J. S. Kirkaldy, Can. J. phys., 1958, 36. 899-906.

[4]   J. S. Kirkaldy, D. J. Young, Diffusion in the Condensed State, The Institute of Metals, London, 1987, 226-72.

[5]   Balluffi RW, Allen SM, Carter WC. "Kinetics of Materials", John Wiley & Sons, Inc., (2005).

[6]   Clarke DR, Levi CG. Annu. Rev. Mater. Res., (2003), 33, p.383.

[7]   Smialek JL and Lowell CE, J. Electrochem. Soc., (1974), 121(6), 800.

[8]   Levine SR, Metall. Trans., (1978), 9A, p.1237.

[9]   Susan DF, Marder AR. Acta Mater., (2001), 49 (7), p.1153.

[10]   Fujiwara K, Horita Z. Acta Mater., (2002), 50 (6), p.1571.

[11]   Ikeda T, Almazouzi A, Numakura H, Koiwa M, Sprengel W, Nakajima H. Acta Mater., (2002), 46 (15), p.5369

[12]   Numakura, H, Ikeda T, Mat. Sc. Eng. A., (2000), A312, p.109

[13]   Watanabe M, Horita Z, Smith DJ, McCartney MR, Sano T, Nemoto M. Acta Met. Mater., (1994), 42(10), p.3381

[14]   Watanabe M, Horita M, Sano T, Nemoto M. Acta Met. Mater., (1994), 42(10), p.3389

[15]   Nesbitt JA, Heckel RW. Metall. Trans. A., (1987), 18A, p.2061.

[16]   Jin C, Morral JE. Scripta. Mater., (1997), 37, p.621.

[17]   Kobayashi R. Physica D 1993;63:410.

[18]   Wheeler AA, Boettinger WJ, McFadden GB. Phys Rev A, 1992;45:7424.

[19]   Caginalp G, Xie W. Phys Rev E 1993;48:1897.

[20]   Kim SG, Kim WT, Suzuki T. Phys Rev E 1999;60:7186.

[21]   Karma A, Lee YH, Plapp M. Phys Rev E 2000;61:3996.

[22]   H. Nishimori and A. Onuki. Phys. Rev., B42, 980(1990).

[23]   A. Onuki and H. Nishimori. Phys. Rev., B43, 13649(1991).

[24]   A. Onuki. J. Phys. Soc., Jpn 58, 3065(1989).

[25]   C. Sagui, A.M. Somoza and R. Desai. Phys. Rev., E50, 4865(1994).

[26]   C. Sagui, D. Orlikowski, A. Somoza and C. Roland. Phys. Rev., E58, 569(1998).

[27]   Y. Wang, L.Q. Chen and A.G. Khachaturyan. Acta Metall. Mater., 41, 279 (1993).

[28]   T.M. Rogers, K.R. Elder and R.C. Desai. Phys. Rev., B37, 9638(1988).

[29] D.J. Seol, S.Y. Hu, Y.L. Li, J. Shen, K.H. Oh and L.Q. Chen. Acta Mater., 51, 5173(2003).

[30] Y. Wang, D. Banerjee, C.C. Su and A.G. Khachaturyan. Acta Mater., 46, 2983(1998).

[31] D.Y. Li and L.Q. Chen. Acta Mater., 47, 247-57(1998).

[32] V. Venugopalan and L.Q. Chen. Scripta Mater., 42, 967(2000).

[33] Y.H. Wen, Y. Wang, A.L. Bendersky and L.Q. Chen. Acta Mater., 48, 4125(2000).

[34] L. Proville and A. Finel. Phys. Rev., B64, 054104(2001).

[35] D.N. Fan and L.Q. Chen. J. Am. Ceram. Soc., 78, 769(1995).

[36] Y. Wang, H.Y. Wang, L.Q. Chen and A.G. Khachaturyan. J. Am. Ceram. Soc., 76,3029(1993).

[37] D.N. Fan and L.Q. Chen. J. Am. Ceram. Soc., 78, 1680(1995).

[38] Y. Le Bouar, A. Loiseau and A.G. Khachaturyan. Acta Mater., 46, 2777(1998).

[39] Y. Le Bouar and A.G. Khachaturyan. Acta Mater., 48, 1705 (2000).

[40] L.Q. Chen and Y.H. Wen. Phys. Rev., B50, 15752(1994).

[41] I. Steinbach, F. Pezzolla, B. Nestler, M. Seesselberg. R. Prieler, et al. Physica D, 94,135(1996).

[42] D.N. Fan and L.Q. Chen. Philos. Mag. Lett., 75, 187(1997).

[43] D.N. Fan and L.Q. Chen. Acta Mater., 45, 611(1997).

[44] B. Nestler. J. Cryst. Growth, 204, 224(1999).

[45] D.N. Fan and L.Q. Chen. J. Am. Ceram. Soc., 80, 1773(1997).

[46] A. Kazaryan, Y. Wang, S.A. Dregia and B.R. Patton. Phys. Rev., B61, 14275(2000).

[47] A. Kazaryan, Y. Wang, S.A. Dregia and B.R. Patton. Phys. Rev., B63, 184102(2001).

[48] Y. Wang and A.G. Khachaturyan. Acta Mater., 45, 759(1997).

[49]   Y.M. Jin, A. Artemev and A.G. Khachaturyan. Acta Mater., 49, 2309(2001).

[50]   Chen LQ. Annu. Rev. Mater. Res., (2002), 32, p.113.

[51]   Cahn JW, Hilliard JE. J. Chem. Phys., (1958), 28(2), p.258.

[52]   Grafe U, Botteger B, Tiaden J and Fries SG. Scripta Mater., (2000), 42, p.1179.

[53]   Wu K, Chang YA, Wang Y. Scripta Mater., (2004), 50, p.1145.

[54]   Chen Q, Ma N, Wu K , Wang Y. Scripta Mater., (2003), 50, p. 471.

[55]   Engstrom A, Morral JE, Agren J. Acta mater. 1997; 45: 1189.

[56]   Campbell C, Boettinger WJ, KAttner UR. Acta mater. 2002; 50: 775.

[57]   Wu K, Morral, JE, Wang Y. Acta mater. 2001; 49: 3401.

[58]   B. Böttger, J. Eiken, and I. Steinbach, Acta Mater., 54, 2006, 2697.

[59]   Wen Y, Wang B, Simmons JP, Wang Y. Acta mater. 2006; 54: 2087.

[60]   M. Mahadevan, R. M. Bradley, Physica D, 126, 1999, 201.

[61]   M. Mahadevan, R. M. Bradley, Physical Rev. B, 59(16), 1999,11037.

CHAPTER 2
INTERDIFFUSION IN MULTICOMPONENT ALLOYS

2.1 Diffusion Under a Concentration Gradient

2.1.1 Fick's Law of Diffusion

In 1855 Adolf Fick described diffusion in solids by a simple yet powerful equation [1], which is known after him, and has been used in numerous diffusion studies. Fick's 1st law relates the flux of a component to its concentration gradient, and is similar in form to Ohm's law for current density or to the basic heat-flow equation. This was derived on the basis that matter flows from a region of higher to lower concentration to decrease the concentration gradient. The flow ceases when the concentration becomes the same everywhere. In one dimension Fick's 1st law is written as

$$J_i = -D_i \frac{\partial c_i}{\partial x} \tag{2.1}$$

where, c_i and J_i are, respectively, the concentration and flux of component i. D_i is the diffusion coefficient and is assumed independent of the concentration gradient. In three dimensions, Fick's law can be written as:

$$\mathbf{J}_i = -\mathbf{D}_i \nabla c \tag{2.2}$$

where $\mathbf{D}$ is a second-rank tensor. Depending on the type of reference frame used to define the diffusion equation, the flux and the diffusion coefficients can have different annotations. In the

lattice fixed frame of reference, they represent the intrinsic flux and intrinsic diffusion coefficient, whereas in the laboratory fixed frame of reference, they are denoted as the interdiffusion flux and interdiffusion coefficient [2].

Apart from the concentration gradient, the flow of matter can also be caused by an external force or driving force if present in the system. Such a driving force can cause the particles to move with a velocity v and produce a flux contribution of vc_i. Therefore, the flux can be expressed in one dimension as a combination of the Fickian or diffusional flux due to concentration gradient and drift term due to the driving force [3].

$$J_i = -D_i \frac{\partial c_i}{\partial x} + vc_i \qquad (2.3)$$

The effect of the driving force on diffusion will be discussed in more detail in the next section by means of thermodynamics of irreversible processes.

The flux equations described in Equation 2.1 through 2.3 do not provide information on the variation in composition with time. For the time-dependent case where the flux varies at every point with time in one dimension, the continuity equation can be invoked to describe the variation of concentration with time:

$$\frac{\partial c_i}{\partial t} = -\frac{\partial J}{\partial x} = \frac{\partial}{\partial x}\left(D\frac{\partial c_i}{\partial x}\right) - \frac{\partial}{\partial x}(vc) \qquad (2.4)$$

In the absence of the drift term the above equation would contain only the first term on its right hand side known as Fick's 2nd law:

$$\frac{\partial c_i}{\partial t} = \frac{\partial}{\partial x}\left(D\frac{\partial c_i}{\partial x}\right) \tag{2.5}$$

This equation is a second-order partial differential equation for which, if the diffusivity is constant, it is possible to obtain explicit analytical solutions depending on the type of initial and boundary conditions [4]. When the diffusivity is a function of composition or position, as is the case in real situations, an analytical solution is difficult to obtain, and numerical methods are used [5].

2.1.2 Onsager's Formalism of Fick's Law

The diffusion process becomes more complex in an *n*-component system. The complexity arises because all the elements interact with each other, and the diffusion of one element is no more only due to its own concentration gradient, but is also due to the concentration gradients of other elements present. Therefore, for a complete description of the diffusion process in an *n*-component system, $(n-1)^2$ diffusion coefficients are necessary with $(n-1)$ independent composition variables and their gradients. This is described by invoking the phenomenological description of diffusion based on Onsager's formalism that extends Fick's law [6-8] into multicomponent systems. According to this formalism the interdiffusion flux $\tilde{J}_i$ of element *i* in an *n*-component system is expressed by:

$$\tilde{J}_i = -\sum_{j=1}^{n-1}\tilde{D}_{ij}^n\frac{\partial c_i}{\partial x} \qquad (i = 1, 2, ..., n\text{-}1), \tag{2.6}$$

where $\tilde{D}_{ij}^n$ are the interdiffusion coefficients and n is the dependent component. Similarly, in the lattice fixed frame of reference the intrinsic flux J_i of component i is expressed by:

$$J_i = -\sum_{j=1}^{n-1} D_{ij}^n \frac{\partial c_i}{\partial x} \qquad (i = 1, 2, ..., n\text{-}1), \qquad (2.7)$$

where D_{ij}^n are the intrinsic diffusion coefficients. The relationship between the interdiffusion and intrinsic diffusion fluxes is given by

$$\tilde{J}_i = J_i + c_i v_m, \qquad (2.8)$$

where v_m is the velocity of the lattice frame relative to the laboratory fixed frame of reference [2].

2.2 Diffusion Under a Temperature Gradient

In addition to mass fluxes caused by the presence of composition gradients in an isothermal system, a temperature gradient alone can also produce such fluxes. This leads to the redistribution of compositions in an initially homogeneous system, and is known as the thermotransport or thermomigration effect. This phenomenon is also called the Ludwig-Soret effect or simply the Soret effect.

For a multicomponent system with a unidirectional temperature gradient, the intrinsic flux of an element in the direction parallel to the direction of temperature gradient can be obtained by the modification of Fick's 1st law [9]:

15

$$J_i = -\sum_{j=1}^{n-1} D_{ij}^n \frac{\partial c_i}{\partial x} - c_i \beta_i Q_i^* \frac{1}{T}\frac{\partial T}{\partial x} \qquad (i = 1, 2, ..., n\text{-}1), \qquad (2.9)$$

where β_i is the atomic mobility of the element i and Q_i^* is called the heat of transport term, which is a measure of the heat carrying capacity of an atom. Q_i^* can be either positive or negative and determines the direction and magnitude of the temperature gradient contribution to the total flux. The physical definition of Q_i^* arises from the concepts of irreversible thermodynamics, which will be considered in Chapter 8 in detail. Expressions for interdiffusion fluxes are similar to those of intrinsic fluxes and they are again related through Equation 2.8.

It can be implied from Equation 2.9 that a steady state can be obtained in a closed system when $J_i = 0$. This happens when the flux contribution due to composition gradient becomes equal and opposite in direction to the contribution due to temperature gradient. Experimental determination of Q^* is generally done at steady state, as it does not require the knowledge of diffusion coefficient and the absolute value of composition. At steady state, using Einstein relationship $D_i = \beta_i RT$ Equation 2.9 can be written as:

$$-\frac{Q_i^*}{T}\frac{dT}{dx} \cong \frac{RTd\ln(c_i)}{dx} \qquad (2.10)$$

or

$$\ln(c_i) = \frac{Q_i^*}{R} d\left(\frac{1}{T}\right), \qquad (2.11)$$

16

where R is the universal gas constant. With this equation Q_i^* values can be determined by plotting ln c_i vs. 1/T. Q_i^* values in various materials have been reviewed by Oriani [10]. It should be noted here that for an interstitial binary solution thermotransport behavior could be described by means of one flux equation that requires only the Q^* value of the interstitial element. Whereas, in substitutional solutions, Q^* values of all the elements are required in order to describe the thermotransport flux [11].

2.2 Phenomenological Theory of Diffusion

In Section 2.1, Fick's law was introduced as the elementary law of diffusion on the basis of its analogy with other physical laws such as Ohm's law. This was done without proper justification of the nature of the driving force for diffusion. The macroscopic nature of Fick's law requires a more rigorous analysis to derive its exact relations with the type of driving forces present. Being an irreversible process, a general formulation for diffusion is therefore obtained from thermodynamics of irreversible processes [7]. The formalism is based on the Onsager reciprocity theorem, which has been the subject of many extensive analyses [12]. In this section a brief overview of the thermodynamics of irreversible processes is provided, while its applications to diffusion in the presence of chemical and thermal driving forces are described in Chapter 4 and Chapter 8, respectively.

2.2.1 Definition of Fluxes, Forces and Rate of Entropy Production

In order to approach equilibrium in a system that contains gradients of temperature, chemical potential, and other intensive thermodynamic driving forces, flow of extensive

17

quantities such as heat, mass, etc., is required. The gradients of intensive quantities are the driving forces, which are associated with the fluxes, and in general, the fluxes may be a function of all the driving forces acting in the system:

$$J_\Phi = J_\Phi \left(F_\Phi, F_q, F_e, ..., F_i \right), \tag{2.12}$$

where F_Φ is the conjugate force of the flux J_Φ. At near equilibrium, when the driving forces are small, a Taylor series expansion of fluxes near the equilibrium point [4] can produce a relationship between the flux and the driving forces, which can be represented in its abbreviated form:

$$J_\alpha = \sum_\beta L_{\alpha\beta} F_\beta \qquad (\alpha, \beta = \phi, q, e, ...,i), \tag{2.13}$$

where, the coefficients $L_{\alpha\beta}$ are called phenomenological coefficients. The diagonal terms, $L_{\alpha\alpha}$, are called direct coefficients as they couple each flux to its conjugate driving force and the off-diagonal terms, $L_{\alpha\beta}$, are called coupling coefficients which represent the cross effects.

Production of entropy is the characteristic feature of an irreversible process, and the basic postulate of irreversible thermodynamics is mainly based on the rate of entropy production. It states that near equilibrium or when the departure from thermodynamic equilibrium is sufficiently small, the entropy production is nonnegative:

$$\dot\sigma \equiv \frac{\partial s}{\partial t} + \nabla \cdot \vec{J}_s \geq 0, \tag{2.14}$$

18

where, J_s is the entropy flux.

Howard and Lidiard [14] extended the calculation of the rate of entropy production for fluids given by de Groot [12] and de Groot and Mazur [15] to solids with minor modification. The rate of entropy production per unit volume is given by

$$T\sigma = \sum_k^n J_k \cdot X_k + J_q \cdot X_q + \text{viscosity terms}, \tag{2.15}$$

where, J_k and J_q are the fluxes of component k and heat, respectively. X_k and X_q are the imbalances or forces that generate these fluxes. For solids the viscosity terms are generally negligible. If F_k is the external force per atom of component k, and μ_k is the chemical potential of k (i.e. the partial derivative of the Gibbs free energy with respect to the number of atoms of k), then

$$X_k = F_k - T\nabla\left(\mu_k / T\right) \tag{2.16}$$

and

$$X_q = -\frac{1}{T}\nabla(T) \text{ with } \nabla \equiv \text{ gradient operator.} \tag{2.17}$$

2.2.2 Onsager Reciprocity Theorem

Onsager reciprocity theorem governs the relationship between the fluxes and the forces through linear macroscopic laws. These linear laws include cross-phenomena, such as the

influence of concentration or chemical potential gradient of one component upon the flow of another, or the effect of temperature gradient on the flow of constituent components. Neglecting the viscous forces, the laws can be written as:

$$J_k = \sum_i^n L_{ki} X_i + L_{kq} X_q \qquad (2.18a)$$

$$J_q = \sum_i^n L_{qi} X_i + L_{qq} X_q . \qquad (2.18b)$$

According to Onsager's theorem the matrix of the phenomenological coefficients **L** is symmetric if magnetic fields and rotations are absent, as expressed by:

$$L_{ik} = L_{ki} \text{ and } L_{qi} = L_{iq} . \qquad (2.19)$$

The second law of thermodynamics states that the rate of entropy production is always semi-positive definite, i.e. the function in Equation 2.15 is greater than or equal to zero. Substitution of fluxes defined in Equation 2.18 into Equation 2.15 would the provide the following inequalities:

$$L_{ii} \geq 0 \qquad \text{(for all i)} \qquad (2.20a)$$

$$L_{qq} \geq 0 \qquad (2.20b)$$

$$L_{ii} L_{kk} - L_{ik} L_{ki} \geq 0 \qquad (2.20c)$$

$$L_{ii} L_{qq} - L_{iq} L_{qi} \geq 0 \qquad \text{(for all i, k)} \qquad (2.20d)$$

These phenomenological coefficients are kinetic parameters that are dependent on the thermodynamics of the system and are independent of the forces X_k to which the system may be subjected.

2.2.3 Alternative Fluxes and Forces

In certain cases it is useful to have alternative choices of fluxes and forces to represent the same phenomena. These alternate choices are made through the transformation of the original quantities. If the entropy production is given by the Equation 2.15 and the Onsager relations are obeyed, then for the symmetric L matrix:

$$L = \tilde{L} \quad (\tilde{L} \text{ is the transpose of } \mathbf{L}). \tag{2.21}$$

The entropy production σ can be rewritten as:

$$T\sigma = \tilde{J}X = \tilde{J}'X = \tilde{J}'\tilde{X}', \tag{2.22}$$

Here the new fluxes J_i' and the new forces X'_i are related to the original quantities through the transformations expressed by:

$$J' = AJ \tag{2.23a}$$

and

$$X' = \tilde{A}^{-1}X, \tag{2.23b}$$

21

where **A** is a non-singular matrix. Equation 2.22 is invariant under the transformations given in Equation 2.21. Rewriting the phenomenological equation 2.18 as:

$$J = LX,\qquad(2.22)$$

it follows that

$$J' = AJ = ALX = AL\tilde{A}X' \equiv L'X'\qquad(2.23)$$

and if **L** is symmetric then so is **L'**. Thus, if the Onsager relations are valid for the original fluxes and forces, they are also valid for the transformed quantities.

The importance of this kind of transformation as given in Equation 2.23 is realized when a temperature gradient exists in the system. A commonly used transformation for this purpose is as follows:

$$J'_k = J_k\qquad(2.24a)$$

$$J'_q = J_q - \sum_{k}^{n} h_k J_k\qquad(2.24b)$$

with

$$X'_k = X_k + h_k X_q\qquad(2.24c)$$

$$X'_q = X_q,\qquad(2.24d)$$

where h_k is the partial enthalpy of component k and J'_q is the reduced heat flow, which is obtained by subtracting from the total heat flow the part that is associated with the mass flow. Now the new forces can be defined explicitly by

$$X'_k = F_k - (\nabla \mu_k)_T \tag{2.25a}$$

and

$$X'_q = -\frac{1}{T} \nabla T, \tag{2.25b}$$

where $(\nabla \mu_k)_T$ is the part of the gradient of μ_k due to gradients in pressure or concentration, but not temperature. This transformation is utilized in the simulation of the thermotransport effect described in Chapter 8.

2.2.4 Diffusion Coefficients and Phenomenological Coefficients

To show how the intrinsic diffusion coefficients and interdiffusion coefficients are related through the phenomenological coefficients, a simple isothermal binary system is used where a vacancy mechanism of diffusion is assumed to operate and vacancies are everywhere present in their equilibrium concentrations, i.e. $\mu_v = 0$ and $X_v = 0$. For an isothermal system in the absence of any external fields, fluxes of atoms of A and B relative to the local lattice frame of reference can be defined as:

$$J_A = L_{AA}X_A + L_{AB}X_B, \tag{2.26a}$$

$$J_B = L_{BA}X_A + L_{BB}X_B, \tag{2.26b}$$

where X_A and X_B are the chemical potential gradients of A and B. Using Gibbs-Duhem relation $c_A X_A + c_B X_B = 0$ in which c_A and c_B are the mole fractions of A and B respectively, J_A becomes

$$J_A = \left(L_{AA} - \frac{c_A}{c_B} L_{AB} \right) X_A .$$
(2.27)

Defining chemical potential as:

$$\mu_A = \mu_A^\circ (T,P) + kT\ln\left(c_A \gamma_A \right),$$
(2.28)

where k is the Boltzmann constant and γ_A is the activity coefficient, the following expression is obtained.

$$J_A = -\left(\frac{L_{AA}}{c_A} - \frac{L_{AB}}{c_B} \right) kT\left(1 + \frac{\partial \ln \gamma_A}{\partial \ln c_A} \right) \nabla c_A .$$
(2.29)

Comparing this with Fick's 1st law given in Equation 2.1, the intrinsic diffusion coefficient of A can be defined as:

$$D_A = \frac{kT}{n} \left(\frac{L_{AA}}{c_A} - \frac{L_{AB}}{c_B} \right) \left(1 + \frac{\partial \ln \gamma_A}{\partial \ln c_A} \right) ,$$
(2.30a)

where n is the total number of lattice sites per unit volume. A similar equation is obtained for the intrinsic diffusion coefficient of component B, as:

$$D_B = \frac{kT}{n} \left(\frac{L_{BB}}{c_B} - \frac{L_{BA}}{c_A} \right) \left(1 + \frac{\partial \ln \gamma_B}{\partial \ln c_B} \right)$$
(2.30b)

24

2.3 Summary

The purpose of the present chapter was to provide a very basic introduction of the general diffusion equations namely, Fick's 1st and 2nd laws, and also to briefly review the theory of irreversible thermodynamics as applicable to the diffusion process. Diffusion in solids is a very well documented subject and detailed description can be found from many sources [2-4,13]. Nevertheless, there are few comments to be made before closing this chapter.

In solids, the rate of diffusion can vary significantly in the regions of structural irregularities such as grain boundaries, dislocations, etc., and the applicability of Equations 2.1 through 2.4 depends on the length scale of the irregularities. If the scale is appreciably small compared to the size of the diffusion zone, the above equations can be used to provide an overall description of the diffusion process in the system with an effective diffusion coefficient that is an average over those distinct regions. This work is concerned only with the diffusion in a regular crystal lattice, and diffusion through grain boundaries, dislocations and other irregularities are neglected.

Diffusion coefficients of components are not directly used in this work. Instead chemical mobilities are used, which are functions of atomic mobilities and compositions. Though the proper analogy between them will be shown in the following chapters, it can be said at this point that the chemical mobilities are related to diffusivities in the actual system. In many crystal lattice the diffusion coefficient, being a second-rank tensor, can have different values in different directions. Hence, for simplicity, the diffusion coefficients and other mobilities in the present work are considered isotropic and diffusion is assumed to occur along one principal direction. Such approximations make it possible to use only one diffusion coefficient for each element and

treat them as scalars. Wherever appropriate, the temperature and the concentration dependence of diffusion coefficients has been considered through the description of atomic and chemical mobilities. The last factors in Equation 2.30a and 2.30b are equal to one another by Gibbs-Duhem relation, but this generally does not hold for ternary and higher order alloys. Nevertheless, the description shown in Section 2.2.4 can easily be extended to ternary systems and will be shown in Chapter 4. A similar treatment is presented in Chapter 8 to include temperature gradient or thermotransport effect.

2.4 References

[1]   A. Fick, Progg. Ann., vol. 94 (1855) pp.59.

[2]   P. Shewmon, <u>Diffusion in Solids</u>, 2nd Edition, The Minerals, Metals and Materials Socety, Warrendale, PA (1989).

[3]   J. Philibert, <u>Atom Movements - Diffusion and Mass Transport in Solids</u>, Les Edition de Phisique, Paris (1991).

[4]   R. W. Balluffi, S. M. Allen, W. C. Carter, <u>Kinetics of Materials</u>, 1st Edition, John Wiley & Sons, Inc., New Jersey (2005).

[5]   J. Crank, <u>Mathematics of Diffusion</u>, 2nd Edition, Clarendon Press, Oxford (1975).

[6]   L. Onsager, Phys. Rev., vol. 37 (1931) pp. 405.

[7]   L. Onsager, Phys. Rev., vol. 38 (1931) pp. 2265.

[8]   L. Onsager, Ann. New York Acad. Sci., vol. 46 (1945) pp. 241.

[9]   J. R. manning, <u>Diffusion Kinetics for Atoms in Crystals</u>, D. Van Nostrand Co., Inc. (1968).

[10] R. A. Oriani, J. phys. Chem. Sol., vol. 30 (1969) pp. 339.

[11] D. Jaffe, P.G. Shewmon, Acta Metall. 12 (1964) pp. 515.

[12] S. R. De Groot, Thermodynamics of Irreversible Processes, North-Holland Publishing Co., Amsterdam, 1st Edition, (1952).

[13] A. R. Allnatt, A. B. Lidiard, Atomic Transport in Solids, Cambridge University Press, Cambridge, 1st Edition, (1993).

[14] R.E. Howard, A.B. Lidiard, Rep. Prog. Phys., vol.27 (1964) pp.161.

[15] S. R. De Groot, P. Mazur, Non-Equilibrium Thermodynamics, North-Holland Publishing Co., Amsterdam, 1st Edition, (1962).

CHAPTER 3
THEORY OF THE PHASE-FIELD MODEL

The field of computational materials science and engineering has made fast progress in last couple of decades owing to the tremendous advancements in computational methods and power. Among various modeling methods used at different length scales, the phase-field method has emerged as a powerful computational approach to model and predict mesoscale morphological and microstructure evolution in materials. The phase-field model is based on the diffuse-interface description, which was developed mainly by Cahn and Hilliard [1] almost 40 years ago. The term "phase-field" is derived from the way the spatial and temporal order parameter fields are defined in a continuum diffuse-interface model. In other words, the phase-field model uses a set of conserved and/or non-conserved field variables that are continuous across the interfacial regions and their spatial distribution describes the microstructure in the material. It is worth mentioning here that a parallel advancement in the field of computational thermodynamics and kinetics led to the development of various packages like ThermoCalc™ and DICTRA™. The ability of the phase-field model to directly link to the database of the packages made it possible to predict the evolution of arbitrary morphologies and complex microstructures in many real material systems and processes.

Microstructure is compositional and structural inhomogeneity that may consist of spatially distributed phases of different compositions and/or crystal structures, grains of different orientations, domains of different structural variants, domains of different electric or magnetic polarizations, and structural defects. The size, shape, and spatial arrangement of these structural features usually have a length scale in nanometers to micrometers range, and they play a critical role in determining the physical and mechanical properties of materials. Microstructure evolution

28

in materials occurs to reduce the total free energy of the system, and the phase-field model is based on the minimization of this energy.

Mathematically the microstructure evolution process is nonlinear in nature and numerical methods are often required to find the solution. Conventional approaches known as sharp interface models treat the boundary between two compositional or structural domains as a sharp interface, over which a field variable varies discontinuously. This treatment requires explicit tracking of the interface position, which can be possible in one-dimensional systems, but becomes impractical in two- or three-dimensions. In contrast to the conventional sharp interface models, the phase-field model does not require the explicit tracking of the positions of a moving interface and contains the corresponding sharp- or thin-interface descriptions as a particular limit [2]. The temporal evolution of the field variables is governed by the Cahn-Hilliard nonlinear diffusion equation [3], and the Allen-Cahn relaxation equation or time-dependent Ginzburg-Landau equation [4].

Applications of phase-field models are divided into two main categories depending on the nature of field variables. One is the interface-tracking approach, where field variables have no physical meaning and are merely introduced for the sole purpose of avoiding tracking of interfaces. This approach is used in all solidification modeling. In the other case, the field variables correspond to well-defined physical order parameters such as long-range order parameters for order-disorder transformations and the composition fields for phase separations. Phase-field models can also be classified as those derived from a thermodynamic formulation and those derived from geometrical arguments. A brief overview of phase-field model is provided in this chapter.

3.1 General Overview

The following steps can describe a general procedure for the phase-field model. The first step involves the determination of the number and the type of field variables in order to properly describe the microstructure. As mentioned earlier, simulation of the temporal and spatial microstructure evolutions requires knowledge of the total free energy of the inhomogeneous microstructure. In the second step the total free energy of microstructure G is defined as a function of field variables, which can be a sum of the chemical free energy density (f_c), the gradient energy density (f_{grad}), the elastic strain energy density (f_{el}), and the energy contributions (f_{ex}) due to the presence of any external force fields such as electric and magnetic fields. The total energy functional G can be written as:

$$G\big[c_i(r,t), \eta(r,t)\big] = \int_r \Big[f_c\big(c_i, \eta_j\big) + f_{grad}\big(c_i, \eta_j\big) + f_{el}\big(c_i, \eta_j\big) + f_{ex}\big(c_i, \eta_j\big) \Big] dr^3 \tag{3.1}$$

where $c_i(\mathbf{r},t)$ and $\eta_i(\mathbf{r},t)$ are the order parameters of the conserved and non-conserved fields, respectively, and are functions of spatial position $\mathbf{r}$ and time t. The subscripts i and j are used to distinguish different species, phases or domains. The chemical free energy and gradient energy are the contributions to total energy caused by the short-range chemical interactions. The gradient energy term is non-zero only at and around the interfaces, and it defines the interfacial energy. The other two energy contributions (f_{el} and f_{ex}) are from any one or more of the long-range interactions, such as elastic interactions, dipole-dipole interactions, electrostatic interactions, etc. The treatment of various contributions to the total energy distinguishes one phase-field model from the other. Finally, the temporal evolution of field variables are obtained

by applying Cahn-Hilliard and Allen-Cahn or Ginzburg-Landau (TGL) equations and finding their numerical solutions with the available materials parameters as input.

3.2. Free Energy Description

3.2.1 Chemical Free Energy

One of the important components in a phase-field model is the chemical free energy or local free energy density function. Depending on the requirements of the system, several types of description for chemical free energy are used, but they can be mainly classified into two categories. One is based on the Landau expansion method [5] that expresses the chemical free energy as a polynomial expansion with respect to the order parameters. The other is the case where the chemical free energies of different phases are well defined and are connected to each other continuously by phase-field variables.

Landau Expansion for a System with Different Crystal Structure Phases:

A Landau expansion can be used in those solid-state phase transformations where the field variables correspond to well-defined physical order parameters. The local free energy density function is then expressed as a polynomial of order parameters, where all the terms in the expansion are required to be invariant with respect to the symmetry operations of the high-temperature phase [6]. Precipitation of an ordered phase ($L1_2$) from a disordered face-centered-cubic (FCC) matrix in a binary alloy is an example of such transformations, for which the chemical free energy can be described by a polynomial with expansion terms up to the fourth order as given by [7-11]:

31

$$f(c, \eta_1, \eta_2, \eta_3) = f_o(c, T) + \frac{1}{2} B_2(c, T)(\eta_1^2 + \eta_2^2 + \eta_3^2) + \frac{1}{3} B_3(c, T)\eta_1 \eta_2 \eta_3$$
$$+ \frac{1}{4} B_{41}(c, T)(\eta_1^4 + \eta_2^4 + \eta_3^4) + \frac{1}{4} B_{42}(c, T)(\eta_1^2 \eta_2^2 + \eta_2^2 \eta_3^2 + \eta_1^2 \eta_3^2)$$

(3.2)

where $f_o(c, T)$ is the free energy of the disordered phase, and B_1, B_2, B_3, B_{41} and B_{42} are the expansion coefficients that are functions of composition and temperature. This free energy corresponds to a non-equilibrium free energy of a spatially homogeneous state. To obtain the equilibrium state, the coefficients B_i need to be chosen in such a way that they provide a global minimum corresponding to the L1$_2$ phase. If $B_3(c, T) < 0$, the free energy minima would be located at

$$(\eta_o, \eta_o, \eta_o), (\eta_o, -\eta_o, -\eta_o), (-\eta_o, \eta_o, -\eta_o), (-\eta_o, -\eta_o, \eta_o),$$

(3.3)

where η_o is the equilibrium long-range order parameter at a given composition and temperature and is determined by the solution of the following equation.

$$\frac{\partial f(c, \eta_1, \eta_2, \eta_3)}{\partial \eta_p} = 0, \text{ where } p = 1, 2, 3$$

(3.4)

The free energy of the ordered phase, as a function of composition, is obtained by substituting the equilibrium order parameter values from Equation 3.4, which also describes the four energetically and structurally equivalent antiphase domains of L1$_2$ ordered phase

Use of Thermodynamic Database for a system with Different Crystal Structure Phases

If the free energy expressions for the phases present in the alloy are known, then they can be combined by means of the order parameters to construct a continuous chemical free energy function. This approach was first proposed for the phase-field model for alloy solidification [12-14], but can be used for solid-state transformations. The basic methodology of this approach is as follows.

Consider a two-phase binary A-B alloy where phases α and β have different crystal structures and their chemical free energies are denoted by $f^{\alpha}(c,T)$ and $f^{\beta}(c,T)$, respectively. Here, c is the composition of the component B and T is the temperature. The free energy data can be obtained from various thermodynamic databases such as ThermoCalc[TM], Pandat[TM], etc. The phase-field variable $\phi(\mathrm{r},t)$, which corresponds to the probability of finding the β phase at position $\mathbf{r}$ and time t, varies between 0 and 1. Therefore, the conditions $\phi=0$ and $\phi=1$ correspond to α and β single phases, respectively. Now the total chemical free energy of the two-phase mixture can be obtained as a function of c and ϕ, which is expressed as

$$f(c,\phi,T)=f^{\alpha}(c,T)\left[1-p(\phi)\right]+f^{\beta}(c,T)p(\phi)+w^{\alpha\beta}(T)g(\phi) \qquad (3.5)$$

where $g(\phi)$ is a double-well function, $p(\phi)$ is an interpolating function [15], and $w^{\alpha\beta}$ is the height of the energy barrier or the double well potential. A common choice for these two functions is

$$g(\phi)=\phi^{2}\left(1-\phi\right)^{2} \qquad (3.6)$$

and

$$p(\phi)=\phi^{3}\left(6\phi^{2}-15\phi+10\right). \qquad (3.7)$$

Note that the functions are chosen in such a way that $g(\phi)$ and $p(\phi)$ become 0 and 1 when $\phi = 0$ and $\phi = 1$, respectively. They also ensure that $\partial f / \partial \phi = 0$ when $\phi = 0$ and $\phi = 1$. The free energy surface defined by Equation 3.6 has no strict physical meaning. For instance, the atomic arrangement that corresponds to the state of $\phi = 0.5$ is not defined in the phase-field model, and is not necessary due to the continuum nature of the model where only the energy is evaluated depending on the local order parameter values.

This model can easily be extended to define the chemical free energy of a multicomponent and multiphase system:

$$f\left(c_1, c_2, ..., c_n, \phi_1, \phi_2, ..., \phi_p, T\right) = \sum_{i=1}^{p} f^{\alpha_i}\left(c_1, c_2, ..., c_n, T\right) p(\phi_i) + \frac{1}{2} \sum_{i=1}^{p} \sum_{j=1}^{p} w^{\alpha_i \alpha_j}(T) g\left(\phi_i, \phi_j\right), \quad (3.8)$$

where n and p are the number of components and phases, respectively. The function $f^{\alpha_i}\left(c_1, c_2, ..., c_n, T\right)$ is the free energy of the phase α_I, and the phase-field variable $\phi_i(\mathbf{r}, t)$ again corresponds to the probability of finding the phase α_i at position $\mathbf{r}$ and time t. Therefore, the following condition must be satisfied along with the condition for conservation of mass as:

$$\sum_{i=1}^{p} \phi_i(\mathbf{r}, t) = 1. \quad (3.9)$$

For a binary system the $g\left(\phi_i, \phi_j\right) \equiv \left(1 - \delta_{ij}\right) \phi_i^2 \phi_j^2$ and for other multicomponent systems $g\left(\phi_i, \phi_j\right) \equiv \left(1 - \delta_{ij}\right) \phi_i \phi_j$, where δ_{ij} is Kronecker's delta, given by $\delta_{ij} = 1$ for $i = j$ and $\delta_{ij} = 0$ for $i \neq j$.

3.2.2 Gradient Energy

Interfaces are associated with compositional and/or structural inhomogeneities and are inherent features of a microstructure. Interfaces are often the sites of excess free energy known as the interfacial energy. In phase-field approach, the interfacial energy is expressed by means of gradient energy terms, which are generally derived by the gradient square approximation of the order parameter profile as described by Cahn and Hilliard in their classic work [1]. The gradient energy is expressed as:

$$F_{grad} = \int_r \left[\tfrac{1}{2} \sum_{i=1}^{n} \kappa_c \left(\nabla c_i\right)^2 + \tfrac{1}{2} \sum_{i=1}^{p} \kappa_\Phi \left|\nabla \Phi_i\right|^2 \right] dr, \qquad (3.10)$$

where κ_c and κ_ϕ are the gradient energy coefficients. For composition or long-range order parameter fields, the gradient energy coefficients can be expressed in terms of pair-wise interactions. In diffuse interface theory, as will be shown later, the interfacial energy is a combination of gradient energy and chemical free energy.

Free Energy of a Flat Interface

Following Cahn and Hilliard [1], the energy of a flat interface between two phases, α and β, can be considered as described below. Let us consider a binary alloy A-B system where the solute composition of B component is referred to c(r,t). Assuming the composition gradient ∇c and the curvature $\nabla^2 c$ as independent variables, the chemical free energy of an inhomogeneous solution can be expanded in Taylor series form as:

$$f\left(c,\nabla c,\nabla^2 c\right) \cong f_0\left(c,0,0\right) + K_0\left(c\right)\left(\nabla c\right) + K_1\left(c\right)\left(\nabla^2 c\right) + K_2\left(c\right)\left(\nabla c\right)^2, \qquad (3.11)$$

35

where the higher order terms have been ignored and the function $f_0(c,0,0)$ corresponds to chemical free energy of a homogeneous solution. $K_i(c)$ is an expansion coefficient considered as a function of composition. These coefficients, in general, are tensors reflecting crystal symmetry (tensor notations have been omitted for simplicity) and for a cubic or an isotropic case $K_0 = 0$. Then, Equation 3.11 reduces to:

$$f(c, \nabla c, \nabla^2 c) \cong f_0(c,0,0) + K_1(c)(\nabla^2 c) + K_2(c)(\nabla c)^2 . \qquad (3.12)$$

By integrating the gradient terms over a volume V of the solution, the gradient energy can now be expressed as:

$$
\begin{aligned}
F_{grad} &= \int_V \left[K_1(c)(\nabla^2 c) + K_2(c)(\nabla c)^2 \right] dV \\
&= \int_V \left[K_2(c) - \frac{\partial K_1}{\partial c} \right](\nabla c)^2 dV
\end{aligned}
\qquad (3.13)
$$

where, Gauss's divergence theorem $\int_V f \nabla \cdot g \, dV = \int_S f g \cdot n \, dS - \int_V \nabla f \cdot g \, dV$ is used. By choosing a boundary of integration in such a manner that $\nabla c \cdot n = 0$ at the boundary, the first term on the right hand side of Equation 3.13 is represented as:

$$\int_V K_1(c)(\nabla^2 c) dV = -\int_V \frac{\partial K_1}{\partial c}(\nabla c)^2 dV . \qquad (3.14)$$

Defining the gradient energy coefficient $\kappa(c)$ by:

$$\kappa(c) = K_2(c) - \frac{\partial K_1}{\partial c} , \qquad (3.15)$$

36

the expression for the gradient energy is finally obtained as:

$$F_{grad} = \int_V \kappa(c)(\nabla c)^2 \, dV .$$

(3.16)

$\kappa(c)$ is often assumed to be constant in many applications.

Using Equation 3.16 for a one dimensional composition change across the interface, the total free energy of the system can be written as:

$$F = A \int_{-\infty}^{+\infty} \left[f_0(c) + \kappa(\nabla c)^2 \right] dx .$$

(3.17)

Cahn and Hilliard defined the specific interfacial energy, σ, as the difference per unit area of interface between the actual free energy of the system and that which it would have if the properties of the phases were continuous throughout. Therefore, σ is defined by:

$$\sigma = \int_{-\infty}^{+\infty} \left[\Delta f(c) + \kappa(\nabla c)^2 \right] dx ,$$

(3.18)

where $\Delta f(c)$ is defined as the free energy referred to a standard state of an equilibrium mixture of two phases, i.e.,

$$\Delta f(c) = f_0(c) - \left[c\mu_B(e) + (1-c)\mu_A(e) \right]$$
$$= c\left[\mu_B(c) - \mu_B(e) \right] + (1-c)\left[\mu_A(c) - \mu_A(e) \right]$$

(3.19)

where $\mu_A(e)$ and $\mu_B(e)$ are the chemical potentials of species A and B in the two phases.

37

In practice, it is difficult to measure interfacial free energy by direct experimental techniques, but the fact that measurable quantities are sensitive to the interfacial free energy has made it possible for the development of indirect techniques. Most of these techniques have been used for pure materials and binary alloys, and have been reviewed comprehensively [16-18]. Recently, grain boundary groove technique [19,20] is applied to determine both the solid/liquid and solid/solid interfacial energy. Computationally, atomistic simulation has emerged as a promising technique [21] for the determination of interfacial energy. In most phase-field calculations, the gradient energy coefficient is generally obtained by relating it to the known interfacial energy and other parameters, or used as pure approximations such that it meets the requirements of the system under consideration. Nevertheless, phase-field methods have been used extensively to address interfaces in binary, ternary, and three phase systems [22-24].

3.2.3 Elastic Strain Energy

During coherent phase transformations in solids, lattice mismatch between phases and domains are accommodated by elastic displacements in order to maintain continuity of lattice planes and directions across the interfaces. This causes the transformation-induced elastic strain, which is particularly essential in the development of some important microstructural features such as multiphase patterns in alloys responsible for many technologically important properties. Though the strain effect has not been considered in this work, a general description on its incorporation into the phase-field equations will be provided here for the sake of completeness of this chapter.

The strain effect is generally incorporated into the phase-field equations by means of the strain energy (F_{el}) as a functional of concentration or order parameter fields, which forms a part of the total free energy functional, F. The description is based on Khachaturyan's general theory of elastic strain energy [6], which can be reformulated to write the strain energy as a functional of phase-field variables. In Khachaturyan's approach, the multiphase heterogeneous microstructure is treated as a coherent aggregate of discrete and internally homogeneous particles of constituent phases and their orientation variants, with the local crystalline state corresponding to either the parent or product phase. Hence, the strain energy of an arbitrary distribution of coherent precipitates of arbitrary geometry is represented as a functional of the stress-free strain field, $\varepsilon_{ij}^{0}(\mathbf{r})$. If the point $\mathbf{r}$ lies within the parent phase, $\varepsilon_{ij}^{0}(\mathbf{r}) = 0$, otherwise it takes one of the values, $\varepsilon_{ij}^{00}(p)$, $(p=1,2,...,n)$, if the point $\mathbf{r}$ is within the pth type of particle. The tensor $\varepsilon_{ij}^{00}(p)$ describes the stress-free transformation strain that transforms the parent phase into the new phase particle of pth type at the stress-free state. However, in the phase-field approach, the multiphase microstructure is described by continuous concentration ($c(\mathbf{r})$) and/or structure order parameter ($\eta(\mathbf{r})$) fields, and the strain energy needs to be expressed through these fields. Therefore, following a similar approach to Equation 3.11, and writing only the first non-vanishing term of the Taylor expansion of the strain with respect to composition or order parameter, the stress-free strain can be written as:

$$\varepsilon_{ij}^{0}(\mathbf{r}) = \left[c(\mathbf{r}) - c_0 \right] \varepsilon_{ij}^{00}, \tag{3.20}$$

$$\varepsilon_{ij}^{0}(\mathbf{r}) = \sum_{p=1}^{n} \eta_p^2(\mathbf{r}) \varepsilon_{ij}^{00}(p), \tag{3.21}$$

where c_o is the average composition and

$$\varepsilon_{ij}^{00} = \frac{1}{a}\frac{da}{dc} \tag{3.22}$$

$$\varepsilon_{ij}^{00}(p) = \frac{1}{\left(\eta_p^0\right)^2}\frac{a_p - a_m}{a_m}, \tag{3.23}$$

Here, η_p^0 is the equilibrium value of the structure order parameter, a_p and a_m are the lattice parameters of the equilibrium product and matrix phases at the stress-free state, respectively. The elastic strain energy density is calculated by:

$$f_{el}(c,\eta) = \frac{1}{2}\sigma_{ij}\left(\varepsilon_{ij} - \varepsilon_{ij}^0\right), \tag{3.24}$$

where σ_{ij} is the local elastic stress and the unknown total local train ε_{ij} is determined by solving the following mechanical equilibrium condition,

$$\frac{\partial \sigma_{ij}}{\partial r_j} = 0, \tag{3.25}$$

Based on the linear elasticity theory and Hook's law

$$\sigma_{ij} = \lambda_{ijkl}\left(\varepsilon_{kl}(r) - \varepsilon_{kl}^0(r)\right), \tag{3.26}$$

where λ_{ijkl} is the elastic moduli tensor.

The strain energy functional can be written as

40

$$F_{el} = \frac{1}{2} \int \frac{d^3k}{(2\pi)^3} B\left(\frac{\mathbf{k}}{k}\right) |\tilde{c}(\mathbf{k})|^2 \qquad (3.27)$$

if the strain is associated with the concentration heterogeneity, or

$$F_{el} = \frac{1}{2} \sum_{pq} \int \frac{d^3k}{(2\pi)^3} B_{pq}\left(\frac{\mathbf{k}}{k}\right) \left\{\eta_p^2(\mathbf{r})\right\}_{\mathbf{k}} \left\{\eta_q^2(\mathbf{r})\right\}_{\mathbf{k}}^* \qquad (3.28)$$

if the strain is associated with the structure order parameters heterogeneity resulting in symmetry changes. In Equation 3.27 and 3.28, $e = \mathbf{k}/k$ is a unit vector in the reciprocal space and e_i is the ith component, $\tilde{c}(\mathbf{k})$ and $\left\{\eta_p^2(\mathbf{r})\right\}_{\mathbf{k}}$ are the Fourier transform of $c(\mathbf{r})$ and $\eta^2(\mathbf{r})$, respectively, and $\left\{\eta_q^2(\mathbf{r})\right\}_{\mathbf{k}}^*$ is the complex conjugate of $\left\{\eta_p^2(\mathbf{r})\right\}_{\mathbf{k}}$. The functions B and B_{pq} are given by

$$B = \lambda_{ijkl}\varepsilon_{ij}^{00}\varepsilon_{kl}^{00} - e_i\sigma_{ij}^0\Omega_{jk}(e)\sigma_{kl}^0 e_l \qquad (3.29)$$

and

$$B_{pq} = \lambda_{ijkl}\varepsilon_{ij}^{00}(p)\varepsilon_{kl}^{00}(q) - e_i\sigma_{ij}^0(p)\Omega_{jk}(e)\sigma_{kl}^0(q)e_l, \qquad (3.30)$$

respectively, where $\Omega_{ij}(e)$ is a Green function tensor, which is the inverse to the tensor $\Omega(e)_{ij}^{-1} = \lambda_{ijkl}e_k e_l$. These functions carry all the information on the elastic properties of a system and the crystallography of the phase transformation.

41

3.3. Evolution Equations and Numerical Solutions

The total free energy of the microstructure (G) is defined as the combination of all the energy contributions, as discussed above. Utilizing this total free energy, the evolution of field variables in a phase-field model can be obtained by solving the following Cahn-Hilliard [1] and Allen-Cahn [4] or time-dependent Ginzburg-Landau (TDGL) equations expressed by:

$$\frac{\partial c_i(\mathrm{r},t)}{\partial t} = \nabla \cdot \left[M_{ij} \left(\nabla \frac{\delta G}{\delta c_j(\mathrm{r},t)} \right) \right] \qquad (3.31)$$

$$\frac{\partial \eta_p(r,t)}{\partial t} = -L_{pq} \frac{\delta G}{\delta \eta_q} = L_{pq} \left[\kappa_\eta \nabla^2 \eta_p - \frac{\partial f}{\partial \eta_q} \right] \qquad (3.32)$$

where the M_{ij} and L_{pq} are the atom or interface mobility associated with the conserved and non-conserved field variables, respectively. They can be functions of the order parameters, but in many calculations, the mobilities are considered as constants for simplicity. The symbol 'δ' in Equation 3.31 and 3.32 denotes variational derivative. The simulation of microstructure evolution is then reduced to finding solutions to the kinetic Equations 3.31 and 3.32.

The non-linear nature of these equations makes it imperative to use numerical methods to obtain their solutions. Though many numerical methods have been proposed and implemented, a simple second-order finite difference method using a uniform spatial grid and explicit time stepping is used in most phase-field models. This explicit scheme suffers from the constraint of a smaller time step to maintain numerical stability. In another method, fast Fourier transformation technique can be used along with periodic boundary conditions to convert the integral-

differential equations into algebraic equations [25-27]. In the reciprocal space, the method provides spectral accuracy for spatial discretization, but is only first-order accurate in time as it uses an explicit forward Euler differencing scheme for time-stepping. This method again suffers from the issues of numerical stability.

Recently, semi-implicit Fourier-spectral methods have been developed [28,29], which are more efficient and accurate in solving the phase-field kinetic equations. Adaptive nonuniform meshing techniques have also been developed which overcome the difficulty of resolving extremely sharp interfaces with moderate number of grid points in uniform grid techniques. Implementation of these real-space adaptive grid algorithms significantly reduces the number of variables, which allows for the use of much larger system and longer simulation time, but at the cost of increased complexities.

3.3.1 Finite Difference Method

Finite difference method (FDM) is based on the discretization of apace and time into finite grids or steps. In FDM, the differential equations are solved on a system discretized into a uniform grid (mesh) of points in real space. FDMs are often categorized on the basis of the discretization scheme used for time, i.e. explicit and implicit. When values at subsequent time step is estimated based on the values from previous time step estimates while moving forward in time, it is called explicit time scheme. Whereas, for implicit schemes progression in time is achieved by estimating the values for subsequent time step based on the estimates from the previous time step and the time step at which the calculation is done. The accuracy of the solutions to the differential equations depends on the degree of discretization; higher order

discretizations provide higher accuracy, but at the cost of computational time. In FDM, forward, central or backward difference algorithms can be used for the spatial discretization, where each scheme has its own advantages and disadvantages, and is suited for specific applications.

A central difference for Laplacian and an explicit forward difference scheme in time for Ginzburg-Landau equation (Equation 3.32), gives rise to a discretized equation of the form (in two-dimension):

$$\frac{\eta_i^{n+1}(x,y) - \eta_i^n(x,y)}{\Delta t} = -L\left[\left(\frac{\partial f}{\partial \eta_i}\right)^n (x,y) - \kappa_n \frac{1}{\Delta^2}\left(\begin{array}{l}\eta_i^n(x+\Delta,y) - \eta_i^n(x-\Delta,y) \\ +\eta_i^n(x,y+\Delta) + \eta_i^n(x,y-\Delta) - 4\eta_i^n(x,y)\end{array}\right)\right] \quad (3.33)$$

where n represents the time discretization and (x,y) represents the spatial discretization. The time step (Δt) used for solving this scheme depends on the grid spacing (Δ), and the magnitude of time step is proportional to the square of grid spacing $(\Delta)^2$ for each Laplacian operator involved. Therefore, the time step is proportional to fourth power of $(\Delta)^4$ for the Cahn-Hilliard equation, which involves two Laplacian operators. The advantages of finite-difference method lies in its flexibility for use with any kind of boundary condition, and also the use of adaptive grid spacing over uniform grid spacing without further mathematical complexities, if required. The disadvantage is the requirement of small time step and hence large computation time.

3.3.2 Semi-implicit Fourier-spectral Method

It is well known that the second and higher order explicit Euler finite difference methods have a time step constraint, which is a consequence of explicit treatment of the biharmonic and

Laplacian operators encountered in the expanded versions of Equations 3.31 and 3.32. For the Cahn-Hilliard equation, the constraint is dictated by $\Delta t \approx (\Delta x)^4$, and for Allen-Cahn or TGL equation by $\Delta t \approx (\Delta x)^2$. The semi-implicit technique proposed by Chen et al [28,29] can provide more efficient and accurate solutions with less number of grid points and larger time steps. A brief description of the method is provided below.

The Cahn-Hilliard equation for a system without elastic energy terms for a binary system can be written as

$$\frac{\partial c}{\partial t} = \nabla \cdot \left[M(c) \nabla \left(g(c) - \kappa \nabla^2 c \right) \right],\tag{3.34}$$

where $g(c) = \partial f / \partial c$ is the bulk driving force term. If the mobility, M, is a constant, the Fourier transform of Equation 3.324 can be written as

$$\frac{\partial \tilde{c}(\mathrm{k},t)}{\partial t} = -k^2 M \tilde{g}(c) - \kappa M k^4 \tilde{c}(\mathrm{k},t),\tag{3.35}$$

where $\mathbf{k} = (k_1, k_2)$ is a vector in the Fourier space with magnitude $k = \sqrt{k_1^2 + k_2^2}$, $\tilde{c}(\mathrm{k},t)$ and $\tilde{g}(c)$ are the Fourier transform of $c(\mathbf{r},t)$ and $g(c)$, respectively. The semi-implicit treatment involves treating the linear fourth order operator explicitly and non-linear terms implicitly. Applying the first order semi-implicit scheme to Equation 3.35, one gets:

$$\tilde{c}^{t+\Delta t} = \frac{\tilde{c}^t - \Delta t k^2 M \tilde{g}(c^t)}{1 + M \kappa k^4 \Delta t},\tag{3.36}$$

where Δt is the time step. In case of a variable mobility in Cahn-Hilliard equation, the semi-implicit scheme produces

$$\frac{\tilde{c}^{t+\Delta t}(\mathrm{k},t)-\tilde{c}^{t}(\mathrm{k},t)}{\Delta t}=i\mathrm{k}\cdot\left\{M(c)\left[i\mathrm{k}'\left(\tilde{g}(c)+\kappa k'^{2}\tilde{c}^{t}(\mathrm{k},t)\right)\right]_{r}\right\}_{k},\qquad(3.37)$$

where $[.]_{k}$ and $[.]_{r}$ represent the forward and reverse Fourier transforms, respectively. However, as described by Chen et al, the above scheme has a severe time constraint dictated by:

$$\Delta t\kappa k^{4}\leq 1\qquad(3.38)$$

This constraint can be eliminated by adding the terms $A\kappa k^{4}\tilde{c}^{t+\Delta t}(\mathrm{k},t)$ and $A\kappa k^{4}\tilde{c}^{t}(\mathrm{k},t)$ to the left and right hand side of the Equation 3.37, where A is a suitable constant.

Following the above approach, implementation of the semi-implicit Fourier-spectral method to the Allen-Cahn or TDGL equation is fairly straightforward. For a system with single structure order parameter field, η, the TDGL Equation 3.32 can be written as

$$\frac{\partial\eta(\mathrm{r},t)}{\partial t}=-L\left(g_{\eta}-\kappa_{\eta}\nabla^{2}\eta\right),\qquad(3.39)$$

where $g_{\eta}=\dfrac{\partial f}{\partial\eta}$. The Fourier transform of the above equation has the following form:

$$\frac{\partial\tilde{\eta}(\mathrm{k},t)}{\partial t}=-L\left[\tilde{g}_{\eta}+\kappa k^{2}\tilde{\eta}(\mathrm{k},t)\right]\qquad(3.40)$$

where $\tilde{\eta}(k,t)$ and $\tilde{g}_\eta$ are the Fourier transform of $\eta(r,t)$ and g_η, respectively. Applying the semi-implicit scheme to Equation 3.40 and rearranging the terms, yield:

$$\tilde{\eta}^{t+\Delta t} = \frac{\tilde{\eta}^t - \Delta t L \tilde{g}_\eta^t}{1 + \kappa_\eta k^2 L \Delta t} \tag{3.41}$$

The accuracy in time for the semi-implicit Fourier-spectral method can be improved by using higher order semi-implicit schemes, such as a second order backward difference for $\partial \tilde{c}/\partial t$ or $\partial \tilde{\eta}/\partial t$ and a second order Adams-Bashforth for the explicit treatment of non-linear terms.

3.4 Summary

The chapter provides a brief description on the general methodology utilized in formulating a phase-field model. The model can deal with arbitrary microstructures produced by diffusional and/or displacive phase transformations without any *priori* assumptions on the microstructure. Within the same physical and mathematical formalism, the phase-field approach can describe different processes such as phase transformations and coarsening. One issue concerning the phase-field model is the length scale of computation. For numerical stability the phase-field model requires the interface to be properly resolved into at least a few grid spacing. This requirement is difficult to meet when the interface is relatively sharp, as in most material systems. Hence, in the phase-field model, the interface width is usually increased artificially, which makes the system size large requiring very long computational time. Nevertheless, the advantages associated with the phase-field approach make it a very attractive tool for modeling microstructure evolutions in materials.

3.5 References

[1]   J. W. Cahn, J. E. Hilliard, J. Chem. Phys., vol.28 (1958) pp.258.

[2]   L. Q. Chen, Annu. Rev. Mater. Res, vol.32 (202) pp.113.

[3]   J. W. Cahn, Acta Metall. Vol.9 (1961) pp.795.

[4]   S. M. Allen, J. W. Cahn, J. Phys., vol.38 (1977) pp. C7-51.

[5]   C. Kittel, H. Kroemer, Thermal Physics, Freeman, New York, (1980).

[6]   A. G. Khachaturyan, Theory of Structural Transformations in Solids, Wiley, New York, (1983).

[7]   Z. W. Lai, Phys. Rev. B, vol.41 (1990) pp.9239.

[8]   R. J. Braun, J. W. Cahn, G. B. McFadden, H. E. Rushmeier, A. A. Wheeler, Acta Mater., vol.46 (1998) pp.1.

[9]   R. J. Braun, J. W. Cahn, G. B. McFadden, A. A. Wheeler, Philos. Trans. R. Soc. London Ser. Vol. A355 (1997), pp.1787

[10] Y . Wang, D. Banerjee, CC Su, A. G. Khachaturyan, Acta Mater., vol.46 (1998) pp.2983.

[11] D. Y. Li, L. Q. Chen, Acta Mater., vol.46 (1998) pp.2983.

[12] R. Kobayashi, Physica D, vol.63 (1993) pp.410.

[13] A. A. Wheeler, W. J. Boettinger, G. B. McFadden, Phys. Rev. vol.45A (1992) pp.7424.

[14] J. A. Warren, W. J. Boettinger, Acta Mater., vol.43 (1995) pp.689.

[15] W. J. Boettinger, J. A. Warren, C. Beckermann, A. Karma, Annu. Rev. Mater. Res, vol.32 (202) pp.163.

[16] D. P. Woodruff, The Solid-Liquid Interface, Cambridge University Press, (1973).

[17] N. Eustathopoulos, Int. Met. Rev., vol.28 (1983) pp.189.

[18] K. F. Kelton, Solid State Phys. Vol.45 (1991) pp.75.

[19] M. Gündüz, J. D. Hunt, Acta Mater., vol.33 (1985) pp.1651.

[20] N. Marasli, J. D. Hunt, Acta Mater., vol.44 (1996) pp.1085.

[21] J. J. Hoyt, M. Asta, A. Karma, Mater. Sci. Eng., vol.41 (2003) pp.R121.

[22] C. Huang, M. Olvera de la Cruz, p. W. Vorhees, Acta Mater., vol.47 (1999) pp.4449.

[23] A. A. Wheeler, W. J. Boettinger, G. B. McFadden, Phys. Rev. E., vol.47 (1993) pp.1893.

[24] T. S. Lo, A. Karma, M. Plapp, , Phys. Rev. E., vol.63 (2001) pp.031504.

[25] Y. Wang, L. Q. Chen, A. G. Khachaturyan, Acta Metall. Mater., vol.41 (1991) pp.279.

[26] D. Fan, L. Q. Chen, J. Am. Ceram. Soc., vol.78 (1991) pp.769.

[27] Y. Wang, L. Q. Chen, A. G. Khachaturyan, J. Am. Ceram. Soc., vol.79 (1991) pp.987.

[28] L. Q. Chen, J. Shen, Comput. Phys. Commun., vol.108 (1998) pp.147.

[29] J. Z, Zhu, L. Q. Chen, J. Shen, V. Tikare, Phys. Rev. E., vol.60 (1999) pp.3564.

CHAPTER 4
CONCENTRATION PROFILES, ZERO-FLUX PLANES AND INTERFACE MORPHOLOGY IN SINGLE-PHASE AND TWO-PHASE TERNARY DIFFUSION COUPLES

4.1 Introduction

The limited number of studies on modeling and prediction of multicomponent diffusion behavior is, first, due to the difficulty associated with determining the diffusion coefficients experimentally, second, due to lack of reliable analytical and numerical methods to handle the composition dependence of the diffusion coefficients, and third, due to the lack of sufficient thermodynamic and kinetic data. Many analytical methods and solutions are available on literature based on the error functions [1-5]. These analytical methods can be used when the diffusion coefficients are assumed constants and is valid only for small compositional heterogeneities. Therefore, numerical methods are necessary to describe the interdiffusion behavior in diffusion couples with concentration-dependent interdiffusion coefficients and large concentration gradients.

Generally, the isothermal interdiffusion in ternary systems is described by means of composition profiles and diffusion paths between the two terminal alloys. A diffusion path, by definition is the locus of the average compositions in planes parallel to the original interface in the diffusion zone of the diffusion couple and is drawn on the ternary isotherm [6]. The diffusion path maps the sequence of compositions developed between the two terminal alloys and is considered time-invariant [7]. It depends on the chemical potential gradient and atomic mobilities of each component. The construction of diffusion path follows a set of general rules [8-13]. For single-phase diffusion couples: (i) a diffusion path is uniquely defined by the

terminal compositions on a ternary isotherm, (ii) for solid-solid diffusion couples under infinite boundary conditions, the diffusion paths must cross the straight line joining the terminal compositions at least once, and (iii) for vapor-solid diffusion couples, the diffusion path need not cross the straight line joining the terminal compositions. A schematic representation of two diffusion paths on a ternary isotherm is shown in Figure 1. The path-I is an s-shaped path that corresponds to a solid-solid diffusion couple a vs. b, and path-II is for a solid-vapor diffusion couple a vs. v. For multiphase diffusion couples, there are additional rules that apply to diffusion paths. For example, when a diffusion path passes through a two-phase region parallel to an equilibrium tie-line, it corresponds to a planar interface whose local equilibrium is specified by that tie-line (e.g. path-III for x vs. z couple in Figure 1). If the diffusion path crosses the two-phase region inclined to an equilibrium tie-line, it corresponds to a wavy or non-planar interface whose local equilibrium is specified by the series of tie-lines (e.g. path-IV for y vs. z couple in Figure 1). Isolated particles of the second phase can develop in the diffusion zone if the diffusion path exits to the same single-phase region it has originated before passing the two-phase region at an angle to tie-lines (e.g. path-V for y vs. p couple in Figure 1).

There are interesting and important phenomena such as occurrence of up-hill diffusion and zero-flux planes that can occur in a ternary diffusion couple during isothermal interdiffusion. The up-hill diffusion, as the name suggests, occurs against the concentration gradient, but down the chemical potential gradient. It was first illustrated by Darken's famous experiment on Fe-C-Si system where up-hill diffusion was observed in the concentration profile of carbon. The reason for this was ascribed to the diffusion of the second solute, silicon, which drives the diffusion of the first, i.e. carbon. A schematic concentration profile illustrating an up-hill diffusion is presented in Figure 2.

51
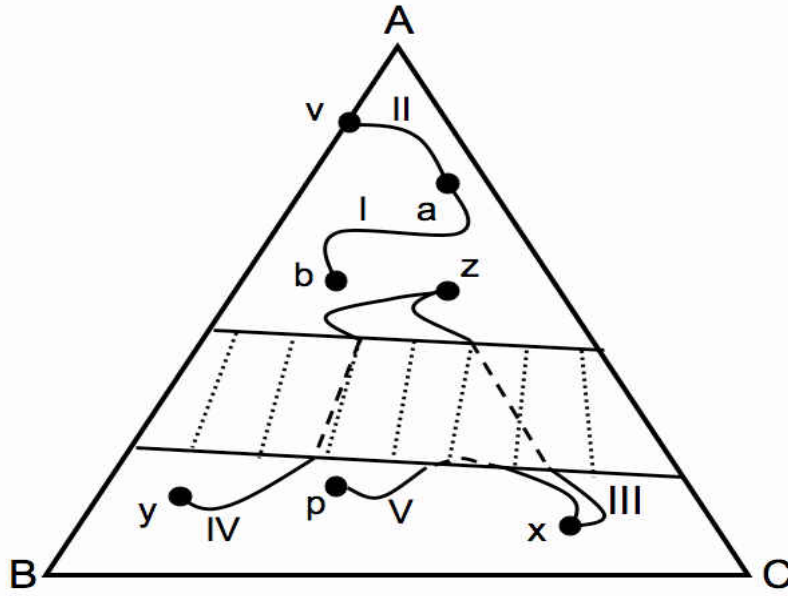
Figure 1: A schematic representation of diffusion paths between single-phase and two-phase diffusion couples depicting various attributes of diffusion paths.

The zero-flux planes (ZFPs) first observed by Dayananda and Kim [14] are the planes in a diffusion couple where the interdiffusion flux of a component goes to zero. A change or reversal in the flux direction occurs on either side of the ZFP. Occurrence of ZFPs has been reported in many ternary alloy systems [15-18], but they are not found in all diffusion couples. Based on their investigations, Dayananda et al. have suggested that ZFPs occur only when the diffusion path drawn on a ternary isotherm intersects one of the isoactivity lines that pass through the terminal alloy compositions, and the composition of the point of intersection corresponds to the composition at the ZFP.
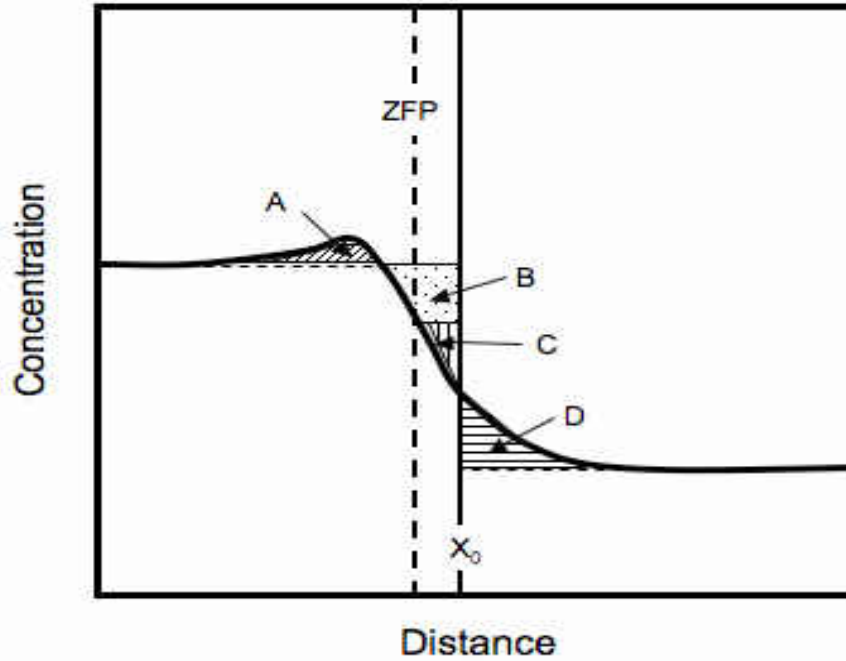
Figure 2: A schematic representation of a composition profile showing up-hill diffusion. Location of the zero flux plane (ZFP) is the point where area A = area B and area C = area D. X_0 is the Matano plane determined by mass balance.
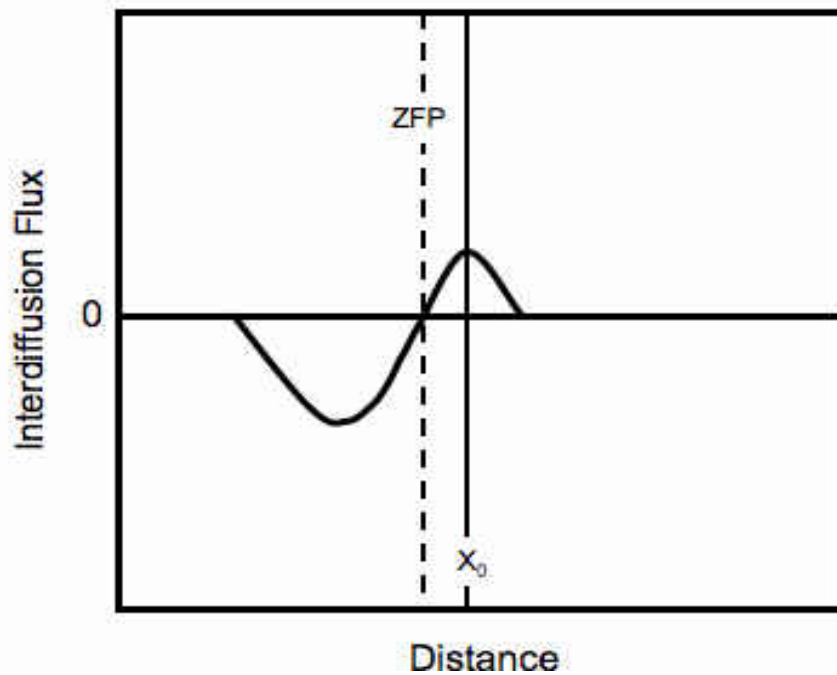
Figure 3: A schematic representation of a flux profile showing one zero flux plane (ZFP) and flux reversal. x0 is the Matano plane determined by mass balance.

Further, based on theoretical analysis, Thompson et al. [19] have shown that the ZFPs occur when the initial concentration differences fall on a specific range. Form the schematic composition profile presented in Figure 2, the location of a zero flux plane can be determined using Boltzmann-Matano analysis [20], which gives the flux of a component at any position in a diffusion couple as being proportional to the integral of its concentration profile. As the interdiffusion flux is zero at the ZFP, according to Matano, Area A = Area B and Area C = Area D, as shown in Figure 2. A schematic of the interdiffusion flux profile is shown in Figure 3, which shows the location of the ZFP and reversal in flux direction.

In multiphase diffusion couples, the regions near the joining interface undergo various morphological and structural changes, which may affect the stability of the interface. Many experimental investigations have been carried out to understand the development of diffusion structures and diffusion paths in various alloy systems such as Ni-Cr-Al and Fe-Ni-Al [21-26]. In these studies different interface structures were observed such as non-planar or wavy interfaces, lamellar two-phase region or particles of second phase in the diffusion zone.

In this work a phase-field model is developed to assess and predict the development of concentration profiles and microstructures in multicomponent single- and multi-phase solid-to-solid diffusion couples. Interdiffusion in hypothetical ternary single-phase and two-phase diffusion couples are examined using phase-field model by numerically solving the nonlinear Cahn-Hilliard and Ginzburg-Landau equations. For diffusion couples assembled with a regular single-phase solution, constant chemical mobilities were employed to examine the development of concentration profiles including uphill diffusion and zero-flux plane. Zero-flux plane for a component was observed to develop for a diffusion couple at the composition that corresponds

the activity of that component in one of the terminal alloys. Experimental thermodynamic parameters and composition-dependent chemical mobilities were employed to examine the morphological evolution of interphase boundary in solid-to-solid two-phase diffusion couples. Instability at the interphase boundary was introduced initially (t=0) by a small compositional fluctuation at diffuse-interface, and its evolution varied largely as a function of terminal alloys and corresponding composition-dependent chemical mobility.

The work has been divided into two parts. First, development of zero-flux planes in single-phase diffusion couples is examined with respect to the thermodynamic description. Specifically addressed in this work is the development of zero-flux plane for a component and its relation to the activity of that component in one of the terminal alloys. In the second part, development of planar and non-planar interfaces in two-phase solid-to-solid diffusion couples is examined based on initial interface perturbation and composition-dependent chemical mobility.

4.2 Phase-field Model Description

4.2.1 Thermodynamic Descriptions

Two models were employed in this study, one used for the simulation of single-phase diffusion couples, and the other used for the two-phase diffusion couples. While the basic framework of the formulation is the same, formulation for the single-phase couples is characterized by a difference in the composition only, whereas that for the two-phase couples is characterized by a difference in composition as well as structure.

55

For a ternary substitutional alloy containing elements A, B and C, compositionally distinct phases are represented by the conserved composition field variable, the mole or atom fraction of individual element, $c_i(x,t)$. A non-conserved field variable, $\eta(x,t)$ is used along with the composition variable to represent chemically as well as structurally distinct phases. Hereafter, η is referred as the structure order (SO) parameter. The constraint of 'conservation of mass' leads to:

$$\sum_{i=0}^{n} c_i(x,t) = 1.0, c(x,t) \geq 0 \qquad (4.1)$$

where x and t are the position and time variables, respectively. Assuming that the lattice mismatch between different phases is negligible and externally applied force fields are absent, the total chemical free energy, F_{chem} of the system can be expressed as the sum of the bulk chemical free energy, F_{bulk}, and total interfacial energy, F_{int}. This total energy of the system is represented as the Helmoltz free energy, F by using the extended Cahn-Hilliard free energy functional [27-28]:

$$F_{chem} = F_{bulk} + F_{int} = F = N_V \int_V \left[f(c_i, \eta) + \kappa_i (\nabla c_i)^2 + \kappa_\eta (\nabla \eta)^2 \right] dV, i = A, B, C \quad (4.2)$$

where $f(c_A, c_B, \eta)$ is the bulk chemical free energy per atom of the homogeneous alloy, and N_V is the number of atoms per unit volume, assumed to be constant. In Equation 4.2, K_i and K_η are the gradient energy coefficients associated with gradients of compositions of individual elements and η, respectively. The system evolves into its equilibrium condition by minimizing the total

chemical free energy, F. For single-phase diffusion couples in this study, a simple regular solution approximation for $f(c_i)$ is employed [29] as given by:

$$f(c_A, c_B, c_c) = RT \sum_i c_i \ln c_i + \sum_{i \neq j} \varpi_{ij} c_i c_j \qquad (4.3)$$

where ω_{ij} are the binary regular solution parameters. In this study it wa assumed $\omega_{ij} = \omega_{ji} = 2.0$, which produces a single-phase solid solution without any miscibility gap [29].

For two-phase diffusion couples, the free energy was derived by directly using the procedure described by Wu et al [30] and Wang et al [31]. Here the bulk chemical free energy is approximated by a Landau polynomial expansion as a function of composition and SO parameter given by:

$$f(c_A, c_B, \eta) = f^\gamma(c_A, c_B, 0) + \frac{A_2(c_A, c_B)}{2} \eta^2 + \frac{A_4(c_A, c_B)}{4} \eta^4 + \ldots \qquad (4.4)$$

Molar volume for the system is assumed constant, and component C is taken as the dependent component. Thus, there are only two composition variables in the equation. $F^\gamma(c_A, c_B, 0)$ is the free energy of one phase (namely γ), calculated from the thermodynamic data available [32]. The equilibrium free energy of the second phase (namely β) is obtained from Equation 4.4 by substituting the equilibrium SO parameter value, $\eta_0(c_A, c_B)$ determined by:

$$\frac{\partial f(c_A, c_B, \eta)}{\partial \eta} = 0 \qquad (4.5)$$

$A_2(c_A, c_B)$ in Equation 4.4 is represented by a polynomial, which was obtained from [30].

4.2.2 Diffusion Equations

Kinetic equations that govern the temporal evolution of the composition variables and SO parameter were employed following Huang [29] and Mohanty [33]. The intrinsic flux of individual components relative to a lattice-frame of reference is expressed using a linear and homogeneous function of the gradient in its chemical potential as:

$$J_i = -M_i \nabla \mu_i \tag{4.6}$$

where M_i is the intrinsic mobility of the component *i*, which is always positive. The interdiffusion flux of each component $\tilde{J}_i$ in a laboratory frame of reference is given by [8]:

$$\tilde{J}_i = J_i - c_i \left(J_A + J_B + J_C \right) \tag{4.7}$$

where $\sum_i \tilde{J}_i = 0$. Substituting Equation 4.6 into Equation 4.7 yields:

$$\tilde{J}_i = -\left(1 - c_i\right) M_i \nabla \mu_i - c_i \sum_{j \neq i} M_j \nabla \mu_j, \text{ where } j = A, B, C \tag{4.8}$$

Using Gibbs-Duhem relation, $\sum_i c_i \nabla \mu_i = 0$ with Equation 4.8 yields:

$$
\begin{aligned}
\nabla \mu_A &= \left(1 - c_A\right) \nabla \mu_A^{eff} - c_B \nabla \mu_B^{eff} \\
\nabla \mu_B &= \left(1 - c_B\right) \nabla \mu_B^{eff} - c_A \nabla \mu_A^{eff} \\
\nabla \mu_c &= -c_A \nabla \mu_A^{eff} - c_B \nabla \mu_B^{eff}
\end{aligned}
\tag{4.9}
$$

where $\mu_A^{eff} = (\mu_A - \mu_C)$ and $\mu_B^{eff} = (\mu_B - \mu_C)$. Now substitution of Equation 4.9 into Equation 4.8

gives:

$$\tilde{J}_A = -\left[(1-c_A)^2 M_A + c_A^2 M_B + c_A^2 M_C \right] \nabla \mu_A^{eff}$$
$$+ \left[c_B (1-c_A) M_A + c_A (1-c_B) M_B - c_A c_B M_C \right] \nabla \mu_B^{eff} \qquad (4.10a)$$

and

$$\tilde{J}_B = -\left[(1-c_B)^2 M_B + c_B^2 M_A + c_B^2 M_C \right] \nabla \mu_B^{eff}$$
$$+ \left[c_B (1-c_A) M_A + c_A (1-c_B) M_B - c_A c_B M_C \right] \nabla \mu_A^{eff} \qquad (4.10b)$$

In this study, the intrinsic mobility of each element was introduced as a linear function of

its composition, i.e. $M_i = \beta_i c_i$, where β_i is the atomic mobility of individual element. Then,

Equation 4.10 for interdiffusion flux of individual component becomes:

$$\tilde{J}_A = -\left[(1-c_A)^2 \beta_A c_A + c_A^2 \beta_B c_B + c_A^2 \beta_C c_C \right] \nabla \mu_A^{eff}$$
$$+ \left[c_B (1-c_A) \beta_A c_A + c_A (1-c_B) \beta_B c_B - c_A c_B c_C \beta_C \right] \nabla \mu_B^{eff} \qquad (4.11a)$$

and

$$\tilde{J}_B = -\left[(1-c_B)^2 \beta_B c_B + c_B^2 \beta_A c_A + c_B^2 \beta_C c_C \right] \nabla \mu_A^{eff}$$
$$+ \left[c_B (1-c_A) \beta_A c_A + c_A (1-c_B) \beta_B c_B - c_A c_B c_C \beta_C \right] \nabla \mu_B^{eff} \qquad (4.11b)$$

Equation 11 can be rewritten as:

$$\tilde{J}_A = -M_{AA} \nabla \mu_A^{eff} - M_{AB} \nabla \mu_B^{eff} \qquad (4.12a)$$

and

$$\tilde{J}_B = -M_{BA}\nabla\mu_A^{eff} - M_{BB}\nabla\mu_B^{eff} \tag{4.12b}$$

where M_{ij} are the effective chemical mobilities defined as:

$$
\begin{aligned}
M_{AA} &= \left(1 - c_A\right)^2 \beta_A c_A + c_A^2 \beta_B c_B + c_A^2 \beta_C c_C \\
M_{BB} &= \left(1 - c_B\right)^2 \beta_B c_B + c_B^2 \beta_A c_A + c_B^2 \beta_C c_C \\
M_{AB} &= M_{BA} = -c_B\left(1 - c_A\right)\beta_A c_A - c_A\left(1 - c_B\right)\beta_B c_B + c_A c_B c_C \beta_C
\end{aligned}
\tag{4.13}
$$

For an inhomogeneous system, μ_i^{eff} is defined as the variational derivative of F with respect to c_i:

$$\mu_i^{eff} = \frac{\delta F}{\delta c_i} \quad (i = A, B) \tag{4.14}$$

Using Equations 4.2 and 4.16, we arrive at the following equations;

$$
\begin{aligned}
\mu_A^{eff} &= \frac{\partial f}{\partial c_A} - 2\left(\kappa_A + \kappa_C\right)\nabla^2 c_A - 2\kappa_C\nabla^2 c_B \\
\mu_B^{eff} &= \frac{\partial f}{\partial c_B} - 2\left(\kappa_B + \kappa_C\right)\nabla^2 c_B - 2\kappa_C\nabla^2 c_A
\end{aligned}
\tag{4.15}
$$

The governing temporal equations can be expressed using continuity equation by:

$$\frac{\partial c_i}{\partial t} = -\nabla \cdot \tilde{J}_i \quad (i = A, B) \tag{4.16}$$

From Equations 4.11, 4.13, 4.15 and 4.16, the final governing equations to be solved are obtained as:

$$\frac{\partial c_A(x,t)}{\partial t} = \nabla \left[M_{AA} \nabla \left(\frac{\partial f}{\partial c_A} - 2\kappa_{AA}\nabla^2 c_A - 2\kappa_{AB}\nabla^2 c_B \right) \right]$$
$$+ \nabla \left[M_{AB} \nabla \left(\frac{\partial f}{\partial c_B} - 2\kappa_{AB}\nabla^2 c_A - 2\kappa_{BB}\nabla^2 c_B \right) \right] \quad \text{(4.17a)}$$

and

$$\frac{\partial c_B(x,t)}{\partial t} = \nabla \left[M_{BA} \nabla \left(\frac{\partial f}{\partial c_A} - 2\kappa_{AA}\nabla^2 c_A - 2\kappa_{AB}\nabla^2 c_B \right) \right]$$
$$+ \nabla \left[M_{BB} \nabla \left(\frac{\partial f}{\partial c_B} - 2\kappa_{AB}\nabla^2 c_A - 2\kappa_{BB}\nabla^2 c_B \right) \right] \quad \text{(4.17b)}$$

where $\kappa_{AA} = \kappa_A + \kappa_C$, $\kappa_{BB} = \kappa_B + \kappa_C$ and $\kappa_{AB} = \kappa_{BA} = \kappa_C$.

4.2.3 Evolution of Structure Order Parameter

The evolution of non-conserved field variable η is described by a relaxation equation often called as time dependent Ginzburg-Landau equation or Allen-Cahn equation [34]:

$$\frac{\partial \eta(x,t)}{\partial t} = -M_\eta \frac{\delta F}{\delta \eta} \quad \text{(4.18)}$$

and

$$\frac{\delta F}{\delta \eta} = \frac{\partial f}{\partial \eta} - 2\kappa_\eta \nabla^2 \eta \quad \text{(4.19)}$$

where M_η is the relaxation constant that characterizes the interface mobility. Combining Equations 4.18 and 4.19 yields:

$$\frac{\partial \eta(x,t)}{\partial t} = -M_\eta \left[\frac{\partial f}{\partial \eta} - 2\kappa_\eta \nabla^2 \eta \right] \qquad (4.20)$$

4.2.4 Initial Interface Perturbation for Multiphase Diffusion Couples

A random fluctuation, $\xi(x,t)$ was incorporated to introduce compositional fluctuations at the γ/β diffused-interface for multiphase diffusion couple at $t = 0$ (i.e., not sustained) using $\xi(x,t)$ as given by Cook [35]:

$$C_i(r,t=0) = C_i\big|_{nonoise} + \xi(r) \qquad (4.21)$$

where x and t are position and time, respectively. The fluctuation used is a Gaussian random noise with mean zero. The range of fluctuation varied from +0.005 to -0.005 of composition within the diffuse-interface.

4.2.5 Numerical Implementation

Equations 4.17 and 4.20 were solved by using explicit central finite difference scheme. The system was divided into a 256 by 256 mesh, and the mesh size is equal to dimensionless number 1.0 on both x and y coordinates. The dimensionless time step used in the simulation is 10^{-5}.

4.3. Results

4.3.1 Single Phase Ternary Diffusion Couples

The main objective of this part of the study was to predict concentration profiles, diffusion paths and the occurrence of up-hill diffusion and zero-flux planes in single-phase vs. single-phase solid-to-solid diffusion couples using the phase-field model. The simulations were carried out on a hypothetical (A-B-C) and a real (Cu-Ni-Zn) alloy systems. In terms of the phase-field description, all the phases considered have same crystal structure, but they differ by their compositions. A regular solution approximation was used to describe the thermodynamics of the system, where as the kinetic information was either based on assumptions or derived from the experimental data, if deemed necessary. For example, in Cu-Ni-Zn system the chemical mobilities were assumed constant, and chosen based on average ternary interdiffusion coefficients determined from experimental concentration profiles [36]. Figure 4 shows the free energy surface with energy contours employed for the regular solution model with $\omega = 2.0$. The compositions of some of the single-phase alloys employed in this study are listed in Table I, and chemical mobilities assumed constant on either side of the diffusion couples are listed in Table II.

The development of concentration profiles was studied mainly using the Cu-Ni-Zn alloys (α_5, α_7, α_{12} and α_{20}) and the results were compared to the experimental results. The simulated and experimental [37] concentration profiles from the Cu-Ni-Zn diffusion couples α_5 vs. α_7, α_5 vs. α_{12} and α_5 vs. α_{20} annealed at 775ºC for 48 hours are presented in Figure 5, 6 and 7, respectively. From these figures it can be noticed that all the trends observed in experimental

63

profiles are consistently depicted in the simulated concentration profiles. The model is well capable of predicting features like up-hill diffusion in all these diffusion couples.

The occurrence of zero-flux planes in single-phase diffusion couples was investigated using the hypothetical ternary system containing components A, B and C. A detailed analysis was carried out by employing various combinations of composition and mobilities in conjunction with the isoactivity lines for the components calculated from the regular solution model [29]. Terminal alloy compositions and mobility values of two such diffusion couples are provided in Table I and Table II. The compositions for these alloys were chosen with respect to the isoactivity lines of component B. For the couple θ_1 vs. θ_2, compositions of both terminal alloys lie on one isoactivity line, whereas for θ_3 vs. θ_4, composition of terminal alloys lie on two slightly different isoactivity lines.
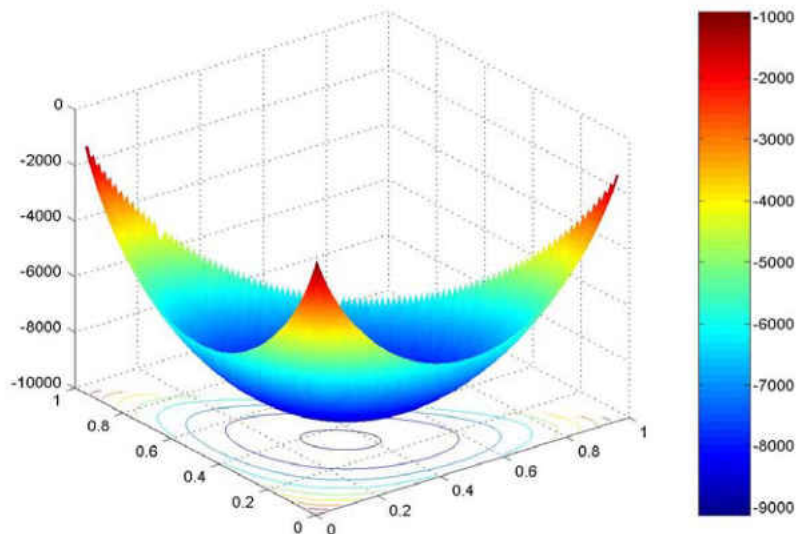
Figure 4: Free energy surface with energy contours for a single-phase solution without any miscibility gap in A-B-C ternary alloy.

Table 1: Compositions of alloys employed in phase-field simulation of solid-to-solid ternary diffusion couples. For alloys α5 and α7, components A, B, and C correspond to Cu, Ni, and Zn respectively. Alloys θ1, θ2, θ3, and θ4 have been selected based on activity of component B, a_B = 0.6682, a_B = 0.6682, a_B = 0.4599, a_B = 0.5641, respectively.

Alloy Designation	Composition (atom fraction)		
	A	B	C
α_5	0.225	0.325	0.450
α_7	0.010	0.550	0.440
θ_1	0.500	0.313	0.187
θ_2	0.336	0.364	0.300
θ_3	0.300	0.150	0.550
θ_4	0.365	0.235	0.400
γ_1	0.200	0.100	0.700
γ_2	0.300	0.130	0.570
β_1	0.100	0.350	0.550
β_2	0.050	0.450	0.500

Table 2: Chemical mobilities employed on either side of the solid-to-solid ternary diffusion couples examined in this study.

Diffusion Couple	Chemical Mobility	Left-hand-side (LHS)	Right-hand-side (RHS)
α_5 (LHS) vs. α_7 (RHS)	M_{BB}	3.44	4.58
	M_{BC}	-0.05	0.62
	M_{CB}	26.45	15.25
	M_{CC}	23.9	9.73
θ_1 (LHS) vs. θ_2 (RHS)	M_{BB}	1.1	2.0
	M_{BC}	-0.8	-3.0
	M_{CB}	-1.2	-3.0
	M_{CC}	1.9	6.0
θ_3 (LHS) vs. θ_4 (RHS)	M_{BB}	0.2	0.5
	M_{BC}	-0.2	-0.8
	M_{CB}	-0.8	-0.1
	M_{CC}	8.1	6.8
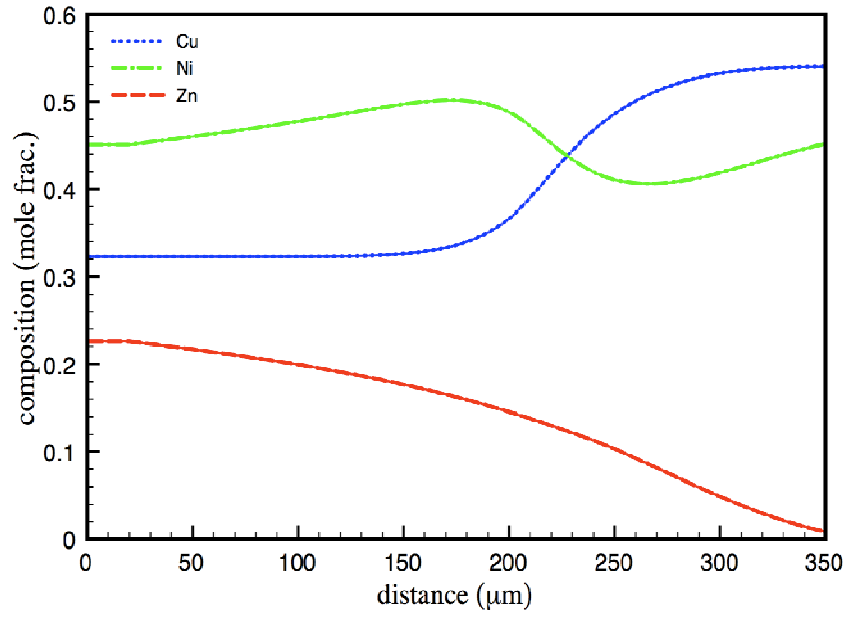
(a)
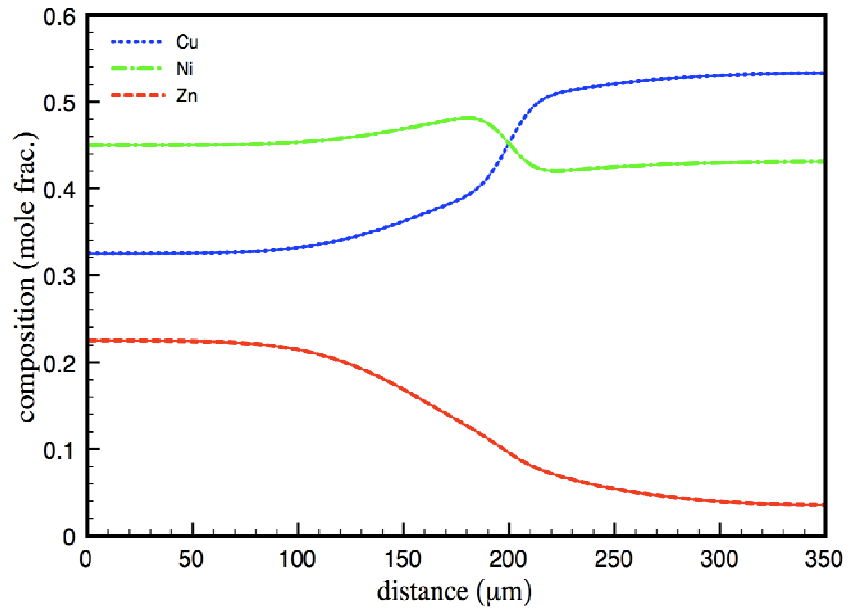
(b)

Figure 5: (a) Experimental and (b) simulated concentration profile of solid-to-solid diffusion couple α_5 vs. α_7.
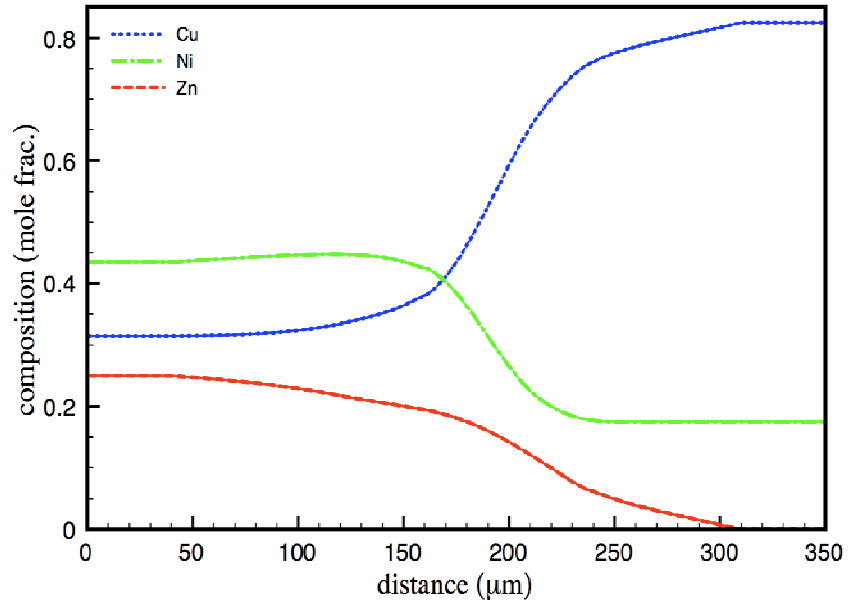
(a)
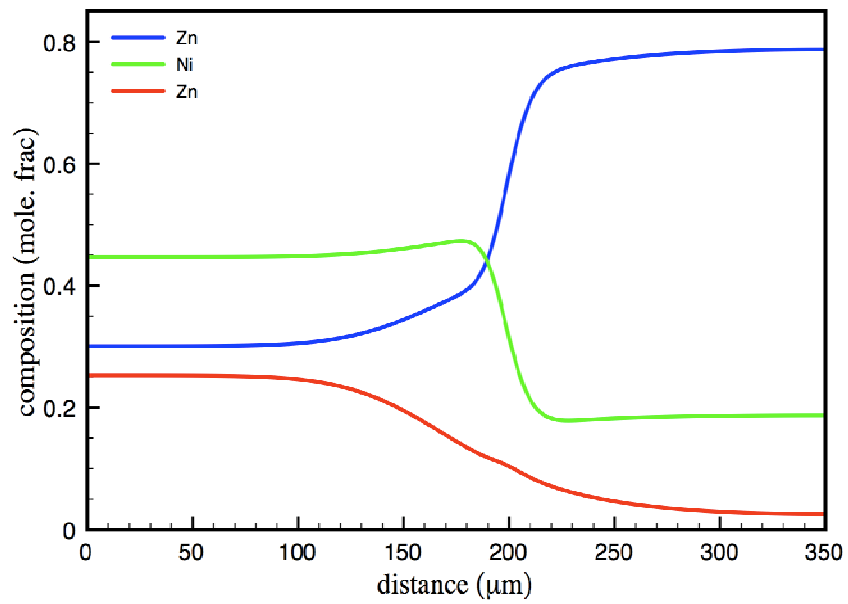
(b)

Figure 6: (a) Experimental and (b) simulated concentration profile of solid-to-solid diffusion couple α_5 vs. α_{12}.
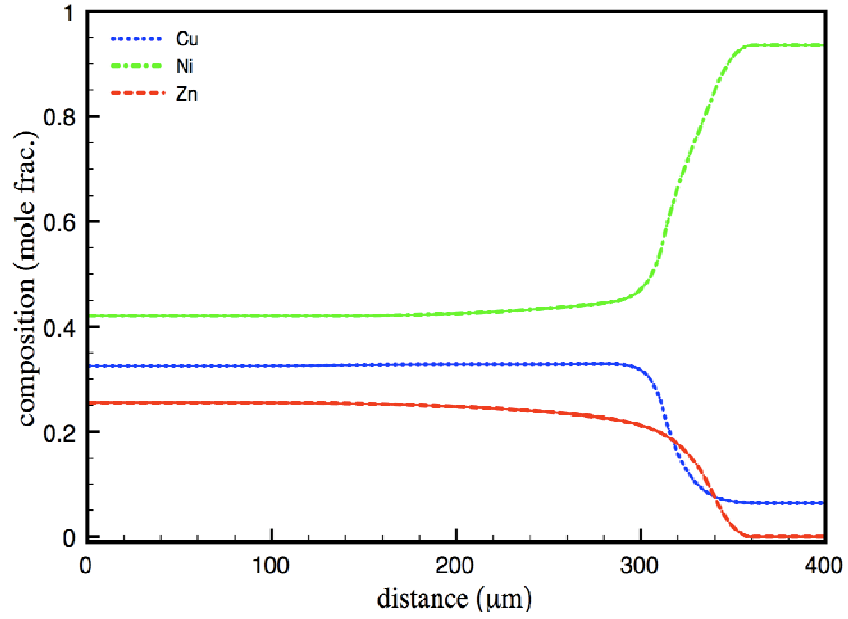
(a)
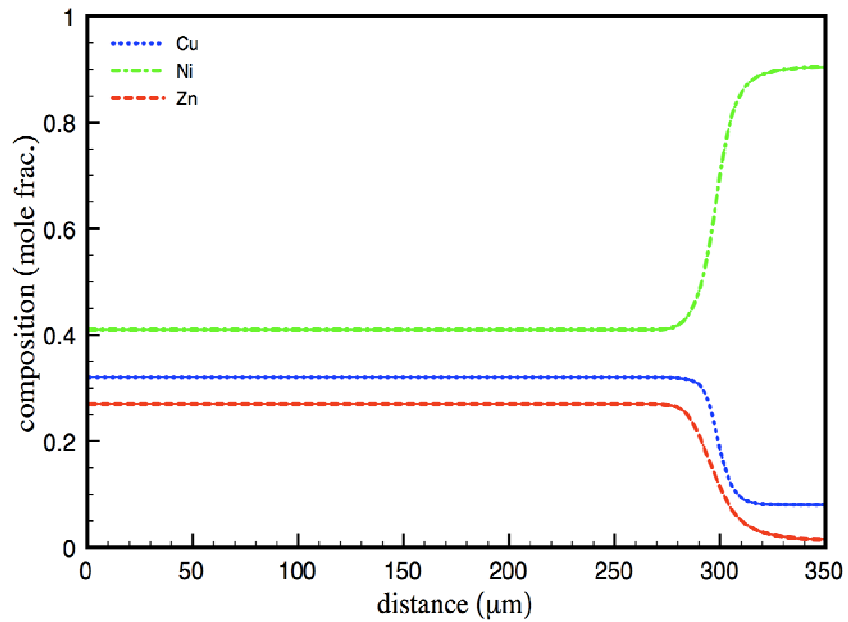
(b)

Figure 7: (a) Experimental and (b) simulated concentration profile of solid-to-solid diffusion couple α_5 vs. α_{20}.

The alloy compositions are identified on the ternary isotherms along with their diffusion paths in Figures 8(a) and 9(a), respectively. Composition and activity profiles of these diffusion couples are plotted in Figures 8(b) and 9(b). In both the couples an uphill diffusion in the profiles of concentration and activity for component B was observed, but from the flux profiles presented in Figures 8(c) and 9(c) ZFP was only observed for the couple θ_3 vs. θ_4. The activity of component B at the zero-flux plane composition (0.34A-0.235B-0.425C) corresponds to the activity of component B in terminal alloy (a_B = 0.5641) on the right-hand-side of Figure 8(b). The simulated results for the couple θ_3 vs. θ_4 agrees with the experimentally observed phenomena [14-18] that a ZFP occurs at the composition where the diffusion path intersects the isoactivity line extended from a terminal alloy.

In Figures 10 to 15, some more examples of simulated diffusion paths, composition profiles and flux profiles obtained from various diffusion couples are presented. All the diffusion couples shown in these figures are hypothetical and their terminal alloy compositions lie either on a single or two different isoactivity lines. For the diffusion couple shown in Figure 10 (a), the terminal alloy compositions are on a single isoactivity line and the diffusion path crosses it at a composition near 0.38A-0.27B-0.35C. From the Matano analysis on the composition profile shown in Figure 10(b), the ZFP lies at the Matano interface (x_0). The composition at the ZFP is observed to be near 0.38A-0.27B-0.35C.
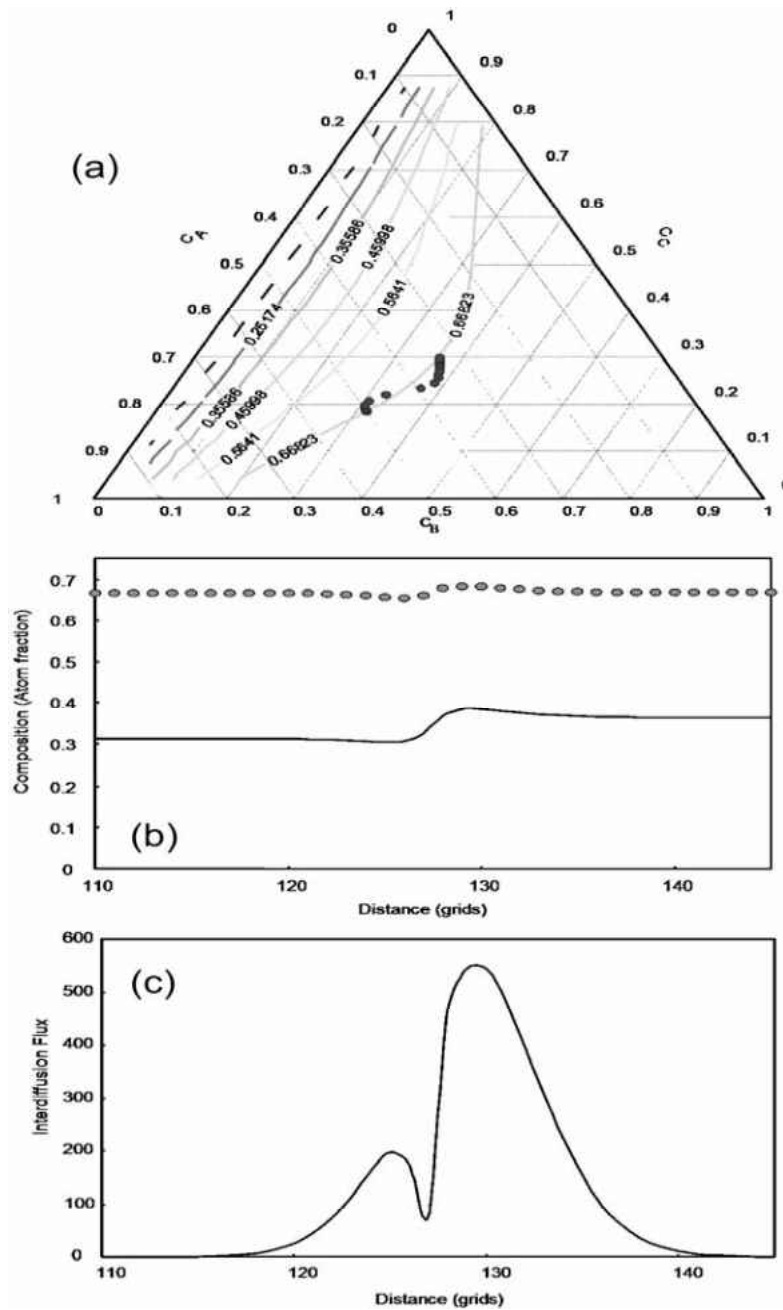
Figure 8: (a) Diffusion path, (b) profiles of concentration and activity for component B, and (c) interdiffusion flux of component B simulated from diffusion couple θ_1 vs. θ_2. The activity of B in both terminal alloys is the same at 0.6682. No ZFP is observed although an uphill diffusion for component B is observed.
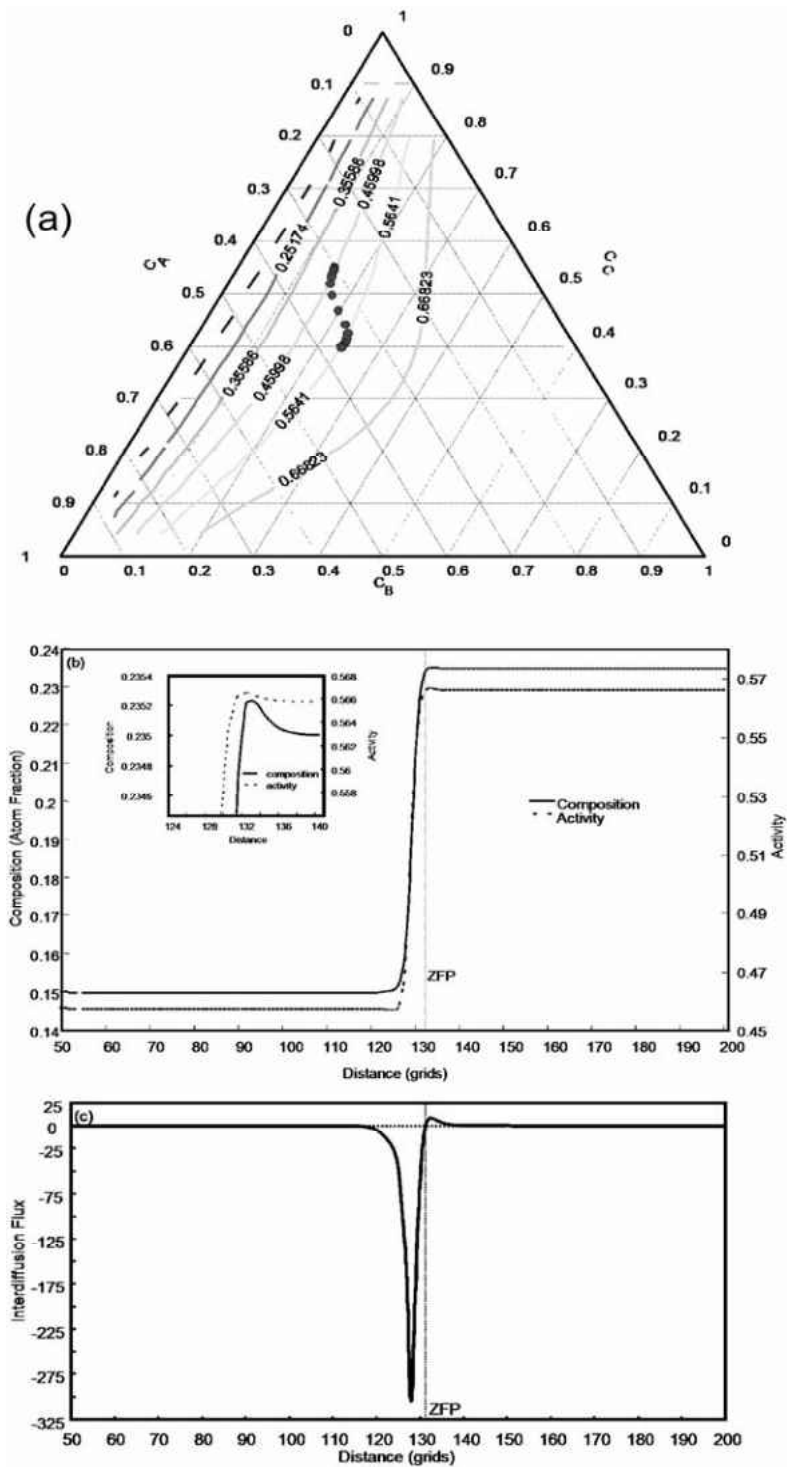
Figure 9: (a) Diffusion path, (b) profiles of concentration and activity for component B, and (c) interdiffusion flux of component B simulated from diffusion couple θ3 vs. θ4. The activities of B in θ3 and θ4 alloys are 0.4599 and 0.5641, respectively. A ZFP is observed with an uphill diffusion for component B. The activity of B at the ZFP composition is 0.5641.
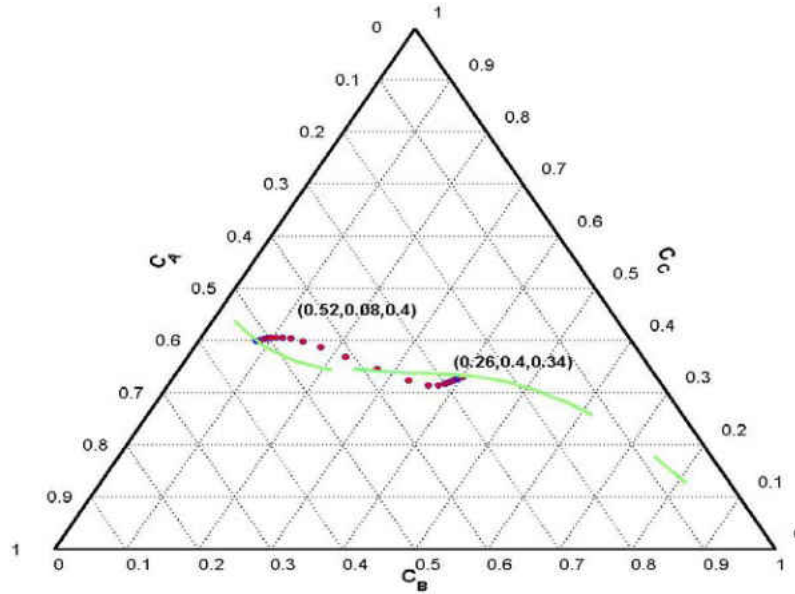
(a)
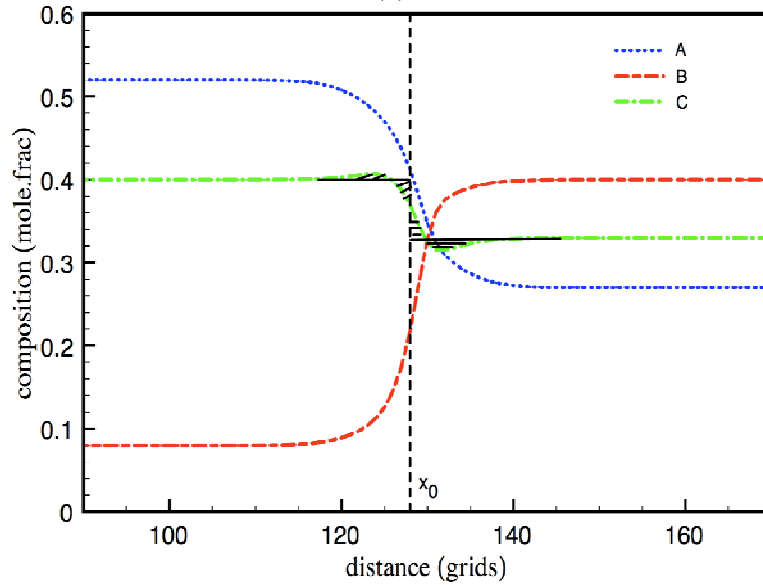
(b)

Figure 10: (a) Diffusion path of a hypothetical diffusion couple drawn on the ternary isotherm with the terminal alloy compositions laying on one isoactivity line of component C, (b) corresponding composition profiles showing up-hill diffusion of component C. The ZFP is located at the Matano interface.

The diffusion path of the couple shown in Figure 11(a) again have the terminal alloys on one isoactivity line, but in this case two ZFPs are observed on either side of the Matano plane, as shown in Figure 11(b). This is also proved from the flux profile in Figure 11(c). In certain cases, a ZFP may not develop, even though there is up-hill diffusion and an extremum present in the composition profile of a component, as shown in Figure 12. Here the terminal alloy compositions of the diffusion couple are on one of the isoactivity lines of component A, as shown in Figure 12(a) and the diffusion path crosses the isoactivity line at one point. But upon analyzing the concentration profile presented in Figure 12(b), no ZFP could be determined. The hatched areas in the composition profile are used to determine the Matano plane where Area A = Area B. When the terminal alloys lie on two different isoactivity lines, two or more ZFPs can occur as the diffusion path can cross the isoactivity lines at number of points. The diffusion path and flux profile for such a couple are shown in Figure 13(a) and (b).
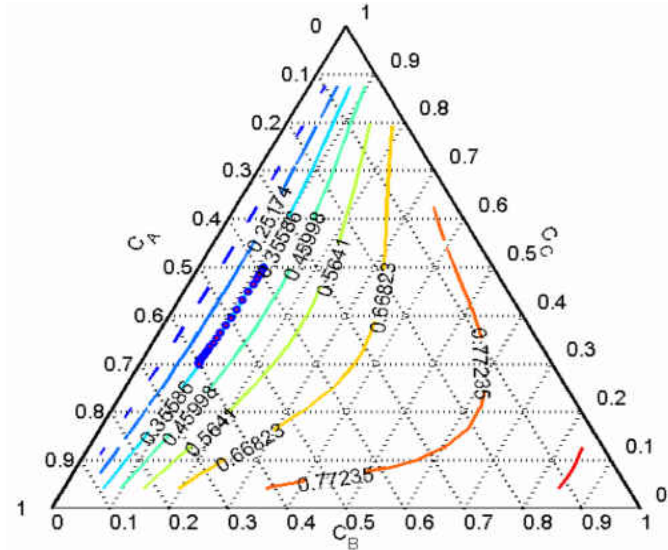
(a)
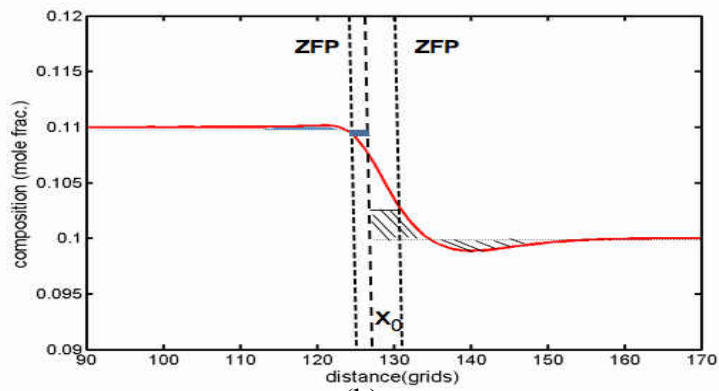
(b)
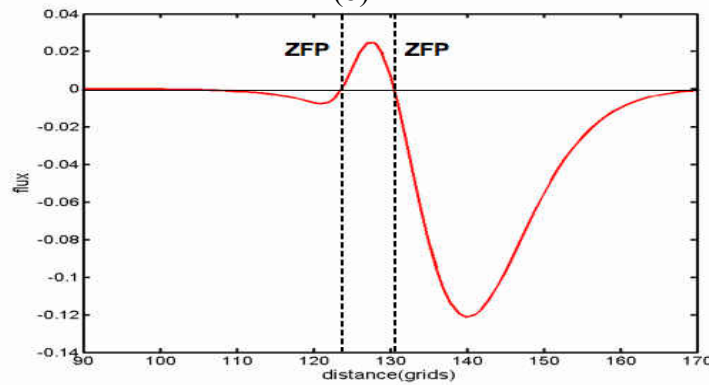
(c)

Figure 11: (a) Diffusion path of a hypothetical diffusion couple drawn on the ternary isotherm with the terminal alloy compositions laying on one isoactivity line of component B, (b) corresponding composition profiles showing up-hill diffusion of component B and two ZFPs located on either side of the Matano interface. (c) Flux profile that confirms the presence of two ZFPs.

74

(a)

(b)
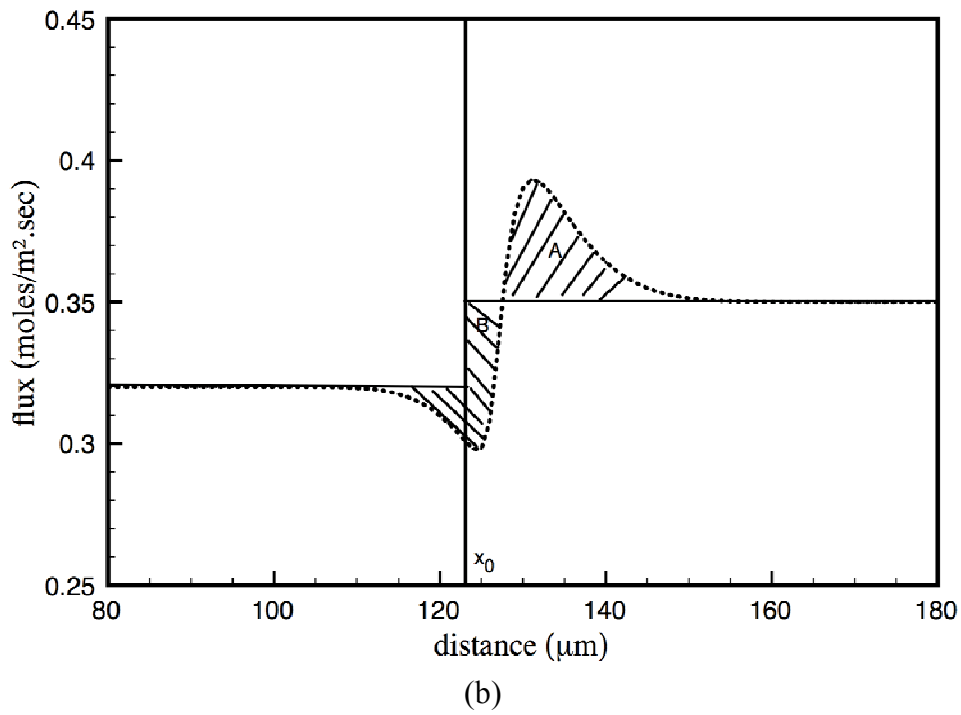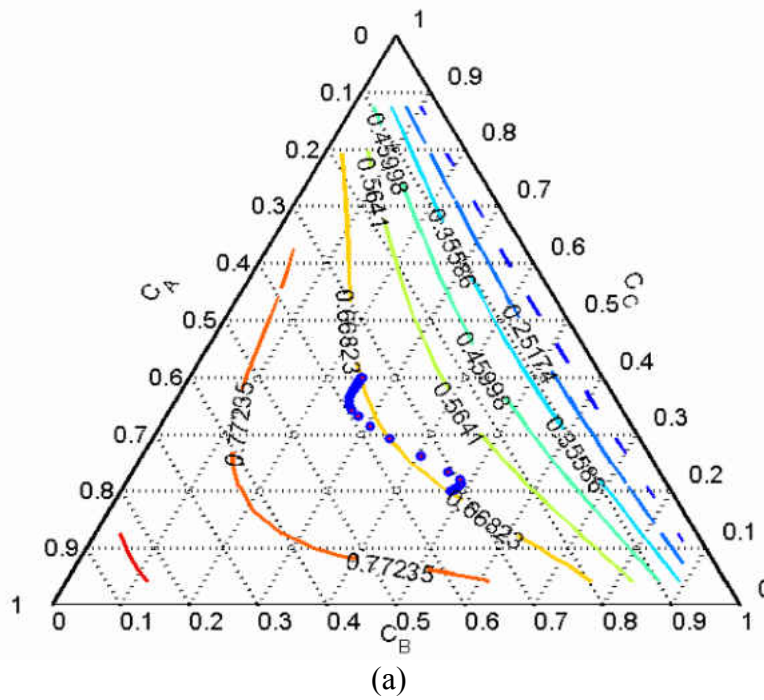
Figure 12: (a) Diffusion path of a hypothetical diffusion couple drawn on the ternary isotherm with the terminal alloy compositions laying on one isoactivity line of A, (b) corresponding composition profile showing up-hill diffusion of component A and no ZFPs is present.
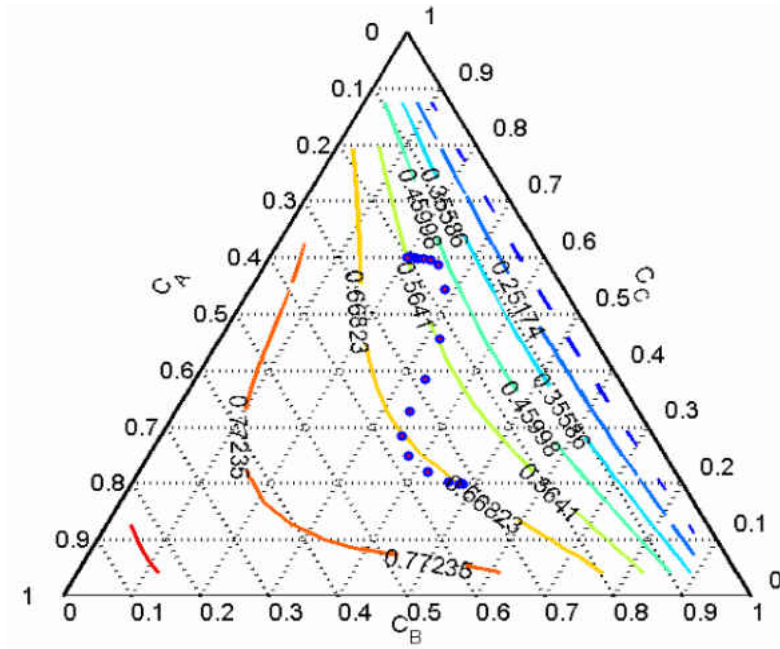
(a)
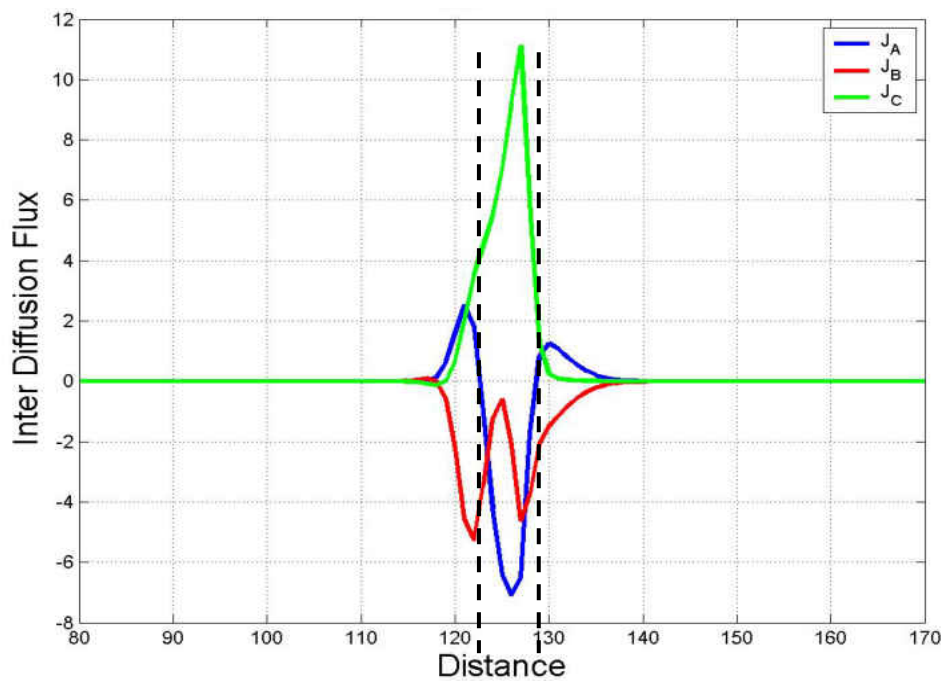
(b)

Figure 13: (a) Diffusion path of a hypothetical diffusion couple drawn on the ternary isotherm with the terminal alloy compositions laying on one isoactivity line of A, (b) corresponding flux profile showing locations of two ZFPs.

4.3.2 Effect of Concentration Dependent Chemical Mobility On The Appearance of ZFPs

The chemical mobilities defined in Equation 4.13 are functions of composition and atomic mobilities of each component, but the results described so far were obtained using constant chemical mobilities. Therefore, the variation in terminal alloy compositions of all the diffusion couples is only manifested through the variation in the chemical free energy, which in turn creates differences in respective chemical potentials. In order to study the effect of kinetic parameters such as chemical mobilities on ZFPs, various combinations of atomic mobilities were used with fixed terminal alloy compositions that kept the thermodynamics of the system constant. Results obtained from two series of simulations are presented below in Figure 14 and 15, where diffusion paths for two diffusion couples are shown along with the variation in their flux profiles as a function of atomic mobilities.

Table 3: Constant atomic mobility values of components A, B, and C used for the study of the occurrence of ZFPs.

Case	Atomic Mobilities		
	β_A	β_B	β_C
a	0.005	0.01	0.03
b	0.001	0.01	0.1
c	0.001	0.01	0.09
d	0.001	0.01	0.095
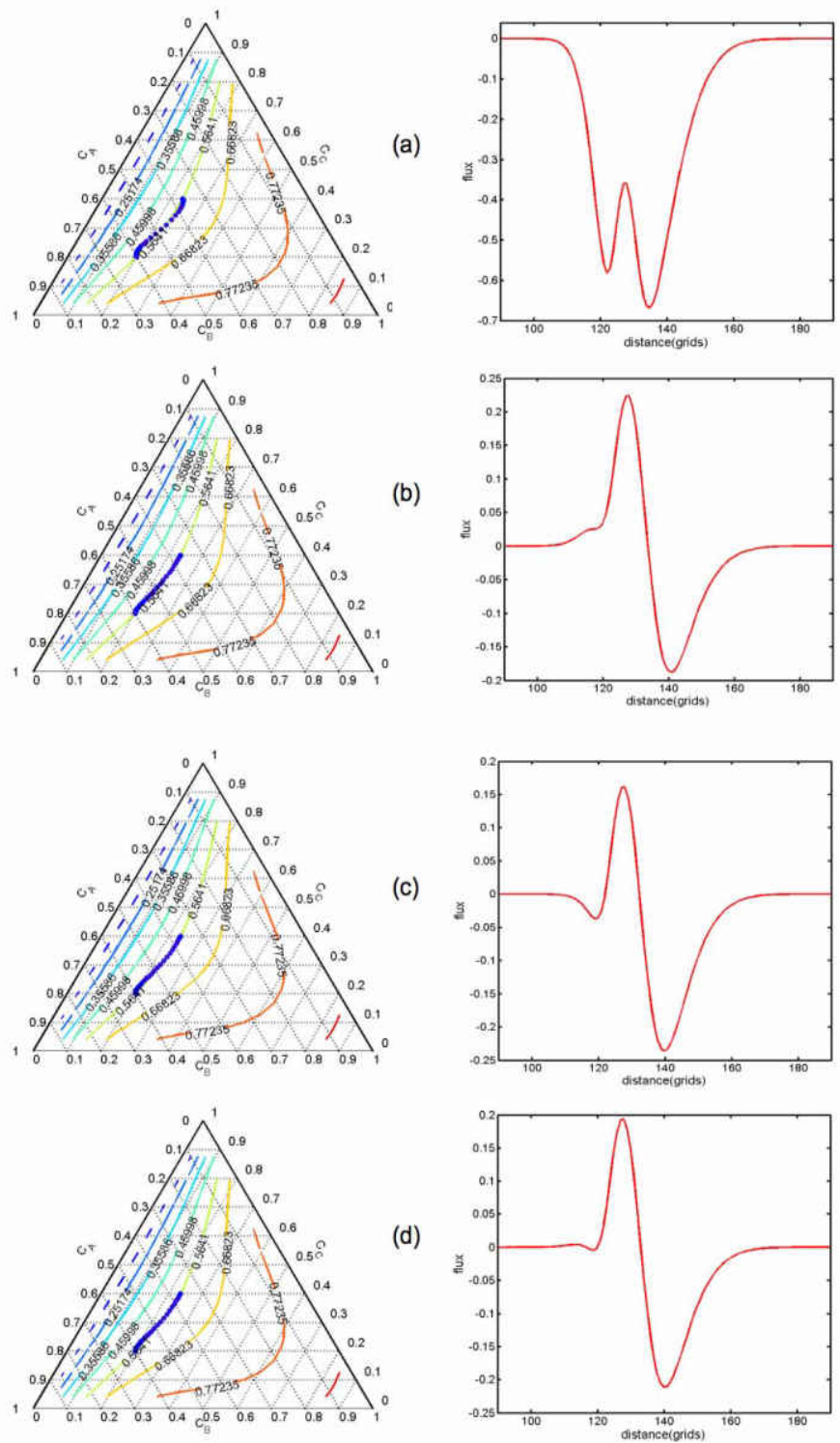
Figure 14: Development of diffusion paths and flux profiles for a diffusion couple as a function of atomic mobilities of components described by series-1. ZFP occurrence and their location changes with change in the mobility values.

78
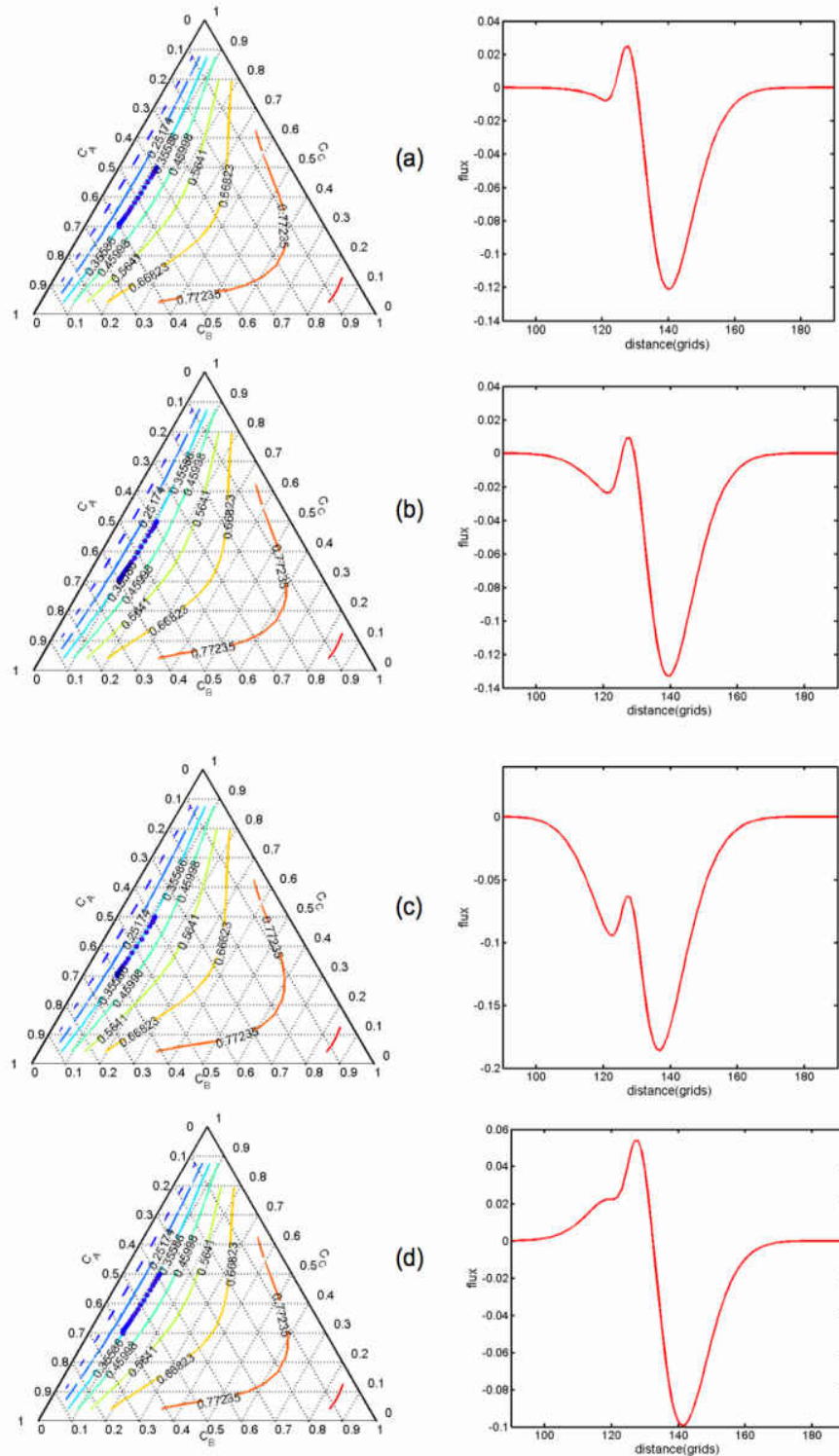
Figure 15: Development of diffusion paths and flux profiles for a diffusion couple as a function of atomic mobilities of components described by series-2. ZFP occurrence and their location changes with change in the mobility values.

The same set of atomic mobilities was used for the two diffusion couples, and is given in Table 3. In series-1, as shown in Figure 14, *case-a* does not produce any ZFP, whereas in cases b, c, and d, ZFP are observed. However, the location of occurrence of ZFPs varied with the variation in atomic mobility for the same diffusion couple. In series-2, the ZFP was observed in all the cases except *case c*. The observed differences between series-1 and 2 occur only due to a difference in the terminal alloy compositions of the two diffusion couples.

4.3.3 Two-Phase Diffusion Couples and Interface Morphology

To examine the morphological evolution of interface between two-phase ternary diffusion couples, say γ vs. β, the free energy formulation given in the Equation 4.4 was used. The free energy of γ phase was derived from the thermodynamic database available for the Ni-Cr-Al system at 1200°C [32]. Also, composition dependent chemical mobilities, M_{ij} based on Equation 4.13 were employed in these simulations from constant atomic mobilities ($\beta_A = 2.0$, $\beta_B = 1.2$, $\beta_C = 6.0$). Two two-phase diffusion couple simulations were conducted: (1) first simulation was carried out without using any compositional fluctuations; and (2) second simulation was carried out with a uniform random fluctuation across the interfacial region only in the first step of time-iteration to introduce compositional perturbations into the system.

Since the two phases are in thermodynamic equilibrium, small random fluctuations introduced into the system does not result in the nucleation of precipitates or other phases. Each simulation is started with an initial homogeneous composition as determined by the thermodynamic equilibrium calculations. Terminal alloy compositions used in this study are provided in Table 1. The gradient energy terms are of similar values to avoid the formation of

80

any preferential interface layers. Equilibrium values of SO parameters ($\eta = 0$ for γ and $\eta = \eta_{eq}$ for β) for both the phases are used, and microstructures are presented with time snapshots using a gray scale representation of the local values of η. Figure 16 shows the temporal microstructure evolution in a γ vs. β diffusion couple where no interfacial perturbation is applied. In Figure 17, temporal microstructure evolution in the same γ vs. β diffusion couple is shown, but in this case the interface perturbation is applied to the system. The darker region in the microstructure corresponds to γ phase ($\eta = 0$) and the brighter region corresponds to β phase ($0 < \eta = \eta_{eq} < 1.0$). The results show that, without the introduction of perturbation, the γ/β interface moves parabolically and remains planar. With perturbation introduced at the interface at $t = 0$ only, the γ/β interface can become non-planar.

Figure 18 presents the resulting microstructure from diffusion couples of different terminal alloy compositions, subjected to the same fluctuation to study the effect of composition-dependent chemical mobilies on the morphological evolution of interface. It is observed that the initial terminal alloy compositions, and thus the composition-dependent chemical mobility, have a pronounced effect on the morphological evolution of the γ/β interface: planar in Figure 18(a) vs. non-planar in Figure 18(b).
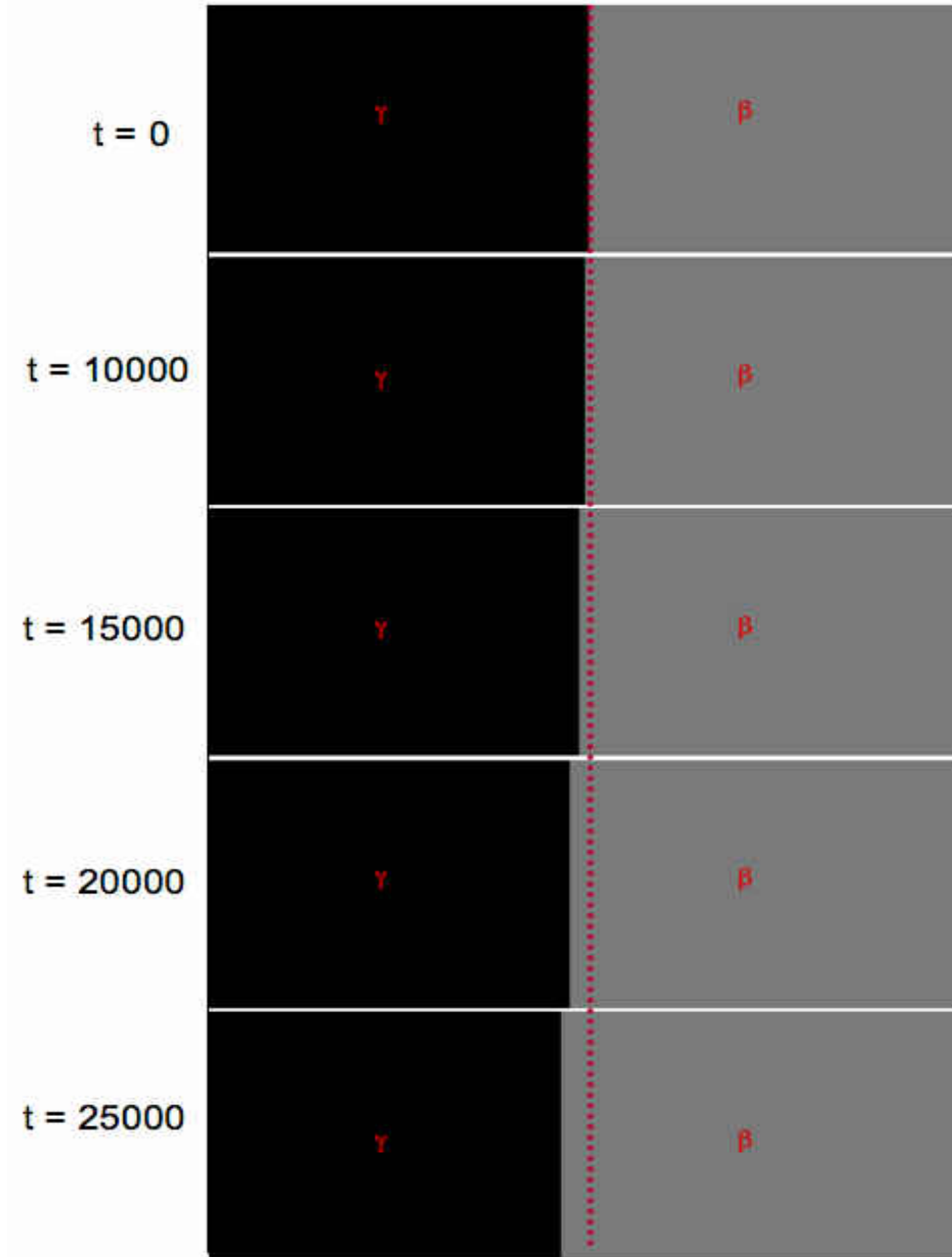
Figure 16: Morphological evolution of γ/β interface with no initial fluctuation in solid-solid two-phase diffusion couple γ_1 vs. β_1 with the same terminal alloy compositions. The interface remains planar with time. Non-planar interface is observed to develop with initial fluctuation.
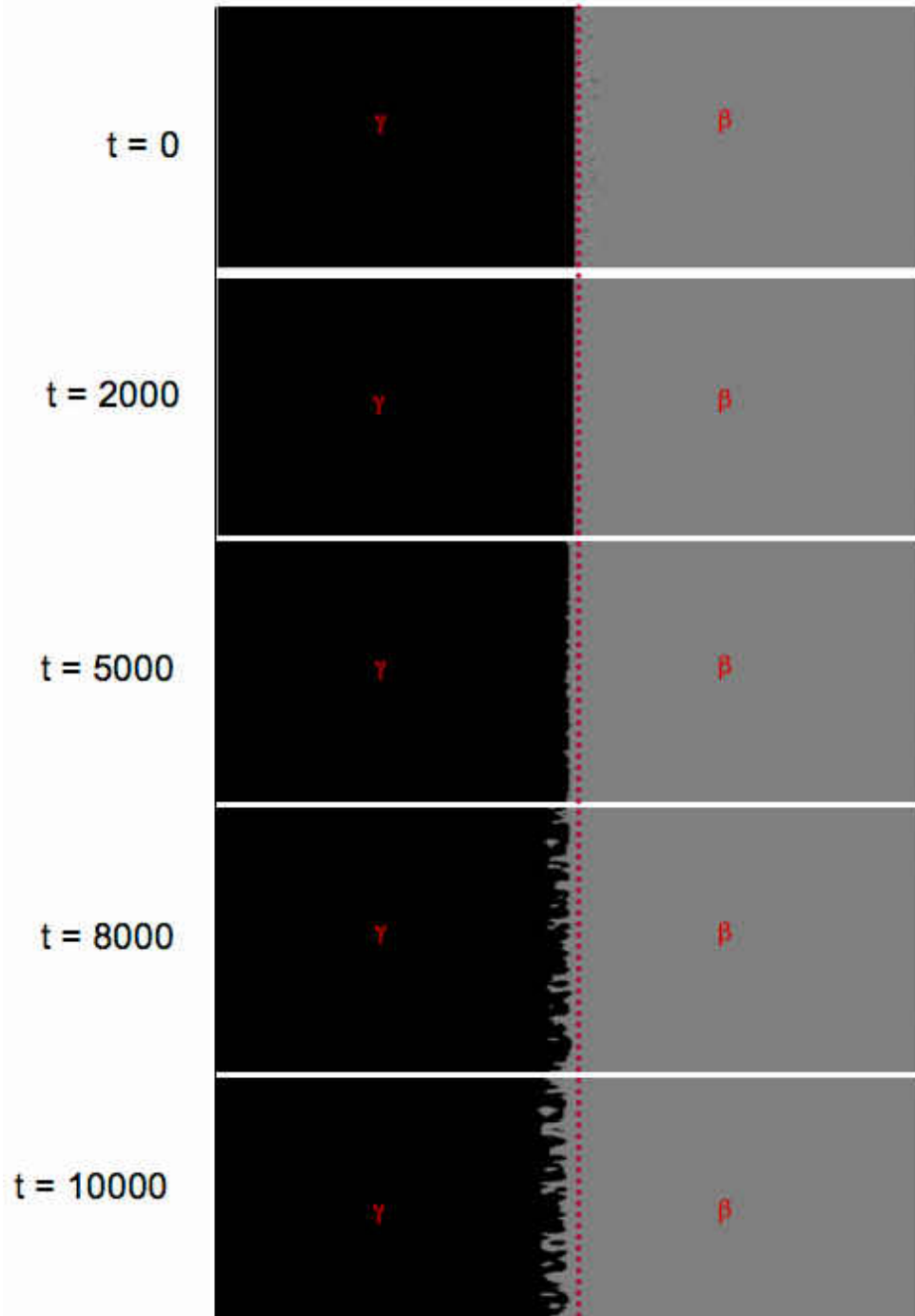
Figure 17: Morphological evolution of γ/β interface with initial fluctuation in solid-solid two-phase diffusion couple γ1 vs. β1 with the same terminal alloy compositions. Non-planar interface is observed to develop with initial fluctuation.
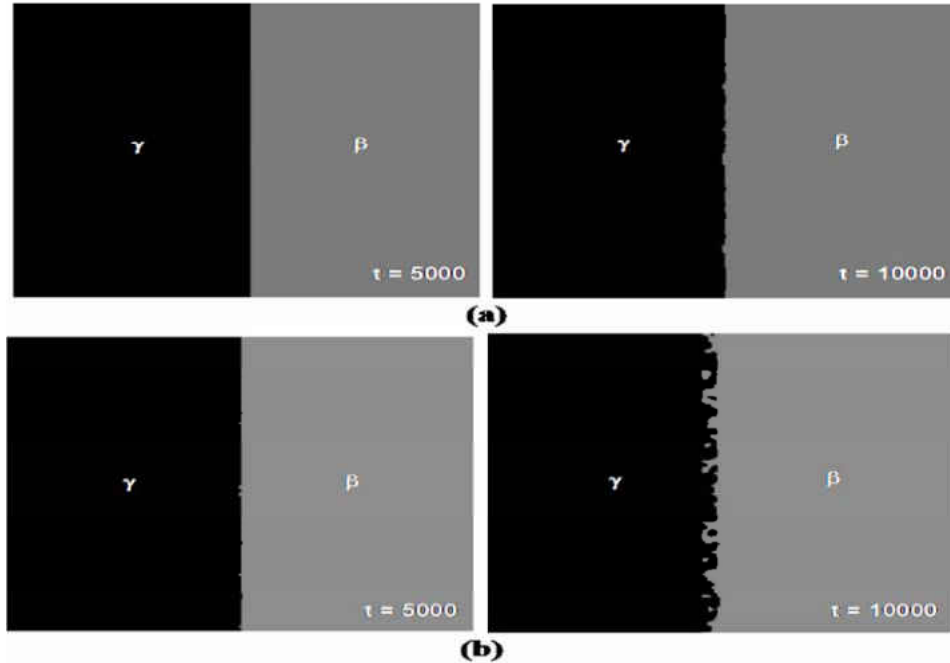
Figure 18: Morphological evolution of γ/β interface in solid-to-solid diffusion couple: (a) γ1 vs. β1 and (b) γ2 vs. β2. Magnitude of the initial fluctuation is same for both couples while the terminal alloy compositions and composition-dependent chemical mobility vary.

4.4. Discussions

Appropriate use of the kinetic parameters with a simple regular solution model allowed prediction of concentration profiles that are commonly observed in ternary diffusion including uphill diffusion and zero-flux planes. From the simulation results it is observed that a ZFP develops in a ternary system when the diffusion path intersects the isoactivity line passing through the terminal alloy compositions. The composition at the point of intersection corresponds closely to the activity of one of the terminal alloys. The simulation results also confirmed that ZFPs to occur, extrema in concentration profiles caused by the up-hill diffusion is necessary, but the presence of an extremum might not always necessarily produce a ZFP.

84

To elucidate the above point, let us consider the diffusion couple described in Figure 12(a) where the diffusion path is crossing the isoactivity line passing through its terminal alloys. But no ZFP is observed in the composition profile of the diffusion couple plotted in Figure 12(b), though up-hill diffusion is clearly evident. This can be illustrated on the basis of Figure 2, which suggests that a ZFP is located at the point in the composition profile where the Area A = Area B and Area C = Area D. This criteria does not hold in Figure 12(b) because of the location of the Matano plane, so that at all positions in the reaction zone the area A+B > 0. Hence, there will be no ZFP in this composition profile. As it is evident form the simulation results shown in Figures 14 and 15 that the development of ZFPs can only occur in diffusion couples whose terminal alloys lie in a particular composition range, which is determined by the above criteria.

4.5. Conclusions

Phase-field model was developed and employed to simulate development of concentration profiles and interface morphology observed in solid-to-solid ternary diffusion couples. Using a simple regular solution model, and constant chemical mobilities, development of concentration profiles including uphill diffusion and zero-flux plane were simulated. Zero-flux plane for a component can be observed to develop at the composition that corresponds to the intersection of the diffusion path and the isoactivity line drawn from one of the terminal alloys. There could be more than one ZFP developed on either side of the Matano plane. It was also demonstrated that the terminal alloy compositions, and thus composition-dependent chemical mobility, play an important role in morphological evolution of interphase boundary in solid-to-solid two-phase diffusion couples.

4.6 References

[1]   J. S. Kirkaldy, D. J. Young, Diffusion in the Condensed State, The Institute of Metals, London, (1987) pp.172.

[2]   T. O. Ziebold, R. E. Ogilvie, Trans. TMS_AIME, vol.239 (1967), pp.942.

[3]   M. A. Dayananda, P. F. Kirch, R. E. Grace, TMS_AIME, vol.242 (1968), pp.885.

[4]   H. Fujita. L. J. Gosting, J. Am. Chem. Soc., vol.78 (1956), pp.1099.

[5]   J. S. Kirkaldy, Can. J. Phys., vol.36 (1958), pp.899.

[6]   K. J. Rönkä, A. A. Kodentsov, P. J. J. van Loon, J. K. Kivilahti, F. J. J. van Loo, Metall. Mater. Trans. A, vol.27A (1996), pp.2229.

[7]   Y. H. Sohn, Ph.D. Dissertation, Purdue University, (1999).

[8]   P. Shewmon, Diffusion in Solids, 2nd Edition, The Minerals, Metals and Materials Socety, Warrendale, PA (1989).

[9]   J. Philibert, Atom Movements - Diffusion and Mass Transport in Solids, Les Edition de Phisique, Paris (1991).

[10] J. S. Kirkaldy, Adv. Mater. Res., vol.4 (1970), pp.55.

[11] F. J. J. van Loo, Prog. Solid State Chem. vol.20 (1990), pp.47.

[12] M. A. Dayananda, Defect Diff. Forum, vol.83 (1992), pp.73.

[13] R. T. DeHoff, K. J. Anusavice, C. C. Wan, Metall. Trans., vol.5 (1974), pp.1113.

[14] M. A. Dayananda, C. W. Kim, Metall. Trans. A, vol.10A (1979), pp.1333.

[15] C. W. Kim, M. A. Dayananda, Metall. Trans. A, vol.14A (1983), pp.857.

[16] M. A. Dayananda, *Metall. Trans. A,* vol.14A (1983), pp. 1651.

[17] J. G. Duh and M. A. Dayananda, Metall. Trans. A, 15A (1984) pp. 649.

[18] J. G. Duh, M. A. Dayananda, Diffusions and Defects Data, vol.39 (1985), pp.1.

[19] M. S. Thompson, J. E. Morral, Metall. Trans. A, vol.18A (1987), pp.1565.

[20] J. S. Kirkaldy, Can. J. Phys., vol.35 (1957), pp.435.

[21] S. M. Merchant, M. R. Notis, J. I. Goldstein, Metall. Trans. A, vol.21A (1990), pp.1901.

[22] S. M. Merchant, M. R. Notis, J. I. Goldstein, Metall. Trans. A, vol.21A (1990), pp.1911.

[23] J. A. Nesbitt, R. W. Heckel, Metall. Trans. A, vol.18A (1987), pp.2061.

[24] Y. H. Sohn, M. A. Dayananda, Metall. Trans. A, vol.33A (2002), pp.3375.

[25] Y. H. Sohn, A. Puccio, M. A. Dayananda, Metall. Trans. A, vol.36A (2005), pp.2361.

[26] R. D. Sisson, Jr. and M. A. Dayananda, Metall. Trans., vol.3 (1972) pp. 647.

[27] J. W. Cahn and J. E. Hilliard, J. Chem. Phys.,vol.28 (1958) pp. 258.

[28] D. Fan and L. Q. Chen, J. Am. Ceram. Soc., vol.78 (1995) pp.1680.

[29] C. Huang, M. Olvera de la Cruz and B. W. Swift, Macromolecules, vol. 28 (1995) pp. 7996.

[30] K. Wu, Y. A. Chang and Y. Wang, Scripta Mater., vol.50 (2004) pp.1145.

[31] Y. Wang, D. Banerjee, C. C. Su and A. G. Khachaturyan, Acta Mater, vol.46 (1999) pp.2983.

[32] W. Huang and Y. A. Chang, Intermetallics, vol.7 (1999), pp.863.

[33] R. R. Mohanty, Masters. Thesis, Dept. of Metallurgy, Indian Institute of Science, Bangalore, 2002.

[34] S. M. Allen and J. W. Cahn, Acta. Metall.vol.27 (1979), pp.1085.

[35] H. E. Cook, Acta. Metall., vol.18 (1970) pp. 297.

[36] M.A. Dayananda, Y.H. Sohn, Metall. Mater. Trans. A, vol.30A (1999), 30A(3) pp. 535.

[37] R. D. Sission and M. A. Dayananda, Metall. Trans. A, vol.8A (1977), pp.1849.

CHAPTER 5
INTERDIFFUSION MICROSTRUCTURE EVOLUTION IN ISOTHERMAL DIFFUSION COUPLES OF Ni-Al SYSTEM

5.1 Introduction

Ordered intermetallic compounds such as Ni_3Al (i.e. $L1_2$ ordered phase) are important components in Ni-base superalloys for their higher strength at high temperature. In these alloys the ordered γ' phase is generally dispersed as precipitates in the matrix of a disordered Ni solid solution, γ phase. The performance and durability of these alloys depend on the microstructure and the stability of γ' precipitates at high temperature. Interdiffusion plays a significant role in determining the phase stability of these alloys, especially when they are in contact with each other as substrates and coatings, by changing the composition and the microstructure near their joining interfaces. For example, the oxidation resistance and lifetime of γ (Ni) + γ' ($L1_2$) coatings depend on the volume fraction and morphology of the γ' phase. Diffusion of the fast diffusing species Al into the substrate reduces the lifetime of these coatings drastically [1,2] as Al is the protective oxidation layer-forming element in the coating. Extensive experimental studies have been carried out to study the interdiffusion behavior and the lifetime of γ (Ni) + γ' (Ni_3Al) coating on γ (Ni) substrate alloys [3-8].

Many phase-field simulations have been performed on Ni-Al systems dealing with the coarsening kinetics, morphology and distribution of the γ' phase in γ matrix [9-11]. The present work reports the use of a 2D phase-field model to predict the interdiffusion microstructures in γ vs. γ', γ vs. $\gamma+\gamma'$ and $\gamma+\gamma'$ vs. $\gamma+\gamma'$ solid-to-solid diffusion couples in Ni-Al system. Development of interdiffusion microstructure was characterized according to types of boundaries, (e.g., type 0,

type 1 and type 2) allowed in binary diffusion couples [12]. Movement of such boundaries via dissolution or growth of phases across the boundary was analyzed. In agreement with experimental observations [4], the results of this study show the dissolution kinetics of the γ' phase in γ vs. $\gamma+\gamma'$ diffusion couples are interdiffusion controlled.

5.2 Description of Phase-Field Model

5.2.1 The Phase-field Variables

The Ni-Al system considered in this study has a disordered face-centered cubic (fcc) γ phase and an ordered Ni$_3$Al-γ' (L1$_2$) intermetallic phase. The structural relationship between the two phases can be viewed as four interpenetrating simple cubic sublattices, defined by points 1,2,3 and 4 shown in Figure 19. The four points are located at $(0,0,0)$, $\left(\frac{1}{2},\frac{1}{2},0\right)$, $\left(0,\frac{1}{2},\frac{1}{2}\right)$ and $\left(\frac{1}{2},0,\frac{1}{2}\right)$, respectively. For the fcc-γ phase, all the four sites are equivalent and occupied by Ni and Al atoms randomly. On the other hand, for the L1$_2$-γ' phase, the corner position (site 1) is occupied by Al atoms and the rest three equivalent face center positions (sites 2, 3, 4) are occupied by Ni atoms. The L1$_2$ structure can originate from any of the four sublattices of the fcc lattice that produces four distinguishable translational domains or antiphase domains [13,14]. A site occupation factor s_i ($i = 1,2,3,4$) can be defined in order to represent the four ordered states (s_1, s_2, s_3, s_4) as (1,-1,-1,-1), (-1,1,-1,-1), (-1,-1,1,-1) and (-1,-1,-1,1), where s_i is the occupation of the ith sublattice, and can either be +1 or -1 depending on whether the sublattice is occupied by an Al or a Ni atom, respectively. A three component order parameter field (η_i, i=1,2,3) can now be introduced to represent the four ordered domains such that [13]:

89

$$\eta_1 = \frac{\eta_0}{2}\left[s_1 - s_2 - s_3 + s_4\right] \tag{5.1a}$$

$$\eta_2 = \frac{\eta_0}{2}\left[s_1 - s_2 + s_3 - s_4\right] \tag{5.1b}$$

$$\eta_3 = \frac{\eta_0}{2}\left[s_1 + s_2 - s_3 - s_4\right] \tag{5.1c}$$

where η_0 is the equilibrium value of the long range order (lro) parameter. The four domains in terms of order parameters (η_1, η_2, η_3) are correspondingly $(1,1,1)\eta_0$, $(-1,-1,1)\eta_0$, $(-1,1,-1)\eta_0$, and $(1,-1,-1)\eta_0$, as described earlier in Equation 3.3. The sign of the individual order parameters are exactly opposite, if the sign of s_i is switched. This produces four energetically and structurally invariant states.

The microstructure of the substitutional binary alloy Ni-Al containing two compositionally and structurally distinct phases (fcc-γ and L1$_2$-γ′) can be represented by two field variables, i.e. a composition field, $c(r)$, and the structural order parameter field, $\eta_i(r)$, which describe the spatial compositional inhomogeneities and the structural difference between the phases, respectively.
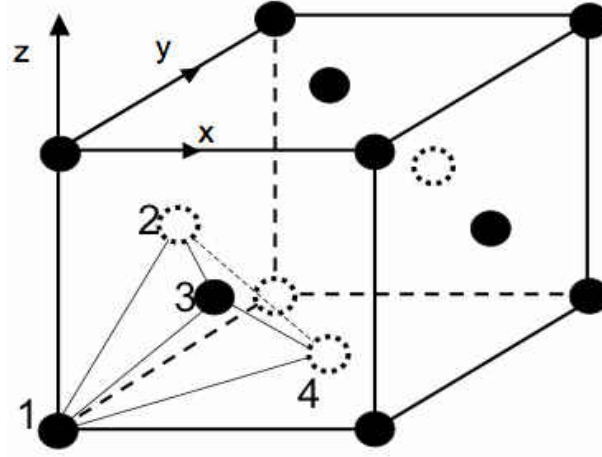
Figure 19: Schematic representation of the fcc lattice showing four equivalent lattice sites.

5.2.1 Phase-Field Formulation

In this phase-field simulation only a single ordered domain is considered, which reduces the number of order parameters from three to one by $\eta_1=\eta_2=\eta_3=\eta$. The lro parameter assumes a value of zero for the disordered phase and a finite value η_e for the ordered phase such that $\eta_1=\eta_2=\eta_3=\eta_e$ [15], where η_e is the equilibrium order parameter that corresponds to the minimum of the free energy. In both phases, the composition field corresponds to its equilibrium values determined by the thermodynamic description of the system, which is used to construct the phase diagram. In this study the effect of coherent elastic strain caused by the crystal lattice mismatch on the interdiffusion microstructure is ignored for simplicity. The total free energy of the inhomogeneous system is given by extended Cahn-Hilliard free energy functional, F [16,17]:

$$F = \int_V \left[f(c,\eta) + \kappa_c (\nabla c)^2 + \kappa_\eta (\nabla \eta)^2 \right] dV \tag{5.2}$$

91

where, $f(c, \eta)$ is the bulk chemical free energy per unit volume of the homogeneous alloy. c is the mole fraction of Al, κ_i and κ_η are the gradient energy coefficients associated with gradients of composition and lro parameter, respectively. The system evolves into its equilibrium condition by minimizing the total chemical free energy, F.

Landau polynomial approximation has been extensively used [9,10,14,15,18] to represent the bulk chemical free energy of a two-phase binary alloy of ordered and disordered phases. The details of the free energy approximation are described by Wang et al. [15], and have been used for the present simulation. For a single ordered domain, the free energy expression in Equation 3.2 can be rewritten as

$$f(c,\eta) = \frac{1}{2}b_0(c - c_1)^2 + \frac{1}{2}b_2(c_2 - c)\eta^2 + \frac{1}{3}b_3\eta^3 + \frac{1}{4}b_4\eta^4 \tag{5.3}$$

where $f_0(c) = \frac{1}{2}b_0(c - c_1)^2$, $B_2(c) = \frac{1}{2}b_2(c_2 - c)$, b_0, b_{02}, b_3, b_4, c_1 and c_2 are constants. The projection of the minimum of the approximated free energy vs. composition diagram is plotted in Figure 20, which was calculated for the equilibrium values of lro parameters for γ and γ' phases.

Using isotropic interfacial energy terms and neglecting the coherency stain effect, the governing field kinetic equations for the composition and lro parameter fields can be written as:

$$\frac{\partial c(\mathbf{r},t)}{\partial t} = \nabla\left[M_c(c)\nabla\left(\frac{\partial f}{\partial c} - 2\kappa_c\nabla^2 c\right)\right] \tag{5.4a}$$

and

$$\frac{\partial \eta(\mathbf{r},t)}{\partial t} = -M_{\eta}\left[\frac{\partial f}{\partial \eta} - 2\kappa_{\eta}\nabla^2\eta\right] \quad\quad\quad (5.4b)$$

where $M_c = \chi c(1-c)$ is the chemical mobility, and $\chi = D_o/k_B T M_{\eta}l^2$, where D_o is related to diffusivity in dilute solutions. M_{η} is the kinetic relaxation constant associated with the lro parameter and it characterizes the interface mobility. These kinetic equations are made dimensionless for numerical convenience and spatial dimensions are scaled by a length unit 'l'. In its dimensionless form, Equation 5.4 can be written as:

$$\frac{\partial \bar{c}(\mathbf{x},\tau)}{\partial \tau} = -\bar{\nabla}\left[\bar{M}_c(\bar{c})\bar{\nabla}\left(\frac{\partial \bar{f}}{\partial \bar{c}(\mathbf{x},\tau)} - \phi_c\bar{\nabla}^2\bar{c}(\mathbf{x},\tau)\right)\right] \quad\quad\quad (5.5a)$$

and

$$\frac{\partial \eta(\mathbf{x},\tau)}{\partial \tau} = -\left[\frac{\partial \bar{f}}{\partial \eta(\mathbf{x},\tau)} - \phi_{\eta}\bar{\nabla}^2\eta(\mathbf{x},\tau)\right] \qu\quad\quad (5.5b)$$

In Equation 5.5 $\bar{c} = \left[c(x,\tau) - c_{\gamma'}\right]/\left[c_{\gamma} - c_{\gamma'}\right]$, where c_{γ} and $c_{\gamma'}$ are the equilibrium composition of γ and γ' phases, respectively, calculated from the minima in f vs. c diagram shown in Figure 20. Also in Equation 5.5, τ is the reduced time defined by $\tau = M_{\eta}|\Delta f|t$, $\mathbf{x}$ is the reduced length scale defined by $\mathbf{x} = \mathbf{r}/l$, $\bar{\nabla} = (\partial/\partial\mathbf{x})$, and $\bar{f} = f/|\Delta f|$. In addition, $\bar{M}_c(\bar{c})$, ϕ_c and ϕ_{η} are the dimensionless chemical mobility, and gradient energy coefficients for composition, and lro parameter, respectively.

As shown in Figure 20, $|\Delta f|$ is the driving force for the phase transformation typically seen as the local maximum in the free energy diagram between the two equilibrium phases, and is located at the composition where the free energies of the two phases have the same values. The Ni-Al phase diagram was generated by the Thermo-Calc™ software using the PBIN™ database to illustrate the alloy compositions in the γ and γ+γ′ phase region used in this study as shown in Figure 21.

Starting with the flux equations in lattice frame of reference and following a similar approach outline in Section 4.2.2, the expression for the chemical mobility $M(c)$ in the laboratory frame of reference can be derived [19] as a function of concentration and atomic mobility:

$$M(c) = c(1-c)\left[c\beta_{Ni} + (1-c)\beta_{Al}\right] \tag{5.6}$$

where β_i is the atomic mobility of species i.
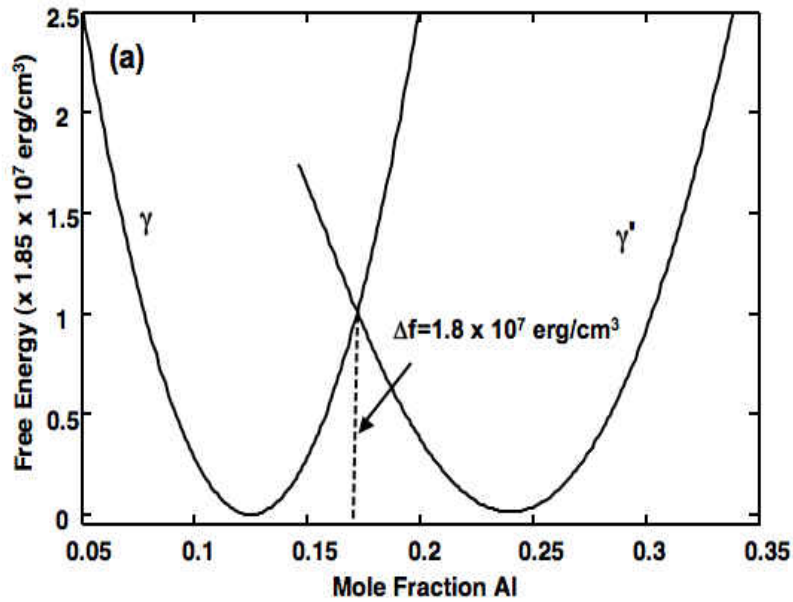
Figure 20: Approximated free energy vs. composition curve obtained for the equilibrium lro parameters. Δf is the driving force for the phase transformation [15].
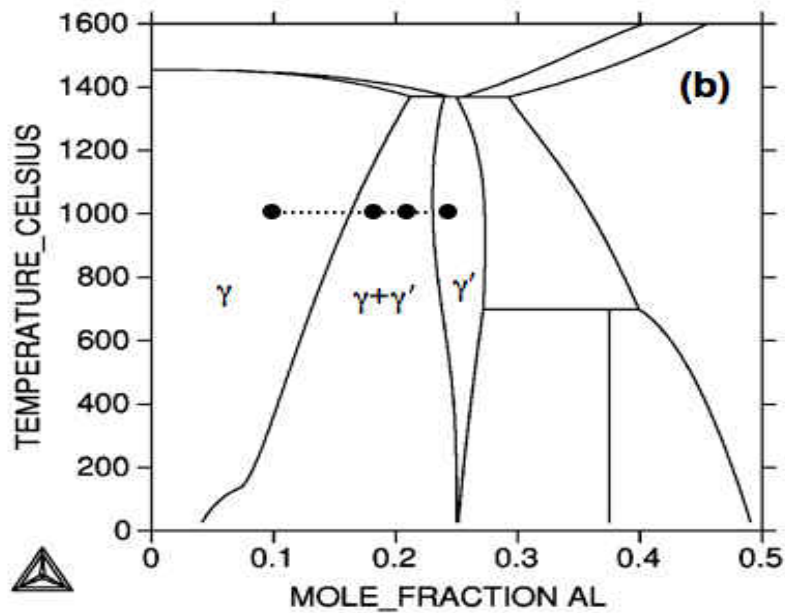
Figure 21: Ni-Al phase diagram determined from ThermoCalc™ with PBIN™ database.

The atomic mobility can be expressed [20] as:

$$\beta_i = \frac{1}{RT} \exp\left(-\Delta Q_i \Big/ RT\right) \tag{5.7}$$

where R is the gas constant, T is the temperature and ΔQ_i is the activation energy of diffusion for a component i in the disordered phase. For all practical purposes, in a dilute solution the value of β_{Al} determines the value of $\left[c\beta_{Ni} + (1-c)\beta_{Al}\right]$ term in Equation 5.7. So in this study $\left[c\beta_{Ni} + (1-c)\beta_{Al}\right]$ term is approximated as constant $\left(D_o / k_B T\right)$ in isothermal diffusion couples for simplicity [15].

5.2.2 Numerical Implementation

The semi-implicit Fourier-spectral method [21] as described in Section 3.3.2 is used to solve the kinetic Equations 5.5(a) and 5.5(b), which converts the set of partial differential equations into ordinary differential equations in Fourier space. The linear terms in the equations are solved explicitly whereas the nonlinear terms are solved implicitly. Random γ′ precipitates with a Gaussian size distribution were introduced in a γ matrix to develop individual two-phase alloys of system size of 512 x 512 grid points. To resemble closely with an experimental diffusion couple preparation, these individual alloys of different volume fractions of γ′ phase were joined together to make the diffusion couples of size 512 x 1,024 grid points. The dimensionless time step used in the simulation is 10^{-4}. With a length unit of $l \approx 167$ nm, real dimensions of all diffusion couples are 8,550 nm x 17,100 nm. All the simulations were carried out with periodic boundary condition applied in both dimensions.

5.3 Results

5.3.1 Growth of A Planar Interface

Movement of the γ/γ' interface was initially studied in 1D to assess the growth kinetics. Figures 22 and 23 show the composition profile of Al and the rate of movement of the γ/γ' interface. In Figure 22, the phase on the right side is at the equilibrium composition of γ' phase, and the phase on the left has an initial average composition slightly higher than the equilibrium composition of γ phase. The γ' phase grows towards the left, where the left-side composition decreases and finally attends the equilibrium composition of γ phase after a very long time. In Figure 23 the interface position vs. time curve shows that the interface movement follows a parabolic path that is typical of diffusion controlled growth kinetics.

5.3.2 γ vs. γ' Diffusion Couples

The first set of diffusion couples were made of single-phase γ and γ' alloys. 2D micrographs of γ vs. γ' diffusion couples at 1000°C for three different times are shown in Figure 24. The initial composition of γ and γ' phases are 10 and 25 mole% Al respectively, as shown in the phase diagram in Figure 21. The interface is observed to move towards the right-hand-side (i.e. γ' phase), which is a result of growth of γ phase and dissolution of γ' phase. This type of boundary is defined as a type 2 boundary, where one phase is added and the other is subtracted across it. The boundary is denoted by $\gamma > \gamma'$ notation. Composition profiles of Al at different times in Figure 25 show the movement of the boundary towards the γ' region and diffusion of Al from γ' to γ phase region.

97
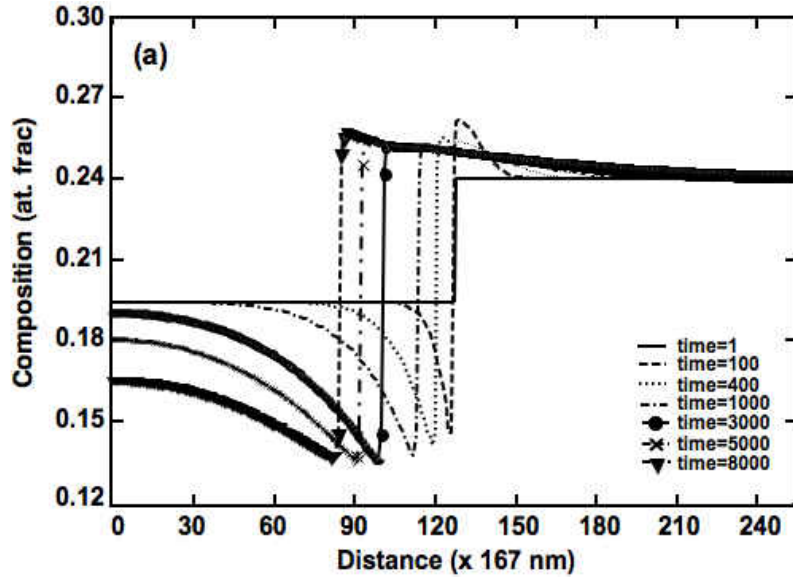
Figure 22: Composition profile of a γ vs. γ′ diffusion couple where the right side of the couple is at the equilibrium composition of γ′ phase, whereas the left side has an initial average composition slightly higher than the equilibrium composition of γ phase. The interface moves to the left and the left-hand-side composition gradually decreases to attend the equilibrium composition of γ phase.
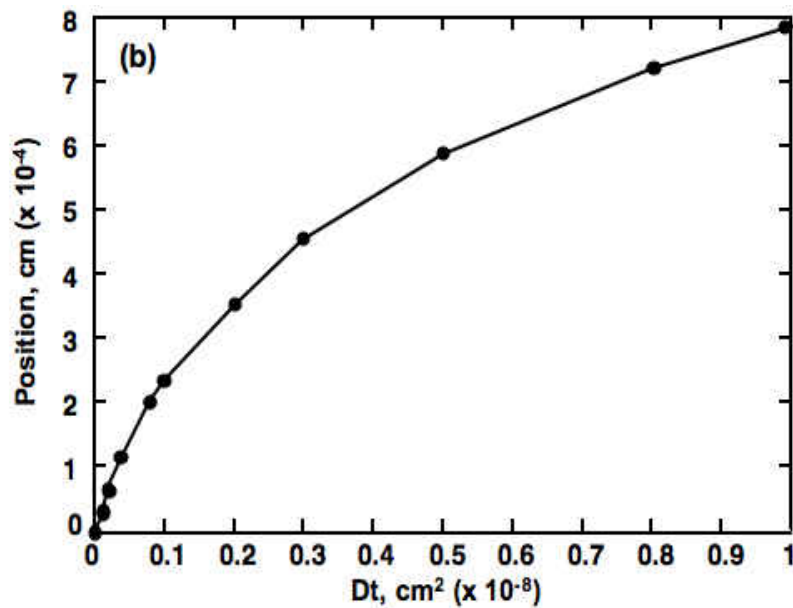
Figure 23: Interface position vs. Dt plot demonstrates a diffusion controlled parabolic rate of interface movement.
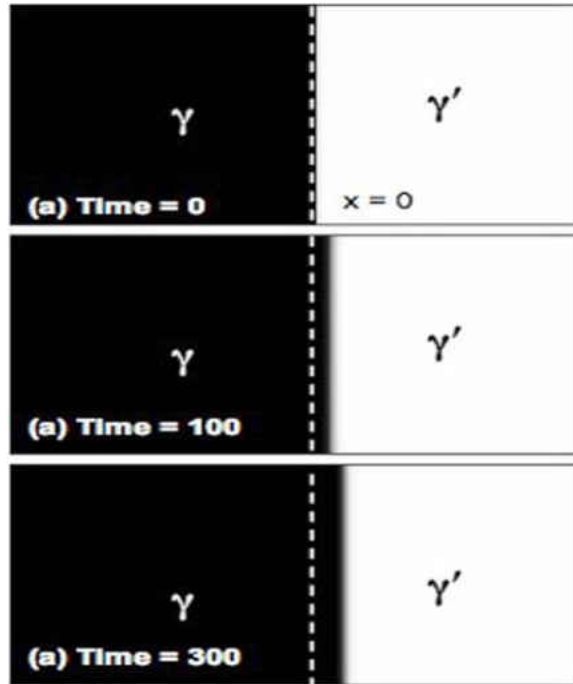
Figure 24: Magnified interdiffusion microstructures of a diffusion couple γ vs. γ′ at 1000˚C as a function of time. The initial boundary (x = 0) between γ and γ′ phase moves towards the γ′ phase defined by a type 2 boundary (γ > γ′).
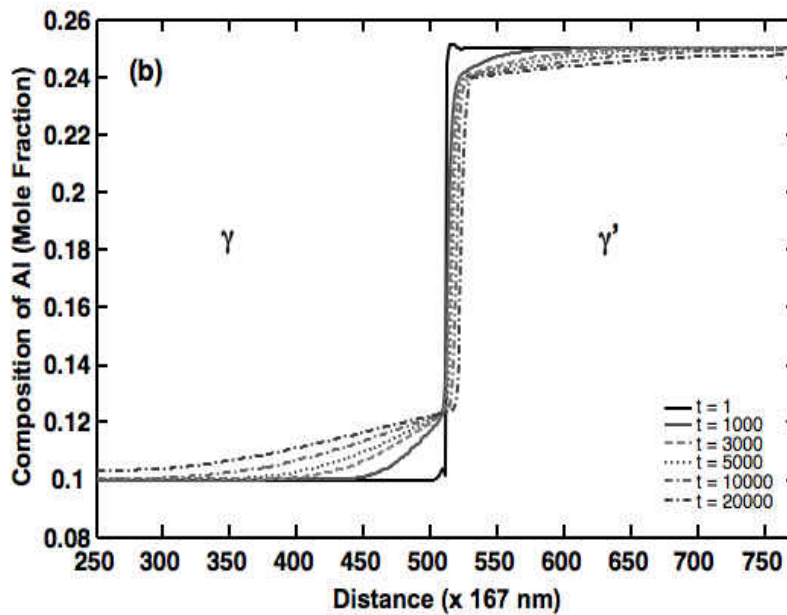
Figure 25: Composition profile of Al at different times showing the movement of initial boundary towards the γ′ phase and diffusion of Al from γ′ to γ phase.

5.3.3 γ vs. γ+γ′ Diffusion Couples

γ vs. γ+γ′ diffusion couples were utilized to study the dissolution of γ′ phase. Diffusion couples between single-phase (γ) and two-phase (γ+γ′) alloys were prepared with different volume fractions of γ′ phase. Two-phase alloys were generated with approximately 20%, 40% and 60% volume fractions of γ′ phase in a γ matrix, and they were joined with a single-phase γ alloy to produce the diffusion couples which describes the composition profile in 2D at the initial time t = 0. The evolution of interdiffusion microstructures in these couples were studied at 1000˚C by increasing the time of diffusion anneal during simulation. In Figure 26(a) and 26(b) are shown the interdiffusion microstructures of two γ vs. γ+γ′ diffusion couples with 0.4 and 0.6 volume fractions of γ′ phase, respectively. The initial boundary between γ and γ+γ′ phase-region is observed to move towards the two-phase region. Note that the formation of a γ phase layer on the right-hand end of the couple is due to the applied periodic boundary conditions. The volume fraction profile in Figure 27 shows a decrease in the fraction of γ′ phase near the interface, or in other words an increase in volume fraction of γ phase. The γ region grows at the expense of γ+γ′ region. This type of boundary is defined as type 1 boundary across which one phase is added or subtracted. The boundary is denoted by γ>γ+γ′ notation. A significant coalescence and growth of the second phase is observed in the two-phase region of the diffusion couple.
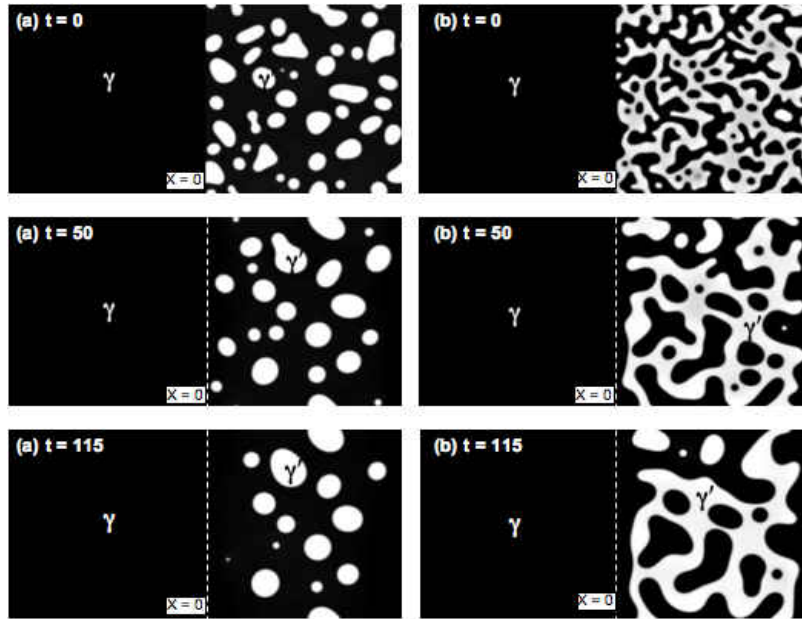
Figure 26: Interdiffusion microstructures of γ vs. γ+γ′ diffusion couples at 1000˚C as a function of time. The γ+γ′ alloys contain approximately (a) 0.4 and (b) 0.6 volume fraction of γ′ phase. The single-phase γ region grows at the expense of the two-phase (γ+γ') region. The initial boundary is at x = 0.
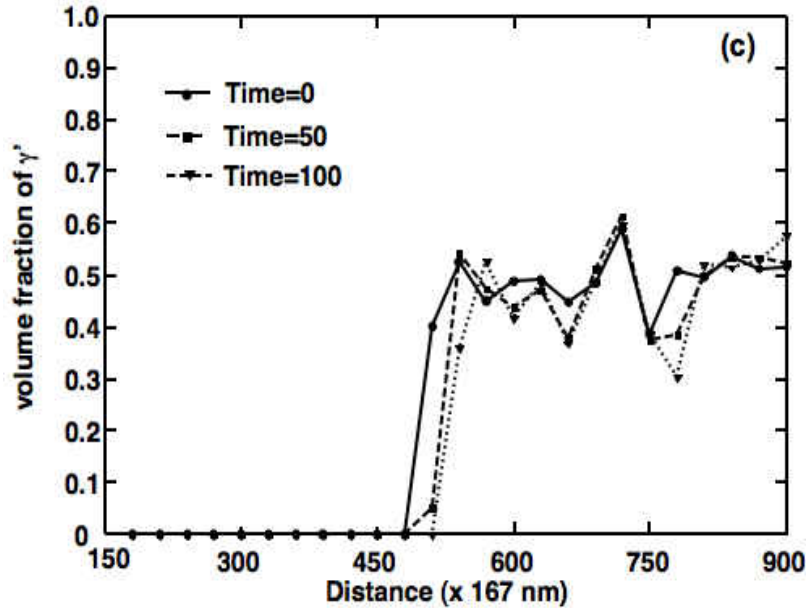
Figure 27: Volume fraction profiles of the diffusion couple shown in Figure 26. (b). The volume fraction profile was calculated by utilizing the order parameter of the microstructure. A decrease in the volume fraction of γ′ phase is marked by the movement of the initial interface towards the two-phase region. The boundary is defined as type 1 boundary (γ > γ+γ′).

5.3.4 γ+γ′ vs. γ+γ′ Diffusion Couples

Two-phase vs. two-phase (γ+γ′/γ+γ′) diffusion couples with different volume fractions of γ′ phase are simulated at 1000˚C and the resulting interdiffusion microstructures at different times are shown in Figure 28. In all the diffusion couples the initial boundary remains stationary with no addition or subtraction of phases across the boundary, although coalescence of γ′ particles across the boundary due to coarsening effect are prevalent. The volume fraction profiles in Figure 29 confirms the above observation made from the interdiffusion microstructure, as the volume fractions of phases remain almost constant throughout the diffusion couple with annealing time. This type of boundary is defined as the type 0 boundary and is denoted by γ+γ′|γ+γ′ notation, where no addition or subtraction of phases occurs.

5.3.5 Effect of Diffusivity and Gradient Energy Coefficients

Magnitudes of diffusivity and gradient energy coefficients were varied to study their effects on the interdiffusion microstructures. While the gradient energy coefficients affect the morphology of the second phase particles, they have no effect on the overall interdiffusion microstructure of the diffusion couples, whereas the diffusivity has an effect on the final interdiffusion microstructure. The γ vs. γ+γ′ diffusion couples with two different volume fractions of γ′ phase, and with three different values of diffusivity ratio 1:10:50 (i.e. χ = 0.04, 0.4 and 2.0 respectively) are simulated, while keeping all other parameters the same. Snapshots of the simulated interdiffusion microstructure of these couples at a time step t = 100 are shown in

Figure 30. The left and right columns of microstructures represent diffusion couples with γ′ phase volume of approximately 40% and 60%, respectively.

Figure 31 shows the variation in the width of the two-phase region with time as a function of diffusivity for γ vs. γ+γ′ diffusion couples with initial γ′ phase volume of approximately 60%. The difference in the microstructure can be described by the difference in the rate of dissolution of the second phase or the rate of movement of the Type 1 boundary towards the two-phase region. Two observations can be made: first, the time for the initiation of the dissolution of the second phase, i.e. the time for the start of any observable movement of the initial boundary between γ and γ+γ′ region depends on the diffusivity values. Second, the rate of depletion of the γ′ phase in two-phase region also depends on the diffusivity values. The lower is the diffusivity, the longer is the start time and the lower is the rate of depletion.

Simulated microstructures of γ vs. γ+γ′ diffusion couples with three different gradient energy coefficients in the ratio 1:2.5:3.5 are shown in Figure 32, where diffusivity is the same for the three couples. These microstructures are obtained at the same time steps of simulation. Volume fraction of γ′ phase on the right side remains approximately 40%. They show little difference in interdiffusion microstructure, e.g., dissolution or growth of phases.
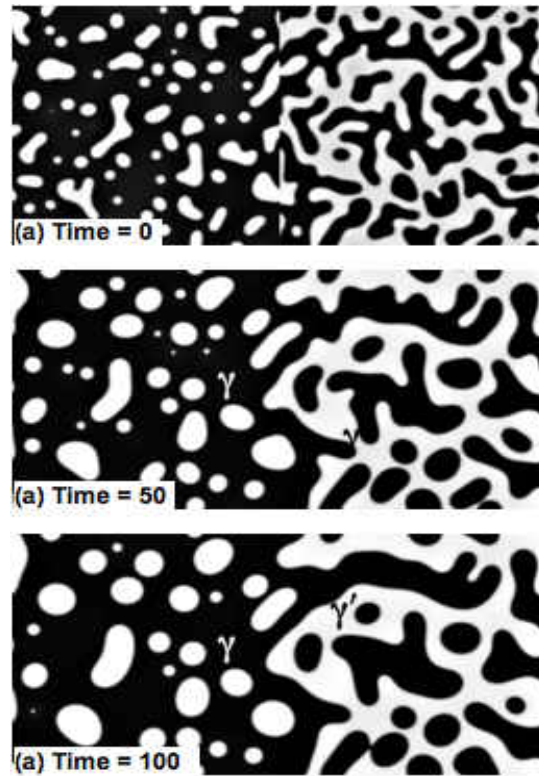
Figure 28: Interdiffusion microstructures of γ+γ' vs. γ+γ' diffusion couples at 1000˚C as a function of time. The two-phase alloys contain approximately 0.4 and 0.6 volume fractions of γ' phase on the left and right hand side of the couple, respectively. There is no movement of the boundary although some microstructural change due to coalescence is observed.
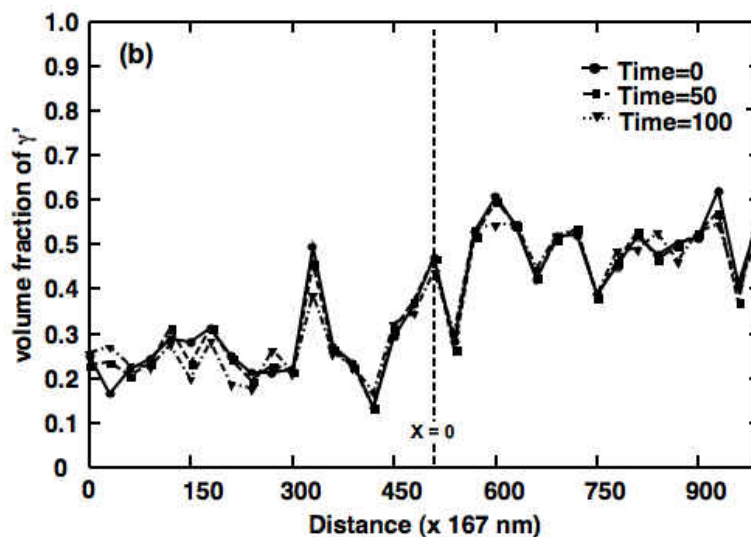
Figure 29: Volume fraction profiles of the diffusion couples shown in the Figure 15. Volume fractions of γ' phase remain constant across the boundary (x = 0) and characterized by a type 0 boundary (γ+γ' | γ+γ').

5.4 Discussions

Three types of boundaries can be formed in a diffusion couples based on the number of components and phases present [12]. In the present simulation of binary Ni-Al system, boundary of the type 2 is observed in the γ vs. γ' couples where the boundary moves towards γ' phase, and can be symbolically defined as $\gamma > \gamma'$. This boundary is characterized by the addition of γ phase and removal of γ' phase across the boundary.
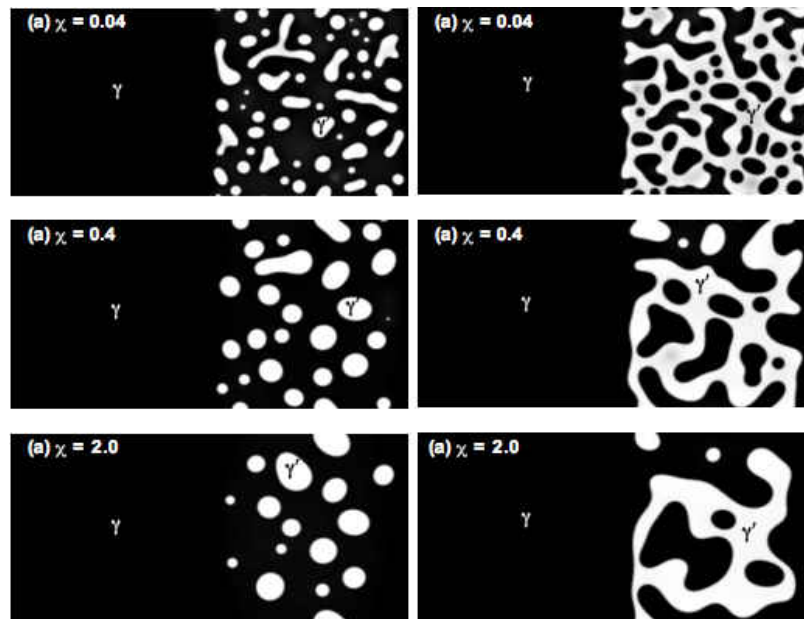
Figure 30: Interdiffusion microstructures of γ vs. $\gamma+\gamma'$ diffusion couples with different values of diffusivities in the ratio 1:10:50 (i.e. $\chi = 0.04$, 0.4 and 2.0 respectively) at time step = 100. The left and right columns of microstructures represent diffusion couples with γ' phase volume of approximately 40% and 60%, respectively.
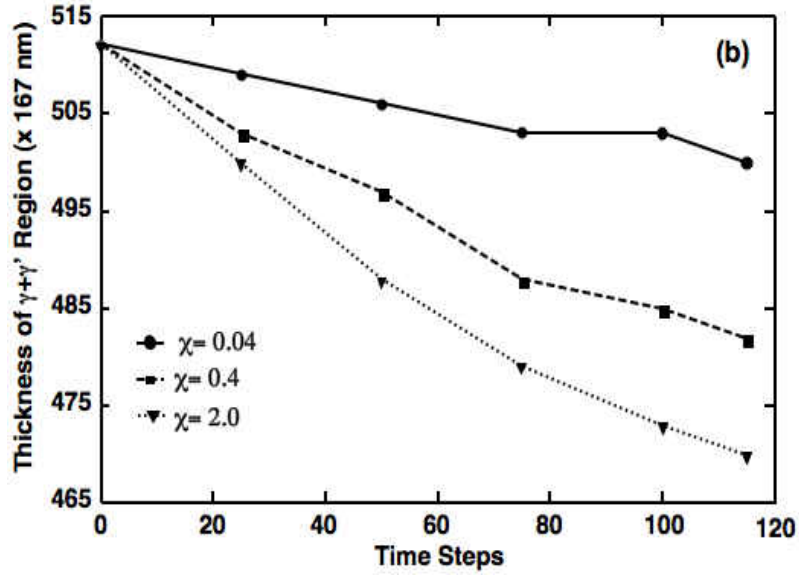
Figure 31: A plot between the width of the two-phase zone vs. time for three γ vs. γ+γ′ diffusion couples with the γ′ phase volume of approximately 60% as shown in Figure 26(b).
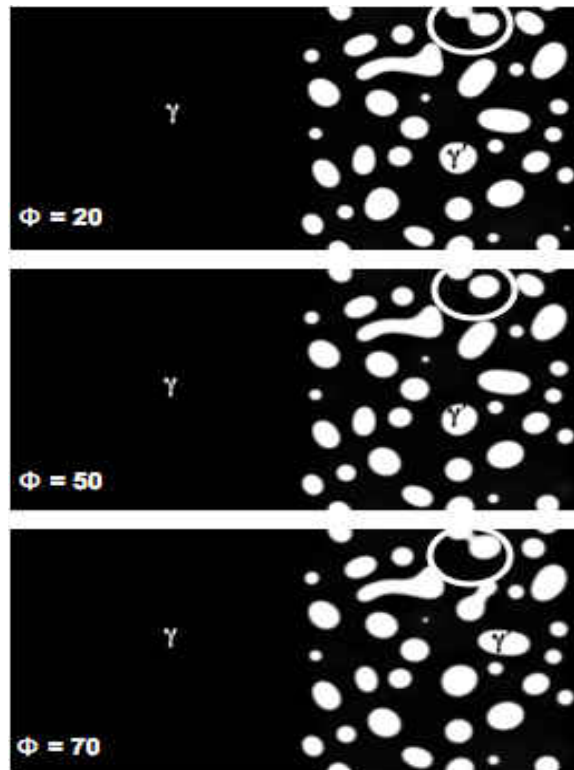
Figure 32: Interdiffusion microstructures of three γ vs. γ+γ′ diffusion couples with different values of gradient energy coefficients (ϕ_c) in the ratio 1:2.5:3.5 at time step = 50. The circled areas represent some of the observed differences in the microstructures.

.

The experimental observations made by Watanabe *et al* [7,8] in Ni (γ) vs. Ni$_3$Al (L1$_2$-γ') diffusion couples suggest that the initial boundary moves towards the γ' phase with diffusion of Al out of γ' phase and into the γ phase. Our simulation results agree with these experimental observations.

In the case of γ vs. $\gamma+\gamma'$ diffusion couples, the boundary is type 1 denoted by $\gamma > \gamma+\gamma'$. Here dissolution of γ' phase occurs at the boundary and the boundary is moving towards the two-phase region. The simulation results agree with the experimental observation made by Susan *et al* [4] in Ni-Al diffusion couples with γ and $\gamma+\gamma'$ phases. Their results show an increasing dissolution of γ' phase in the two-phase region with time of annealing, forming a single-phase γ layer near the boundary. Furthermore, in their study, the width of the $\gamma+\gamma'$ region decreased whose rate depended on the temperature of diffusion anneal. In other words this rate of dissolution depends on the diffusivity that changes exponentially with temperature according to the Arrhenius relationship. Interdiffusion coefficients in γ and γ'(L1$_2$) phases show almost an order of magnitude change with every 100°C change in temperature at constant values of Al compositions [8]. The kinetics of dissolution of the γ' phase near the boundary depends on interdiffusion coefficients that can vary with temperature and composition.

In the $\gamma+\gamma'$ vs. $\gamma+\gamma'$ diffusion couple, the boundary is stationary which is type 0 in nature. In the two-phase region in a binary alloy, there is no chemical potential gradient, and therefore no interdiffusion occurs. The only observable feature seen across such a boundary is the coalescence of phases that makes an initially discontinuous boundary diffused.

5.5 Summary

Evolution of interdiffusion microstructures in a two-dimension (2D) was examined for binary Ni-Al solid-to-solid diffusion couples using a phase-field approach. Utilizing semi-implicit Fourier-spectral solutions to Cahn-Hilliard and Allen-Cahn equations, multiphase diffusion couples of fcc Ni solid solutions γ vs. $L1_2$ Ni_3Al solid solutions γ', γ vs. $\gamma+\gamma'$, $\gamma+\gamma'$ vs. $\gamma+\gamma'$ with sufficient thermodynamic and kinetic database, were simulated with alloys of varying compositions and volume fractions of second phase (e.g., γ'). Chemical mobility as a function of composition was used in the study with constant gradient energy coefficient, and their effect on the final interdiffusion microstructure was examined. The microstructures were characterized by the type of boundaries formed, i.e. Type 0, Type I, and Type II, following various experimental observations in literature and thermodynamic considerations. Type 0, Type I, and Type II boundaries were found in $\gamma+\gamma'$ vs. $\gamma+\gamma'$, γ vs. $\gamma+\gamma'$ and γ vs. γ' diffusion couples, respectively. The dissolution kinetics of the γ' phase in γ vs. $\gamma+\gamma'$ diffusion couples were simulated as a function of varying diffusivities. Rate of dissolution of γ' phase and thus the rate of movement of $\gamma/(\gamma+\gamma')$ boundary was interdiffusion controlled. The gradient energy coefficient that governs the interface energy did not affect the type of boundaries although a slight difference in coalesced-final microstructure was observed. The present study demonstrates the applicability of the phase-field model to simulate interdiffusion microstructure in solid-to-solid diffusion couples.

5.6 References

[1]   J. L. Smialek, C. E. Lowell, J. Electrochem. Soc., vol.121 (1974) pp.800.

[2]   S. R. Levine, Metall. Trans., vol 9A (1978), pp.1237.

[3]   K. Fujiwara, Z. Horita, Acta Mater., vol.52 (2002), pp.1571.

[4]   D. F. Susan, A. R. Marder, Acta Mater., vol.49 (2001), pp.1153.

[5]   T. Ikeda, A. Almazouzi, H. Numakura, M. Koiwa, W. Sprengel, H. Nakajima, Acta Mater., vol.46 (2002), pp.5369.

[6]   H. Numakura, T. Ikeda, Mat. Sc. Eng. A., vol.A312 (2000), pp.109.

[7]   M. Watanabe, Z. Horita, D. J. Smith, M. R. McCartney, T. Sano, M. Nemoto, Acta Met. Mater., vol.42 (1994) pp.3381.

[8]   M. Watanabe, Z. Horita, T. Sano, M. Nemoto, Acta Met. Mater., vol.42 (1994) pp.3389.

[9]   D. Y. Li, L. Q. Chen, Scripta Mater., vol.37 (1997), pp.1271.

[10] V. Vaithyanathan, L. Q. Chen, Acta Mater., vol.50 (2002), pp.4061.

[11] J. Z. Zhu, T. Wang, A. J. Ardell, S. H. Zhou, Z. K. Liu, L. Q. Chen, Acta Mater., vol.52 (2004), pp.2837.

[12] J. E. Morral, C. Jin, A. Engstrom, and J. Ågren, Scripta Mater., vol.34 (1996) pp.1661.

[13] Z. W. Lai, Phy. Rev. B., vol.41 (1990), pp.9239.

[14] V. Vaithyanathan. Phase-field Simulation of Coherent Precipitate Morphology and Coarsening Kinetics. Ph. D. Thesis, The Pennsylvania State Univ., (2002).

[15] Y. Wang, D. Banerjee, C. C. Su, A. G. Khachaturyan, Acta Mater., vol.46 (1998) pp.2983.

[16] J. W. Cahn, J. E. Hilliard, J. Chem. Phys, vol.28 (1958) pp.258.

[17] D. Fan, L. Q. Chen, J. Am. Ceram. Soc., vol.78 (1995) pp.1680.

[18] V. Vaithyanathan, L. Q. Chen, Scripta Mater., vol.42 (2000) pp.967.

[19] R. R. Mohanty, Y. H. Sohn, J. Phase Eq. Diff., vol.27 (2006) pp.676.

[20] A. Engstrom, J. Ågren, Z Metallkd., vol.87 (1996) pp.92.

[21] L. Q. Chen, J. Shen, Comp. Phy. Comm. Vol.108 (1998) pp.147.

CHAPTER 6
INTERDIFFUSION MICROSTRUCTURE EVOLUTION
IN ISOTHERMAL DIFFUSION COUPLES OF Ni-Cr-Al SYSTEM

6.1 Introduction

Coating-substrate systems are often encountered in many practical and industrial applications. High-temperature gas turbine blades coated with oxidation and corrosion resistant coatings (e.g. thermal barrier coatings) is one such example. The Ni-based superalloy in turbine blades is generally coated with a metallic layer known as bond coat, and is typically made of MCrAlY (M=Ni and/or Co) or β-NiAl with additions such as Pt. An understanding of the phase stability is necessary in order to produce such a coating-substrate system and sustain it under extreme operating conditions. Interdiffusion phenomenon plays a critical role in determining the stability of these systems as the diffusion of alloying elements between the substrate and coating can cause significant changes in the composition and microstructure near the interface.

The coating microstructure typically contains a Ni solid solution (fcc-γ) phase dispersed with NiAl (B2-β) phase. Degradation of these coatings predominantly occurs due to the dissolution of the β phase caused by the depletion of the Al content as a result of the coating-substrate interdiffusion and oxidation [1,2] to form thermally grown oxide (TGO) layer. The complex chemistry of most Ni-based superalloy substrates makes it difficult to understand the interdiffusion process. Hence, investigations are generally carried out on a simplified system of the ternary Ni-Cr-Al alloys [3]. Many experimental results are available to provide excellent qualitative understanding of the degradation phenomena involved in this system [4-8]. Various computational models [9-12] have been also developed to simulate and predict the interdiffusion

110

behavior in coating-substrate systems. Most of these models are only applicable in one dimension and assume an average concentration for the two-phase region to solve the moving boundary problem without any consideration for the microstructure. In this regard, the phase-field model can be used as an efficient tool to predict microstructure evolution in various material systems. In previous two chapters it has been established that the phase-field model can predict the interdiffusion behavior and microstructure evolution in multiphase diffusion couples of binary Ni-Al and ternary Ni-Cr-Al systems.

The purpose of the present study is to predict the interdiffusion microstructure in single-phase (γ) vs. two-phase ($\gamma+\beta$) and two-phase ($\gamma+\beta$) vs. two-phase ($\gamma+\beta$) diffusion couples of Ni-Cr-Al system by computer simulation using phase-field model, and to examine the dissolution kinetics of the Al-rich β phase as a function of the alloy composition and phase volume fraction in γ vs. $\gamma+\beta$ diffusion couples. A comparison with experimental results [6] reported in the literature was carried out to validate the simulation results.

6.2 Procedure and Details of Simulation

6.2.1 Formulation of Phase-field Model

As described in previous chapters, the Cahn-Hilliard free energy functional [13,14] is again used to express the total chemical free energy, F_{chem}, of the system as the sum of the bulk chemical free energy, F_{bulk}, and total interfacial energy, F_{int}, expressed by:

$$F_{chem} = F_{bulk} + F_{int} = F = N_V \int_V f(c_i, \eta) + \kappa_i (\nabla c_i)^2 + \kappa_\eta (\nabla \eta)^2 \text{ where } i = Al, Cr \qquad (6.1)$$

where $f(c_{Al}, c_{Cr}, \eta)$ is the bulk chemical free energy per atom of the homogeneous alloy, $c_{Cr}(x,t)$ and $c_{Al}(x,t)$ are the mole or atom fraction of Cr and Al, $\eta(x,t)$ is the non-conserved structure order (SO) parameter that describes the symmetry change involved in fcc $\leftrightarrow$ B2 phase transformation, N_V is the number of atoms per unit volume, assumed to be constant, κ_i and κ_η are the gradient energy coefficients associated with gradients of compositions of individual elements and η, respectively.

The SO parameter represents the tetragonality of the β phase [15] and is zero for the fcc phase and assumes an equilibrium value, η_0 in the β phase. This requirement is met by choosing $\eta = \frac{c}{a} - 1$, as illustrated in Figure 33, so that $\eta = 0$ for fcc phase and $\eta = \sqrt{2} - 1$ for B2 phase. Only single order parameter is used in this formulation as antiphase domains within the B2 phase are not considered.
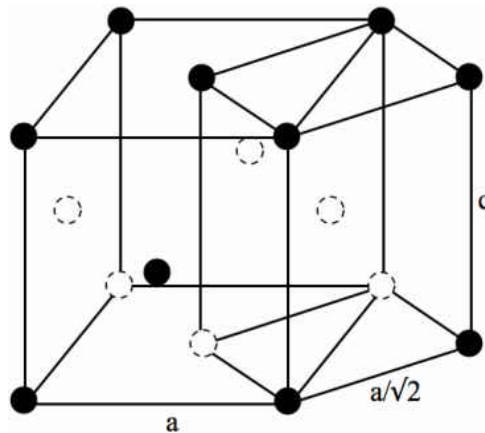
Figure 33: Schematic representation of structural relationship between fcc and bcc structures (borrowed from Wu's Thesis [16]).

Determination of bulk chemical free energy follows a similar procedure described in Section 5.2.1 where a Landau polynomial approximation is used and is given by [12]:

$$f\left(c_{Al}, c_{Cr}, \eta\right) = f^{\gamma}\left(c_{Al}, c_{Cr}, 0\right) + \frac{A_2\left(c_{Al}, c_{Cr}\right)}{2}\eta^2 + \frac{A_4\left(c_{Al}, c_{Cr}\right)}{4}\eta^4 + \ldots \tag{6.2}$$

where $f\left(c_{Al}, c_{Cr}, 0\right)$ is the free energy of the γ phase, calculated from the thermodynamic data provided by Huang et. al. [18]. The parameter A_2 is a 4th order polynomial of compositions and A_4 is a constant. The details of free energy approximation is provided elsewhere [12,15] and is directly borrowed in this work. For the second phase β, the free energy is obtained from Equation 6.2 by substituting the equilibrium SO parameter value, $\eta_0(c_{Al}, c_{Cr})$ determined by:

$$\left.\frac{\partial f\left(c_{Al}, c_{Cr}, \eta\right)}{\partial \eta}\right|_{\eta=\eta_0} = 0 \tag{6.3}$$

The field kinetic equations for temporal evolution of composition variables and SO parameter were derived [18,19] and reduced to their dimensionless form. The final governing equations for composition variables are:

$$
\begin{aligned}
\frac{\partial c_{Al}(\tilde{x}, \tau)}{\partial \tau} = &\tilde{\nabla} \cdot \left[\tilde{M}_{AlAl} \tilde{\nabla}\left(\frac{\partial \tilde{f}}{\partial c_{Al}} - 2\tilde{\kappa}_{AlAl}\tilde{\nabla}^2 c_{Al} - 2\tilde{\kappa}_{AlCr}\tilde{\nabla}^2 c_{Cr} \right) \right] \\
&+ \tilde{\nabla} \cdot \left[\tilde{M}_{AlCr} \tilde{\nabla}\left(\frac{\partial \tilde{f}}{\partial c_{Cr}} - 2\tilde{\kappa}_{AlCr}\tilde{\nabla}^2 c_{Al} - 2\tilde{\kappa}_{CrCr}\tilde{\nabla}^2 c_{Cr} \right) \right]
\end{aligned}
\tag{6.4a}
$$

and

$$
\begin{aligned}
\frac{\partial c_{Cr}(\tilde{x}, \tau)}{\partial \tau} = &\tilde{\nabla} \cdot \left[\tilde{M}_{CrAl} \tilde{\nabla}\left(\frac{\partial \tilde{f}}{\partial c_{Al}} - 2\tilde{\kappa}_{AlAl}\tilde{\nabla}^2 c_{Al} - 2\tilde{\kappa}_{AlCr}\tilde{\nabla}^2 c_{Cr} \right) \right] \\
&+ \tilde{\nabla} \cdot \left[\tilde{M}_{CrCr} \tilde{\nabla}\left(\frac{\partial \tilde{f}}{\partial c_{Cr}} - 2\tilde{\kappa}_{AlCr}\tilde{\nabla}^2 c_{Al} - 2\tilde{\kappa}_{CrCr}\tilde{\nabla}^2 c_{Cr} \right) \right]
\end{aligned}
\tag{6.4b}
$$

113

The chemical mobility terms, $\tilde{M}_{ij}$ are functions of compositions and atomic mobilities of individual components, and has the same form given in Equation 4.13 of Chapter 4. The atomic mobilities used in this study were functions of concentration in the γ phase [20] and constants in the β phase [12].

The evolution of non-conserved field variable η is described by the time-dependent Ginzburg-Landau equation or Allen-Cahn equation [19]:

$$\frac{\partial \eta(\tilde{x}, \tau)}{\partial \tau} = -\tilde{M}_\eta \left[\frac{\partial \tilde{f}}{\partial \eta} - 2\tilde{\kappa}_\eta \tilde{\nabla}^2 \eta \right] \tag{6.5}$$

where $\tilde{M}_\eta$ is the relaxation constant that characterizes the interface mobility.

6.2.2 Numerical Implementation

The governing equations for composition and SO parameter fields, Equations 6.4 and 6.5, were solved numerically using semi-implicit Fourier-spectral [21,22] method to obtain the interdiffusion microstructure evolution in diffusion couples. In this method the linear terms in the equations are solved explicitly whereas the nonlinear terms are solved implicitly. The evolution equations were made dimensionless by multiplying both sides of the equations with $l^2/B\nabla f$, where l is the length scale of the calculation, Δf is the normalization factor for the free energy, and B is a constant in the units of atomic mobility. In their dimensionless reduced form, the chemical mobilities are $\tilde{M}_{ij} = M_{ij} V_m / B$, the gradient energy coefficients are $\tilde{\kappa}_{ij} = \kappa_{ij} / \Delta f l^2$ and

$\tilde{\kappa}_\eta = \kappa_\eta / \Delta f l^2$, and the relaxation constant is $\tilde{M}_\eta = M_\eta l^2 / V_m B$, where V_m = 12x10^{-6} m^3/mol, is

the molar volume, which was assumed to be constant. In the simulation $\tilde{\kappa}_{CrCr} = \tilde{\kappa}_{AlAl} = \tilde{\kappa}_\eta = 0.75$,

$\tilde{\kappa}_{AlCr} = \tilde{\kappa}_{CrAl} = -0.375$ and $\tilde{M}_\eta = 1.0$ [12]. The dimensionless mesh size is $\Delta x = 1.0$, along both x

and y coordinates and the dimensionless time step is 10^{-5}, which corresponds to a length scale of

5μm and time scale of 10^{-5} hour respectively. All the simulations were carried out with periodic

boundary condition applied in two dimensions.

6.2.3 Initial Microstructure for Simulation

Generally, an initial composition distribution is introduced as the initial microstructure to

start the diffusion couples simulations. One way to do this for a diffusion couple containing at

least one two-phase region is to introduce random spherical particles of the second phase with

Gaussian size distribution on a desired matrix phase. In this work a different approach was

employed to generate the initial microstructure for the diffusion couples which resembles closely

with an experimental diffusion couple preparation. In this approach random β precipitates with a

Gaussian size distribution were introduced in a γ matrix, and were annealed to develop individual

two-phase alloys of system size of 256 x 256 grid points. These individual alloys of different

average compositions or volume fractions of β phase were then joined with single-phase γ alloys

generated with a size of 256 x 256 grid points to make the diffusion couples of size 256 x 512

grid points. Another reason to follow this procedure instead of introducing β particles in the

diffusion couple itself at the beginning of the simulation is to avoid the effect of initially-rapid

coarsening on the recession distance of the γ+β side of the diffusion couple. The influence of this

procedure on the final interdiffusion microstructure is presented and discussed in subsequent

sections of this chapter. With a length unit of $l \approx 5\mu m$, real dimensions of all diffusion couples are 1,280 μm x 2,560 μm.

6.2.4 Alloy Compositions

The alloy compositions used in this study and their volume fractions of β phase are given in Table I. The locations of these compositions on the Ni-Cr-Al phase diagram are also shown in Figure 33. The alloy compositions are similar to the alloys used in the experimental work by Nesbitt and Heckel [6], but it should be noted here that Huang's thermodynamic data [17] used in this study for the phase diagram calculation predicts higher Al content for the γ+β/γ equilibrium boundary than the experimental phase diagram determined by Nesbitt. Hence, the volume fraction of β phase in the simulation is slightly and always lower than the experimental volume fraction for the same average composition of the alloy. Comparison with other thermodynamic database available in the literature [23,24] suggests that the location of γ+β/γ phase boundary is at close proximity to the one used in this work.

Table 4: Composition and volume phase fraction of Ni-Cr-Al alloys employed in phase-field simulation.

Alloy Designation	Composition (mole frac.)		Phases Present	Volume Fraction β
	Al	Cr		
W	0.005	0.125	γ	0
X	0.005	0.25	γ	0
Y	0.005	0.35	γ	0
Z	0.005	0.45	γ	0
Al1	0.005	0.2	γ	0
Al2	0.1	0.2	γ	0
Al3	0.14	0.2	γ	0
1A	0.192	0.162	γ+β	0.20
2A	0.272	0.115	γ+β	0.70
1C	0.135	0.242	γ+β	0.35
2C	0.12	0.22	γ+β	0.55
4	0.242	0.127	γ+β	0.55
T	0.235	0.215	γ+β	0.55

Figure 34: Alloy designations and compositions shown on the Ni-rich part of the Ni-Cr-Al phase diagram.

6.3 Results

6.3.1 Influence of Initial Microstructure With and Without Annealing

Figure 35 and Figure 36 show the evolution of interdiffusion microstructures as a function of time for the couple 4 vs. X, with two types of initial conditions. The microstructures in Figure 35 were simulated with the initial microstructure of pre-annealed two-phase alloy 4, while those in Figure 36 were simulated with β nuclei without pre-annealing. In both the cases the two-phase $\gamma+\beta$ region receded with time by dissolution of the β phase, but the recession distance was found to be larger for the couple with initial microstructure containing β nuclei without pre-annealing. The volume fraction of the β phase within the two-phase alloy away from the diffusional interaction zone remains constant
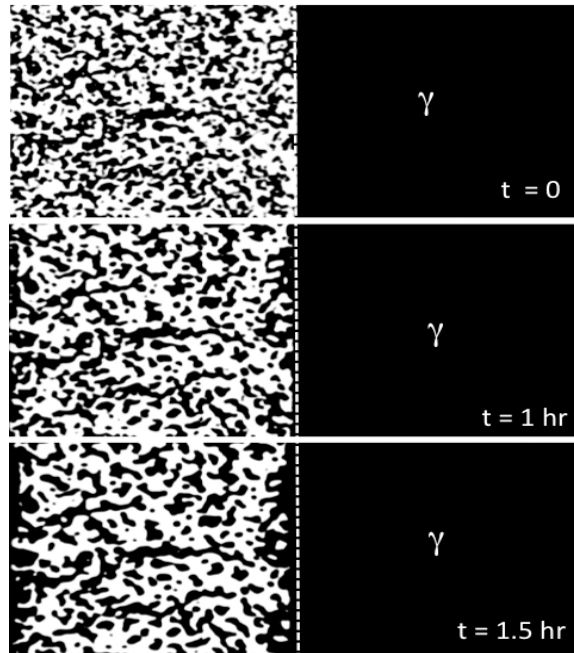
Figure 35: Simulated interdiffusion microstructure evolution in γ+β vs. γ diffusion couple (4 vs. X) showing the dissolution of β phase with time. The simulation was started with pre-annealed initial microstructure. The dark region is γ phase and the bright region is β phase. The dotted line is the location of the initial γ+β and γ interface. This convention is followed in all figures in this manuscript.
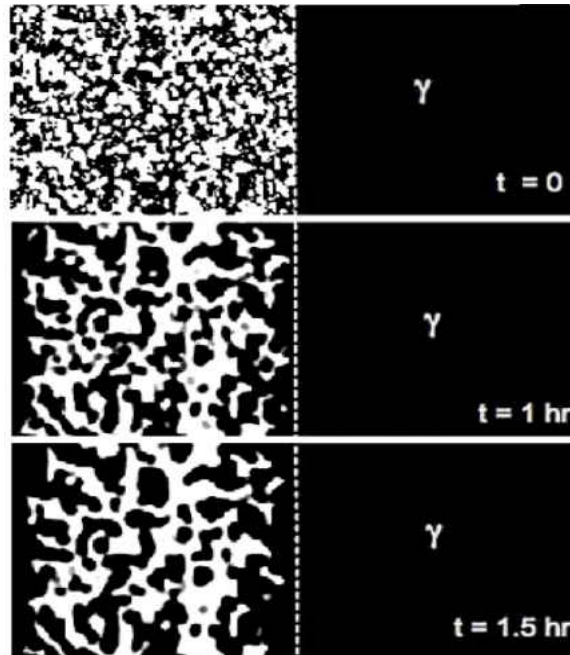
Figure 36: Simulated interdiffusion microstructure evolution in γ+β vs. γ diffusion couple (4 vs. X) showing the dissolution of β phase with time. The simulation was started with β nuclei in the initial microstructure.

119

6.3.2 Effects of Composition and Volume Fraction

To study the effect of alloy composition on the dissolution rate of β phase, diffusion couples of increasing Cr and Al content in the single-phase γ alloys were simulated. In all the couples, the same two-phase alloy was used. In the diffusion couples shown in Figure 37, Cr content of the γ phase was increased keeping the Al content fixed. Similarly, in Figure 38, Al content of the γ phase was increased keeping the Cr content fixed. The resulting microstructures show that an increase in the Cr or Al content of the γ phase decreased the rate of β dissolution and the recession of the two-phase region. A plot of the recession distance vs. concentration of Cr and Al in the γ phase alloy, presented in Figure 39, illustrates that the effect of variation of Al concentration on the recession distance is more significant than Cr concentration.

Effect of volume fraction of the β phase in the two-phase alloy on the dissolution kinetics was investigated using diffusion couples containing different volume fractions of the β phase. Simulated microstructures of two sets of diffusion couples are presented in Figure 40. The dissolution or recession rate is higher in the couple 1A vs. Z compared to 2A vs. Z and in 1C vs. W compared to 2C vs. W, as shown in Figure 40(a) and (b), respectively. This suggests that the rate of β dissolution is also influenced by the amount of β present in the γ+β alloy. The lower the volume fraction of β, the higher is the dissolution rate.
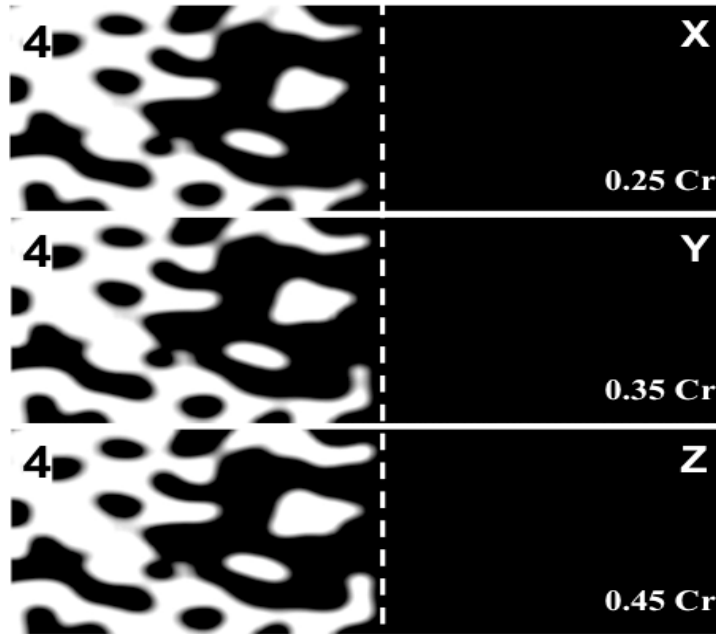
Figure 37: Expanded view of simulated interdiffusion microstructures for diffusion couples with same γ+β alloy but different γ alloys at t = 1.5 hour. The initial Al concentration of the γ alloy is fixed at 0.005 and Cr concentration varies as 0.25 (4 vs. X), 0.35 (4 vs. Y) and 0.45 (4 vs. Z).
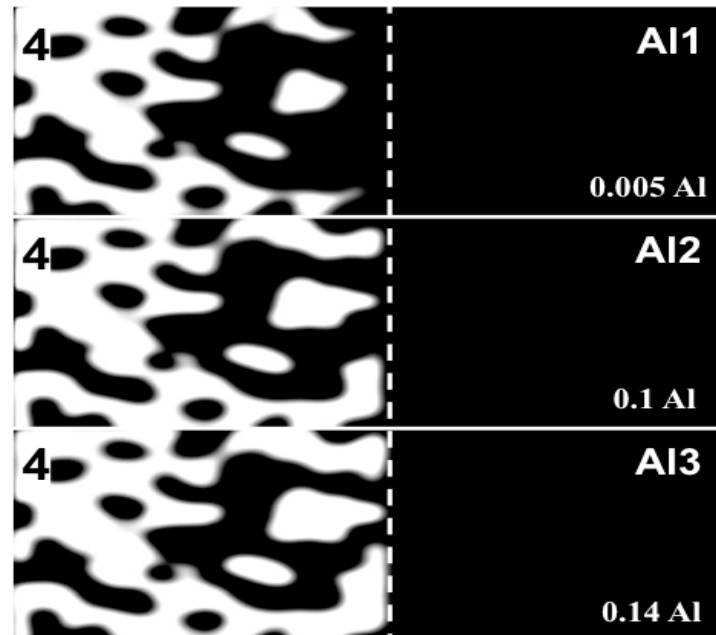
Figure 38: Expanded view of simulated interdiffusion microstructures for diffusion couples with same γ+β alloy but different γ alloys at t = 1.5 hour. The initial Cr concentration of the γ alloy is fixed at 0.005 and Al concentration varies as 0.005 (4 vs. Al1), 0.1 (4 vs. Al2) and 0.14 (4 vs. Al3).
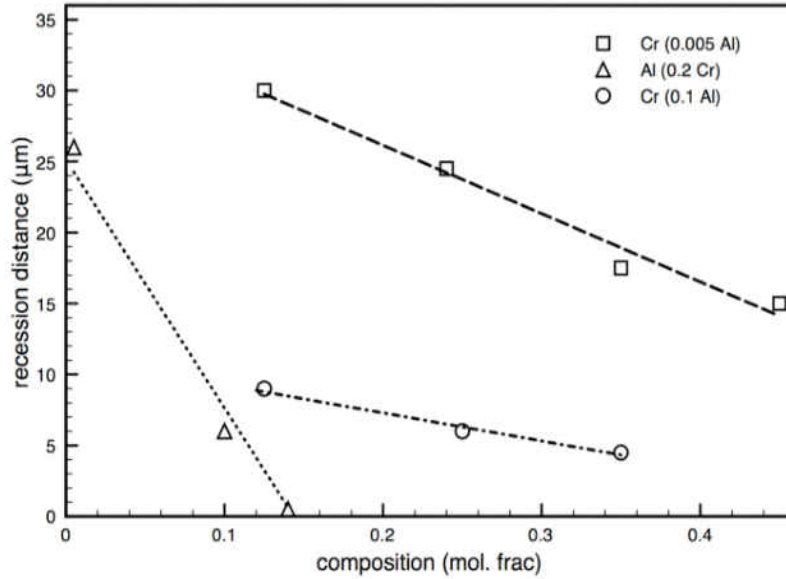
Figure 39: Recession distance of γ+β region at 1.5 hour vs. concentration of Al and Cr in the single-phase γ alloy as predicted by phase filed simulation.

(a)   (b)
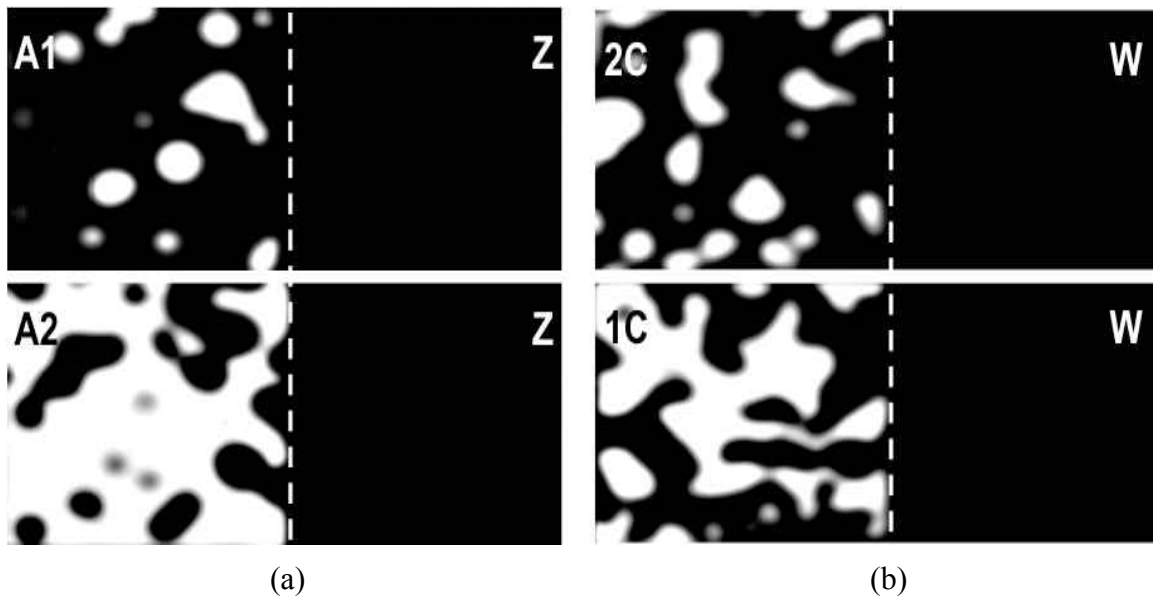
Figure 40: Expanded view of simulated interdiffusion microstructures for diffusion couples with same γ alloys and γ+β alloys of different volume fractions of β phase at t = 1.5 hour. The initial concentration of the γ alloy for all the couples is 0.005 Al and 0.45 Cr. Volume fraction of β is 0.20 (A1 vs. Z), 0.70 (A2 vs. Z), 0.35 (2C vs. W) and 0.55 (1C vs. W).

6.3.3 Concentration Profiles and Diffusion Paths

Concentration profiles for diffusion couples 4 vs. X and 4 vs. Y are shown in Figure 41 and 42, respectively. In these figure the compositions of γ and β phases are presented separately in the γ+β region, and compositions were found in close proximity to the γ+β/γ phase boundary in the phase diagram. For both Cr and Al, concentration gradients are observed in both phases, which implies that diffusion occurred in the γ phase as well as between γ and β phases within the γ+β region.

Diffusion paths for the diffusion couples 4 vs. X, Y, Z and 4 vs. A1, A2, A3 are plotted on the phase diagram in Figure 43 and 44, respectively. All the diffusion paths in the single-phase γ region were continuous and extended till the γ+β/γ phase boundary. Due to large scattering in composition, the paths in the two-phase region were calculated as the average concentrations over cells of dimensions 256 x 16 in the vertical and horizontal directions of diffusion couples, respectively. For the single-phase region, the average was calculated on a cell size of 256 x 1.

6.3.4 Comparison to Experimental Results

Calculated recession distance of γ+β region obtained from two types of simulations, i.e. simulation started with pre-annealed γ+β alloy and that with β nuclei without pre-annealing, are plotted with the experimental recession distance for couples 4 vs. X, 4 vs. Y and 4 vs. Z in Figure 45. For the purpose of comparison with the experimental recession distance at 100 hours, the simulated recession distance was extrapolated to 100 hours by the parabolic law ($x \propto \sqrt{t}$). The

validity of the parabolic approximation was established by the observations made from 1D simulations that the γ-β interface movement follows the parabolic law, as shown in Figure 46. The comparison shows that a very good agreement between the simulated and experimental [6] recession distance was obtained for the pre-annealed case, whereas the recession distance was overestimated when β phases were introduced as nuclei.
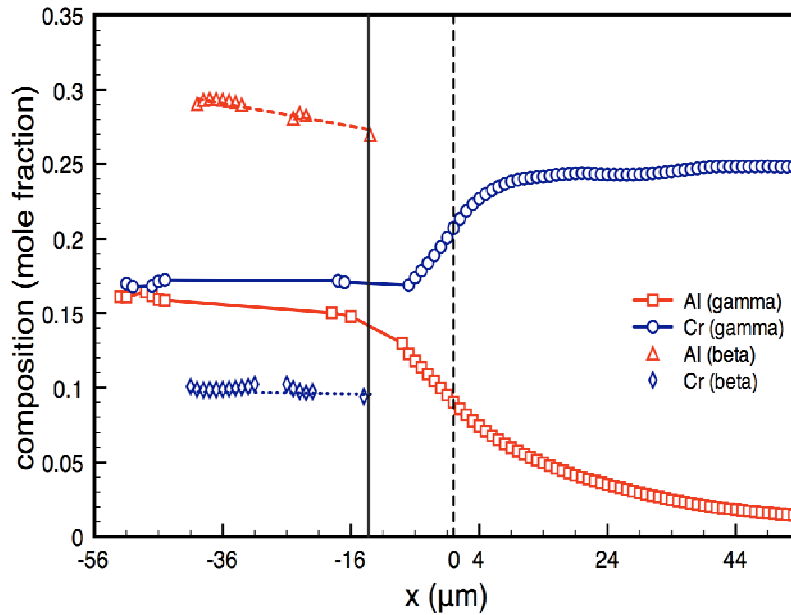
Figure 41: Simulated composition profile for the γ+β vs. γ couple (4 vs. X). The dashed and solid vertical lines are the location of the interface at t = 0 and t = 2.5 hour, respectively. Concentrations of γ and β phases in the γ+β region are shown separately.
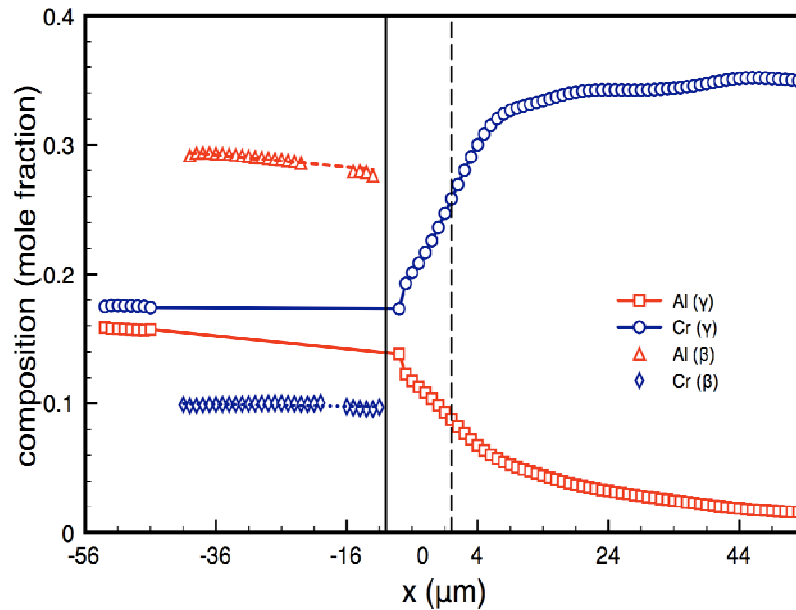
Figure 42: Simulated composition profile for the γ+β vs. γ couple (4 vs. Y). The dashed and solid vertical lines are the location of the interface at t = 0 and t = 2.5 hour, respectively. Concentrations of γ and β phases in the γ+β region are shown separately.

125
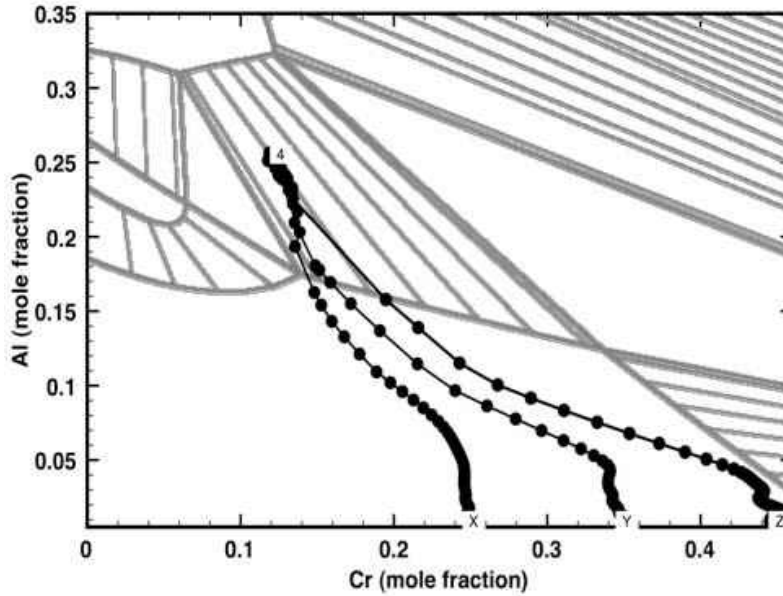
Figure 43: Simulated diffusion paths for the γ+β vs. γ couples (4 vs. X, 4 vs. Y and 4 vs. Z) shown in Figures. 2. Each data point for the path inside the two-phase region was determined by calculating the average composition over a cell of dimensions 16x256 grid points, whereas in the single-phase region, it was calculated as the average over a cell of dimensions 1x256.
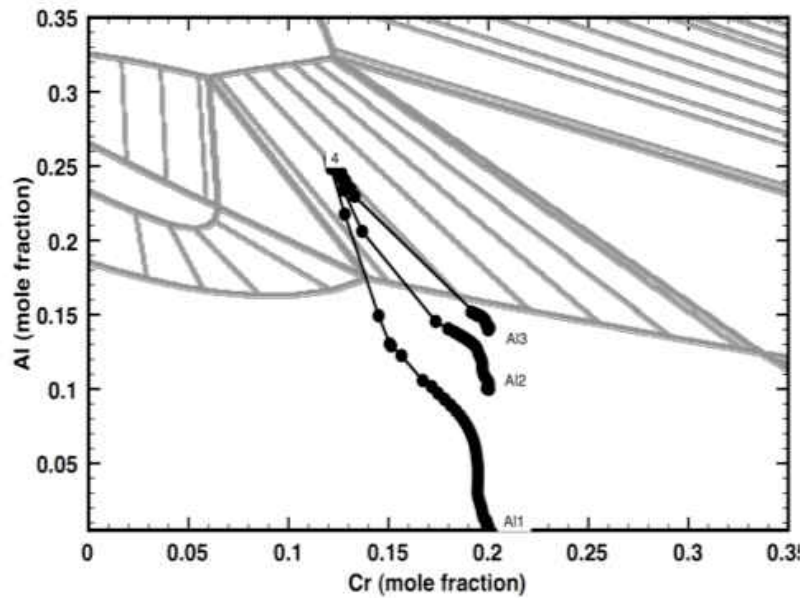
Figure 44: Simulated diffusion paths for the γ+β vs. γ couples (4 vs. Al1, 4 vs. Al2 and 4 vs. Al3) shown in Figures. 2. Each data point for the path inside the two-phase region was determined by calculating the average composition over a cell of dimensions 16x256 grid points, whereas in the single-phase region, it was calculated as the average over a cell of dimensions 1x256.
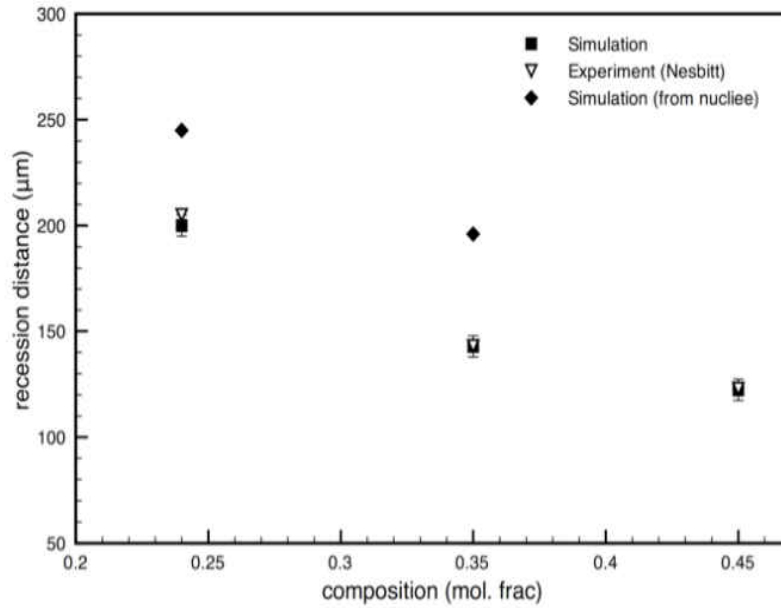
Figure 45: Comparison between predicted recession distance obtained from simulation with two types of initial conditions (i.e., β phase pre-annealed vs. nuclei), and experimental recession distance [4]. The predicted recession distance was extrapolated to 100 hours for the comparison.
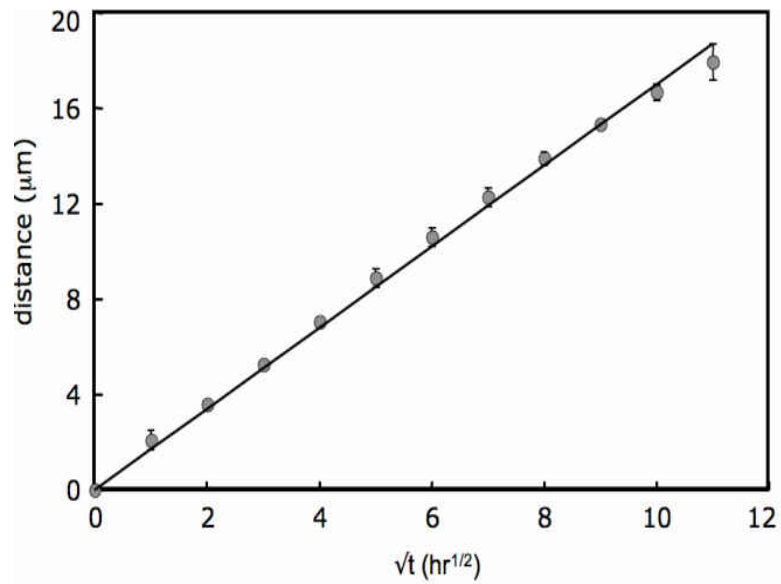
Figure 46: Plot between the interface position or distance vs. square root of time. The straight line relationship suggests a parabolic behavior (x ∝ √t).

Two-phase vs. two-phase (γ+β vs. γ+β) diffusion couples containing different volume fractions of the β phase was simulated. The microstructures of one such diffusion couples are presented in Figure 47. The microstructures in all the diffusion couples show no movement of the γ+β/γ+β interface, characterized by type 0 boundary. The volume fractions remain constant on either side of the diffusion couples.
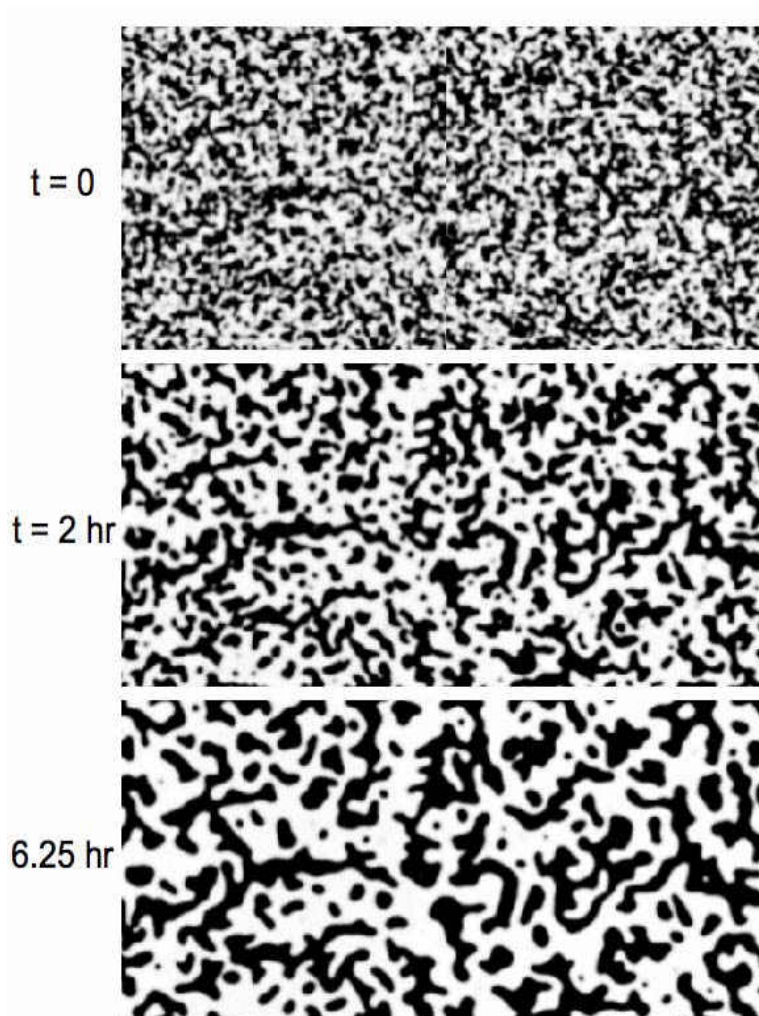
Figure 47: Interdiffusion microstructure evolution in the couple 4 vs. 1C shows stationary γ+β|γ+β boundary with no dissolution of phases.

6.4 Discussions

For an accurate prediction of the recession distance of γ+β region, it is important to minimize the effect of initial particle coarsening. This was achieved by pre-annealing the two-phase alloys with the artificially introduced circular particles as the second phase before joining them to form the actual diffusion couples.

In the simulated microstructures, the γ+β region receded by maintaining a planar interface, as was observed in the experiment by Nesbitt et al. The simulations also clearly demonstrated that the rate of dissolution of the β phase decreases with increasing concentrations of Al and Cr in the single-phase γ alloy. This can be attributed to the cross-effects of Al and Cr on each other. According to experimental observations, the cross-term Cr on Al flux and that of Al on Cr flux can drive the respective components to diffuse up their own concentration gradient. This cross-term effect depends on the concentration dependent diffusivity and the sign and magnitude of concentration gradients present in the diffusion couple. This effect can actually increase or decrease the activity of Al and Cr in a system and even cause their fluxes to move in the opposite directions.

A rough estimate on the relative effects of the concentration variation of Al and Cr can be obtained from the slope of the lines in Figure 39. The Al line has a much higher slope than that of the Cr, which suggests that the variation of Al concentration in the single-phase γ has more pronounced effect on the rate of β dissolution than that of the Cr concentration. At the same time the slopes for the two lines for Cr variations with fixed Al contents (i.e. 0.005 and 0.1) are approximately same in magnitude, though the recession is higher for lower Al content couple.

This can be attributed to the higher diffusivity of Al, as from the mobility database used in this work for the Ni solid solution γ phase [20]. The atomic mobilities are in the order of $\beta_{Al} > \beta_{Cr} > \beta_{Ni}$, where β_i is the atomic mobility of element 'i'. This ordering is supported by the fact that intrinsic diffusivities are in the order of $D_{Al} > D_{Cr} > D_{Ni}$ [7, 25-27].

The simulated concentration profiles in Figure 42 and 43 confirmed the experimental observation [6] that diffusion of all elements occurred between the γ phases on both sides of the couple as well as within the $\gamma+\beta$ region, while local equilibrium was maintained between γ and β phases with the composition lying close to the $\gamma+\beta/\gamma$ phase boundary on the phase diagram. The simulated Cr concentration profile does not exhibit a maximum as observed by Nesbitt and Heckel, and warrants further assessment of thermodynamic and mobility data.

The relative importance of concentrations of single-phase γ and volume fraction of β phase on the dissolution kinetics can be analyzed by the three series of diffusion couple simulations mentioned earlier in the results. Series-1 contained couples 1A vs. Z and 2A vs. Z, with the volume fractions of β as 0.20 and 0.70, respectively. Alloys 1A and 2A are on the same tie-line and hence there is effectively no composition difference within the γ phases on each side of the couple. In series-2, couples 1C vs. W and 2C vs. W had 0.35 and 0.55 volume fraction of β, respectively, where the average compositions of 1C and 2C lay on different tie-lines. Series-3 contained diffusion couples 4 vs. W and T vs. W, where the β phase volume fraction is the same in both the couples ($\sim 55\%$), but the composition gradients are different (0.127 Al and 0.2 Cr in the couple T vs. W compared to 0.162 Al and 0.063 Cr in the couple 4 vs. W). As described earlier, the simulation results showed that in series-1 and 2, the recession distance was found to

130

be less for the couples with the higher volume fraction of β as presented in Fig. 4, whereas for series-3, although the volume fraction was same, recession distance in the two couples was different (~136 μm for T vs. W and ~180 μm for 4 vs. W after 1 hour). The above comparison qualitatively suggests that concentration of the terminal alloy has more influence on the dissolution kinetics of β phase than that of the volume fraction of the β phase.

In experimental diffusion couples [4], Kirkendall pores can form due to supersaturation of vacancy concentration caused by the unequal vacancy flux across the diffusion couples, as a result of unequal intrinsic diffusivities. The phase-field model presented does not account for the Kirkendall porosity as such, since the model was derived in the laboratory frame of reference, where the net fluxes of three components sum to zero.

6.5 Conclusions

A two-dimensional phase-field model was employed to examine the evolution of interdiffusion microstructures in ternary Ni-Cr-Al solid-to-solid diffusion couples containing γ+β (fcc+B2) vs. fcc-γ and γ+β vs. γ+β diffusion couples. Alloys of varying compositions and volume fractions of the second phase (β) were examined to simulate the dissolution kinetics of the β phase (i.e., recession of γ+ β two-phase region) observed in γ vs. γ+β diffusion couples. Simulation results showed that the rate of recession of γ+β two-phase region was dependent on the composition of the single-phase γ alloy and the volume fraction of the β phase in the two-phase alloy of the couple. Specifically, higher Cr and Al content in the γ alloy and higher volume fraction of β in the γ+β alloy lower the rate of dissolution. Although the volume fraction played a

role, the concentration gradients of Al and Cr in the γ phase (e.g., between the matrix of γ+β alloy and single-phase γ alloy) also influenced the recession of the β phase. Simulated results were found to be in good agreement with the experimental observations in ternary Ni-Cr-Al solid-to-solid diffusion couples containing fcc-γ and γ+β alloys. In case of γ+β vs. γ+β diffusion couples no interface movement was observed and the volume fractions of the second phase on either side of the couples remained constant.

6.6 References

[1]   D. R. Clarke, C. G. Levi, Annu. Rev. Mater. Res. Vol.33 (2003) pp.383.

[2]   N. Padture, M. Gell and E. Jordan, "Thermal Barrier Coatings for Gas-Turbine Engine Applications", vol. 296 (2002) pp. 280.

[3]   S. M. Merchant, M. R. Notis, J. I. Goldstein, Metall. Trans. A, vol.21A (1990), pp.1901.

[4]   S. Hayashi, W. Wang, D. J. Sordelet, B. Gleeson, Metall. Trans. A. vol.36A (2005) pp.1769.

[5]   K. Fujiwara, Z. Horita, Acta mater. vol.50 (2002) pp.1571.

[6]   J. A. Nesbitt, R. W. Heckel, Metall. Trans. A. vol.18A (1987) pp.2061

[7]   J. A. Nesbitt, R. W. Heckel, Metall. Trans. A. vol.18A (1987) pp.2075

[8]   E. Perez, T. Patterson, Y. H. Sohn, J. Phase Eq. Diffusion, vol.27 (2006) pp.659.

[9]   A. Engstrom, J. E. Morral, J. ågren, Acta mater., vol.45 (1997) pp.1189.

[10] C. Campbell, W. J. Boettinger, U. R. KAttner, Acta mater., vol.50 (2002) pp.775

[11] Y. Wen, B. Wang, J. P. Simmons, Y. Wang, Acta mater., vol.54 (2006) pp.2087

[12] K. Wu, A. Chang, Y. Wang, Scripta mater., vol.50 (2004) pp.1145.

[13] J. W. Cahn and J. E. Hilliard, J. Chem. Phys.,vol.28 (1958) pp. 258.

[14] D. Fan and L. Q. Chen, J. Am. Ceram. Soc., vol.78 (1995) pp.1680.

[15] Y. Wang and A. G. Khachaturyan, Acta Metall. Mater., vol. 43 (1995) pp. 1837.

[16] K. Wu, Ph.D. Thesis, Pennsylvania State Univ., (2003).

[17] W. Huang, Y. A. Chang, Intermetallics. Vol.7 (1999) pp.863.

[18] C. Huang, M. Olvera de la Cruz and B. W. Swift, Macromolecules, vol. 28 (1995) pp. 7996.

[19] S. M. Allen and J. W. Cahn, Acta. Metall.vol.27 (1979), pp.1085.

[20] A. Engstrom, J. Agren, Z Metallkd., vol.87 (1996) pp.92.

[21] L. Q. Chen, J. Shen, Comput. Phys. Commun., vol.108 (1998) pp.147.

[22] J. Z, Zhu, L. Q. Chen, J. Shen, V. Tikare, Phys. Rev. E., vol.60 (1999) pp.3564.

[23] N. Saunders, M. Fahrmann, C. Small, 9th Int Symp on Superalloys, (2000).

[24] N. Dupin, I. Ansara, B. Sundman, CALPHAD, vol, 25 (2001) pp.279.

[25] M. M. P. Janssen, Metall. Trans., vol.4 (1973) pp.1623.

[26] S. Shankar, L.L. Seigle, Metall. Trans. A, vol.9A (1978) pp.1467.

[27] A.V. Pawar, D.R. Tenney, Metall. Trans., vol.5 (1974) pp.2139.

CHAPTER 7
EXPERIMENTAL INVESTIGATION OF
TERNARY SINGLE-PHASE VS. TWO-PHASE DIFFUSION COUPLES

7.1 Introduction

The interdiffusion microstructures in ternary diffusion couples were investigated by experimental methods using single-phase and two-phase alloys in Ni-Cr-Al and Fe-Ni-Al systems. The single-phase vs. two-phase diffusion couples containing $\gamma(fcc)$ and $\gamma+\gamma'(L1_2)$ phases were prepared from Ni-Cr-Al alloys and two-phase vs. two-phase diffusion couples containing $\gamma+\beta(B2)$ phases from Fe-Ni-Al alloys. The diffusion couples were subjected to isothermal diffusion annealing at 1000˚C for different time spans. Then the composition and microstructures were analyzed using standard metallographic and characterization techniques. The detail procedure and the results are described in subsequent sections.

7.1 Experimental Procedure

7.1.1 Alloy Preparation

The alloys were prepared at Oak Ridge National Laboratory (ORNL), USA. The four single-phase (γ) and one two-phase ($\gamma+\gamma'$) Ni-Cr-Al alloys and four two-phase ($\gamma+\beta$) Fe-Ni-Al alloys were cast. These alloys were prepared with 99.9% pure Ni, Cr, Fe and Al by induction melting in alumina crucibles under an argon atmosphere. The alloys were chill-cast in the form of rods of 10 mm diameter (approximately) by drawing the melt into quartz tubes under vacuum. The alloy rods were placed in quartz capsules, flushed several times with argon and hydrogen,

134

evacuated to a pressure less than 10^{-5} torr and finally sealed with argon. The alloys were then placed in a horizontal Lindberg^{TM} 3-zone tube furnace at 1000˚C for 7 days for homogenization heat treatment. After the heat treatment the alloys were water-quenched in order to preserve the high temperature microstructure and the composition distribution. Samples were cut from the alloy rods and prepared metallographically by polishing through 0.25 μm diamond paste for composition and microstructure analysis by optical microscopy (OM), scanning electron microscopy (SEM) and electron probe micro analysis (EMPA).

Pure standards of the four elements Fe, Ni, Cr and Al were used with a JEOL^{TM} 733 Super Probe (EPMA) to measure the compositions of the alloys. An accelerating voltage of 20 KeV and a sample current of 20 nanoamperes (nA) were applied with appropriate ZAF corrections and composition data collected from 10 random points on the sample were averaged to determine the composition of the alloys. The standard deviations in the compositions due to alloy inhomogeneity were estimated to be approximately ± 0.3 at%. The measured alloy compositions and the phases present are listed in Tables 4 and 5 along with the designations used in this study for their identification. The alloys are identified on Ni-Cr-Al and Fe-Ni-Al isotherms as shown in Figure 42 and 43, respectively. A representative set of microstructures after homogenization heat treatment is shown in Figure 44 and 45.

7.1.2 Diffusion Couple Experiments

As mentioned earlier, two types of diffusion couple experiments were performed in this study; one with single-phase (γ) vs. two-phase (γ+γ′) couples using Ni-Cr-Al alloys, and the other with two-phase (γ+β) vs. two-phase (γ+β) couples using Fe-Ni-Al alloys. These diffusion

couples and their isothermal annealing conditions are listed in Table 6. The series of diffusion couples containing γ vs. γ+γ′ were designed to study the dissolution of γ′ phase, and the effect of composition of single-phase γ on the dissolution rate. The other series containing γ+β vs. γ+β were designed to examine interdiffusion between the two two-phase (γ+β) terminal alloys and possible demixing [1] of phases at the interface.

Table 5: Nominal compositions of Ni-Cr-Al alloys.

Phase	Alloy	Atom Percent			Weight Percent		
		Ni	Cr	Al	Ni	Cr	Al
γ	Ni	100	-	-	100	-	-
	γ₁	76.9	23.1	-	79.0	21.0	-
	γ₂	77.8	16.0	6.2	82.1	14.9	3.0
	γ₃	72.3	21.4	6.3	76.8	20.1	3.1
γ+γ′	G	79.1	5.1	15.8	87.0	5.0	8.0
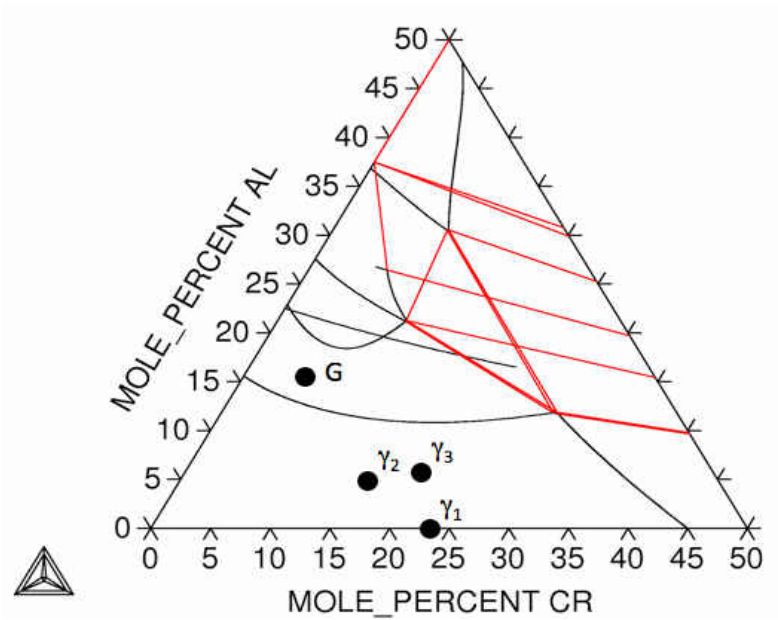
Figure 48: compositions marked on the Ni-Cr-Al isotherm at 1000˚C obtained from TCNI1 [2] database in ThermoCalc. The isotherm has been expanded to show the relevant phase-fields.

Table 6: Nominal compositions of Fe-Ni-Al alloys.

Phase	Alloy	Atom Percent			Weight Percent		
		Fe	Ni	Al	Fe	Ni	Al
γ+β	B₁	35.2	44.7	20.1	38.1	51.4	10.5
	B₂	49.8	30.2	20.0	54.8	34.6	10.6
	B₃	50.0	31.8	18.2	54.1	34.4	9.5
	B₄	50.1	34.0	15.9	53.5	38.2	8.3
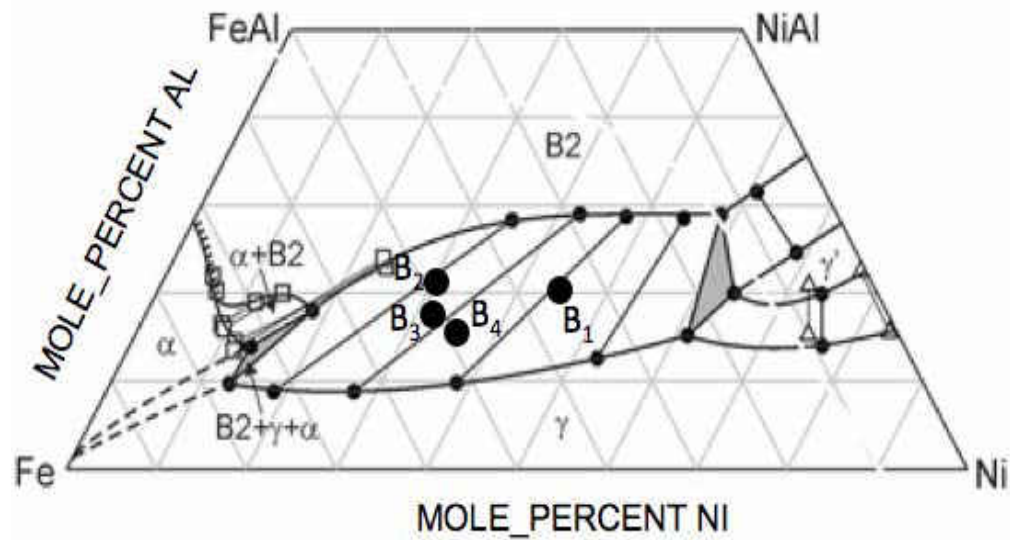
Figure 49: compositions marked on the Fe-Ni rich section of the Fe-Ni-Al isotherm at 1000˚C (borrowed from Chumak et al [3]).

138
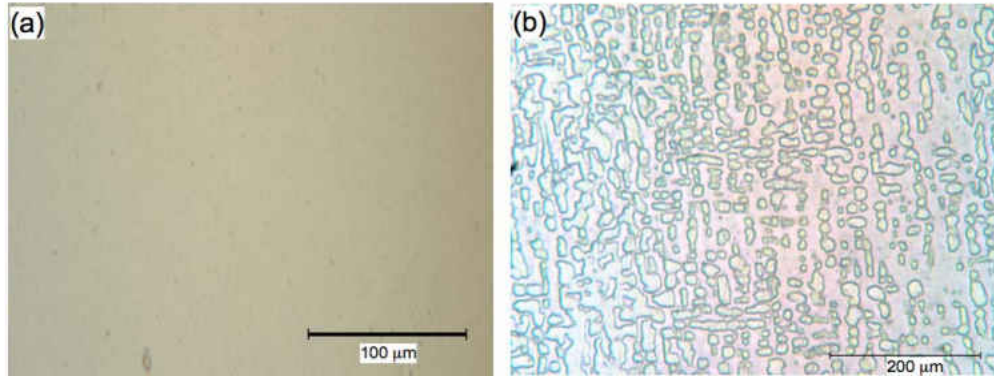
Figure 50: Representative optical micrographs of (a) single-phase (γ) and (b) two-phase ($\gamma+\gamma'$) Ni-Cr-Al alloy after homogenization treatment at 1000˚C for 7 days. The bright and dark areas are γ and γ' phases, respectively.
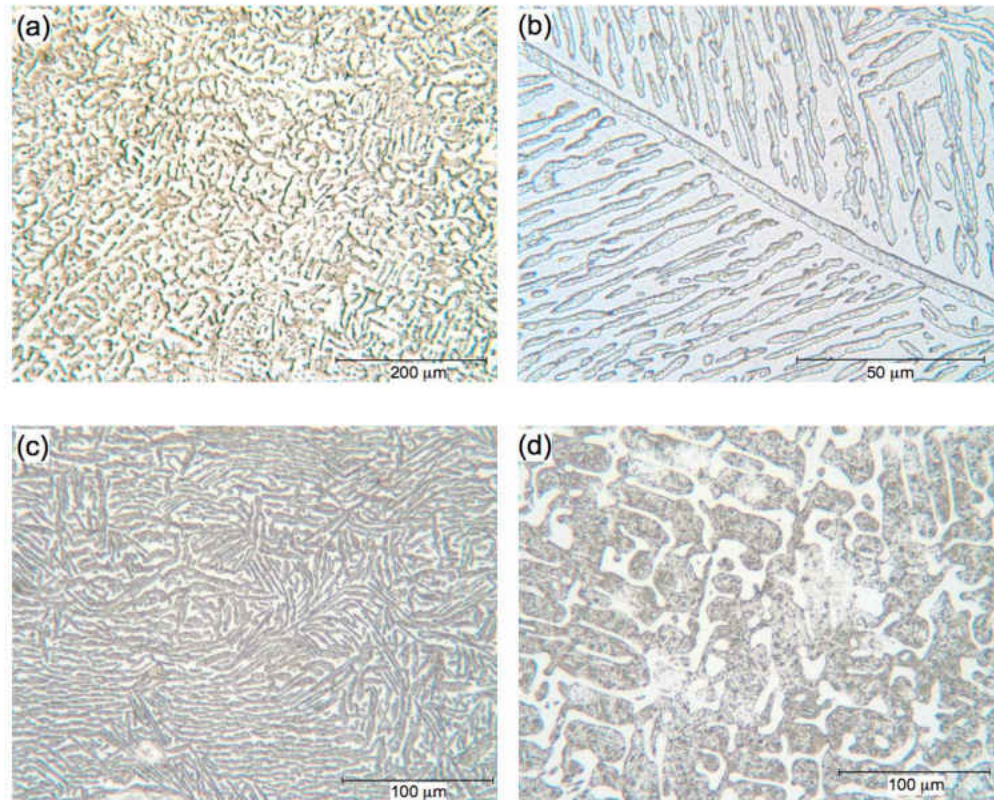
Figure 51: Representative optical micrographs of Fe-Ni-Al two-phase ($\gamma+\beta$) alloys (a) B_1 (b) B_2 (c) B_3 and (d) B_4 after homogenization treatment at 1000˚C for 7 days. The bright and dark areas are γ and β phases, respectively.

Disks of thickness approximately 4 mm were sectioned from the alloy rods, and subsequently ground and polished through 0.25 μm diamond paste. Diffusion couples were assembled by joining the alloy disks together in steel jigs consisting of two end plates and three threaded screws. Each assembled couple was placed in a quartz capsule, which was sealed at one end while the other end was connected to a vacuum system. The capsules were evacuated to a pressure less than 10^{-5} torr and flushed with argon and hydrogen several times before sealing them with argon at a desired pressure. The diffusion couples were annealed isothermally in a horizontal Lindberg^{TM} 3-zone tube furnace at a temperature of 1000˚C for 48 or 96 hours. After the diffusion annealing, the couples were quenched in water to preserve the high-temperature microstructure.

The diffusion couples were mounted, sectioned, polished, and etched with a solution of glycerin (30 vol%)-HCl (20 vol%)-HF, for the microstructure analysis by optical and scanning electron microscopy. The etched surface was polished with 1 μm diamond paste for electron probe micro analysis by the JEOL^{TM} 733 Super Probe Analyzer to determine the composition profiles. Average concentrations were measured in the two-phase regions with a larger probe diameter ranging between 5 and 10 μm.

7.3. Results

7.3.1 γ vs. γ+γ′ Diffusion Couples in Ni-Cr-Al System

Four diffusion couples were studied in Series-I as listed in Table 6. These diffusion couples are characterized by a common two-phase alloy (G) joined with γ alloys of varying compositions. The couples were annealed for 96 hours at 1000˚C. The resulting microstructures and the concentration profiles are presented in Figures 46 through 49.
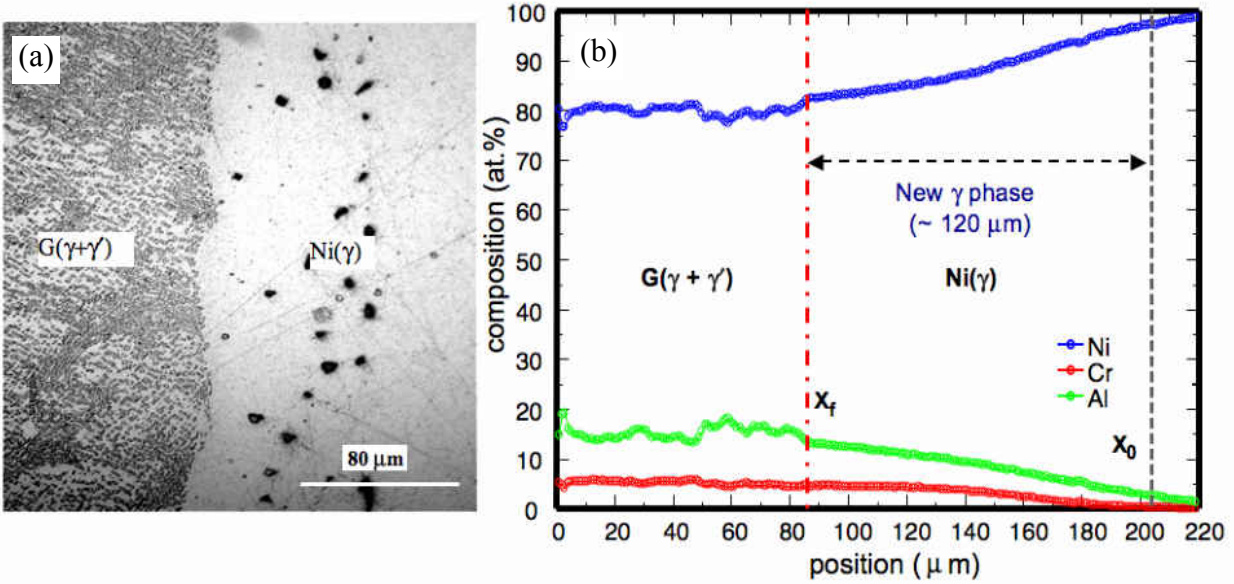
Figure 52: (a) Optical micrograph of diffusion couple G vs. Ni (γ) in Series-I obtained after diffusion anneal at 1000˚C for 96 hours. The bright and dark areas are γ and γ′ phases, respectively. The two-phase region has moved away from the initial phase boundary. (b) Composition profiles showing the newly formed γ region due to dissolution of γ′.
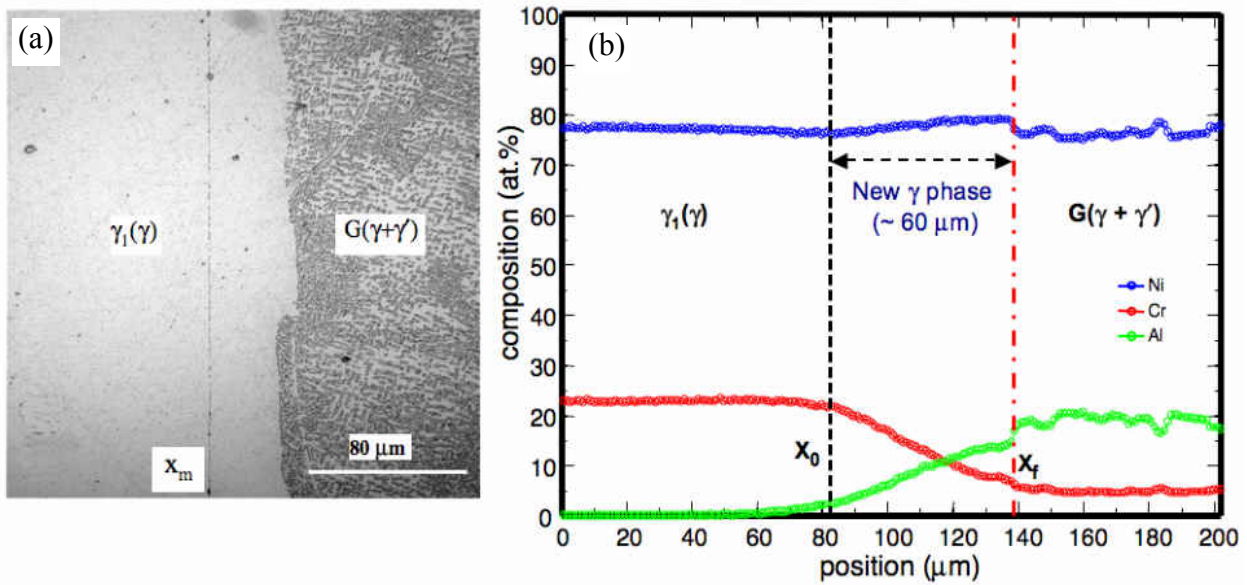
Figure 53: (a) Optical micrograph of diffusion couple G vs. γ₁ (γ) in Series-I obtained after diffusion anneal at 1000˚C for 96 hours. The bright and dark areas are γ and γ′ phases, respectively. The two-phase region has moved away from the initial phase boundary. (b) Composition profiles showing the newly formed γ region due to dissolution of γ′.

141
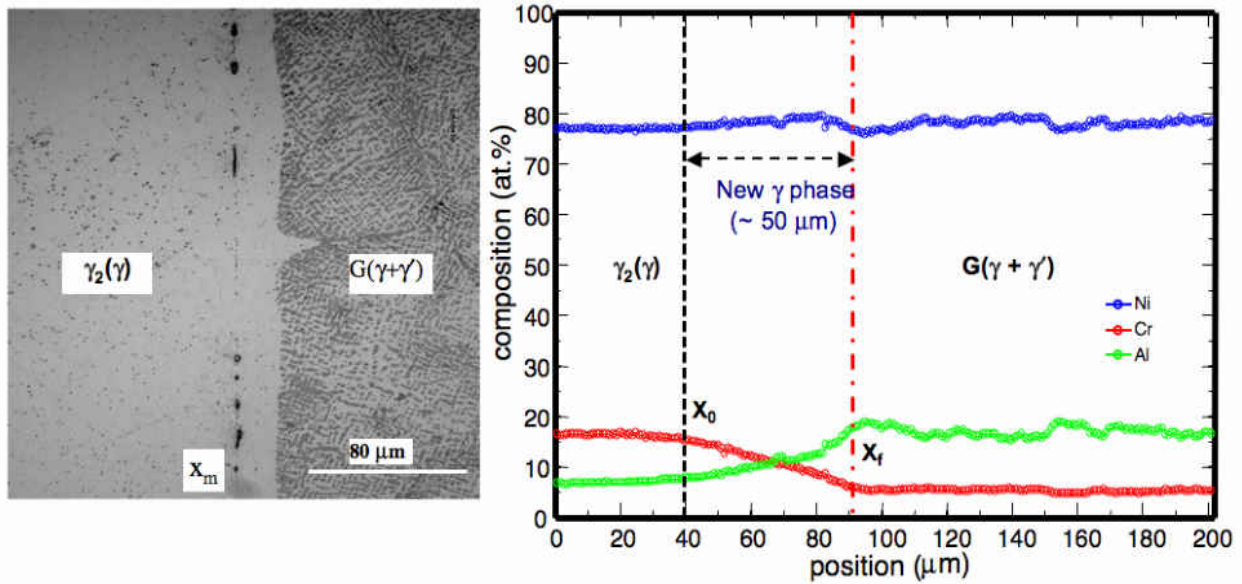
Figure 54: (a) Optical micrograph of diffusion couple G vs. γ_2 (γ) in Series-I obtained after diffusion anneal at 1000°C for 96 hours. The bright and dark areas are γ and γ' phases, respectively. The two-phase region has moved away from the initial phase boundary. (b) Composition profiles showing the newly formed γ region due to dissolution of γ'.
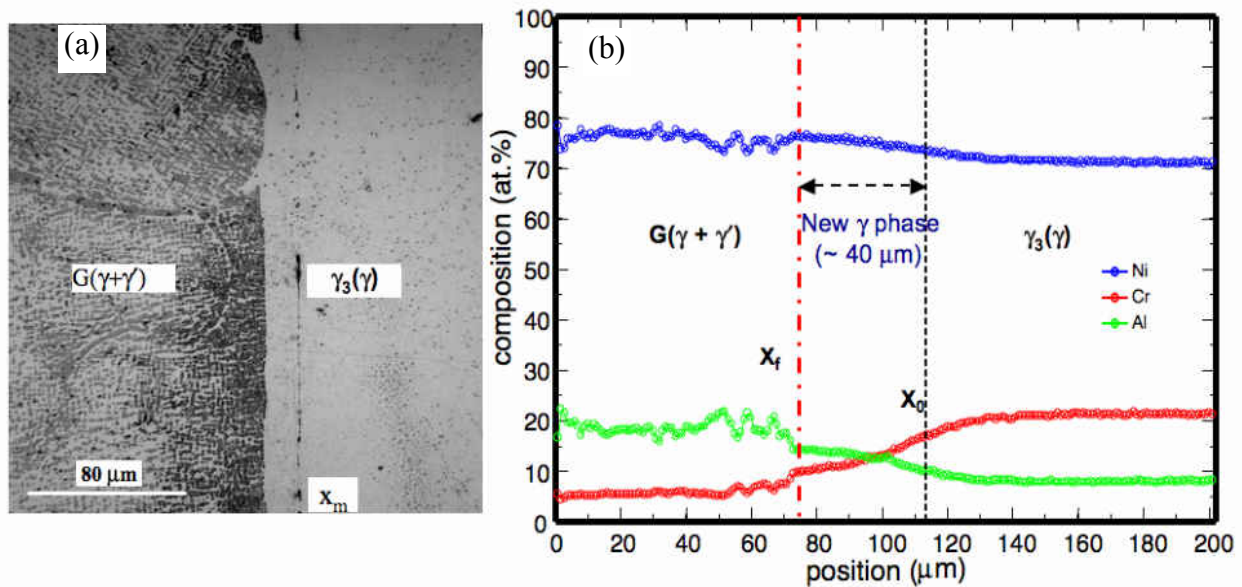
Figure 55: (a) Optical micrograph of diffusion couple G vs. γ_3 (γ) in Series-I obtained after diffusion anneal at 1000°C for 96 hours. The bright and dark areas are γ and γ' phases, respectively. The two-phase region has moved away from the initial phase boundary. (b) Composition profiles showing the newly formed γ region due to dissolution of γ'.

142

The original location of the boundary between γ and γ+γ′ region is marked by the position x_0. After annealing the boundary moved towards the two-phase region in all the four couples and its final location is marked by the plane x_f. This is also confirmed by the change in compositions across the interface in the composition profiles. The boundary movement occurs by the recession of the γ+γ′ region with a planar surface. It can be noticed from the microstructures and composition profiles that the recession distance greatly depends on the composition of the single-phase γ alloy. The trend obtained from the plot of relative concentrations of single-phase γ alloys vs. recession distance in Figure 50 shows that an increase in the content of Cr and/or Al in γ decreases the recession distance.
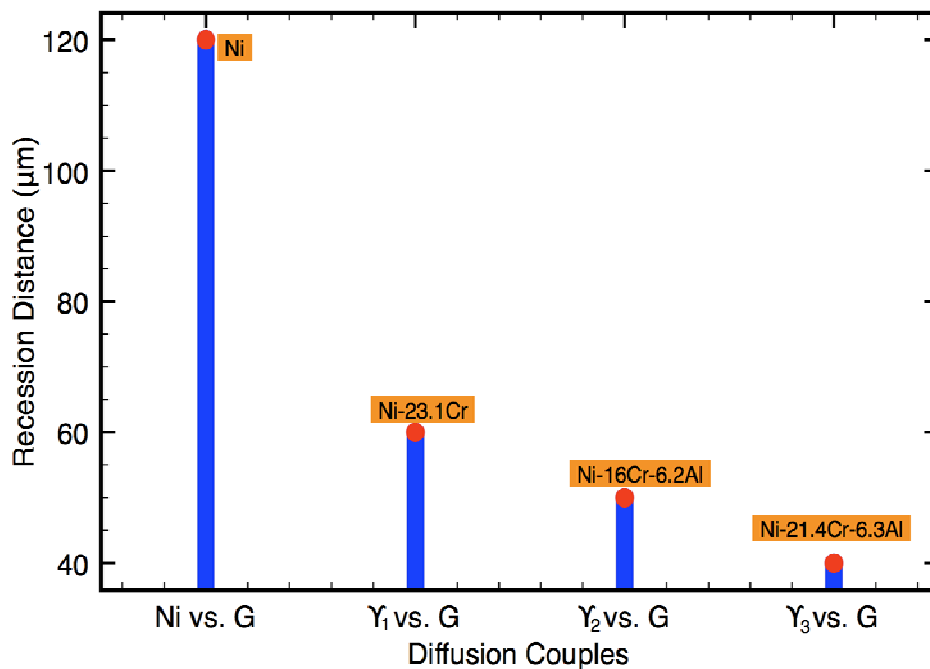
Figure 56: A plot between the relative concentrations of single-phase (γ) alloys and the recession distance of the two-phase (γ+γ′) region after diffusion anneal at 1000˚C for 96 hours. The trend shows with an increasing Cr and Al content, the recession distance decreases.

7.3.2 γ+β vs. γ+β Diffusion Couples in Fe-Ni-Al System

The four two-phase (γ+β) Fe-Ni-Al alloys were joined with each other into six diffusion couples, B_1 vs. B_2, B_1 vs. B_3, B_1 vs. B_4, B_2 vs. B_3, B_2 vs. B_4, and B_3 vs. B_4. Two series of such couples were diffusion annealed at 1000˚C for 48 and 96 hours. The microstructures were analyzed using optical and scanning electron microscopy. Optical micrographs and backscatter SEM micrographs for Series-II and Series-III diffusion couples are presented in Figures 51 and 52, respectively. In all the diffusion couples, apart from the joining of second phase particles across the boundary, no other noticeable change in the microstructure was observed. The boundary remained stationary without any formation or dissolution of phases at its vicinity.

7.4 Discussions

Dissolution of γ′ phase along with the movement of the boundary towards the two-phase region was observed in the microstructures of the Series-I diffusion couples G vs. Ni, $γ_1$, $γ_2$, $γ_3$. Many investigators have previously reported this type of observations [4,5]. The dissolution process is of critical concern in thermal barrier coatings (TBCs) for gas turbine applications, where the γ′ phase dispersed in a γ matrix is typically used as the bond coat material on the superalloy substrate for high-temperature resistance and protection. Dissolution of γ′ phase detoriates the high-temperature performance of the bond coat. Al diffusion from the bond coat into the superalloy substrate is usually held accountable for the dissolution of γ′ phase. Results of the present study show that there is a strong dependence of the recession distance on the single-phase γ alloy composition. Figure 50 provides a qualitative understanding of this dependence. It is clear that increase in alloying additions, i.e. Cr and Al to Ni-γ reduces the recession distance.

144
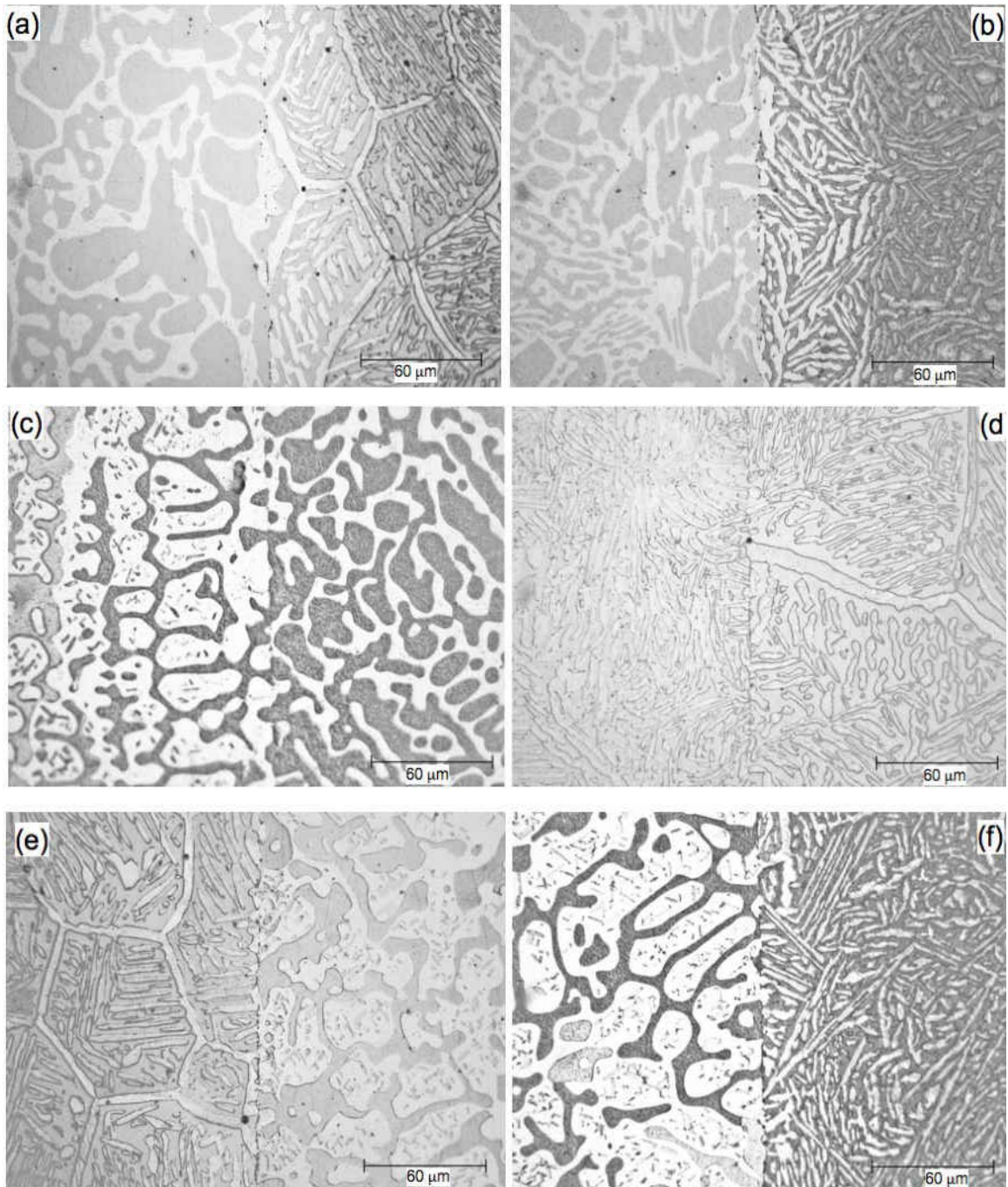
Figure 57: Optical micrographs of diffusion couples (a) B_1 vs. B_2, (b) B_1 vs. B_3, (c) B_1 vs. B_4, (d) B_2 vs. B_3, (e) B_2 vs. B_4, and (f) B_3 vs. B_4 in Series-II obtained after diffusion anneal at 1000°C for 48 hours. The bright and dark areas are γ and β phases, respectively. No boundary movement is observed.
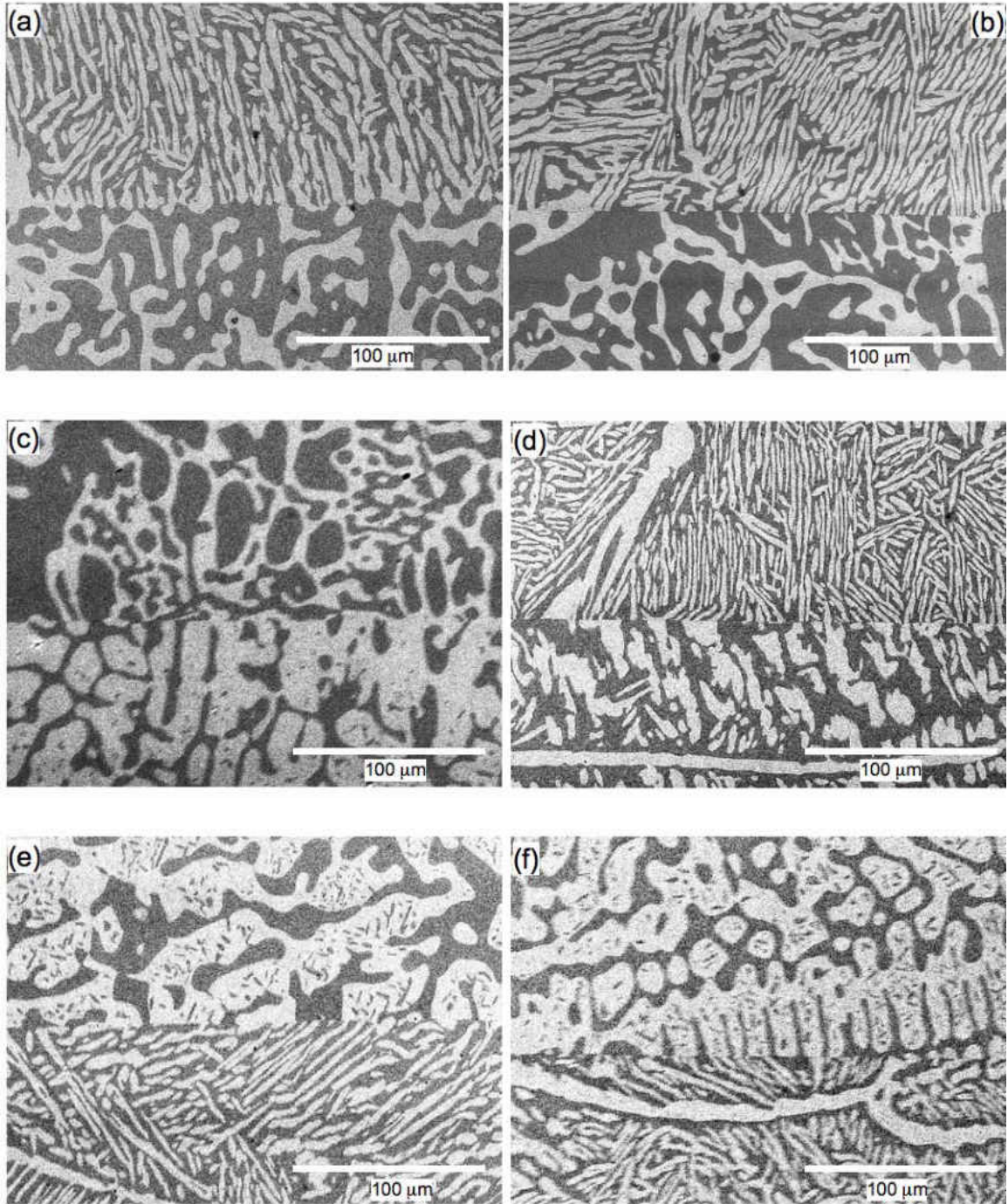
Figure 58: SEM micrographs of diffusion couples (a) B_1 vs. B_2, (b) B_1 vs. B_3, (c) B_1 vs. B_4, (d) B_2 vs. B_3, (e) B_2 vs. B_4, and (f) B_3 vs. B_4 in Series-III obtained after diffusion anneal at 1000˚C for 96 hours. The bright and dark areas are γ and β phases, respectively. No boundary movement is observed.

Sohn et al [1,6,7] first reported the formation of single-phase γ and β layers at the boundary in two-phase vs. two-phase (γ+β vs. γ+β) diffusion couples of Fe-Ni-Al system and named the phenomenon as "demixing". Similar microstructures were observed for Cu-Ni-Zn multiphase diffusion couples during isothermal diffusion [8]. During demixing each phase dissolves in the matrix of the other and gives rise to adjacent single-phase layer in the diffusion zone with appreciable reduction in interfacial area. However, demixing was not observed in this study for γ+β vs. γ+β diffusion couples of Fe-Ni-Al alloys. This discrepancy in results suggests that demixing is not a general phenomenon common to all two-phase vs. two-phase diffusion couples of any alloy, rather demixing can be considered as a special case where reduction in interfacial area cannot be the only criteria for its occurrence.

Morral et al [5,9] have classified planar boundaries in multicomponent diffusion couples as type 0, type 1 and type 2 boundaries. According to their definition, across a type 0 boundary no phases are added or subtracted, across a type 1 boundary one phase is added or subtracted and across a type 2 boundary one phase is added and another is subtracted. In this study two types of boundaries were observed: type 1 boundary in γ vs. γ+γ′ diffusion couples where γ phase was added to the boundary denoted by γ > γ+γ′, and type 0 boundary in γ+β vs. γ+β diffusion couples where no phases were added or subtracted to the boundary denoted by γ+β|γ+β.

7.5 Conclusions

The isothermal diffusion analysis of the three aforementioned series of couples in Ni-Cr-Al and Fe-Ni-Al alloys did not produce any new results, but they supplemented the findings made by many earlier experimental investigations on ternary single-phase vs. two-phase and

147

two-phase vs. two-phase diffusion couples. The results also qualitatively confirmed the simulation results obtained from the phase-field model studies on Ni-Cr-Al diffusion couples. To summarize, dissolution of second phase (γ') occurs in single-phase vs. two-phase diffusion couples when subjected to isothermal annealing. The dissolution causes recession of the two-phase region forming single-phase γ at the interface. The rate of recession or dissolution depends on the composition of the single-phase (γ) alloy. As the Cr and/or Al content of the γ alloy increases the recession rate decreases. In case of two-phase vs. two-phase diffusion couples only stationary boundary between the two-phase regions were observed without the occurrence of any demixing phenomena at the boundary. This warrants a more systematic study to properly understand the demixing phenomenon.

7.6 References

[1]   Y. H. Sohn, Ph.D. Dissertation, Purdue University, (1998).

[2]   TCNI1-Ni alloys database v.1, ThermoCalc Software™.

[3]   I. Chumak, K. W. Richter, H. Ipser, J. Phase Equili. Diff., vol. 29 (2008), pp.300.

[4]   J. A. Nesbitt, R. W. Heckel, Metall. Trans. A, vol.18A (1987), pp.2061.

[5]   C. Jin, J. E. Morral, Scripta Mater, vol.37 (1997) pp.621.

[6]   Y. H. Sohn, M. A. Dayananda, Metall. Trans. A, vol.33A (2002), pp.3375.

[7]   Y. H. Sohn, A. Puccio, M. A. Dayananda, Metall. Trans. A, vol.36A (2005), pp.2361.

[8]   M. A. Dayananda, Def. Diff. Forum, vol. 83 (1992), pp. 73.

[9]   J. E. Morral, C. Jin, A. Angström, J. Ågren, Scripta Mater, vol.34 (1995) pp.1661.

CHAPTER 8
PHASE-FIELD SIMULATION OF THERMOTRANSPORT
PHENOMENON IN BINARY ALLOYS

8.1 Introduction

It is well known that when a temperature gradient is applied to a homogeneous alloy of more than one component, a concentration gradient can develop and eventually reach a steady state, with the concentration gradient being a characteristic of the system [1]. This phenomenon is known as the thermomgration or thermotransport effect, or the Soret or Ludwig-Soret effect. The thermomigration effect is gaining importance in many applications, such as, in interconnects of electronic circuits, metallic nuclear fuel alloys, superalloy coatings used in gas turbine engines, etc., where the temperature gradient can be significant, owing to increasing operating temperatures and/or reducing length scales of these systems. For example, in modern aero gas turbine engines, the width of the material between the hot end and the cooling channels is typically 2 to 5 mm where a temperature gradient of $\approx 40°C/mm$ can be present. Similarly, in nuclear reactors, the metallic alloy fuels e.g., U-Pu-Zr alloys could experience a temperature gradient of $\approx 22°C/mm$.

Thermomigration can produce significant redistribution of elements and constituent phases in single- and multi-phase alloys. This redistribution can induce many unwanted changes such as melting by varying the solidus temperature, causing phase transformations and altering physical and mechanical properties, which can affect the stability and performance of alloys during operation. Examples of the thermomigration effect can be found in literature published over the last five decades [2-14].

149

There are two important parameters in the thermomigration study: the mobility of atoms of the components present, which are related to the isothermal diffusivity, and the heat of transport (Q_i*), which is related to the amount of heat carried per atom of species i [3]. In general, the value of Q_i* is the contribution of the flux of species i to the flux of heat and determines the affinity of a species towards the cold or hot end. When the solute diffusivity is much higher than the solvent, e.g. interstitial solute, only one heat of transport term is sufficient to describe the flux under a temperature gradient. But as explained by Shewmon [5], both mobility and heat of transport terms of each component are required to accurately describe the atom flux in a binary substitutional alloy subjected to a temperature gradient. In such cases, the complexity of the problem often necessitates the use of computational modeling to understand and predict the thermomigration behavior in alloys.

Tikare et al. [15] used a Potts Monte Carlo technique to simulate grain growth and pore migration in a thermal gradient, where they utilized the atomic interaction energy in the model. In another study, Snyder et al. [16] simulated the Ostwald ripening under the influence of temperature gradient, where they neglected the Soret effect and considered only the mass flow due to the temperature dependence of the local equilibrium interfacial compositions. There are other computational models [17-21] used to investigate the thermomigration problem, but these models are valid for one-dimension only and operate under the assumptions that (i) the transport of the solute takes place only in the matrix phase, (ii) the second phase particles act as sources or sinks for the solute atoms in solid solution, (iii) that the solute diffusivity is much faster than the solvent, and (iv) local thermodynamic equilibrium exists at the boundary between the two phases. Such *a priori* assumptions require that the positions of the boundary between the phases be known, which makes the numerical solution difficult to achieve. Unlike these models, a

150

diffuse interface (Cahn-Hilliard) model [22] does not require the above assumptions to be made beforehand and eliminates the requirement of tracking the boundary by treating the interface as diffused over a certain width [23]. Another advantage of such a model is that it can be derived phenomenologically and material specific thermodynamic and kinetic data can be used as input parameters.

This chapter documents the development of a diffuse interface model for computer simulation to study the time evolution of composition profiles and microstructures in single and multi-phase alloys of a binary system, subjected to a temperature gradient. A simple regular solution model with various combinations of atomic mobility and heat of transport terms were used for the above purpose.

8.2 The Model

8.2.1 Mathematical Formulation:

Consider a binary substitutional alloy of elements A and B, whose molar volume (V_m) and density (ρ) are assumed to be constant. Let n_i and c_i represent the concentration and mole fraction of an element *i*, so that:

$$\sum_i n_i = \rho = \frac{1}{V_m} \text{ and } \sum_i c_i = 1.0 \tag{8.1}$$

Flux of an element under the gradients of concentration and temperature can be defined by the following equation given by de Groot [24]:

$$J_k = \sum_{i=1}^{n-1} L_{ki}\left(X_i - X_n + Q_i^* X_q\right) \tag{8.2}$$

where n is the total number of elements, Q_i^* is the heat of transport term, X stands for the driving forces. In the absence of external forces,

$$X_i = -\left(\nabla \mu_i\right)_T, X_q = -\frac{\nabla T}{T} \tag{8.3}$$

Note that Equation 8.2 is obtained by the linear transformation and the gradient in chemical potential, i.e. $\left(\nabla \mu_i\right)_T$ is due to gradients in concentration, but not temperature [24-26].

Howard and Lidiard [25] applied the above equation to describe thermotransport on the basis of a vacancy mechanism in a binary substitutional alloy. So the general flux equations for an alloy of elements A and B are

$$J_A = L_{AA}\left(X_A - X_v + Q_A^* X_q\right) + L_{AB}\left(X_B - X_v + Q_B^* X_q\right) \tag{8.4a}$$

and

$$J_B = L_{BA}\left(X_A - X_v + Q_A^* X_q\right) + L_{BB}\left(X_B - X_v + Q_B^* X_q\right), \tag{8.4b}$$

where v corresponds to vacancies. Again following Howard and Lidiard [25], assuming that vacancies exist everywhere in their equilibrium concentration, $\nabla \mu_v = 0$, but in a temperature gradient $\left(\nabla \mu_v\right)_T \neq 0$. Hence,

$$X_v = -\left(\nabla \mu_v\right)_T = -kT \frac{\nabla c_v}{c_v} = -h_{fv} \frac{\nabla T}{T} = h_{fv} X_q, \qquad (8.5)$$

where h_{fv} is the enthalpy of vacancy formation. Substituting Equation 8.5 in Equation 8.4 yields:

$$J_A = L_{AA}\left[X_A + \left(Q_A^* - h_{fv}\right)X_q\right] + L_{AB}\left[X_B + \left(Q_B^* - h_{fv}\right)X_q\right] \qquad (8.6a)$$

and

$$J_B = L_{BA}\left[X_A + \left(Q_A^* - h_{fv}\right)X_q\right] + L_{BB}\left[X_B + \left(Q_B^* - h_{fv}\right)X_q\right]. \qquad (8.6b)$$

From Prigogine's theorem [26-27], which is a re-expression of the Gibbs-Duhem equation,

$$c_A X_A + c_B X_B + c_v X_v = 0, \qquad (8.7a)$$

but $c_v \ll c_A, c_B$, so

$$c_A X_A + c_B X_B \approx 0 \qquad . \qquad (8.7b)$$

Applying Equation 8.7b and the condition for conservation of mass given in Equation 8.1,

$$L_{AA} X_A + L_{AB} X_B = \frac{c L_{AA} - (1-c) L_{AB}}{c} X_A = \rho(1-c)\beta_A X_A \qquad (8.8a)$$

and

$$L_{BB} X_B + L_{BA} X_A = \frac{(1-c) L_{BB} - c L_{BA}}{1-c} X_B = \rho c \beta_B X_B, \qquad (8.8b)$$

where c is the composition of B and β_i is the atomic mobility of element i. The general flux equation under isothermal conditions, i.e. $J_i = -n_i \beta_i X_i$ has been used to derive Equation 8.8. Now substituting Equation 8.8 into flux equations Equation 8.6 yields:

$$J_A = -\rho(1-c)\beta_A \nabla \mu_A + \left[L_{AA}\left(Q_A^* - h_{fv}\right) + L_{AB}\left(Q_B^* - h_{fv}\right)\right]X_q , \qquad (8.9a)$$

$$J_B = -\rho c \beta_B \nabla \mu_B + \left[L_{BA}\left(Q_A^* - h_{fv}\right) + L_{BB}\left(Q_B^* - h_{fv}\right)\right]X_q . \qquad (8.9b)$$

For a vacancy mechanism being operative, it is convenient to choose a laboratory frame of reference where the sum of the fluxes for two elements vanishes [28], such that

$$\tilde{J}_A + \tilde{J}_B = 0 \qquad (8.10)$$

and

$$\tilde{J}_A = -\tilde{J}_B = J_A - (1-c)(J_A + J_B) = c J_A - (1-c) J_B . \qquad (8.11)$$

Substituting respective intrinsic fluxes from Equation 8.9 in Equation 8.11 yields:

$$\begin{aligned} \tilde{J}_A = &-\rho c(1-c)\beta_A \nabla \mu_A + \rho c(1-c)\beta_B \nabla \mu_B + \\ & c\left[L_{AA}\left(Q_A^* - h_{fv}\right) + L_{AB}\left(Q_B^* - h_{fv}\right)\right]X_q \\ &-(1-c)\left[L_{BA}\left(Q_A^* - h_{fv}\right) + L_{BB}\left(Q_B^* - h_{fv}\right)\right]X_q \end{aligned} \qquad (8.12)$$

Using Equation 8.8 along with the Onsager's reciprocal relationship $L_{ij} = L_{ji}$,

$$\tilde{J}_A = -\rho c(1-c)\beta_A \nabla \mu_A + \rho c(1-c)\beta_B \nabla \mu_B +$$
$$[cL_{AA} - (1-c)L_{BA}]\tilde{Q}_A^* X_q + [cL_{AB} - (1-c)L_{BB}]\tilde{Q}_B^* X_q$$
$$= -\rho c(1-c)\beta_A \nabla \mu_A + \rho c(1-c)\beta_B \nabla \mu_B \qquad (8.13)$$
$$+ [\rho c(1-c)\beta_A \tilde{Q}_A^* - \rho c(1-c)\beta_B \tilde{Q}_B^*] X_q$$

where

$$\tilde{Q}_i^* = Q_i^* - h_{fv}. \qquad (8.14)$$

Again using the Gibbs-Duhem equation $(1-c)\nabla \mu_A + c\nabla \mu_B = 0$,

$$\nabla \mu_A = c\nabla \mu_A^{eff}, \nabla \mu_B = -(1-c)\nabla \mu_A^{eff}, \qquad (8.15)$$

where

$$\nabla \mu_A^{eff} = -\nabla \mu_B^{eff} = \nabla(\mu_A - \mu_B). \qquad (8.16)$$

Now substituting Equation 8.15 into Equation 8.12 yields:

$$\tilde{J}_A = -\rho c(1-c)[c\beta_A + (1-c)\beta_B]\nabla \mu_A^{eff}$$
$$+ \rho c(1-c)[\beta_A \tilde{Q}_A^* - \beta_B \tilde{Q}_B^*] X_q$$
$$= -M_c \nabla \mu_A^{eff} + M_Q X_q \qquad (8.17)$$
$$= M_c \nabla \mu_B^{eff} - M_Q \frac{\nabla T}{T}$$

and

$$\tilde{J}_B = -\tilde{J}_A = -M_c \nabla \mu_B^{eff} + M_Q \frac{\nabla T}{T}, \tag{8.18}$$

where the chemical mobility is defined as:

$$M_c = \rho c (1-c) \left[c\beta_A + (1-c)\beta_B \right] \tag{8.19}$$

and the heat of transport term is expressed by:

$$M_Q = \rho c (1-c) \left[\beta_A \tilde{Q}_A^* - \beta_B \tilde{Q}_B^* \right] \qquad . \tag{8.20}$$

In Equation 8.17, the effective chemical potential for a heterogeneous system is defined as:

$$\mu_B^{eff} = \frac{\delta F}{\delta n_B} = V_m \frac{\delta F}{\delta c} \tag{8.21}$$

where δ stands for the variational derivative and F is the Cahn-Hilliard free energy functional consisting of the bulk free energy and interfacial energy contributions, expressed by:

$$F = F_{bulk} + F_{int} = N_V \int_V \left[f(c,T) + \kappa (\nabla c)^2 \right] dV. \tag{8.22}$$

Here, again following the convention of the previous chapters, $f(c,T)$ is the Helmholtz free energy density, approximated by the regular solution model in the present study, and κ is the gradient energy coefficient associated with the gradient of composition. Note that $f(c,T)$ can be directly adopted from the thermodynamic databases if available for a particular alloy system.

Using Equation 8.21 and 8.22 in Equation 8.18, the flux equation becomes

$$\tilde{J}_B = -V_m M_c \nabla \left(\frac{\partial f}{\partial c} - 2\kappa_c \nabla^2 c \right) + M_Q \frac{\nabla T}{T} \tag{8.23}$$

The spatio-temporal evolution of the composition can now be described by the continuity equation:

$$\frac{\partial n_B}{\partial t} = \frac{1}{V_m} \frac{\partial c(x,t)}{\partial t} = -\nabla \cdot \tilde{J}_B = \nabla \cdot \left[V_m M_c \nabla \left(\frac{\partial f}{\partial c} - 2\kappa_c \nabla^2 c \right) - M_Q \frac{\nabla T}{T} \right]. \tag{8.24}$$

Both constant as well as temperature dependent atomic mobility and heat of transport values can be used in the above equation. For the simulation of single-phase alloys constant atomic mobility and heat of transport terms are employed. For the two-phase alloys the following Arrhenius and linear relations are used to express the temperature dependency of atomic mobility and heat of transport terms, respectively [9,29-30]:

$$\beta_i = \beta_0 \exp\left(-Q_i \middle/ RT \right) \tag{8.25}$$

and

$$\tilde{Q}_i^* = C_i + D_i T, \quad i = A, B \tag{8.26}$$

8.2.2 Numerical Procedure:

For numerical convenience, the governing Equation 8.24 was rewritten in the following dimensionless form:

$$\frac{\partial \bar{c}(\mathbf{x},\tau)}{\partial \tau} = \bar{\nabla}\left[\bar{M}_c(\bar{c})\bar{\nabla}\left(\frac{\partial \bar{f}}{\partial \bar{c}(\mathbf{x},\tau)} - \bar{\kappa}\bar{\nabla}^2\bar{c}(\mathbf{x},\tau)\right) - \bar{M}_Q\frac{\bar{\nabla}T}{T}\right] \tag{8.27}$$

by introducing the following reduced quantities:

$$\bar{\nabla} = \left(\frac{\partial}{\partial(x/l)},\frac{\partial}{\partial(y/l)}\right),\ \bar{M}_c = \frac{V_m M_c}{\beta},\ \bar{f} = \frac{V_m f}{\Delta f},\ \bar{\kappa} = \frac{\kappa V_m}{\Delta f l^2},\ \bar{M}_Q = \frac{M_Q V_m}{\Delta f \beta},\ \text{and}\ \ \tau = \frac{\beta \Delta f}{l^2}t\ \text{where}\ \mathbf{x}\ \text{and}\ \tau$$

are the reduced length and time, l is the length scale of the system, $\Delta f = RT_c$ is the normalization factor for the free energy with $T_c = 900$ K, R is the universal gas constant, V_m is the constant molar volume, and β is a constant in the unit of atomic mobility. The above equation was solved numerically using a control volume method implemented by the FiPy partial differential equation (PDE) solver [31].

The applied temperature field obeys Laplace's equation

$$\nabla^2 T = 0 \tag{8.28}$$

with boundary conditions

$$J_q \cdot \hat{n} = 0, T|_{x=0} = T_{\min}, T|_{x=L} = T_{\max}. \tag{8.29}$$

The above conditions produce a linear distribution of temperature across the system. Note that the equation for heat flux is not considered here as the heat flux due to mass flux i.e. the Dufour effect is ignored in this study.

8.3 Results

8.3.1 Single Phase Alloy:

A single-phase alloy with initial homogeneous composition of $c_0 = 0.1$ was subjected to a temperature gradient, where $T_{min} = 773$ K and $T_{max} = 1273$ K. The left end ($L = 0$) of the system is the hotter end for this part of the simulation. Different combinations of atomic mobility and heat of transport terms, which are not functions of temperature, were employed in the study and the resulting composition profiles are shown in Figure 59. The grid resolution was chosen to be $\Delta x = 1$ µm for 1D calculations and value of the gradient energy coefficient was set to zero. The results show that upon the application of the temperature gradient, a composition gradient develops in the alloy, where the elements move towards the hot or cold end depending on the magnitude and sign of the mobility and heat of transport terms. The magnitude of the concentration gradient developed in the alloy is also determined by the above two factors. As is observed from the composition profiles, it can be said without any generalization that the element with a negative heat of transport moves towards the hot end of the system.

A steady state can be achieved with prolonged annealing under thermal gradient when the contribution to the flux due to temperature gradient becomes equal to the contribution due to concentration gradient. In Figure 60, a representative composition profile is shown along with the flux profiles as the system is approaching steady state. It can be noticed that the contributions to the total flux due to the chemical potential gradient and the temperature gradient are almost equal in magnitude and opposite in direction.
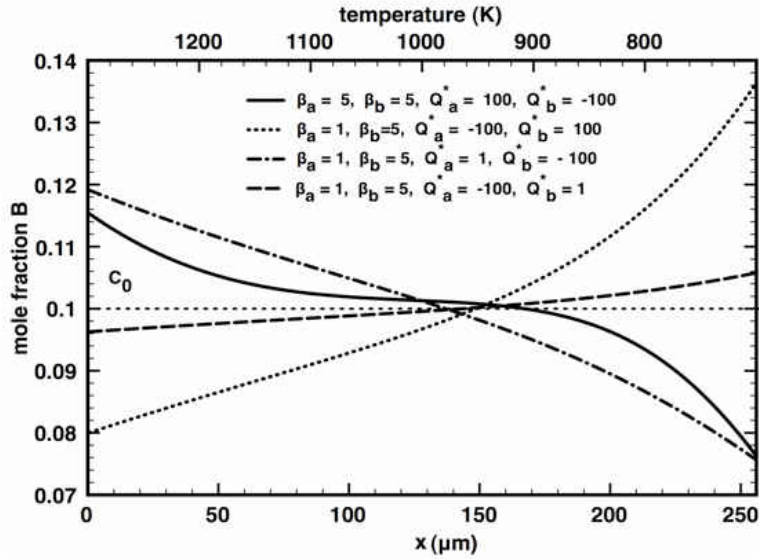
Figure 59: Composition profiles developed in an initially homogeneous single phase alloy after being subjected to annealing in a temperature gradient for 6 hours. The initial composition c_0 = 0.1, temperature range: T_{max} = 1273 K on the left end and T_{min} = 773 K at the right end of the system.
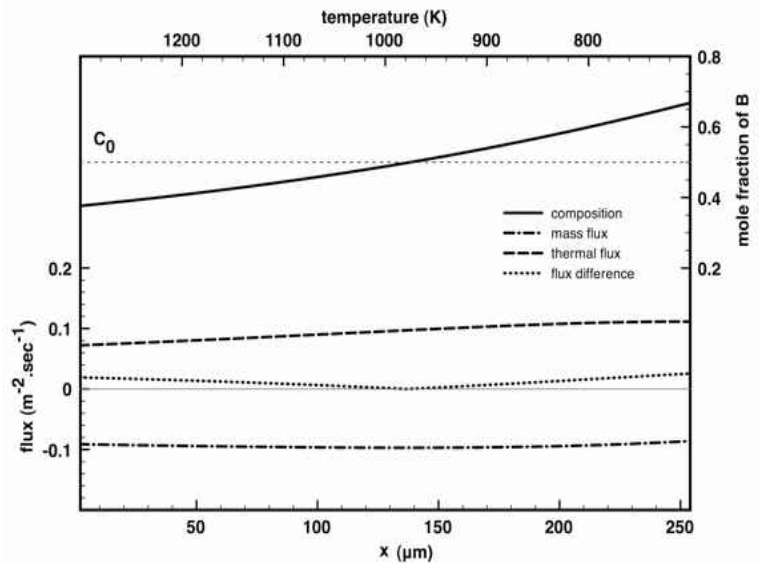
Figure 60: Representative composition profile and flux profiles in an initially homogeneous single-phase alloy approaching steady state after being subjected to annealing in a temperature gradient. The initial composition c0 = 0.5, temperature range: Tmax = 1273 K on the left end and Tmin = 773 K at the right end of the system. "Mass flux" and "thermal flux" are the contributions of chemical potential gradient and temperature gradient respectively, to the total flux and the "flux difference" is the difference between these two contributions.

160

8.3.2 Two-Phase Alloy:

Simulations of thermotransport effect in two-phase alloys were performed by applying a temperature gradient to pre-generated two-phase microstructures. A representative microstructure of such a two-phase alloy is shown in Figure 61, which was generated by introducing β nuclei (second phase) randomly into a α matrix at a temperature of 900 K and annealing them isothermally until the phases attend their equilibrium composition at the said temperature. This two-phase microstructure served as the initial microstructure or composition distribution and was then subjected to a constant temperature gradient of 250°C/mm. The following parameters were chosen: $\Delta x = 5$ μm, and $\bar{\kappa} = 1.0$.

Before starting the simulation for thermomigration, it is interesting to see the microstructural changes that could happen under a temperature gradient without the thermomigration term being considered in the flux equations. For this purpose, a simulation was performed by applying the aforementioned temperature gradient to a two-phase alloy, while turning the thermomigration term off, i.e. $Q_A{}^* = Q_B{}^* = 0$. The resulting microstructure is shown in Figure 62, which shows no redistribution of phases across the system while there is a noticeable difference in the compositions of phases at the hot and cold sides, as is evident from the sharp contrast between phases. This difference in composition is due to the variation in equilibrium composition dictated by the thermodynamic description of the system as a function of temperature.
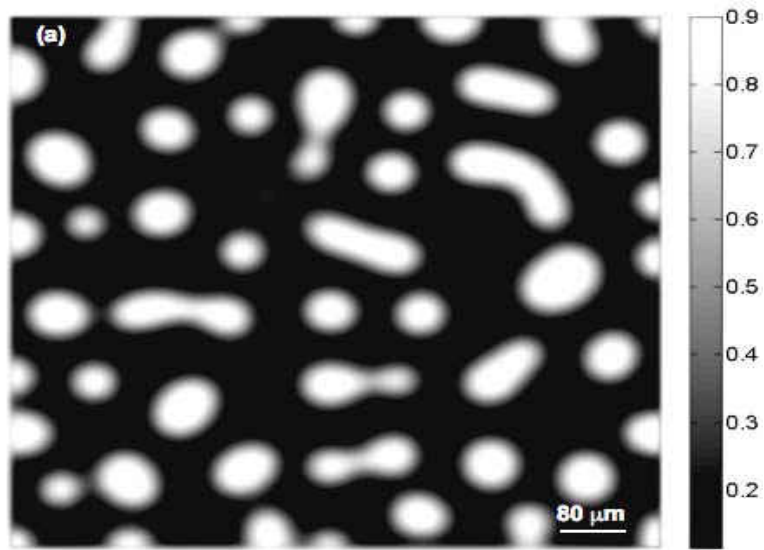
Figure 61: A representative microstructure of the initial microstructure used for thermomigration studies. The bright and dark phases are the B rich and A rich phases respectively. The gray scale bar on the right of the micrograph represents mole fraction of B.
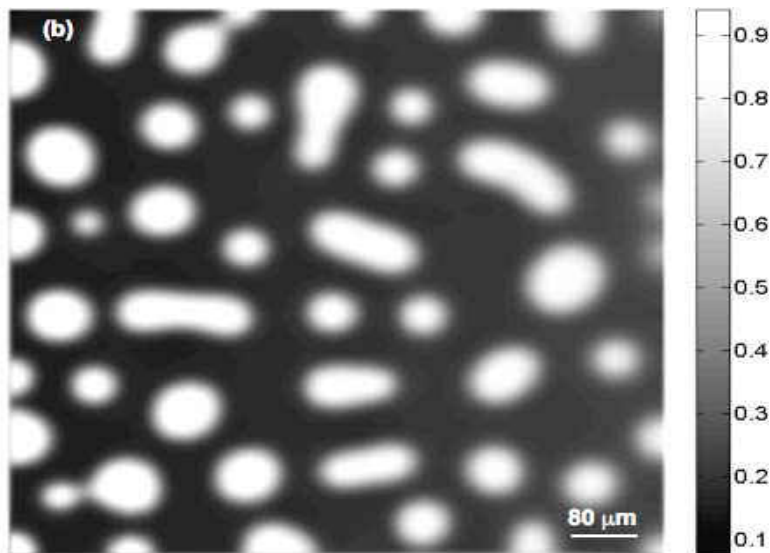
Figure 62: Microstructure of a two phase alloy annealed for 370 hours in a temperature gradient, while the thermotransport effect was switched off in the simulation. The bright and dark phases are the B rich and A rich phases respectively. The gray scale bar on the right of the micrograph represents mole fraction of B. Temperature range: $T_{max} = 1000$ K on the right end and $T_{min} = 800$ K at the left end of the system.

Finally, the thermomigration term was turned on, and four different combinations of heat of transport values were used to study their effect on the final microstructure. In all the four cases studied, the same atomic mobilities were used, wherein $\beta_B > \beta_A$ and Q_A^*, $Q_B^* > 0$. In case - I: Q_A^* = Q_B^* and $M_Q < 0$, in case - II: $Q_B^* >> Q_A^*$ and $M_Q < 0$, in case - III: $Q_B^* << Q_A^*$ and $M_Q > 0$, and in case - IV: $Q_B^* < Q_A^*$ and $M_Q > 0$. The chemical mobility $M_c > 0$ for all the above cases. Microstructures obtained for these four different conditions are presented in Figure 63, 64, 65 and 66, respectively. It can be seen that considerable redistribution of the second phase occurs along with the formation of A and B rich single-phase layers at the hot and cold ends in case - I , II and case - III, while in case - IV no such effect is evident. It is also noteworthy that the movement of elements is in opposite direction to each other in case - I and case - III. As it will be discussed later, the above results suggest that even though the sign of the heat of transport term is positive in all the cases the direction of motion of elements and the final distribution of phases are dependent on the sign and magnitude of M_Q.
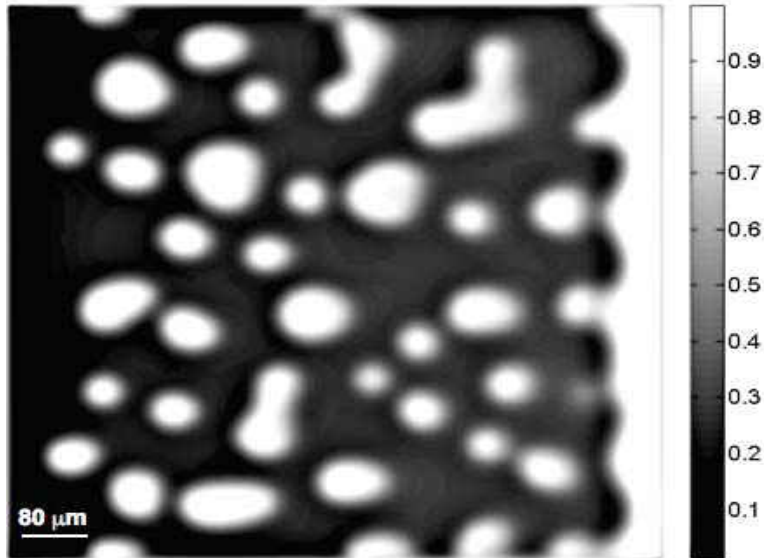
Figure 63: Microstructure of the two-phase alloy obtained after being subjected to annealing for 370 hours in a temperature gradient in Case -I: $Q_A^* = Q_B^*$ and $M_Q < 0$. Temperature range: T_{max} = 1000 K on the right end and T_{min} = 800 K at the left end of the system. B atoms move towards the hot end forming a B rich single-phase at the hot end, while an A rich phase forms at the cold end.
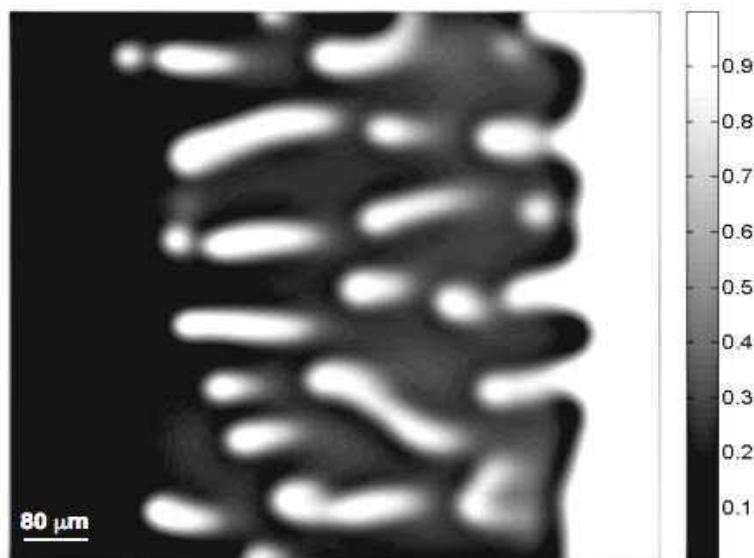
Figure 64: Microstructure of the two-phase alloy obtained after being subjected to annealing for 370 hours in a temperature gradient in Case -II: $Q_B^* \gg Q_A^*$ and $M_Q < 0$. Temperature range: T_{max} = 1000 K on the right end and T_{min} = 800 K at the left end of the system. B atoms move towards the hot end forming a B rich single-phase at the hot end, while an A rich phase forms at the cold end.

164
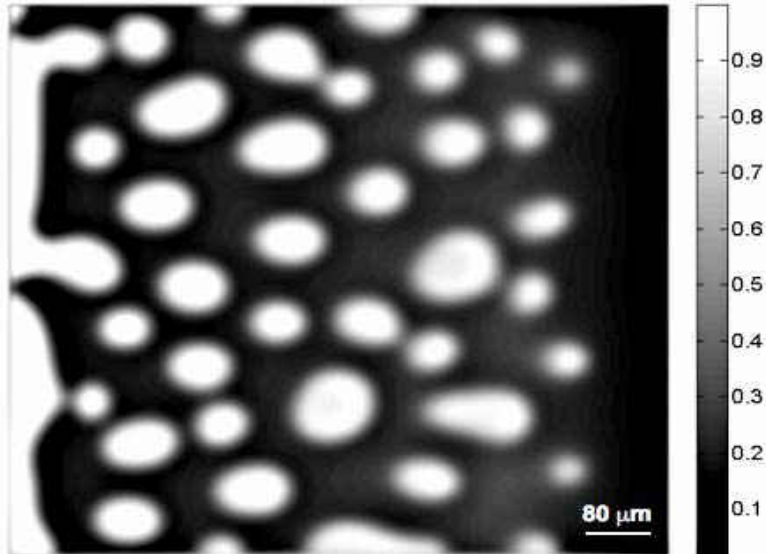
Figure 65: Microstructure of the two-phase alloy obtained after being subjected to annealing for 370 hours in a temperature gradient in Case -II: $Q_B^* \gg Q_A^*$ and $M_Q < 0$. Temperature range: $T_{max} = 1000$ K on the right end and $T_{min} = 800$ K at the left end of the system. B atoms move towards the cold end forming a B rich single-phase at the hot end, while an A rich phase forms at the cold end.
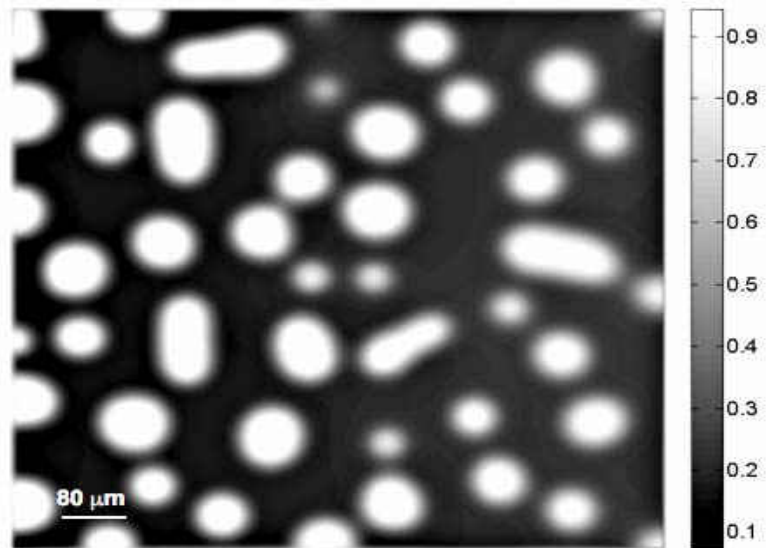
Figure 66: Microstructure of the two-phase alloy obtained after being subjected to annealing for 370 hours in a temperature gradient in Case -IV: $Q_B^* < Q_A^*$, $M_Q > 0$ and $|M_Q|$ is small. Temperature range: $T_{max} = 1000$ K on the right end and $T_{min} = 800$ K at the left end of the system. The effect of thermomigration is less evident.

8.4 Discussions

In the previous section it was demonstrated that redistribution of composition and the second phase can be simulated by a phase-field model when the alloy is subjected to a thermal gradient. The magnitude and direction of this redistribution, i.e. whether towards the hot end or the cold end of the specimen, is dependent on various factors and cannot be predicted simply by the phase diagram and Fickian diffusion. As a result, the flux equation has been modified to include the thermomigration effect. As described earlier, the case of a substitutional alloy where both the elements have comparable mobilities requires that the heat of transport as well as mobilities of both the elements be considered in describing the flux of an element. The combination of these mobilities and heat of transport values determine the magnitude and sign of M_Q, which decides the direction of flow of an element.

In case - I, for two-phase alloys, $Q_A^* = Q_B^*$ and $M_Q < 0$. Since $M_c > 0$, the contribution of the temperature gradient driven term to the flux of B in Equation 8.18 is in the same direction as the term involving the concentration gradient. This causes the B atoms to flow towards the hot end. In case - II, $Q_B^* \gg Q_A^*$ and $M_Q < 0$, where $|M_Q|$ is very large. This produces a similar redistribution of the second phase, as that of case - I, but the effect is much stronger. This is evident from the distinct flow pattern of B atoms towards the hot end throughout the system in Figure 63.

Unlike in case - I and II, $M_Q > 0$ in case – III and IV. The positive sign of M_Q suggests that the contribution of thermotransport term to the flux of B atoms is opposite to the term involving concentration gradient. This means that B atoms will flow towards the cold end,

opposite to the direction predicted by the phase diagram of the alloy system. This is evident from the B rich single-phase formed at the cold end of the specimen in Figure 65 in case – III, where $|M_Q|$ is large. But this redistribution is not appreciable in case – IV as $|M_Q|$ is very small, thus making the contribution of thermotransport to the total flux negligible.

From Equation 8.20 it can be deduced that for a binary solution with an immobile solvent, M_Q is roughly equal to the product of atomic mobility and heat of transport of the solute, i.e. $\beta_B Q_B^*$. In this case the flow direction of the solute can be predicted with a considerable degree of certainty from the knowledge of Q_B^* only. The situation becomes more complex with the presence of a mobile solvent, when heat of transport of solvent and solute both contribute to the value of M_Q. An important consequence of the aforementioned, which is also exemplified by our results is that for a particular solvent, while different solutes can have heat of transport terms (Q_B^*) of same sign, M_Q may or may not have the same sign as that of Q_B^* for all the solutes. Under such circumstances the prediction of the flow direction of solute atoms could be anomalous and has been so experienced in many systems, e.g. Co, Au, Ge and Ag as solutes in Cu [5]. This work demonstrates that the results of the present model can explain the experimental discrepancies on thermotransport in substitutional alloys. Being capable of taking into account the individual mobility and heat of transport terms of elements, this model can be of great help in predicting the flow behavior of solutes in a solvent under applied thermal gradient.

Previous analytical and numerical models [17-21] used to predict the thermotransport behavior in single- and two-phase alloys were derive heavily from the model first proposed by Shewmon [2] for binary alloys. Jaffe and Shewmon [5] represented the drift velocity of solute and solvent in a binary substitutional alloy as:

$$V_i = -\frac{D_i}{RT}\left[RT\frac{\partial \ln c_i}{\partial x} + \frac{Q_i^* - \Delta H_{vi}}{T}\frac{dT}{dx}\right]$$ (8.28)

where ΔH_{vi} is the molar enthalpy change in the lattice for forming a vacancy surrounded by the solute or solvent atoms. At steady state V_1 and V_2 may not be equal to zero, but V_1 is equal to V_2. However, apart from the assumption that local equilibrium concentration of vacancies is maintained at each point, these models were based on two other important assumptions, i.e. only the solute migrates in the alloy and local thermodynamic equilibrium between the solute in solution and the second-phase particles is obtained in those regions where the solubility limit is exceeded. The present phase-field model based on a continuum approach requires only the assumption of equilibrium vacancy concentration to be maintained locally and does not demand the other two aforementioned assumptions to be made beforehand. This is due to the fact that the present model is derived using the actual thermodynamic description of the system. It is also worthwhile to mention that all the previous models are based on a one-dimensional approach to solve the steady state problem, whereas the phase-field model can describe the thermotransport behavior in any number of dimensions, even for non-steady states.

Using this model, the effect of temperature gradient on the composition and microstructure of any alloy can be predicted, provided the knowledge of thermodynamic and mobility data as well as the heat of transport terms are available. Data for some alloy systems where thermotransport is important, such as U-Zr (nuclear fuel), Ni-Al (turbine blade) and Pb-Sn (interconnects) are available in literature. The thermodynamic description for these systems can be obtained from a Calphad database [32-35], whereas the mobility data for Ni-Al and Pb-Sn can be obtained from [29,36]. Experimental data for heat of transport terms in Pb-Sn and U-Zr

168

systems are published in [14,37-38]. The authors could not find any data on mobility for the U-Zr system and heat of transport terms for the Ni-Al system. Simulations using various combinations of these unknown parameters in U-Zr and Ni-Al system can be performed in future work.

8.5 Conclusions

It is well known that a temperature gradient can cause appreciable redistribution of elements and phases present in an alloy. A diffuse interface model was devised to simulate and predict this redistribution phenomenon under applied temperature gradient. The results show that both atomic mobilities and heat of transport values of individual elements play a role in determining the magnitude of the concentration gradient and the flow direction of elements. In certain cases the combination of these parameters can cause an element to flow opposite to the direction as determined by the phase diagram and Fick's first law. This model can be used to simulate real alloy systems by incorporating actual thermodynamic data and materials parameters for the system.

8.6 References

[1]   A.R. Allnatt, A.V. Chadwick, Chem. Rev. 67 (1967) 681.

[2]   P.G. Shewmon, Trans. Met. Soc. AIME 212 (1958) 642.

[3]   P. Shewmon, J. Chem. Phys. 29 (1958) 1032.

[4]   P. Shewmon, Acta Metall. 8 (1960) 605.

[5]   D. Jaffe, P.G. Shewmon, Acta Metall. 12 (1964) 515.

[6]   Y.H. Sohn, M.A. Dayananda, G.L. Hofman, R.V. Strain, S.L. Hayes, J. Nucl. Mater. 279 (2000) 317.

[7]   I.C.I. Okafor, O.N. Carlson, D.M. Martin, Metall. Trans. A 13 (1982) 1713.

[8]   M. Uz, D.K. Rehbein, O.N. Carlson, Metall. Trans. A 17 (1986) 1955.

[9]   S.C. Axtell, O.N. Carlson, Metall. Trans. A 21 (1990) 2141.

[10] J.G. Shaw, W.A. Oates, Metall. Trans. 2 (1971) 2127.

[11] C.J. Meechan, G.W. Lehman, J. Appl. Phys. 33 (1962) 634.

[12] W. Mock Jr., Phys. Rev. 179 (1969) 663.

[13] A.T. Huang, A.M. Gusak, K.N. Tu, Y.S. Lai, Appl. Phys. Lett. 88 (2006) 141911.

[14] F.Y. Ouyang, K.N. Tu, Y.S. Lai, A.M. Gusak, Appl. Phys. Lett. 89 (2006) 221906.

[15] V. Tikare, W. A. Holm, J. Am. Ceram. Soc. 81 (1998) 480.

[16] V. A. Snyder, N. Akaiwa, J. Alkemper, P. W. Voorhees, Metall. Mater. Trans. A 30 (1999) 2341.

[17] S.V. Vaerenbergh, S.R. Coriell, G.B. McFadden, B.T. Murray, J.C. Legros, J. Crystal Growth 147 (1995) 207.

[18] L.L. Zheng, D.J. Larson Jr., H. Zhang, J. Crystal Growth 191 (1998) 243.

[19] G.P. Marino, Nucl. S. Engg. 49 (1972) 93.

[20] D. Yang, B.Y. Wu, Y.C. Chan, K.N. Tu, J. Appl. Phys. 102 (2007) 043502.

[21] G. L. Hofman, S. L. Hayes, M. C. Petri, J. Nucl. Mater. 227 (1996) 277.

[22] J.W. Cahn, J.E. Hilliard, J. Chem. Phys. 28 (1958) 258.

[23] L.Q. Chen, Annu. Rev. Mater. Res. 32 (2002) 113.

[24] S.R. de Groot, Thermodynamics of Irreversible Processes, North-Holland, Amsterdam, 1952.

[25] R.E. Howard, A.B. Lidiard, Rep. Prog. Phys. 27 (1964) 161.

[26] J. Philibert, Atom Movements, Diffusion and Mass Transport in Solids, Monographies De physique, (1991) 326.

[27] A. R. Allnatt, A. B. Lidiard, Atomic Transport in Solids, Cambridge University Press,1993, 165-191.

[28] P. G. Shewmon, Diffusion in Solids, McGraw-Hill, USA, 1963, pp.134-135.

[29] A. Engstrom, J. Agren, Z Metallkd. 87 (1996) 92.

[30] G. Ghosh, Z.K. Liu, J. Electron. Mater. 27 (1998) 1362.

[31] J. E. Guyer, D. Wheeler, and J. A. Warren, FiPy: a finite volume PDE solver using Python, http://www.ctcms.nist.gov/fipy (updated 12 February 2007).

[32] A. T. Dinsdale, SGTE Database for Pure Elements, Calphad 15 (1991) 317.

[33] P Y. Chevalier, E. Fisher, B. Cheynet, Calphad 28 (2004) 15.

[34] I. Ansara, N. Dupin, H. L. Lukas, B. Sundman, J. Alloy and Compounds, 247 (1997) 20.

[35] H. Ohtani, K. Okuda, K. Ishida, J.Phase Equl. 16 (1995) 416.

[36] G. Ghosh, Z. K. Liu, J. Electronic Mater. 27 (1998) 1362.

[37] J. F. D' Amico, H. B. Huntington, J. Phys. Chem. Solids. 30 (1969) 1697.

[38] D. R. Campbell, H. B. Huntington, Phys. Rev. 179 (1969) 601.

CHAPTER 9
CONCLUDING REMARKS AND FUTURE DIRECTIONS

The primary goal of this research is to understand and predict the interdiffusion behavior and microstructure evolution in binary and ternary alloys using the continuum mesoscale diffuse interface phase-field model. The study focuses on interdiffusion process under two types of driving forces, namely, composition gradient and temperature gradient. Several examples were used including hypothetical binary and ternary systems, Ni-Al and Ni-Cr-Al systems. The conclusions of this study are summarized as follows.

9.1 Isothermal Interdiffusion Under Composition Gradient

This investigation has two main objectives, first, to predict concentration profiles, diffusion paths and the occurrence of up-hill diffusion and zero-flux planes in single-phase vs. single-phase solid-to-solid diffusion couples, and second, to predict the interdiffusion microstructure evolution in multi-phase diffusion couples of Ni-Al and Ni-Cr-Al alloys, utilizing the phase-field model. It was demonstrated that using a simple regular solution model, and constant chemical mobilities, development of concentration profiles including uphill diffusion and zero-flux planes can be simulated by a phase-field model. The results showed that a zero-flux plane for a component could develop at the composition that corresponds to the intersection of the diffusion path and the isoactivity line drawn from one of the terminal alloys. The composition at the point of intersection corresponds closely to the activity of one of the terminal alloys. There could be more than one ZFP developed on either side of the Matano plane. The study also showed that the development of ZFPs depends on the terminal alloy compositions and the presence of extremum or up-hill diffusion does not necessarily produce a ZFP. This is the

first phase-field simulation result to support the experimental observations first made by Dayananda et al.

In the multi-phase diffusion couples of Ni-Al and Ni-Cr-Al alloys, three different types of boundaries, namely, type 0, type 1 and type 2 were observed. Dissolution of the second phase, i.e. γ' and β, was observed in all the single-phase vs. two-phase (γ vs. $\gamma+\gamma'$ and γ vs. $\gamma+\beta$) diffusion couples in the binary and ternary alloys. The dissolution rate depends on the composition of the single-phase terminal alloy and the volume fraction of the second-phase in the two-phase alloy; the higher the composition and volume fraction, the lower the dissolution. In two-phase vs. two-phase ($\gamma+\gamma'$ vs. $\gamma+\gamma'$ and $\gamma+\beta$ vs. $\gamma+\beta$) diffusion couples, no phase dissolution was observed and the initial boundary remained stationary. The simulation results agree with both the experimental and theoretical results reported in literature. It is concluded that using thermodynamic and kinetic data with a phase-field model can predict the interdiffusion behavior and microstructure evolution in isothermal multicomponent and multiphase diffusion couples.

9.2 Interdiffusion Under Temperature Gradient

The objective of this portion of the work is to develop a phase-field model to understand and predict the diffusional microstructure evolution under a temperature gradient or thermotransport. The model was applied to single phase and two-phase alloys of a hypothetical binary system A-B. Simulation results showed that an applied temperature gradient could cause significant redistribution of constituents and phases in the alloy. The magnitude and the direction of the redistribution depend on the initial composition, the atomic mobility and the heat of transport of the respective elements. In multi-phase alloys, the thermomigration effect can cause

the formation of single-element rich phases at the cold and hot ends of the alloy. Because of its phenomenological basis, this phase-field model can easily be extended and applied to a ternary system.

9.3 Future Work

1. One of the subjects of focus in this work was the occurrence of zero-flux planes during multicomponent interdiffusion. Though the simulation results confirmed many experimentally observed features associated with ZFPs, and revealed some important information such as the effect of terminal alloy compositions and mobilities on the occurrence of ZFPs, there are issues that need further examination. For example, in order to establish the exact criteria for the occurrence of ZFPs, it is necessary to understand the relative importance of thermodynamic and kinetic factors such as the activities and atomic mobilities of the components. Therefore, utilizing the phase-field model, a detail analysis should be performed on real alloy systems with sufficient thermodynamic and kinetic data.

2. In this study, elastic strain energy effect due to lattice misfit between the phases was neglected during the multiphase diffusion couple simulations. It would be interesting to study the effect of elastic inhomogeneity on the interdiffusion process.

3. Taking the motivation from the results of Ni-Al or Ni-Cr-Al alloys in this study, and its interpretation in terms of diffusional interaction between the bond coat and superalloy substrate in thermal barrier coatings (TBCs), the present phase-field model should be extended to incorporate other critical phenomena associated with TBC failure. With appropriate formulation, the phase-field approach can be used to model sintering of YSZ

topcoat, (t'→f+m) phase transformations in YSZ topcoat, high temperature oxidation of bond coat and growth of TGO, microstructural evolution in multicomponent-multiphase interdiffusion, and fracture at the YSZ/TGO and TGO/bond coat interfaces. This would serve as a mechanism-based model for the life cycle prediction of TBCs.

4. The phase-field model for the thermotransport effect needs to be further developed in order to be applied to important real alloy systems where thermotransport is critical such as Pb-Sn, U-Zr, and Ni-Al.

APPENDIX A
LIST OF PUBLICATIONS FROM THIS DISSERTATION

Journal Publications

1. **R. R. Mohanty**, Y. H. Sohn, "*Phase-field Model for Thermotransport*", to be submitted to Journal of Applied Physics.

2. **R. R. Mohanty**, Y. H. Sohn, "*Occurrence of Zero-Flux Planes in Ternary Alloys - A Phase-field Model Study*", In Preparation.

3. **R. R. Mohanty**, Y. H. Sohn, "*Microstructural Stability of fcc-γ+B2-β Coatings on γ Substrate in Ni-Cr-Al System*", Surface and Coatings Technology, 203, 2008, pp. 407.

4. **R. R. Mohanty**, A. Leon, Y. H. Sohn, "*Phase-field Simulation of Interdiffusion Microstructure Containing fcc- γ and L1$_2$-γ' Phases in Ni-Al Diffusion Couples*", Computational Materials Science, 43, 2008, pp. 301.

5. **R. R. Mohanty**, Y. H. Sohn, "*Phase-field Modeling of Interdiffusion Microstructure in Ni-Cr-Al Diffusion Couples*", Materials Science Forum, 595-598, 2008, pp. 199.

6. **R. R. Mohanty**, Y. H. Sohn, "*Phase-field Investigation of Multicomponent Diffusion in Single-phase and Two-phase Diffusion Couples*", Journal of Phase Equilibria and Diffusion, Vol. 27, 2006, pp. 676.

7. Y. H. Sohn, N. Garimella, E. Perez, **R. R. Mohanty**, J. Liu, "*Integrated, Effective and Average Interdiffusion Coefficients and Their Applications in Multicomponent Alloys for Energy Production Technologies*", Defects and Diffusion Forum, 258, 2006, pp. 346.

Proceedings

1. **R. R. Mohanty**, Y. H. Sohn, "*Phase-field Approach to Microstructural Modeling and Life Prediction of High Temperature Coatings*", Accepted in the Proceedings of the ASME Turbo Expo, June 8-12, 2009, Orlando, Florida, USA.

2. **R. R. Mohanty**, Y. H. Sohn, "Phase-field Modeling of Interdiffusion Induced Microstructure Evolution Under Different Driving Forces", Proceedings of the Fourth International Conference on Multiscale Materials Modeling, October 27 − 31, 2008, Tallahassee, FL, USA, pp. 409-412.

3. **R. R. Mohanty**, Y. H. Sohn, "*Phase-field Modeling of Interdiffusion Induced Microstructure Evolution Under Different Driving Forces*", Proceedings of the Fourth International Conference on Multiscale Materials Modeling, October 27 − 31, 2008, Tallahassee, FL, USA, 409-412.

APPENDIX B
SAMPLE C PROGRAM FOR
ISOTHERMAL DIFFUSION COUPLE SIMULATIONS

The code for the simulation of isothermal diffusion couples was written in the programming language C. For convenience, different parts of the code and the general procedure to run these codes are described in the following.

There are two basic parts: the first part generates the microstructures for alloys of different compositions, and the second part runs the simulation for diffusion couples, which utilizes the microstructures generated in first part to obtain initial microstructure for diffusion couples. So, if a microstructure generated in the first part has m x n grid points, then the initial microstructure of the diffusion couple after joining two such pre-generated microstructures would be of m x 2n grid points. The data conversion and joining is done by two separate codes, namely, convert.c and couple.c, respectively. Please note that all the programs use Fast Fourier Transforms in the West (fftw), a free collection of fast C routines for computing Discrete Fourier Transform in one or more dimensions. For further information please visit www.fftw.org.

Both part-1 and part-2 contain four directories and a Makefile each. The directories are named as 'input/', 'headers/', 'src/' and 'output/'. The source codes are present in 'src/', which read the input data from 'input/' and the output is written to the directory 'output/'. Following is a list of all the contents of above directories.

Contents of input/ directory: constants (for values of constants), syssize (for system size information) and timeinf (for timestep information).

Contents of headers/ directory: functions.h

Contents of src/ directory: frmnucli.c and evolute.c (part-1) and diffcoup.c and evolute.c (part-2).

frmnucli.c and diffcoup.c are the main codes, which read the inputs and calculate the evolution of field variables by calling evolute.c and write data files in the output/ directory. Note that the program evolute.c is same for part-1 and part-2.

frmnucli.c

```c
/*
 This program is used as the main program for part-1. This generates the initial
microstructure for alloys of different compositions and volume fractions of phases.
It reads the input files in input/ directory. Generates the nuclei randomly and calls
the evolute.c program for microstructure evolution.
*/
#include<stdio.h>
#include<stdlib.h>
#include<math.h>
#include <gsl/gsl_rng.h>
#include <gsl/gsl_randist.h>
#include</sw/include/fftw3.h>
#include"../headers/functions.h"

int main(void){

FILE *fpr, *fpw;
int i,j,q,m=15700,p;
int n_x,n_y,time_steps,halfny;
int cenx[m], ceny[m];
double del_x,del_y,del_t;
double rad,dis[m],radsq[m];
double kapa_a,kapa_b,kapa_c,kapa_e,M_aa,M_ab,M_ba,M_bb;
double z00,z01,z02,z03,z04,z10,z11,z12,z13,z20,z21,z22,z30,z31,z40,A2,A4;
double sigma = 1.0,area,v_ord,v_ordc,rat,root;
double avgAl, avgCr, gamaAl, gamaCr, betaAl, betaCr;
const gsl_rng_type * Taus;
gsl_rng * ran_num;

fftw_complex *compa;
fftw_complex *compb;
fftw_complex *compc;
fftw_complex *eta;

/* Get rid of old files in output directory */
 (void) system("rm -rf output/*");
/*
Write input values to README file
*/
if((fpw=fopen("output/README","w"))==NULL){
printf("Unable to open output/README. Exiting");
exit(0);
}

else{
```

181

```c
fpw = fopen("output/README","w");
}

/* read input values from read_input_values file */
if( (fpr = fopen("input/syssize","r")) == NULL){
printf("Unable to open input/syssize. Exiting");
exit(0);
}
else{
fpr = fopen("input/syssize","r");
}
(void) fscanf(fpr,"%d%d%le%le", &n_x, &n_y, &del_x, &del_y);
(void) fclose(fpr);
fprintf(fpw,"n_x = %d\nn_y = %d\n", n_x, n_y);
fprintf(fpw,"del_x = %le\ndel_y = %le\n", del_x, del_y);

/* Read the PFM constants */

if( (fpr = fopen("input/constants","r")) == NULL){
printf("Unable to oepn input/constants. Exiting");
exit(0);
}
else{
fpr = fopen("input/constants","r");
}
(void) fscanf(fpr,"%le%le%le%le", &kapa_a, &kapa_b, &kapa_c, &kapa_e);
(void) fclose(fpr);
fprintf(fpw,"kapa_a = %le\nkapa_b = %le\nkapa_c = %le\nkapa_e = %le\n", kapa_a, kapa_b,
kapa_c, kapa_e);

/*
Let us read the time step and number of time steps
*/

if( (fpr = fopen("input/timeinf","r")) == NULL){
printf("Unable to open input/timeinf. Exiting");
exit(0);
}
else{
fpr = fopen("input/timeinf","r");
}
(void) fscanf(fpr,"%le%d",&del_t,&time_steps);
(void) fclose(fpr);
fprintf(fpw,"del_t = %le\n",del_t);
fprintf(fpw,"time_steps = %d\n",time_steps);
fclose(fpw);
```

```
/*********** Memory allocation for variable comp ***************************/

compa = (fftw_complex*) fftw_malloc(n_x*n_y*sizeof(fftw_complex));
compb = (fftw_complex*) fftw_malloc(n_x*n_y*sizeof(fftw_complex));
compc = (fftw_complex*) fftw_malloc(n_x*n_y*sizeof(fftw_complex));
eta = (fftw_complex*) fftw_malloc(n_x*n_y*sizeof(fftw_complex));
/************ Setting up the GSL random number generator ****************/

(void) gsl_rng_env_setup();
Taus = gsl_rng_taus;
ran_num = gsl_rng_alloc (Taus);

halfny = (int) n_y/2;

/* Generate and Store random centers */
for(q=0; q<m; ++q){
cenx[q] = (gsl_rng_uniform_int(ran_num,n_x));
}
for(q=0; q<m; ++q){
ceny[q] = (gsl_rng_uniform_int(ran_num,n_y));
}

/* Generate and Store random radius and distance */
area = 0.0;
for(q=0; q<m; ++q){
rad = gsl_ran_gaussian(ran_num,sigma);
radsq[q] = del_x*del_y*rad*rad;
area = area+M_PI*radsq[q];
printf("%le\n",rad);
}
v_ordc = area/(n_x*n_y*del_x*del_y);

/* Generating the initial composition profile and eta values */

A4 = 4.0;
z00 = -102.12685;
z01 = 1155.43;              /* Fit thermo data values from literature */
z02 = -4897.04;
z03 = 9332.91;
z04 = -6647.69;
z10 = 10.92678;
z11 = -296.89049;
z12 = 1489.57;
z13 = -1937.45;
z20 = 253.57483;
```

```
z21 = -1032.66;
z22 = 808.6688;
z30 = -259.04708;
z31 = 564.16582;
z40 = 45.79865;

for(i=0; i<n_x; ++i){
for(j=0; j<n_y; ++j){
p = j+n_y*i;
compa[j+n_y*i][0] = 0.161;
compa[j+n_y*i][1] = 0.0;  /**** For gamma (matrix) *****/
compb[j+n_y*i][0] = 0.185;
compb[j+n_y*i][1] = 0.0;
compc[j+n_y*i][0] = 1.0-compa[j+n_y*i][0]-compb[j+n_y*i][0];
compc[j+n_y*i][1] = -compa[j+n_y*i][1]-compb[j+n_y*i][1];
eta[j+n_y*i][0] = 0.0;
eta[j+n_y*i][1] = 0.0;
gamaAl = compa[j+n_y*i][0];
gamaCr = compb[j+n_y*i][0];
}
}

for(q=0; q<m; ++q){
for(i=0; i<n_x; ++i){
for(j=0; j<n_y; ++j){
p = j+n_y*i;

dis[q] = (del_x*del_y)*((i-cenx[q])*(i-cenx[q])+(j-ceny[q])*(j-ceny[q]));

if(dis[q]<=radsq[q]){
compa[j+n_y*i][0] = 0.314;
compa[j+n_y*i][1] = 0.0;
compb[j+n_y*i][0] = 0.077;      /**** For beta phase ********/
compb[j+n_y*i][1] = 0.0;
compc[j+n_y*i][0] = 1.0-compa[j+n_y*i][0]-compb[j+n_y*i][0];
compc[j+n_y*i][1] = -compa[j+n_y*i][1]-compb[j+n_y*i][1];
betaAl = compa[j+n_y*i][0];
betaCr = compb[j+n_y*i][0];

A2 =
z00+z01*compa[p][0]+z02*compa[p][0]*compa[p][0]+z03*compa[p][0]*compa[p][0]*compa[p][0]+z04*compa[p][0]*compa[p][0]*compa[p][0]*compa[p][0]+compb[p][0]*(z10+z11*compa[p][0]+z12*compa[p][0]*compa[p][0]+z13*compa[p][0]*compa[p][0]*compa[p][0])+(compb[p][0]*compb[p][0])*(z20+z21*compa[p][0]+z22*compa[p][0]*compa[p][0])+(compb[p][0]*compb[p][0]*compb[p][0])*(z30+z31*compa[p][0]+z40*compb[p][0]);
```

```c
        rat = A2/A4;
        if(rat>=0.0){

        root = sqrt(rat);

        eta[j+n_y*i][0] =  root;

        eta[j+n_y*i][1] = 0.0;
        }
else{

        eta[j+n_y*i][0] = 0.0;

        eta[j+n_y*i][1] = 0.0;

        }
}
}
}
}

avgAl = 0.0;
avgCr = 0.0;
for(i=0; i<n_x; ++i){
for(j=0; j<n_y; ++j){

avgAl = avgAl+compa[j+n_y*i][0];
avgCr = avgCr+compb[j+n_y*i][0];
}
}
avgAl = avgAl/(n_x*n_y);
avgCr = avgCr/(n_x*n_y);

v_ord = ((gamaAl-avgAl)*(gamaAl-avgAl)+(gamaCr-avgCr)*(gamaCr-avgCr))/((gamaCr-
betaCr)*(gamaCr-betaCr)+(gamaAl-betaAl)*(gamaAl-betaAl));
v_ord = sqrt(v_ord);


/*
 Write ave_comp  values to readme file
*/

if((fpw=fopen("output/README","a"))==NULL){
printf("Unable to open output/README. Exiting");
exit(0);
```

```c
}

else{
fpw = fopen("output/README","a");
}

fprintf(fpw,"v_ord = %lf\nv_ordc= %lf\navgAl = %lf\navgCr = %lf\n", v_ord, v_ordc, avgAl,
avgCr);
fprintf(fpw,"gamaAl = %lf\nbetaAl = %lf\ngamaCr = %lf\nbetaCr = %lf\n", gamaAl, betaAl,
gamaCr, betaCr);
fprintf(fpw,"v_ordc is calculated from the area of random cicles\n");
fprintf(fpw,"v_ord is calculated from the Lever rule using average (calculated) and equilibrium
compositions (input)\n");
(void) fclose(fpw);

/*
 Evolution of Microstructure – call evolute.c
*/

evolute(n_x,n_y,del_x,del_y,del_t,time_steps,kapa_a,kapa_b,kapa_c,kapa_e,M_aa,M_ab,M_ba,
M_bb,compa,compb,compc,eta);

/* release the allocated memory */

fftw_free(compa);
fftw_free(compb);
fftw_free(compc);
fftw_free(eta);

return 0;
}
```

convert.c

```c
/*
This programs converts data obtained from single alloy simulations from 0-n_y to n_y-n_x.
Used for joining two sides of the diffusion couple by couple.c
*/
#include<stdio.h>
#include<stdlib.h>
#include<math.h>
#include</sw/include/fftw3.h>
int main(void)
{
        FILE *fpt,  *fpw;
        int i, j,temp,t1,t2,p,q;
        int n_x = 256, n_y = 256;
        fftw_complex *ca;
        fftw_complex *cb;
        fftw_complex *cc;
        fftw_complex *e;

        ca = (fftw_complex*) fftw_malloc(n_x*n_y*sizeof(fftw_complex));
        cb = (fftw_complex*) fftw_malloc(n_x*n_y*sizeof(fftw_complex));
        cc = (fftw_complex*) fftw_malloc(n_x*n_y*sizeof(fftw_complex));
        e = (fftw_complex*) fftw_malloc(n_x*n_y*sizeof(fftw_complex));
        fpt = fopen("composition file","r");      /* For right hand side */
for(i=0;i<n_x;i++){
        for(j=0;j<n_y;j++){
        fscanf(fpt,"%d%d%lf%lf%lf%lf",&t1,&t2,&(ca[j+n_y*i][0]),&(cb[j+n_y*i][0]),&(cc[j+n
_y*i][0]),&(e[j+n_y*i][0]));
           }
}
fclose(fpt);
fpw = fopen("readf","w");
for(i=0;i<n_x;i++){
        for(j=0;j<n_y;j++){
             p = i+n_x;
        fprintf(fpw,"%d\t%d\t%lf\t%lf\t%lf\t%lf\n",p,j,ca[j+n_y*i][0],cb[j+n_y*i][0],cc[j+n_y*i][
0],e[j+n_y*i][0]);
             }
}
fclose(fpw);
return 0;
fftw_free(ca);
fftw_free(cb);
fftw_free(cc);
fftw_free(e);
}
```

couple.c

```c
/*
This program generates the initial composition for the couple by interchanging the co-ordinates.
It takes the two data files and joins them together. It writes the data in the new co-ordinates into
the file "readcomp". It utilizes the data from one "composition file" and "readf" generated from
convert.c for 2-phase alloys.
*/

#include<stdio.h>
#include<stdlib.h>
#include<math.h>

#include</sw/include/fftw3.h>

int main(void){

FILE *fpw, *fir, *fin;
int i, j, t1, t2;
int n_x=512,n_y=256;
fftw_complex *compa;
fftw_complex *compb;
fftw_complex *compc;
fftw_complex *eta;

/*********** Memory allocation for variable comp ***************************/
compa = (fftw_complex*) fftw_malloc(n_x*n_y*sizeof(fftw_complex));
compb = (fftw_complex*) fftw_malloc(n_x*n_y*sizeof(fftw_complex));
compc = (fftw_complex*) fftw_malloc(n_x*n_y*sizeof(fftw_complex));
eta = (fftw_complex*) fftw_malloc(n_x*n_y*sizeof(fftw_complex));

/* Generating initial composition profile */
/*opening the two files that contains the composition information from previous runs*/

fir = fopen("composition file","r"); /* Left Hand side */
fin = fopen("readf","r");    /* Right Hand side */
for(i=0;i<n_x;i++){
for(j=0;j<n_y;j++){

/* For the left hand side of the couple */

if(i%2==0){
fscanf(fir,"%d%d%lf%lf%lf%lf",&t1,&t2,&(compa[j+n_y*i][0]),&(compb[j+n_y*i][0]),&(compc[j+n_y*i][0]),&(eta[j+n_y*i][0]));

compa[j+n_y*i][1] = 0.0;
compb[j+n_y*i][1] = 0.0;
```

```c
compc[j+n_y*i][1] = 0.0;
eta[j+n_y*i][1] = 0.0;
}
else
{
fscanf(fin,"%d%d%lf%lf%lf%lf",&t1,&t2,&(compa[j+n_y*i][0]),&(compb[j+n_y*i][0]),&(compc[j+n_y*i][0]),&(eta[j+n_y*i][0]));

compa[j+n_y*i][1] = 0.0;
compb[j+n_y*i][1] = 0.0;
compc[j+n_y*i][1] = 0.0;
eta[j+n_y*i][1] = 0.0;
}
}
}
fclose(fir);
fclose(fin);

/*
 Write comp  values to file
*/
if((fpw=fopen("readcomp","w"))==NULL){
printf("Unable to open output/README. Exiting");
exit(0);
}
else{
fpw = fopen("readcomp","w");
}

for(i=0; i<n_y; ++i){
for(j=0; j<n_x; ++j){
fprintf(fpw,"%d\t%d\t%lf\t%lf\t%lf\t%lf\n",i,j,compa[j+512*i][0],compb[j+512*i][0],compc[j+512*i][0],eta[j+512*i][0]);
}
}
(void) fclose(fpw);

/* release the allocated memory */
fftw_free(compa);
fftw_free(compb);
fftw_free(compc);
fftw_free(eta);
return 0;
}
```

```
/*
This program is used as the main program for part-2. This generates the initial
microstructure for alloys of different compositions and volume fractions of phases
by reading data file "readcomp" generated by couple.c. It reads the input files in
input/ directory. Generates the nuclei randomly and calls evolute.c program for
microstructure evolution.
*/
#include<stdio.h>
#include<stdlib.h>
#include<math.h>
#include</sw/include/fftw3.h>
#include"../headers/functions.h"

int main(void){

FILE *fpr, *fpw, *fir;
int i,j,t1,t2;
int n_x,n_y,time_steps;
double del_x,del_y,del_t;
double kapa_a,kapa_b,kapa_c,kapa_e,M_aa,M_ab,M_ba,M_bb;

fftw_complex *compa;
fftw_complex *compb;
fftw_complex *compc;
fftw_complex *eta;

/* Get rid of old files in output directory */
 (void) system("rm -rf output/*");

/*Write input values to README file*/
if((fpw=fopen("output/README","w"))==NULL){
printf("Unable to open output/README. Exiting");
exit(0);
}
else{
fpw = fopen("output/README","w");
}

/* read input values from read_input_values file */
if( (fpr = fopen("input/syssize","r")) == NULL){
printf("Unable to open input/syssize. Exiting");
exit(0);
}
else{
```

```c
fpr = fopen("input/syssize","r");
}
(void) fscanf(fpr,"%d%d%le%le",&n_x,&n_y,&del_x,&del_y);
(void) fclose(fpr);
fprintf(fpw,"n_x = %d\nn_y = %d\n",n_x,n_y);
fprintf(fpw,"del_x = %le\ndel_y = %le\n",del_x,del_y);

/* Read the PFM constants */
if( (fpr = fopen("input/constants","r")) == NULL){
printf("Unable to oepn input/constants. Exiting");
exit(0);
}
else{
fpr = fopen("input/constants","r");
}
(void) fscanf(fpr,"%le%le%le%le",&kapa_a,&kapa_b,&kapa_c,&kapa_e);
(void) fclose(fpr);
fprintf(fpw,"kapa_a = %le\nkapa_b = %le\nkapa_c = %le\nkapa_e =
%le\n",kapa_a,kapa_b,kapa_c,kapa_e);

/*Read the time step and number of time steps*/
if( (fpr = fopen("input/timeinf","r")) == NULL){
printf("Unable to open input/timeinf. Exiting");
exit(0);
}
else{
fpr = fopen("input/timeinf","r");
}
(void) fscanf(fpr,"%le%d",&del_t,&time_steps);
(void) fclose(fpr);
fprintf(fpw,"del_t = %le\n",del_t);
fprintf(fpw,"time_steps = %d\n",time_steps);
fclose(fpw);

/*Memory allocation for variable comp */
compa = (fftw_complex*) fftw_malloc(n_x*n_y*sizeof(fftw_complex));
compb = (fftw_complex*) fftw_malloc(n_x*n_y*sizeof(fftw_complex));
compc = (fftw_complex*) fftw_malloc(n_x*n_y*sizeof(fftw_complex));
eta = (fftw_complex*) fftw_malloc(n_x*n_y*sizeof(fftw_complex));

/* Generating the initial composition profile and eta values */
fir = fopen("readcomp","r");
for(i=0;i<n_x;i++){
for(j=0;j<n_y;j++){

fscanf(fir,"%d%d%lf%lf%lf%lf",&t1,&t2,&(compa[j+n_y*i][0]),&(compb[j+n_y*i][0]),&(com
```

```c
    pc[j+n_y*i][0]),&(eta[j+n_y*i][0]));
    compa[j+n_y*i][1] = 0.0;
    compb[j+n_y*i][1] = 0.0;
    compc[j+n_y*i][1] = 0.0;
    eta[j+n_y*i][1] = 0.0;
    }
    }
    fclose(fir);

    /* Evolution of Microstructure */
    evolute(n_x,n_y,del_x,del_y,del_t,time_steps,kapa_a,kapa_b,kapa_c,kapa_e,M_aa,M_ab,M_ba,
    M_bb,compa,compb,compc,eta);

    /* release the allocated memory */
    fftw_free(compa);
    fftw_free(compb);
    fftw_free(compc);
    fftw_free(eta);
    return 0;
    }
```

evolute.c

```c
/*
This program evolves the microstructure by solving the Cahn-Hilliard and Allen-Cahn equations.
It uses fftw and invovles numerous manipulations to represent the variables in proper form,
which is compatible for fftw.
*/

#include <stdio.h>
#include <stdlib.h>
#include <math.h>
#define R 8.314
#define T 1473.0

#include <gsl/gsl_math.h>
#include</sw/include/fftw3.h>

#include "../headers/functions.h"

void evolute(int n_x,int n_y,double del_x,double del_y,double del_t,int time_steps,double
kapa_a, double kapa_b,double kapa_c,double kapa_e,double M_aa,double M_ab,double
M_ba,double M_bb,fftw_complex *compa,fftw_complex *compb,fftw_complex *compc,
fftw_complex *eta){
FILE *fp,*fpw;
char fn[200];
char NAME[1000];
char name[1000];
int INDEX=0;
int i,j,p;
int half_nx, half_ny;
double kx,ky,kx2,ky2,del_kx,del_ky,k2,k4;
double G0a,G0b,G0c,fccL0_ab,fccL0_ac;
double fccL1_ac,fccL2_ac,fccL0_bc,fccL1_bc,fccL0_abc;
double logariR1,logariR2,logariC1,logariC2,amincLacR,amincLacC;   /* Self defined functions
for ga and gb */
double acR,acC,acamincR,acamincC,bbmincR,bbmincC,bcR,bcC,bamincR;   /* Self defined
functions for ga and gb */
double bamincC,aLacR,aLacC,bmincLR,bmincLC,abmincR,abmincC;       /* Self defined
functions for ga and gb */
double z00,z01,z02,z03,z04,z10,z11,z12,z13,z20,z21,z22,z30,z31,z40,A4;
double casqR,caqR,ca4R,ca_cbR,cbcasqR,cbcaqR,cbsqR,cacbsqR,casq_cbsqR,cbqR,cacbqR,
cb4R;
double casqC,caqC,ca4C,ca_cbC,cbcasqC,cbcaqC,cbsqC,cacbsqC,casq_cbsqC,cbqC,cacbqC,
cb4C;
double etasqR,etasqC,etaqR,etaqC,determin,denome;
double delf,A2R,A2C,dA2_dcaR,dA2_dcaC,dA2_dcbR,dA2_dcbC;
```

```c
double *ca, *cb, *cc, *e;
double term_aR,term_aC,term_bR,term_bC,phi_aa,phi_ab,phi_ba,phi_bb,phie,L;
double A,B,C,D,termgaR,termgaC,termgbR,termgbC;
double Vm,beta_a, beta_b, beta_c, beta, beta_ag, beta_bg, beta_cg;
double Al0, Al1, Al2, Cr0, Cr1, Cr2, Ni0, Ni1, Ni2, QAl, QCr, QNi;
double oAl0, oAl1, oAl2, oCr0, oCr1, oCr2, oNi0, oNi1, oNi2;
double mfunc, betaA, betaB, betaC;
double gamaAl = 0.152, gamaCr = 0.219, betaAl = 0.316, betaCr = 0.092;
size_t otpter;

fftw_complex *ga;
fftw_complex *gb;
fftw_complex *ge;

fftw_plan planaf, planbf, planef, planga, plangb, plange, planab, planbb, planeb;

/* Memory Allocation */

ga = (fftw_complex*) fftw_malloc(n_x*n_y*sizeof(fftw_complex));
gb = (fftw_complex*) fftw_malloc(n_x*n_y*sizeof(fftw_complex));
ge = (fftw_complex*) fftw_malloc(n_x*n_y*sizeof(fftw_complex));

/* Define the Plans for FFTW */

planaf = fftw_plan_dft_2d(n_x,n_y,compa,compa,FFTW_FORWARD,FFTW_ESTIMATE);
planbf = fftw_plan_dft_2d(n_x,n_y,compb,compb,FFTW_FORWARD,FFTW_ESTIMATE);
planef = fftw_plan_dft_2d(n_x,n_y,eta,eta,FFTW_FORWARD,FFTW_ESTIMATE);
planga = fftw_plan_dft_2d(n_x,n_y,ga,ga,FFTW_FORWARD,FFTW_ESTIMATE);
plangb = fftw_plan_dft_2d(n_x,n_y,gb,gb,FFTW_FORWARD,FFTW_ESTIMATE);
plange = fftw_plan_dft_2d(n_x,n_y,ge,ge,FFTW_FORWARD,FFTW_ESTIMATE);
planab = fftw_plan_dft_2d(n_x,n_y,compa,compa,FFTW_BACKWARD,FFTW_ESTIMATE);
planbb = fftw_plan_dft_2d(n_x,n_y,compb,compb,FFTW_BACKWARD,FFTW_ESTIMATE);
planeb = fftw_plan_dft_2d(n_x,n_y,eta,eta,FFTW_BACKWARD,FFTW_ESTIMATE);


/* Memory allocation for composition and eta variables */

ca = (double *) malloc((size_t) n_x*n_y* sizeof(double));
cb = (double *) malloc((size_t) n_x*n_y* sizeof(double));
cc = (double *) malloc((size_t) n_x*n_y* sizeof(double));
e = (double *) malloc((size_t) n_x*n_y* sizeof(double));

/* print the initial composition */

INDEX = 0;
for(i=0; i<n_x; ++i){
```

```c
for(j=0; j<n_y; ++j){
        p = j + n_y*i;
        ca[p] = (compa[p][0]-gamaAl)/(betaAl-gamaAl);
        cb[p] = (compb[p][0]-gamaCr)/(betaCr-gamaCr);
        cc[p] = 1.0-compa[p][0]-compb[p][0];
        e[p] = eta[p][0];
}
}
sprintf(NAME,"output/time%d.dat",INDEX);
fpw = fopen(NAME,"w");
otpter = fwrite(&e[0],sizeof(double),(size_t) n_x*n_y,fpw);
(void) fclose(fpw);
sprintf(name,"time0%d.ps",INDEX);
generate_psfile(NAME,name,n_x,n_y,n_y);

/* Data for fcc-disordered (gama phase)*/

fccL0_ab = -45000+6.0*T;
fccL0_ac = -168343 + 16.0*T;
fccL1_ac = 34311.0;
fccL2_ac = 4162.0 + 27.29*T;
fccL0_bc = 8030.0 - 12.8801*T;
fccL1_bc = 33080.0 - 16.0362*T;
fccL0_abc = -853.0 + 16.245*T;

G0a = -11278.378+188.684153*T-31.748192*T*log(T)-1.231e28*pow(T,-9);
G0b = -1572.94+157.643*T-26.908*T*log(T)+0.00189435*T*T-1.47721e-
6*pow(T,3)+139250/T;
G0c = -5179.159+117.854*T-22.096*T*log(T)-4.8407e-6*pow(T,2);

/**********Coefficients for A2 calculation****************/
delf = 6949.46;
A4 = 4.0;
z00 = -102.12685;
z01 = 1155.43;
z02 = -4897.04;
z03 = 9332.91;
z04 = -6647.69;
z10 = 10.92678;
z11 = -296.89049;
z12 = 1489.57;
z13 = -1937.45;
z20 = 253.57483;
z21 = -1032.66;
z22 = 808.6688;
z30 = -259.04708;
```

```
z31 = 564.16582;
z40 = 45.79865;
/*
 Data for Atomic Mobility of gamma phase
 Fixed Parameter from literature
*/
Al0 = -142000.0 + R * T * log(0.000171);
Al1 = -235000.0 - 82.0 * T;
Al2 = -284000.0 + R * T * log(0.00075);
Cr0 = -261700.0 + R * T * log(0.64);
Cr1 = -235000.0 - 82.0 * T;
Cr2 = -287000.0 - 64.4 * T;
Ni0 = -145900.0 + R * T * log(0.00044);
Ni1 = -235000.0 - 82.0 * T;
Ni2 = -287000.0 - 69.8 * T;
/* Optimized Parameters from literature */
oAl0 = -41300.0 - 91.2 * T;
oAl1 = 335000.0;
oAl2 = -53200.0;
oCr0 = -118000.0;
oCr1 = -487000.0;
oCr2 = -68000.0;
oNi0 = -113000.0 + 65.5 * T;
oNi1 = -211000.0;
oNi2 = -81000.0;
for(INDEX=1; INDEX < time_steps+1; ++INDEX){

printf("Steps = %d\n", INDEX);
for(i=0; i<n_x; ++i){
for(j=0; j<n_y; ++j){
      p = j + n_y*i;
      ca[p] = compa[p][0];
      cb[p] = compb[p][0];
      cc[p] = 1.0-compa[p][0]-compb[p][0];
      e[p] = eta[p][0];
}
}

/** To calculate ga, gb and ge in Real Space. They are all nondimensionalized by dividing with
R*T**/

for(i=0; i<n_x; ++i){
for(j=0; j<n_y; ++j){

p = j + n_y*i;
casqR = (compa[p][0]*compa[p][0])-(compa[p][1]*compa[p][1]);
```

casqC = 2.0*compa[p][0]*compa[p][1];
cbsqR = (compb[p][0]*compb[p][0])-(compb[p][1]*compb[p][1]);
cbsqC = 2.0*compb[p][0]*compb[p][1];
caqR = (compa[p][0]*compa[p][0]*compa[p][0])-3.0*(compa[p][0]*compa[p][1]*compa[p][1]);
caqC = -
(compa[p][1]*compa[p][1]*compa[p][1])+3.0*(compa[p][0]*compa[p][0]*compa[p][1]);
cbqR = (compb[p][0]*compb[p][0]*compb[p][0])-
3.0*(compb[p][0]*compb[p][1]*compb[p][1]);
cbqC = -
(compb[p][1]*compb[p][1]*compb[p][1])+3.0*(compb[p][0]*compb[p][0]*compb[p][1]);
ca4R = casqR*casqR - casqC*casqC;
ca4C = 2.0*casqC*casqR;
cb4R = cbsqR*cbsqR - cbsqC*cbsqC;
cb4C = 2.0*cbsqC*cbsqR;
ca_cbR = compa[p][0]*compb[p][0]-compa[p][1]*compb[p][1];
ca_cbC = compa[p][0]*compb[p][1]+compa[p][1]*compb[p][0];
casq_cbsqR = casqR*cbsqR-casqC*cbsqC;
casq_cbsqC = cbsqC*casqR+casqC*cbsqR;
cacbsqR = compa[p][0]*cbsqR-cbsqC*compa[p][1];
cacbsqC = compa[p][0]*cbsqC+cbsqR*compa[p][1];
cbcasqR = compb[p][0]*casqR-casqC*compb[p][1];
cbcasqC = compb[p][0]*casqC+casqR*compb[p][1];
cacbqR = compa[p][0]*cbqR-compa[p][1]*cbqC;
cacbqC = compa[p][0]*cbqC+compa[p][1]*cbqR;
cbcaqR = compb[p][0]*caqR-compb[p][1]*caqC;
cbcaqC = compb[p][0]*caqC+compb[p][1]*caqR;

etasqR = (eta[p][0]*eta[p][0])-(eta[p][1]*eta[p][1]);
etasqC = 2.0*eta[p][0]*eta[p][1];
etaqR = (eta[p][0]*eta[p][0]*eta[p][0])-3.0*(eta[p][0]*eta[p][1]*eta[p][1]);
etaqC = -(eta[p][1]*eta[p][1]*eta[p][1])+3.0*(eta[p][0]*eta[p][0]*eta[p][1]);

A2R =
z00+z01*compa[p][0]+z02*casqR+z03*caqR+z04*ca4R+z10*compb[p][0]+z11*ca_cbR+z12*
cbcasqR+z13*cbcaqR+z20*cbsqR+z21*cacbsqR+z22*casq_cbsqR+z30*cbqR+z31*cacbqR+z4
0*cb4R;

A2C =
z01*compa[p][1]+z02*casqC+z03*caqC+z04*ca4C+z10*compb[p][1]+z11*ca_cbC+z12*cbcas
qC+z13*cbcaqC+z20*cbsqC+z21*cacbsqC+z22*casq_cbsqC+z30*cbqC+z31*cacbqC+z40*cb4
C;

dA2_dcaR =
z01+2.0*z02*compa[p][0]+3.0*z03*casqR+4.0*z04*caqR+z11*compb[p][0]+2.0*z12*ca_cbR
+3.0*z13*cbcasqR+z21*cbsqR+2.0*z22*cacbsqR+z31*cbqR;

dA2_dcaC =
2.0*z02*compa[p][1]+3.0*z03*casqC+4.0*z04*caqC+z11*compb[p][1]+2.0*z12*ca_cbC+3.0*z13*cbcasqC+z21*cbsqC+2.0*z22*cacbsqC+z31*cbqC;

dA2_dcbR =
z10+z11*compa[p][0]+z12*casqR+z13*caqR+2.0*z20*compb[p][0]+2.0*z21*ca_cbR+2.0*z22*cbcasqR+3.0*z30*cbsqR+3.0*z31*cacbsqR+4.0*z40*cbqR;

dA2_dcbC =
z11*compa[p][1]+z12*casqC+z13*caqC+2.0*z20*compb[p][1]+2.0*z21*ca_cbC+2.0*z22*cbcasqC+3.0*z30*cbsqC+3.0*z31*cacbsqC+4.0*z40*cbqC;

logariR1 = 0.5*(log((compa[p][0]*compa[p][0])+(compa[p][1]*compa[p][1]))-log((1.0-compa[p][0]-compb[p][0])*(1.0-compa[p][0]-compb[p][0])+(compa[p][1]+compb[p][1])*(compa[p][1]+compb[p][1])));/* logari are the real and complex parts of log terms */

logariC1 = atan(compa[p][1]/compa[p][0])-atan((compa[p][1]+compb[p][1])/(compa[p][0]+compb[p][0]-1.0));

logariR2 = 0.5*(log((compb[p][0]*compb[p][0])+(compb[p][1]*compb[p][1]))-log((1.0-compa[p][0]-compb[p][0])*(1.0-compa[p][0]-compb[p][0])+(compa[p][1]+compb[p][1])*(compa[p][1]+compb[p][1])));

logariC2 = atan(compb[p][1]/compb[p][0])-atan((compa[p][1]+compb[p][1])/(compa[p][0]+compb[p][0]-1.0));

amincLacR = -fccL0_ac*(2.0*compa[p][0]+compb[p][0]-1.0) -
fccL1_ac*((2.0*compa[p][0]+compb[p][0]-1.0)*(2.0*compa[p][0]+compb[p][0]-1.0)-(2.0*compa[p][1]+compb[p][1])*(2.0*compa[p][1]+compb[p][1]))-
fccL2_ac*(2.0*compa[p][0]+compb[p][0]-1.0)*((2.0*compa[p][0]+compb[p][0]-1.0)*(2.0*compa[p][0]+compb[p][0]-1.0)-3.0*(2.0*compa[p][1]+compb[p][1])); /* This part is = real((cc - ca)Lac) */

amincLacC = -
(2.0*compa[p][1]+compb[p][1])*(fccL0_ac+2.0*fccL1_ac*(2.0*compa[p][0]+compb[p][0]-1.0)+fccL2_ac*(3.0*(2.0*compa[p][0]+compb[p][0]-1.0)*(2.0*compa[p][0]+compb[p][0]-1.0)-(2.0*compa[p][1]+compb[p][1])*(2.0*compa[p][1]+compb[p][1])));/* = complex((cc - ca)Lac) */

acR = compa[p][0]*(1.0-compa[p][0]-compb[p][0]) + compa[p][1]*(compa[p][1]+compb[p][1]);
/* = real(ca*cc) */

acC = compa[p][1]*(1.0-compa[p][0]-compb[p][0]) - compa[p][0]*(compa[p][1]+compb[p][1]);
/* = complex(ca*cc) */

```
acamincR = (compa[p][0]*(1.0-compa[p][0]-compb[p][0]) +
compa[p][1]*(compa[p][1]+compb[p][1]))*(2.0*compa[p][0]+compb[p][0]-1.0)-
(compa[p][1]*(1.0-compa[p][0]-compb[p][0]) -
compa[p][0]*(compa[p][1]+compb[p][1]))*(2.0*compa[p][1]+compb[p][1]); /* =real(ac(a-c)) */

acamincC = (compa[p][1]*(1.0-compa[p][0]-compb[p][0]) -
compa[p][0]*(compa[p][1]+compb[p][1]))*(2.0*compa[p][0]+compb[p][0]-
1.0)+(compa[p][0]*(1.0-compa[p][0]-compb[p][0]) +
compa[p][1]*(compa[p][1]+compb[p][1]))*(2.0*compa[p][1]+compb[p][1]);
/* =complex(ac(a-c)) */

bbmincR = compb[p][0]*(2.0*compb[p][0]+compa[p][0]-1.0)-
compb[p][1]*(2.0*compb[p][1]+compa[p][1]); /* = real(cb(cb-cc)) */

bbmincC = (4.0*compb[p][0]+compa[p][0]-1.0)*compb[p][1] + compa[p][1]*compb[p][0];
/* = complex(cb(cb-cc)) */

bcR = compb[p][0]*(1.0-compa[p][0]-compb[p][0]) +
compb[p][1]*(compa[p][1]+compb[p][1]);  /* = real(cb*cc) */

bcC = compb[p][1]*(1.0-compa[p][0]-compb[p][0]) - compb[p][0]*(compa[p][1]+compb[p][1]);
/* = complex(cb*cc) */

bamincR = compb[p][0]*(2.0*compa[p][0]+compb[p][0]-1.0)-
compb[p][1]*(2.0*compa[p][1]+compb[p][1]); /* = real(cb(ca-cc)) */

bamincC = compb[p][1]*(2.0*compa[p][0]+compb[p][0]-1.0)-
compb[p][0]*(2.0*compa[p][1]+compb[p][1]); /* = complex(cb(ca-cc)) */

aLacR =  fccL0_ac*compa[p][0]+fccL1_ac*(compa[p][0]*(2.0*compa[p][0]+compb[p][0]-1.0)-
compa[p][1]*(2.0*compa[p][1]+compb[p][1]))+fccL2_ac*(compa[p][0]*((2.0*compa[p][0]+co
mpb[p][0]-1.0)*(2.0*compa[p][0]+compb[p][0]-1.0)-
(2.0*compa[p][1]+compb[p][1])*(2.0*compa[p][1]+compb[p][1]))-
2.0*compa[p][1]*(2.0*compa[p][0]+compb[p][0]-1.0)*(2.0*compa[p][1]+compb[p][1]));
/* = real(ca)Lac) */

aLacC =  fccL0_ac*compa[p][1]+fccL1_ac*(compa[p][1]*(2.0*compa[p][0]+compb[p][0]-
1.0)+compa[p][0]*(2.0*compa[p][1]+compb[p][1]))+fccL2_ac*(compa[p][1]*((2.0*compa[p][0
]+compb[p][0]-1.0)*(2.0*compa[p][0]+compb[p][0]-1.0)-
(2.0*compa[p][1]+compb[p][1])*(2.0*compa[p][1]+compb[p][1]))+2.0*compa[p][0]*(2.0*com
pa[p][0]+compb[p][0]-1.0)*(2.0*compa[p][1]+compb[p][1]));  /* = complex(ca)Lac) */

bmincLR = -fccL0_bc*(2.0*compb[p][0]+compa[p][0]-1.0)-
fccL1_bc*((2.0*compb[p][0]+compa[p][0]-1.0)*(2.0*compb[p][0]+compa[p][0]-1.0)-
(2.0*compb[p][1]+compa[p][1])*(2.0*compb[p][1]+compa[p][1])); /* =real(-(cb-cc))*/
```

```
bmincLC = -fccL0_ac*(2.0*compb[p][1]+compa[p][1]) -
2.0*fccL1_bc*(2.0*compb[p][0]+compa[p][0]-1.0)*(2.0*compb[p][1]+compa[p][1]);
/* =complex(-(cb-cc))*/

abmincR = compa[p][0]*(2.0*compb[p][0]+compa[p][0]-1.0)-
compa[p][1]*(2.0*compb[p][1]+compa[p][1]); /* =real(ca(cb-cc))*/

abmincC = compa[p][1]*(2.0*compb[p][0]+compa[p][0]-
1.0)+compa[p][0]*(2.0*compb[p][1]+compa[p][1]); /* =complex(ca(cb-cc))*/

ga[p][0] = G0a-G0c+R*T*logariR1 + (fccL0_ab - fccL0_bc)*compb[p][0] + amincLacR +
2.0*fccL1_ac*acR + 4.0*fccL2_ac*acamincR - fccL1_bc*bbmincR + fccL1_bc*bcR -
bamincR*fccL0_abc - 0.5*(dA2_dcaR*etasqR-dA2_dcaC*etasqC)*delf;

ga[p][0] = ga[p][0]/delf;

ga[p][1] = R*T*logariC1 + (fccL0_ab - fccL0_bc)*compb[p][1] + amincLacC +
2.0*fccL1_ac*acC + 4.0*fccL2_ac*acamincC - fccL1_bc*bbmincC + fccL1_bc*bcC -
bamincC*fccL0_abc - 0.5*(dA2_dcaC*etasqR+dA2_dcaR*etasqC)*delf;

ga[p][1] = ga[p][1]/delf;

gb[p][0] = G0b-G0c+R*T*logariR2+fccL0_ab*compa[p][0]-
aLacR+fccL1_ac*acR+2.0*fccL2_ac*acamincR+bmincLR+2.0*fccL1_bc*bcR+abmincR*fccL
0_abc - 0.5*(dA2_dcbR*etasqR-dA2_dcbC*etasqC)*delf;

gb[p][0] = gb[p][0]/delf;

gb[p][1] = R*T*logariC2+fccL0_ab*compa[p][1]-
aLacC+fccL1_ac*acC+2.0*fccL2_ac*acamincC+bmincLC+2.0*fccL1_bc*bcC+abmincC*fccL
0_abc - 0.5*(dA2_dcbC*etasqR+dA2_dcbR*etasqC)*delf;

gb[p][1] = gb[p][1]/delf;

ge[p][0] = (-(A2R*eta[p][0]-A2C*eta[p][1]) + A4*etaqR);

ge[p][1] = (-(A2R*eta[p][1]+A2C*eta[p][0]) + A4*etaqC);
}
}
/* calculation of atomic mobility and chemical mobility */
Vm = 12.0e-6;
beta_a = 1.2e-17;
beta_b = 2.0e-17;
beta_c = 6.0e-17;
beta = 1.0e-18;
```

```
/* Evolve the microstructure with time */
half_nx = (int) n_x/2;
half_ny = (int) n_y/2;
del_kx = (2.0*M_PI)/(n_x*del_x);
del_ky = (2.0*M_PI)/(n_y*del_y);

/* Take composition,eta, ga,gb and ge to the Fourier Space */

fftw_execute(planaf);
fftw_execute(planbf);
fftw_execute(planef);
fftw_execute(planga);
fftw_execute(plangb);
fftw_execute(plange);

phi_aa = 2.0*(kapa_a+kapa_c);
phi_ab = 2.0*(kapa_c+kapa_c);
phi_ba = 2.0*(kapa_c+kapa_c);
phi_bb = 2.0*(kapa_b+kapa_c);
phie = 2.0*kapa_e;

for(i=0; i < n_x; ++i){
        if(i < half_nx) kx = i*del_kx;
        else kx = (i-n_x)*del_kx;
        kx2 = kx*kx;
for(j=0; j<n_y; ++j){
        if(j < half_ny) ky = j*del_ky;
        else ky = (j-n_y)*del_ky;
        ky2 = ky*ky;
        k2 = kx2 + ky2;
        k4 = k2*k2;
        L = 1.0;
        p = j + n_y*i;

/* Chemical mobility calculation. Here I did not use Ma =  beta_a*ca. Instead Ma=beta_a. Each
Mij values are nondmensionalized */

        QAl = ca[p] * Al0 + cb[p] * Al1 + (1.0 - ca[p] - cb[p]) * Al2 + ca[p] * (1.0 - ca[p] - cb[p])
* oAl0 + ca[p] * cb[p] * oAl1 + cb[p] * (1.0 - ca[p] - cb[p]) * oAl2;

        QCr = ca[p] * Cr0 + cb[p] * Cr1 + (1.0 - ca[p] - cb[p]) * Cr2 + ca[p] * (1.0 - ca[p] - cb[p])
* oCr0 + ca[p] * cb[p] * oCr1 + cb[p] * (1.0 - ca[p] - cb[p]) * oCr2;

        QNi = ca[p] * Ni0 + cb[p] * Ni1 + (1.0 - ca[p] - cb[p]) * Ni2 + ca[p] * (1.0 - ca[p] - cb[p])
* oNi0 + ca[p] * cb[p] * oNi1 + cb[p] * (1.0 - ca[p] - cb[p]) * oNi2;
```

```
/* Atomic mobilities calculation from Activation Energies*/
        beta_ag = (1.0/(R * T)) * exp(QAl/(R * T));
        beta_bg = (1.0/(R * T)) * exp(QCr/(R * T));
        beta_cg = (1.0/(R * T)) * exp(QNi/(R * T));

        mfunc = exp(10.0*(e[p]*e[p]-0.3))/(exp(10.0*(e[p]*e[p]-0.3))+exp(-10.0*(e[p]*e[p]-
0.3)));

        betaA = beta_ag + mfunc * (beta_a - beta_ag);
        betaB = beta_bg + mfunc * (beta_b - beta_bg);
        betaC = beta_cg + mfunc * (beta_c - beta_cg);

        M_aa = (betaA*(1.0-ca[p])*(1.0-ca[p])+betaB*ca[p]*ca[p]+betaC*ca[p]*ca[p])/beta;
        M_ab = (-betaA*(1.0-ca[p])*cb[p]-betaB*(1.0-cb[p])*ca[p]+betaC*ca[p]*cb[p])/beta;
        M_ba = (-betaA*(1.0-ca[p])*cb[p]-betaB*(1.0-cb[p])*ca[p]+betaC*ca[p]*cb[p])/beta;
        M_bb = (betaB*(1.0-cb[p])*(1.0-cb[p])+betaA*cb[p]*cb[p]+betaC*cb[p]*cb[p])/beta;

        A = M_aa*phi_aa+M_ab*phi_ba;
        B = M_aa*phi_ab+M_ab*phi_bb;
        C = M_ba*phi_aa+M_bb*phi_ba;
        D = M_ba*phi_ab+M_bb*phi_bb;

        determin = 1.0+k4*del_t*(A+D)+k4*k4*del_t*del_t*(A*D-B*C);
        denome = 1.0 + phie*k2*L*del_t;

        termgaR = compa[p][0]-k2*del_t*(M_aa*ga[p][0]+M_ab*gb[p][0]);
        termgaC = compa[p][1]-k2*del_t*(M_aa*ga[p][1]+M_ab*gb[p][1]);
        termgbR = compb[p][0]-k2*del_t*(M_ba*ga[p][0]+M_bb*gb[p][0]);
        termgbC = compb[p][1]-k2*del_t*(M_ba*ga[p][1]+M_bb*gb[p][1]);

        term_aR = (1.0+k4*del_t*D)*termgaR-k4*del_t*B*termgbR;
        term_aC = (1.0+k4*del_t*D)*termgaC-k4*del_t*B*termgbC;
        term_bR = (1.0+k4*del_t*A)*termgbR-k4*del_t*C*termgaR;
        term_bC = (1.0+k4*del_t*A)*termgbC-k4*del_t*C*termgaC;

        compa[p][0] = term_aR/determin;
        compa[p][1] = term_aC/determin;
        compb[p][0] = term_bR/determin;
        compb[p][1] = term_bC/determin;
        eta[p][0] = (eta[p][0]-del_t*L*ge[p][0])/denome;
        eta[p][1] = (eta[p][1]-del_t*L*ge[p][1])/denome;
    }
}

/* Now get the composition and eta back to real space */
```

```c
fftw_execute(planab);
fftw_execute(planbb);
fftw_execute(planeb);

for(i=0; i< n_x; ++i){
for(j=0; j< n_y; ++j){
p = j + n_y*i;
compa[p][0] = compa[p][0]/(n_x*n_y);
compa[p][1] = compa[p][1]/(n_x*n_y);
compb[p][0] = compb[p][0]/(n_x*n_y);
compb[p][1] = compb[p][1]/(n_x*n_y);
eta[p][0] = eta[p][0]/(n_x*n_y);
eta[p][1] = eta[p][1]/(n_x*n_y);
compc[p][0] = 1.0-compa[p][0]-compb[p][0];
}
}
/******** Write the composition data to files ***************/
if((INDEX==1)||(INDEX%1000==0))
{
sprintf(fn,"output/composition%d",INDEX);
fp = fopen(fn,"w");

for(i=0; i< n_x; ++i){
for(j=0; j< n_y; ++j){
p = j + n_y*i;
fprintf(fp,"%d\t%d\t%lf\t%lf\t%lf\t%lf\n",i,j,compa[p][0],compb[p][0],compc[p][0],eta[p][0]);
}
}
fclose(fp);
}
(void)system("rm -rf output/*.dat");
}
/* Release the memory */
fftw_free(ga);
fftw_free(gb);
fftw_free(ge);
fftw_destroy_plan(planaf);
fftw_destroy_plan(planbf);
fftw_destroy_plan(planef);
fftw_destroy_plan(planga);
fftw_destroy_plan(plangb);
fftw_destroy_plan(plange);
fftw_destroy_plan(planab);
fftw_destroy_plan(planbb);
fftw_destroy_plan(planeb);
}
```

Makefile

COMPOPS = -g -Wall
LINKOPS = -L/sw/lib -lgsl -lgslcblas -lfftw3 -lm

Object files

objects = diffcoup.o evolute.o

Header files

headers = stdio.h stdlib.h math.h gsl_rng.h fftw3.h functions.h

Source files (Replace diffcoup.c by frmnucli.c for part-1)

sources = diffcoup.c evolute.c

Paths for the source and header files

vpath %.c src
vpath %.h ./headers
vpath %.h /sw/lib/gcc-lib/i386-apple-darwin8/4.0.3/lib/gcc/i386-apple-darwin8.9.2/4.0.3/include
vpath %.h /usr/include/
vpath %.h /sw/include/
vpath %.h /usr/local/include/gsl

Dependencies and the actions on the source files
diffcoup.c: $(objects) $(headers)
	gcc $(objects) $(LINKOPS)
	rm -rf nohup.out

diffcoup.o: $(sources) $(headers)
	gcc -o $@ -c ./src/diffcoup.c $(COMPOPS)

evolute.o: evolute.c stdio.h stdlib.h math.h gsl_math.h fftw3.h functions.h
	gcc -c $(COMPOPS) $<

generate_psfile.o: generate_psfile.c stdio.h stdlib.h
	gcc -c $(COMPOPS) $<

clean:
	rm -rf *.o
End of Makefile

APPENDIX C
SAMPLE PYTHON PROGRAM FOR
THERMOTRANSPORT SIMULATIONS IN FIPY

A sample program for thermotransport simulation in a two-phase alloy is provided below. The program is written in the Python programming language and uses the finite volume based Fipy partial differential equation solver to solve the Cahn-Hilliard equation. The initial microstructure for the two-phase alloy is first generated isothermally and then the temperature gradient is applied to it.

```python
#!/usr/bin/env python
## For copyright and other info, go to the end of the file.
## This program is for thermotransport in two-phase alloy with Regular solution model.
## The temperature gradient is applied after the phase transformation.
#
import sys
import random
import fipy.tools.numerix as numerix
import math
import gc
#
#### Here I call All Other Imports that Fipy needs ##############################
#
## Numerix
from fipy.tools.numerix import *
from fipy.tools.numerix import log
from fipy.tools.numerix import sqrt
from fipy.tools.numerix import exp

## Mesh
#from fipy.meshes.numMesh.periodicGrid2D import PeriodicGrid2D
from fipy.meshes.grid2D import Grid2D

## Variables
from fipy.variables.cellVariable import CellVariable
from fipy.variables.histogramVariable import HistogramVariable

## Random numbers
#from fipy.variables.gaussianNoiseVariable import GaussianNoiseVariable
from fipy.tools.numerix import random

## Boundary Conditions
from fipy.boundaryConditions.fixedValue import FixedValue
from fipy.boundaryConditions.fixedFlux import FixedFlux
from fipy.boundaryConditions.nthOrderBoundaryCondition import NthOrderBoundaryCondition
```

```python
## Solvers
from fipy.solvers.linearPCGSolver import LinearPCGSolver
from fipy.solvers.linearLUSolver import LinearLUSolver

## Terms
from fipy.terms.implicitDiffusionTerm import ImplicitDiffusionTerm
from fipy.terms.transientTerm import TransientTerm
from fipy.terms.implicitSourceTerm import ImplicitSourceTerm
from fipy.terms.powerLawConvectionTerm import PowerLawConvectionTerm

## Viewers
from fipy.viewers.tsvViewer import TSVViewer
#
############# Define the Mesh ###############################################
#
L = 80.
nx = 160
ny = 160
dx = L/nx
dy = L/ny
Lx = nx * dx
Ly = nx * dy
frac = 100
points = int((nx * ny * frac)/100)
mesh = Grid2D(dx=dx, dy=dy, nx=nx, ny=ny)
#
############# Define the variables ###########################################
#
comp = CellVariable(name="comp", mesh=mesh, hasOld=1)
temp = CellVariable(name="Temp", mesh=mesh, hasOld=1)
#
c = comp.getArithmeticFaceValue()
T = temp.getArithmeticFaceValue()
#
############# Data for phase-field ###########################################
#
R = 8.314 # J / (mol K)
Tc = 900.
kB = 1.38e-23
W = 20000.0
k = 1.0        # Dimensionized = phi_aa in evolve.c
alpha = 1.0   # Conductivity normalized by its own actual value

### Following constants are for temperature dependent mobility and heat of transport
Da = 0.4e-4   #6.4 (m^2/s)
Db = 6.56e-4  # 0.56(m^2/s)
```

```python
Qa = 250000.0 # (J/mol)
Qb = 229000.0 # (J/mol)
#
x = mesh.getCellCenters()[...,0]
y = mesh.getCellCenters()[...,1]
#
comp = CellVariable(name = "phase-field",mesh = mesh,value = 0.2)
#
######### Introduce Random Particles ######################################
#
from fipy.tools.numerix import random
cenx = zeros(points,int)
ceny = zeros(points,int)
rad = zeros(points,float)
radsq = zeros(points, float)
for i in range(0,points):
        cenx[i] = (random.uniform(0.0,Lx))
        ceny[i] = (random.uniform(0.0,Ly))
        rad = random.normal(0.0,0.2)
        radsq[i] = rad * rad
for q in range(0,points):
        cx = cenx[q]
        cy = ceny[q]
        #print cx
        rsq = radsq[q]
        d = (x - cx) * (x - cx) + (y - cy) * (y - cy)
        comp.setValue(.89, where=(d < rsq))
        c = comp.getArithmeticFaceValue()
if __name__ == '__main__':
                import fipy.viewers
                viewer = fipy.viewers.make(vars = comp, limits = {'datamin': 0., 'datamax': 1.0})
                viewer.plot()


#
############# Double derivative of Free Energy Function ####################
#
d2f_dca2 = (R * Tc / (c * (1. - c)) - 2.0 * W)/(R*Tc)  # Non-dimensionalized by R * T
#
########### Define Mobility and Heat of Transport Terms ##################
#
betaa = (Da / (R * Tc)) * exp(-Qa / (R * Tc))
betab = (Db / (R * Tc)) * exp(-Qb / (R * Tc))
print betaa, betab
Mc = (1.0 - c) * (c * betaa + (1.0 - c) * betab)/betab  # Non-dimensionalized by beta_b
```

```
#
#### Boundary Conditions for Composition Equations #########################
#
BCsC = (FixedFlux(mesh.getFacesRight(), 0),
            FixedFlux(mesh.getFacesLeft(), 0),
            FixedFlux(mesh.getFacesTop(), 0),
            FixedFlux(mesh.getFacesBottom(), 0),
            NthOrderBoundaryCondition(mesh.getFacesLeft(), 0, 3),
            NthOrderBoundaryCondition(mesh.getFacesRight(), 0, 3),
            NthOrderBoundaryCondition(mesh.getFacesTop(), 0, 3),
            NthOrderBoundaryCondition(mesh.getFacesBottom(), 0, 3),
            )
#
#### Final Equations for Phase Transformation ###########################
#
solver = LinearLUSolver(tolerance = 1e-10, iterations = 1000)
#solver = LinearPCGSolver(tolerance = 1e-15,iterations = 1000)

diffTerm = ImplicitDiffusionTerm(coeff = (c * Mc * d2f_dca2))
chTerm = ImplicitDiffusionTerm(coeff = (c * Mc, -k))
compEq = TransientTerm() - diffTerm - chTerm
#
############### Print and Display Composition Distribution #############
#
dt = 1.
for step in range(200):
        comp.updateOld()
        compEq.solve(var=comp, boundaryConditions = BCsC, solver = solver, dt = dt)
        if __name__ == '__main__':
                viewer.plot()
        print 'step',step,'dt',dt
        gc.collect()
#
### Phase Transformation is over. Now apply Thermal Gradient #############
######## Solve Laplace's Eq. for Temperature ##########################
#
BCsT = (FixedValue(mesh.getFacesRight(), 1000),
            FixedValue(mesh.getFacesLeft(), 800),
            FixedFlux(mesh.getFacesTop(), 0),
            FixedFlux(mesh.getFacesBottom(), 0),
            )
solver = LinearLUSolver(tolerance = 1e-10, iterations = 1000)
#solver = LinearPCGSolver(tolerance = 1e-15,iterations = 1000)
tempEq = ImplicitDiffusionTerm(coeff=alpha)
tempEq.solve(var=temp,boundaryConditions=BCsT)
#
```

```python
######Print and Display Initial Composition and Temperature Distribution #############
#
TSVViewer(vars=comp).plot(filename="initdA.tsv")

if __name__ == '__main__':
        viewerT = fipy.viewers.make(vars = temp)
        viewer.plot()
        #viewerT.plot()
#
################# Double derivative of Free Energy Function ####################
#
def d2f_dca2(c,T):
        #return (0.2 / (c * (1. - c)) - 1.)/delf
        return (R * T / (c * (1. - c)) - 2.0 * W)/(R*T)  # Non-dimensionalized by R * T
#
################# Define Mobility and Heat of Transport Terms ##################
##### They are functions of Temperature. So defined here after solving  tempEq ########
#
beta_a = 10.*(Da / (R * T)) * exp(-Qa / (R * T))
beta_b = (Db / (R * T)) * exp(-Qb / (R * T))

Q_BT = (574.0 + 1.0 * T) * 1.e3          # (J/mol) Heat of trans. linear funct of temp
Q_AT = (4.0 - 0.001 * T) * 1.e3          # (J/mol) Heat of trans. linear funct of temp
Mc = (1.0 - c) * (c * beta_a + (1.0 - c) * beta_b)/beta_b # dimensionalized by beta_b
MQ = (beta_a * Q_AT - beta_b * Q_BT) / (R * Tc * beta_b) # dimensionalized by (R*T*beta_b)
#
#################### Final Equations #######################################
#
solver = LinearLUSolver(tolerance = 1e-10, iterations = 1000)
#solver = LinearPCGSolver(tolerance = 1e-15,iterations = 1000)

diffTerm = ImplicitDiffusionTerm(coeff = (c * Mc * d2f_dca2(c,T)))
chTerm = ImplicitDiffusionTerm(coeff = (c * Mc, -k))
velocity = (1. - comp).getHarmonicFaceValue() * MQ * (1./temp).getHarmonicFaceValue() *
temp.getFaceGrad()
convectionTerm = PowerLawConvectionTerm(coeff=velocity,diffusionTerm=diffTerm)
compEq = TransientTerm() - diffTerm - chTerm - convectionTerm

dt = 1.e-1
for step in range(3000):
        comp.updateOld()
        temp.updateOld()
        compEq.solve(var=comp, boundaryConditions = BCsC, solver = solver, dt = dt)
        #compEq.solve(comp, solver = solver, dt = dt)
        tempEq.solve(var=temp,boundaryConditions=BCsT)
        avg = comp.getCellVolumeAverage()
```

```python
        print 'step',step,'dt',dt
        if __name__ == '__main__':
                viewer.plot()
                gc.collect()
#
##################Print the final compositions ###########################
#
TSVViewer(vars=(comp, temp)).plot(filename="finaldA.tsv")
if __name__ == '__main__':
        viewer.plot(filename="micro_caseA.ps")
        viewerT.plot(filename="temp.ps")
def _run():
        pass


##
 # ####################################################################
 #  FiPy - Python-based finite volume PDE solver
 # Stolen from: (The original code was not for thermotransport. The basic frame work for a Fipy
code was borrowed)
 #  Author: Jonathan Guyer, Daniel Wheeler
 #  E-mail: guyer@nist.gov
 #          daniel.wheeler@nist.gov
 #    mail: NIST
 #    www: http://ctcms.nist.gov
 # ====================================================================
 # This software was developed at the National Institute of Standards
 # and Technology by employees of the Federal Government in the course
 # of their official duties.  Pursuant to title 17 Section 105 of the
 # United States Code this software is not subject to copyright
 # protection and is in the public domain.  FiPy is an experimental
 # system.  NIST assumes no responsibility whatsoever for its use by
 # other parties, and makes no guarantees, expressed or implied, about
 # its quality, reliability, or any other characteristic.  We would
 # appreciate acknowledgement if the software is used.
 #
 # This software can be redistributed and/or modified freely
 # provided that any derivative works bear some notice that they are
 # derived from it, and any modified versions bear some notice that
 # they have been modified.
 # ====================================================================
 #  modified   by  R R Mohanty 01/15/08 (4:27:47 PM)
 # ---------- --- --- -----------
 #  2007-07-07 JEG 1.0 original
 # ####################################################################
```

APPENDIX D
APPLICATION OF THERMODYNAMIC AND KINETIC DATABASE FOR REAL ALLOYS INCLUDING Pb-Sn, Ni-Al and U-Zr FOR THERMOTRANSPORT

A general procedure for the phase-field model of thermotransport in real alloy systems such as Pb-Sn, U-Zr and Ni-Al systems is presented below. A description of the Fipy implementation is also provided. The description is currently based on the Pb-Sn system, but it can be easily used for other systems.

Model Description for Pb-Sn System

1 Introduction

This model is to simulate thermotransport effect in two-phase ($\alpha + \beta$) alloys of Pb-Sn system. The simulation involves two steps: first, generate a two-phase microstructure at a constant temperature and then apply a temperature gradient across the system. In this document I am describing the first step, where I am trying to produce a solid state phase transformation to form a two-phase alloy microstructure.

The thermodynamic data for the two phases has been obtained from the literature (CALPHAD approach). The kinetic data (mobility/diffusivity) for the system is not complete in the literature and so some approximations has been made. The materials parameters involve some approximation too.

2 Thermodynamic Description

The following approach was taken to describe the total Gibbs free energy.

$$f = p(\phi)f^\alpha(c,T) + [1-p(\phi)]f^\beta(c,T) + \left[(1-c)\frac{W_A}{2} + c\frac{W_B}{2}\right]g(\phi) \tag{1}$$

where, c is the composition of Sn (B) in mole or atom fraction, W_i are the barrier heights, $p(\phi)$ and $g(\phi)$ are the interpolation and double-well functions respectively. This approach has been described in the Fipy examples (Chapter-9), and is followed here.

The free energies of the α and β phases have the following form:

$$f^{\alpha}(c,T)=cf_{A}^{\alpha}(T)+(1-c)f_{B}^{\alpha}(T)+RT[c\ln(c)+(1-c)\ln(1-c)]+c(1-c)l_{A,B}^{\alpha}(T) \qquad (2)$$

$$f^{\beta}(c,T)=cf_{A}^{\beta}(T)+(1-c)f_{B}^{\beta}(T)+RT[c\ln(c)+(1-c)\ln(1-c)]+c(1-c)l_{A,B}^{\beta}(T) \qquad (3)$$

The free energies are in J/mole, which need to be converted to J/m³. This was achieved by dividing with a molar volume $(V_m(c))$ the relevant terms of the free energy that appear in subsequent equations. The molar volume was calculated by using average density (ρ_{avg}) and average atomic weight (M_{avg}) for Pb-Sn system. Hence, the molar volume is expressed as;

$$V_{m}(c)=\frac{\rho_{avg}}{M_{avg}}10^{3} \qquad (4)$$

$$\rho_{avg}=\frac{\rho_{Pb}*\rho_{Sn}}{\rho_{Sn}-c*(\rho_{Sn}-\rho_{Pb})} \qquad (5)$$

$$M_{avg}=\frac{M_{Pb}*M_{Sn}}{M_{Sn}-c*(M_{Sn}-M_{Pb})} \qquad (6)$$

3 Phase-field Formulation

The general phase-field governing equations for composition and the phase-field variable are written as;

$$\frac{\partial c}{\partial t}=V_{m}^{2}(c)\nabla\cdot\left[M(c)\nabla\left(\frac{\partial f}{\partial c}-\kappa\nabla^{2}c\right)\right] \qquad (7)$$

$$\frac{\partial\phi}{\partial t}=M_{\phi}\left[\kappa_{\phi}\nabla^{2}\phi-\frac{\partial f}{\partial\phi}\right] \qquad (8)$$

$M(c)$ is the chemical mobility as a function of composition and atomic mobility,

$$M(c)=\frac{1}{V_{m}(c)}c(1-c)[c\beta_{Pb}+(1-c)\beta_{Sn}] \qquad (9)$$

214

M_ϕ is the phase-field mobility, κ and κ_ϕ are the gradient energy coefficients for c and ϕ variables.

4 Formulation for Fipy

The above governing equations were expanded and rewritten to fit in to the fipy description. This description utilizes the procedure described in the Fipy examples 9.1, 9.2, and 9.3. I write the partial derivatives of free energy terms w.r.t. c below.

$$f' = \frac{\partial f}{\partial c} = p(\phi)\left[f^{\alpha'}(c,T) - f^{\beta'}(c,T)\right] + f^{\beta'}(c,T) + \frac{W_B - W_A}{2}g(\phi) \tag{10}$$

$$f^{\alpha'} = f_A^\alpha(T) - f_B^\alpha(T) + RT\ln\left(\frac{c}{1-c}\right) + (1-2c)l_{A,B}^\alpha(T) \tag{11}$$

$$f^{\beta'} = f_A^\beta(T) - f_B^\beta(T) + RT\ln\left(\frac{c}{1-c}\right) + (1-2c)l_{A,B}^\beta(T) \tag{12}$$

So, Eq 10 can be rewritten in J/m^3 as;

$$f' = \frac{\partial f}{\partial c} = \frac{1}{V_m(c)}\left[p(\phi)G(T) + RT\ln\left(\frac{c}{1-c}\right) + (1-2c)\Delta l(T)p(\phi)\right]$$
$$+ \frac{1}{V_m(c)}\left[f_A^\beta(T) - f_B^\beta(T) + (1-2c)l_{A,B}^\beta(T)\right] + \frac{W_B - W_A}{2}g(\phi) \tag{13}$$

where,

$$G(T) = f_A^\alpha(T) - f_B^\alpha(T) - f_A^\beta(T) + f_B^\beta(T) \tag{14}$$

$$\Delta l(T) = l_{A,B}^\alpha(T) - l_{A,B}^\beta(T) \tag{15}$$

Now,

$$V_m^2(c)\nabla \cdot M(c)\nabla \frac{\partial f}{\partial c} = \nabla \cdot M(c)V_m(c)\big[G(T)+(1-2c)\Delta l(T)\big]\nabla p(\phi)$$

$$-2\nabla \cdot M(c)V_m(c)\big[\Delta l(T)p(\phi)+l_{A,B}^{\beta}(T)\big]\nabla c \tag{16}$$

$$+\frac{\nabla \cdot M(c)RTV_m(c)}{c(1-c)}\nabla c + \nabla \cdot M(c)V_m^2(c)\left[\frac{W_A-W_B}{2}\nabla g(\phi)\right]$$

Here I write the governing equation for composition (Eq. 7) in Fipy compatible terms. Introducing a parameter $M(c)=Dc(1-c)/V_m(c)RT$ or $M(c)V_m(c)=Dc(1-c)/RT$,

$$\frac{\partial c}{\partial t} = \overbrace{\nabla \cdot (D\nabla c)}^{\text{diffusionTerm}}$$

$$+\nabla \cdot \left[c\frac{D(1-c)}{RT}\left(\overbrace{\big[G(T)+(1-2c)\Delta l(T)\big]p(\phi)+\frac{V_m(c)(W_A-W_B)}{2}\nabla g(\phi)}^{\text{phaseTransformation}}\right)\right]$$

$$-\nabla \cdot \left[c\frac{D(1-c)}{RT}\left(\underbrace{\big[2\Delta l(T)p(\phi)+2l_{A,B}^{\beta}(T)\big]\nabla c}_{\text{counterDiffusion}}\right)\right] \tag{17}$$

$$-\underbrace{\nabla \cdot \left[\frac{Dc(1-c)V_m(c)}{RT}\nabla(\nabla \cdot \kappa \nabla c)\right]}_{\text{chTerm}}$$

For the phase-field variable (Eq. 8), the same approach was followed as described in Fipy examples, where an implicit source term was used.

$$S=-\frac{\partial f}{\partial \phi}=-\big[p'(\phi)\big[f^{\alpha}(c,T)-f^{\beta}(c,T)\big]+Wg'(\phi)\big] \tag{18}$$

$$m_{\phi}=-\big[W(1-2\phi)+30\phi(1-\phi)E\big] \tag{19}$$

where, $W=(1-c)\frac{W_A}{2}+c\frac{W_B}{2}$ and $E=\frac{1}{V_m(c)}*\big[f^{\alpha}(c,T)-f^{\beta}(c,T)\big]$

APPENDIX E
METHODOLOGY FOR MECHANISM BASED LIFE PREDICTION MODEL FOR THERMAL BARRIER COATINGS

1 Introduction

Thermal barrier coatings (TBCs) are widely used in gas turbine applications for thermal insulation as well as external protection against hot corrosion and oxidation to the load bearing superalloys. Due to their ability to sustain a high thermal gradient, TBCs are crucial in extending the life of alloy components in the hottest sections of the turbine engine. Over the past thirty years the turbine industry has experienced a substantial increase in the maximum gas temperature at a turbine airfoil, and much of it can be accredited to the development of materials for TBCs. As envisaged from the current trend, further increase in gas temperature would require new generation "prime reliant" TBCs for enhanced protective performance and durability.

There are four primary constituents of a TBC system: the superalloy substrate, the oxidation resistant bond coat containing aluminum, a thermally grown oxide (TGO) layer predominantly made of alumina, and the ceramic top-coat. The substrate is generally a nickel- or cobalt- based superalloy, which contains many other alloying elements for properties such as high-temperature strength, ductility, oxidation resistance, hot corrosion resistance, etc. The bond coat is an oxidation resistant metallic layer that is typically made of MCrAlY (M=Ni and/or Co) or β-NiAl additions such as Pt. The primary role of the bond coat is to act as a reservoir of aluminum in order to form and maintain the TGO between the top-coat and itself. Oxidation of aluminum occurs by the ingress of highly mobile oxygen ions from the engine environment to the bond coat through the ceramic top-coat. Typically, yttria-stabilized zirconia (YSZ) is used as the top-coat material and provides thermal insulation. Lowest thermal conductivity at elevated temperature, high thermal expansion coefficient, good hardness and high melting point are some of the properties, which make YSZ the most suitable material for the top-coat.

Failure of TBCs affects the lifetime of hot-section components and has been the focus of research for last few decades. Though there are numerous factors responsible for the failures and their mechanisms are varied, the most important among them are the interdiffusion of alloying elements that causes continuous change in compositions, microstructures and interfacial morphology, oxidation, thermal expansion mismatch stresses, etc. For example, bond coats typically contain aluminum rich high-temperature phases, e.g. B2-β (NiAl) or L1$_2$-γ' (Ni$_3$Al) dispersed in a fcc-γ matrix. Dissolution of β or γ' phase occurs due to the depletion of Al content of the coatings by selective oxidation and/or coating-substrate interdiffusion, which ultimately causes the failure of the coating. Interdiffusion can also cause Kirkendal porosity at the interface leading to the failure of the coating. Diffusion of elements added to the superalloy substrate for high temperature strengthening also can adversely affect the mechanical properties at the interface and deteriorate the formation and adherence qualities of the oxide layer. Other critical phenomena that are associated with TBC failures include sintering of ytrria-stabilized zirconia (YSZ) topcoat, (t'→f+m) phase transformations in the YSZ topcoat and fracture at the YSZ/TGO and TGO/bond coat interfaces.

Because of the highly cost intensive nature of gas turbine manufacturing processes, various life-prediction models have been increasingly preferred over usual testing methods to predict the TBC life. There are semiempirical models also developed for life prediction, which are mostly used in industries, but they lack a mechanism-based approach. The complexities associated with different failure mechanisms, presence of a large number of operating variables as well as interactions and behavior of various constituents in a truly multicomponent environment, make it extremely challenging for these models to be fundamentally successful. In this regard, finite

element based continuum models show some promise as far as the understanding of the failure mechanisms is concerned.

This Appendix presents a methodology for using the phase-field approach to model critical phenomena associated with TBC failure, namely sintering of YSZ topcoat, (t'→f+m) phase transformations in YSZ topcoat, high temperature oxidation (i.e., growth of thermally grown oxide, TGO) of bond coats, multicomponent-multiphase interdiffusion between bond coats and superalloy substrate, and fracture at the YSZ/TGO and TGO/bond coat interfaces. Conceptual and mathematical descriptions of phase-field model are presented with specific formulation for these critical degradation phenomena. Results from modeling of microstructure evolution due to multiphase-multicomponent interdiffusion between bond coat and superalloy substrates are highlighted with an emphasis on composition-dependent interdiffusion. Typically, in practice, interdiffusion behavior between materials is investigated by means of diffusion couple experiments. Therefore, the simulation of interdiffusion behavior and evolution of microstructure has been performed by utilizing the phase-field model in diffusion couples of binary and ternary systems, e.g. Ni-Al and Ni-Cr-Al. Simulations were carried out on single-phase vs. single-phase, single-phase vs. two-phase and two-phase vs. two-phase diffusion couples using the available thermodynamic and kinetic data. Microstructure was characterized based on the movement of boundaries in the diffusion couples and dissolution or formation of phases across the boundary. Simulated composition profiles and diffusion paths were obtained and analyzed to study the interdiffusion behavior. The dissolution kinetics of the second phase in single-phase vs. two-phase diffusion couples were investigated and compared with the experimental results reported in the literature.

2.1 *Phase-field Model For Interdiffusion and Microstructure Evolution Between The Bond Coat and Super Alloy*

Application of phase-field model to simulate interdiffusion and microstructure evolution in Ni-Al and Ni-Cr-Al diffusion couples was described in Chapter 5 and 6, respectively. These diffusion couples simulations can correlate to the interaction between the bond coat and super alloy substrate. Hence, the phase-field model will not be described further here.

2.2 *Phase-field Model For Sintering*

The high compliance and strain tolerance properties of YSZ topcoat are due to the deliberately engineered porosity and micro-cracks. Prolonged exposure to high temperature can induce sintering, thereby closing the pores and cracks. Sintering also increases the thermal conductivity and deteriorates the insulating ability of the YSZ. There are many efforts to model general sintering phenomena by phase-field model, which can be employed to model and predict sintering in TBCs.

In simulating solid-state sintering, a phase-field model must be able to integrate two important features. First, it should be able to account for different diffusion mechanisms such as grain boundary, surface and bulk diffusion. Secondly, it should incorporate the forces due to rigid-body motion. The driving force for rigid body motion arises due to the movement of atoms away from and vacancies towards the grain boundaries. The system can be represented by means of a density (ρ) field and an order parameter field (η). The kinetic evolution equations follow from the aforementioned Cahn-Hilliard and Allen-Cahn equations and can be written as

$$\frac{\partial \rho}{\partial t} = \nabla \cdot \left[D\nabla \frac{\delta F}{\delta \rho} - \rho v_{\text{adv}} \right] + \xi_p(\text{r},t), \tag{1}$$

and

$$\frac{\partial \eta(\alpha)}{\partial t} = -L\frac{\delta F}{\delta \eta} - \nabla \cdot \left[\eta(\alpha)v_{\text{adv}}(\alpha)\right] + \xi_\eta(r,t;\alpha) \qquad (2)$$

where α stands for the number of particles, v_{adv} is the advection velocity field defined as

$$v_{\text{adv}} = \sum_\alpha v_{\text{adv}}(\alpha) = \sum_\alpha \left[v_t(\alpha) + v_r(\alpha)\right]. \qquad (3)$$

$v_t(r,t;\alpha)$ and $v_r(r,t;\alpha)$ are the velocity fields for translation and rotation of α particle. $\xi_p(r,t)$, and $\xi_\eta(r,t;\alpha)$ are the thermal fluctuations. The diffusivity D is a combination of bulk (D_{vol}), vapor (D_{vap}), surface (D_{surf}) and grain boundary (D_{gb}) diffusivities and is a function of phase-field variables:

$$\begin{aligned} D &= D_{\text{vol}}\phi(\rho) + D_{\text{vap}}\left[1-\phi(\rho)\right] + D_{\text{surf}}\rho(1-\rho) \\ &+ D_{\text{gb}}\sum_\alpha \sum_{\alpha' \neq \alpha} \eta(\alpha)\eta(\alpha') \end{aligned} \qquad (4)$$

where $\phi = \rho^3\left(10 - 15\rho + 6\rho^2\right)$.

2.3 Phase-field Model For Phase Transformation In YSZ

One of the factors critical for the durability of the YSZ topcoat is the presence of the metastable tetragonal prime phase (t'-ZrO$_2$), which is formed by a rapid quenching during the manufacturing process and greatly delays phase transformation to equilibrium room temperature phases. But after an extended period of exposure to high temperature, this metastable phase transforms into a mixture of tetragonal (t) and fluorite-cubic (f) phases. The high temperature

222

equilibrium tetragonal phase then transforms into monoclinic phase upon cooling with a molar volume expansion of 3-5%, and leads to delamination and spallation of the topcoat.

For the phase transformation from t'→t+f→m+f phases, the chemical free energy in the phase-field model should be a function of the density and a structure order parameter which corresponds to the orientation variants of the transformations. These kinds of models have been used for cubic to tetragonal and hexagonal to orthorhombic phase transformations. For example, during a cubic→tetragonal transformation, there are three independent orientation variants represented by the order parameters η_1, η_2 and η_3. The Landau polynomial expansion of the free energy for a binary system can be represented by

$$
\begin{aligned}
f(c,\eta_1,\eta_2,\eta_3) = &\frac{1}{2}A_1(c-c_1)^2 + \frac{1}{2}A_2(c-c_2)^2(\eta_1^2+\eta_2^2+\eta_3^2) - \\
&\frac{1}{4}A_3(\eta_1^4+\eta_2^4+\eta_3^4) + \frac{1}{6}A_4(\eta_1^2+\eta_2^2+\eta_3^2)^3
\end{aligned}
\tag{5}
$$

where c is the average composition, c_1 and c_2 are the compositions of phases present. The strain energy associated with the transformation is then included in the model following the approach described in section 3.2.3.

2.4 Phase-field Model For Spallation Fracture

Fracture or spallation at the YSZ/TGO and TGO/bond coat interfaces cause final failure of TBCs. Phase-field model has been previously applied successfully to model dynamics of fracture in materials. This is done by coupling the displacement field to a scalar field, which distinguishes between "broken" and "unbroken" states of the system and includes macroscopic elasticity in its description.

Considering the displacement field u as a scalar (in one direction), the elastic energy is expressed by:

$$E = \frac{1}{2} \int \mu \bar{\varepsilon}^2 dx \tag{6}$$

where μ is the elastic constant, $\bar{\varepsilon} = \nabla u$ is the strain and ε_c is the critical strain at which the elastic energy becomes strain independent. Assigning a phase-field variable ϕ that defines the broken or unbroken state of the system, the total free energy is then defined by:

$$F = \int \left[w(\phi) + \frac{1}{2} \kappa (\nabla \phi)^2 + \frac{\mu}{2} g(\phi)(\bar{\varepsilon}^2 - \varepsilon_c^2) \right] dx, \tag{7}$$

where $w = \frac{1}{4} \phi^2 (1-\phi)^2$ is a double well potential function and $g(\phi) = \phi^3(4-3\phi)$ is a weight function. The evolution equations for the phase-field and the displacement field are expressed by

$$\tau \frac{\partial \phi}{\partial t} = \kappa \nabla^2 \phi - w'(\phi) - \frac{\mu}{2} g'(\phi)(\bar{\varepsilon}^2 - \varepsilon_c^2) \tag{8}$$

and

$$\rho \frac{\partial^2 u}{\partial t^2} + b \frac{\partial u}{\partial t} = \mu \nabla \cdot \left[g(\phi)\left(1 + \eta \frac{\partial}{\partial t}\right) u \right], \tag{9}$$

where b is a coefficient for the Stokes drag term and η is the viscosity.

2.5 Phase-field Model For Oxidation and TGO Growth

Again a phase-field model can be used to model oxidation process to form TGO. The model approach is similar to that is described earlier in this section. The requirements of the model dictate that along with the composition field variable, we need to have a phase-field variable that distinguishes between the vapor phase and the solid phases present in the system, including the oxide. Such a model also needs to account for the mechanical balance of stresses generated during the oxidation. When the free energy and the stress state are represented by the functions of field variables, the evolution equation follows generalized diffusion and TDGL equations. Using this kind of model, oxidation of zirconium has been modeled by Ammar et. al.. They derived the evolution equations in the form

$$\dot{c} = -\nabla \cdot \left(-L(\phi)\nabla\mu\right) = -\nabla \cdot \left(-L(\phi)\nabla\frac{\partial f}{\partial c}\right) \tag{10}$$

$$\nabla \cdot \overline{\xi} + \pi = -\beta\dot{\phi} + \alpha\Delta\Phi - \frac{\partial f}{\partial \phi} = 0 \tag{11}$$

where $L(\phi)$ is related to diffusivity, β is the phase-field mobility, π is an internal microstress and $\overline{\xi}$ is a vector microstress.